

https://dspace.org/

Cobalt and iron supported on carbon spheres catalysts for Fischer Tropsch synthesis

Moyo, Mahluli

2012-07-19
http://hdl.handle.net/10539/11697

Downloaded from a DSpace repository. https://dspace.org/

COBALT AND IRON SUPPORTED ON CARBON SPHERES CATALYSTS FOR FISCHER TROPSCH SYNTHESIS

Mahluli Moyo

A thesis submitted to the Faculty of Engineering and the Built Environment, University of the Witwatersrand, Johannesburg, in fulfilment of the requirements for the degree of Doctor of Philosophy.

Johannesburg, 2012

DECLARATION

I declare that the work presented in this thesis was carried out by myself under the supervision of Professor Linda L. Jewell and Professor Neil. J. Coville. It is being submitted for the degree of Doctor of Philosophy at the University of the Witwatersrand, Johannesburg. It has not been submitted before for any degree or examination to any other University.

.....
Mahluli Moyo

On this…….day of ……2012

ABSTRACT

Gas-to-liquid (GTL) and coal-to-liquid (CTL) technologies are increasingly becoming important in the future of synthetic fuels. Fischer-Tropsch (FT) synthesis, with a history that dates back over 80 years is a promising route for the production of liquid fuels from coal, natural gas and biomass feed stocks. One of the challenging elements in the Fischer-Tropsch synthesis has been the development of active catalysts. In this study we investigate carbon spheres (CSs) and nitrogen doped carbon spheres (NCSs) as potential supports for Co and Fe FT catalysts.

CSs of average size 480 nm, were produced from acetylene gas by a chemical vapour deposition method. It was found that the as-synthesised CSs are thermally stable up to 560 ^{o}C in air and are purely carbonaceous materials (C > 95%). Functional groups (-OH, -COOH, etc), were introduced on CSs using $KMnO_4$ and HNO_3 functionalising agents and were characterised by FTIR spectroscopy, alkalimetry and TGA. Co metal was loaded onto the differently functionalised CSs using the deposition-precipitation (DPU) method and the Co/CS catalysts were tested for FT activity. Fischer-Tropsch (FT) studies, revealed striking differences in activity and selectivity for the HNO_3 and $KMnO_4$ functionalised catalysts. Investigation of the role of Mn (0.05 %) and K (0.05 %) on Co/CS FT catalysts functionalised with HNO_3 revealed that manganese inhibited the cobalt catalysed hydrogenation reactions and increased C_{5+} and olefin product selectivity. The results revealed that residual MnO_4^- ions from the surface functionalisation reaction impacted on the physical (TPR, TGA) and chemical (FT selectivity) properties of the $KMnO_4$ functionalised CS and Co/CS materials.

In other studies CS spheres were synthesised by a hydrothermal synthesis method in an autoclave (CS_{hydr}). The as-synthesised carbon materials were found to contain large amounts of oligomeric and polymeric compounds as by-products.

The as-synthesised materials were characterised by Raman spectroscopy, TGA, BET, XRD and TEM. The effect of annealing CS_{hydr} to remove volatile by-products was investigated by varying annealing temperature from 250 to 800 ^{o}C under N_2. It was found that annealing these materials at a temperature higher than 450 ^{o}C completely removes oligomeric and polymeric compounds and in turn increases the surface area from 1.8 to 433 m^2/g. Furthermore, the presence of these by-products was investigated on the FT activity and selectivity of Co/CS_{hydr} catalysts. The results showed that the use of cleaner CS_{hydr} as Co supports gave more active FT catalysts.

Studies on nitrogen-doped carbon spheres (NCSs) as supports for Fe FT catalysts were also performed. NCSs were synthesised by three different methods; (i) a chemical vapour deposition (CVD) method in a vertically aligned furnace at 900 ^{o}C, for 30 min, (NCS_{ver}) (ii) a CVD method in a horizontally aligned furnace at 950 ^{o}C, for 1 h (NCS_{hor}) and (iii) a hydrothermal synthesis method carried out at 190 ^{o}C for 4 h (NCS_{hydr}). The as-synthesised carbon spheres showed different chemical and physical properties. XPS results showed that NCS_{ver} contained mainly pyridinic nitrogen groups, while the NCS_{hor} sample contained equal ratios of pyridinic and quaternary nitrogen. NCS_{hydr} contained entirely pyrolic nitrogen. Varying amounts of oxygen functionalities were also detected in all these samples. NCS_{hydr} showed the highest oxygen concentration (24.3 %) as a result of using sucrose as a carbon source in this sample. NCS_{hor} and NCS_{ver} samples showed lower oxygen concentrations (5.9 % and 3.6 % respectively). The presence of oxygen in the CVD synthesized NCSs was a result of oxygen uptake from the atmosphere when these materials were exposed to air. The synthesised NCSs were compared for their use as supports for FT Fe catalysts. It was found that Fe/NCS_{ver} catalysts showed the highest FT activity (% CO conversion = 49.1 %) when compared to its counterparts (with % CO conversion = 40.1 % and 43.7 % for NCS_{hor} and NCS_{hydr} respectively) under identical experimental conditions.

DEDICATION

I would like to dedicate this Thesis to:-

- My father (Edgar Moyo), Mother (Barbara Ndlovu Moyo) who have supported and motivated me through these years.
- My young brothers (Mthokozisi Moyo and Mthabisi Moyo) and my sisters (Thobekani Moyo and Thokozani Moyo) who have been very supportive.
- All my uncles, aunts and friends who have also been very supportive.
- My late grandmother (Cathrine Nkomazana Moyo). She would have loved to see this day.

ACKNOWLEDGEMENTS

I would like to acknowledge the following people for their input on this work:-

- My supervisors Professor Linda L. Jewell and Professor Neil J. Coville for their guidance, ideas, patience, support and much more throughout this project.
- Mr Basil Chassoulas for all the technical assistance.
- NRF, The University of the Witwatersrand Postgraduate Merit Award, The Bradlow scholarship and the Andrew W. Mellon Postgraduate Mentoring Program for financial assistance.
- Mr Rudolf M. Erasmus for helping with the Raman analysis.
- Mr Michael Philpott from the Institute for Soil, Climate and Water, Pertorial for C, H and N elemental analysis.
- The CSIR for XPS analysis
- Professor Mike Witcomb for TEM analysis
- Dr Paul Frankline for HRTEM analysis
- The School of Chemical and Metallurgical Engineering and the Molecular Sciences Institute, school of Chemistry for giving me the grounds to conduct this research.
- Ahmed Shaikjee for proof reading my work
- Michelle, Natsayi and Matthew for helping with XRD analysis
- Catalysis-materials-organometallics group (CATOMAT).
- The Catalysis Society of South Africa (CATSA) for international conference travel grant.
- God almighty for the all the guidance he has given me throughout my life.

Publications and Presentations

Publications

1. Mahluli Moyo, Myriam A.M. Motchelaho, Haifeng Xiong, Linda L. Jewell, Neil J. Coville, "Promotion of Co/carbon sphere Fischer-Tropsch catalysts by residual K and Mn from carbon oxidation by $KMnO_4$" **, Applied Catalysis A: Gen. 413 (2012) 223– 229.**

2. Haifeng Xiong, Mahluli Moyo, Matthew K. Rayner, Linda L. Jewell, David G. Billing, and Neil J.Coville, "Autoreduction and Catalytic Performance of a Cobalt Fischer–Tropsch Synthesis Catalyst Supported on Nitrogen-Doped Carbon Spheres" , **ChemCatChem 2 (2010) 514 – 518.**

3. Myriam A.M Motchelaho, Haifeng Xiong, Mahluli Moyo, Linda L. Jewell and Neil J. Coville, "Effect of acid treatment on the surface of multi-walled carbon nanotubes prepared from Fe-Co supported on CaCO3: Correlation with Fischer-Tropsch catalyst activity", **Journal of Molecular Catalysis A: Chemical 335 (2011) 189-198.**

4. Haifeng Xiong, Myriam A.M Motchelaho, Mahluli Moyo, Linda L. Jewell and Neil J. Coville, "Correlating the preparation and performance of cobalt catalysts supported on carbon nanotubes and carbon spheres in the Fischer-Tropsch synthesis", **Journal of Catalysis 278 (2011) 26-40**.

5. Haifeng Xiong, Mahluli Moyo, Myriam A.M. Motchelaho, Linda L. Jewell and Neil J. Coville, "Fischer-Tropsch synthesis over model iron catalysts supported on carbon spheres: the effect of iron precursor, support pre-treatment, catalyst preparation method and promoters" **Applied Catalysis A., 388 (2010) 168-178.**

6. Mahluli Moyo, Myriam A.M. Motchelaho, Haifeng Xiong, Linda L. Jewell, Neil J. Coville, "Fe supported on N-doped carbon spheres: effect of carbon spheres synthesis method", **to be submitted.**

Presentations and awards

1. Mahluli Moyo, "Promotion of Co/carbon sphere Fischer-Tropsch catalysts by residual K and Mn from carbon oxidation by $KMnO_4$", Oral presentation, CATSA conference, 11 -13 Nov 2011.

2. Mahluli Moyo, "Cobalt supported carbon spheres catalysts for Fischer-Tropsch synthesis", Poster Presentation, EuropaCat X conference, Glasgow, 28 Aug-2 Sep 2011.

3. Mahluli Moyo, "Iron supported N-doped CSs for Fischer-Tropsch synthesis", Poster presentation, Catsa conference, 7-10 Nov 2010.

4. Mahluli Moyo, "Cobalt supported CS_{hydr} for Fischer-Tropsch synthesis", Oral presentation, SANI symposium Johannesburg, 7 may 2010. **1st prize**

5. Mahluli Moyo, "Cobalt supported carbon spheres catalysts for Fischer-Tropsch synthesis, Poster presentation. Catsa conference. Nov 2009 **2nd prize**

6. Mahluli Moyo, "Cobalt supported carbon spheres catalysts for Fischer-Tropsch synthesis", Oral presentation, Wits postgraduate symposium, Faculty of Engineering and the Built Environment, Nov 2008. **2nd prize**

7. Mahluli Moyo, "Synthesis and functionalisation of carbon spheres", Poster presentation, Wits symposium (poster day), Faculty of Engineering and the Built Environment. Nov 2007. .
1st prize

CONTENTS

DECLARATION i
ABSTRACT ii
DEDICATION iv
ACKNOWLEDGEMENTS v
PUBLICATIONS AND PRESENTATIONS vi
LIST OF FIGURES xii
LIST OF TABLES xvii
LIST OF SYMBOLS xviii

Chapter 1: Introduction.

1.1 Overview 1
1.2 Aims and objectives of the study 4
1.3 Thesis outline 5
References 6

Chapter 2: History and Literature Review.

2.1 Introduction 8
2.2 History and Background 8
2.3 Literature Review 11
2.3.1 Fischer-Tropsch Synthesis (FTS) 11
2.3.2 Fischer-Tropsch reaction 12
2.3.3 Proposed molecular mechanisms for FT catalytic conversion of syngas 15
2.3.4 FT product distribution 20
2.3.5 Factors affecting product selectivity 24
2.3.6 FT catalysts 25
2.3.7 Supported FT catalysts 26
2.3.8 Effects of metal precursor crystallite size 27
2.3.9 Deactivation of FT catalysts 29
2.3.10 Catalyst preparation methods 31
2.4 Catalyst support materials 33
2.4.1 Carbon 33
2.4.2 Mechanism of formation of carbon spheres 35
2.4.3 Carbon materials as catalyst supports 37
References 39

Chapter 3: Experimental methods.

3.1 Introduction 47
3.2 Synthesis of carbon spheres (CSs) 47
3.2.1 Chemical vapour deposition method (CVD) in a horizontally aligned furnace 47
3.2.2 Chemical vapour deposition method (CVD) in a vertically aligned furnace 48
3.2.3 Hydrothermal synthesis of carbon spheres 49
3.3 Catalyst characterisation equipment 49
3.3.1 Transmission electron microscopy (TEM) 49
3.3.2 Thermo-gravimetric analysis (TGA) 50
3.3.3 Brunnet Emmett Teller (BET) analysis 51
3.3.4 Temperature programmed reduction (TPR) 52
3.3.5 Chemisorption 53
3.3.6 Raman spectroscopy 54
3.3.7 X-ray diffraction (XRD) 55
3.3.8 Fourier Transform Infra Red spectroscopy (FT-IR) 56
3.3.9 X-ray photoelectron spectroscopy (XPS) 57
3.3.10 Elemental analysis (C, H and N) 57
3.4 Reactor studies 57
3.4.1 Gases 57
3.4.2 Catalyst evaluation 57
3.4.3 Gas chromatography calibration and product analysis 61
3.4.4 Mass balance calculations 64
References 71

Chapter 4: Synthesis, functionalisation and characterisation of carbon spheres.

4.1 Synthesis of carbon spheres 73
4.1.1 Introduction 73
4.1.2 Experimental 74
4.1.3 Results and discussion 75
4.2 Functionalisation of the carbon spheres 78
4.2.1 Introduction 78
4.2.2 Experimental 81
4.2.3 Results and discussion 82
4.3 Characterisation of active acid sites 86
4.3.1 Carbon spheres functionalisation by 55 % HNO_3 86
4.3.2 Carbon spheres functionalisation by $KMnO_4$ 91
4.4 Conclusions 96
References 98

Chapter 5: Preparation and characterisation of cobalt supported on carbon spheres (Co/CS) as Fischer-Tropsch catalysts.

5.1 Introduction 100
5.2 Preparation and characterisation of Co/CS catalyst 103
5.2.1 Experimental 103
5.2.2 Characterisation of Co/CS catalysts 103
5.3 Catalyst evaluation for Fischer-Tropsch synthesis 122
5.3.1 Experimental 122
5.3.2 Results and Discussion 123
5.4 Conclusions 128
References 130

Chapter 6: Cobalt supported on hydrothermally synthesised carbon spheres (Co/CS_{hydr}) for Fischer-Tropsch synthesis.

6.1 Facile hydrothermal synthesis of carbon spheres (CS_{hydr}) 133
6.1.1 Introduction 133
6.1.2 Experimental 134
6.1.3 Results and Discussion 135
6.2 Cobalt supported on CS_{hydr} Fischer-Tropsch catalysts 148
6.2.1 Results and Discussion 148
6.3 Conclusions 153
References 154

Chapter 7: Preparation and characterisation of iron supported on N-doped carbon spheres (Fe/NCSs) as Fischer-Tropsch catalysts.

7.1 Introduction 156
7.2 Experimental 159
7.2.1 Synthesis of N-doped CSs 159
7.2.2 Fe metal loading on N-doped CSs 160
7.2.3 Characterisation of NCS and 5 % Fe/NCS catalysts 161
7.2.4 Catalysts evaluation in FTS 162
7.3 Results and Discussion 163
7.4 Conclusions 180
References 182

Chapter 8: Conclusions. 184

APPENDIX A 189
APPENDIX B 191
APPENDIX C 196
APPENDIX D 200

LIST OF FIGURES

Figure 1.1	Projected world liquid fuels supply and demand [1]	2
Figure 1.2	History of crude oil price [1]	2
Figure 2.1	Industrial process overview for the production of fuels and chemicals by FTS [8]	12
Figure 2.2	Schematic diagram of the alkyl mechanism showing (a) methylene formation, (b) chain initiation, (c) initial chain growth and (d) chain propagation [28]	17
Figure 2.3	Schematic diagram of the -CO insertion mechanism [23]	18
Figure 2.4	Schematic diagram showing the enol mechanism [23, 31]	19
Figure 2.5	Schematic diagram of vinyl/alkenyl mechanism (a) chain initiation, (b) chain growth and methylene insertion, (c) chain propagation. [28]	20
Figure 2.6	Theoretical product selectivity as a function of chain growth probability [47-48]	24
Figure 3.1	Image of horizontal furnace equipment	48
Figure 3.2	Image of CVD vertical furnace equipment	49
Figure 3.3	Image of FEI Tecnai G^2 Spirit TEM instrument	50
Figure 3.4	Image of PerkimElmer TGA 4000 instrument	51
Figure 3.5	Image of ASAP-2000 Tristar analyser BET instrument	52
Figure 3.6	Image of Micromeritics Autochem II TPR instrument	53
Figure 3.7	Image of Micromeritics ASAP 2020 Chemisorption instrument	54
Figure 3.8	Image of Jobin-Yvon T64000 Raman spectrometer	55
Figure 3.9	Image of Bruker D2 phaser XRD instrument	56
Figure 3.10	Image of Bruker Tensor 27 IR instrument	56
Figure 3.11	Flow sheet diagram of FT rig set up (insert: 6 way valve connecting to GC-FID and GC-TCD)	58
Figure 3.12	Schematic diagram of fixed bed reactor	60
Figure 3.13	(a) GC-FID and (b) GC-TCD trace of calibration gas with CH_4 (2.5%), C_2H_4 (0.2%), C_2H_6 (0.5%), CO (10.0%), CO_2	62

	(5.0%) and balance of Ar gas composition	
Figure 3.14	GC-TCD trace of syngas calibration H_2 (60%), N_2 (10%) and CO (30%)	63
Figure 4.1	Schematic diagram of the chemical vapour deposition equipment and reaction	74
Figure 4.2	Image of the bulk carbon spheres products	75
Figure 4.3	TEM images of as-synthesised CSs (a) single sphere and (b) accreted spheres (insert showing CSs diameter distribution)	75
Figure 4.4	Cartoon illustration of heat treatment of CSs	76
Figure 4.5	Shows SEM image of as-synthesised CSs	77
Figure 4.6	TGA of as-synthesised CSs run in air	77
Figure 4.7	Raman spectra of the synthesised CSs	78
Figure 4.8	Possible surface functional groups found on CSs [6]	80
Figure 4.9	(a) Typical potentiometric titration curve of functionalised CSs and (b) the derivative graph	83
Figure 4.10	Effect of sample size on the determination of end point	84
Figure 4.11	Effect of increasing volume	85
Figure 4.12	FTIR of (a) as-synthesised, CSs and 55 % HNO_3 functionalised CSs for (b) 96 h at room temperature (c) 24 h at 40 ^oC and (d) 2 h under reflux	86
Figure 4.13	TGA profiles run in nitrogen: Effect of functionalising conditions: (a) 55 % HNO_3/ 40 ^oC/ 24 h (b) 55 % HNO_3/ reflux/ 2 h (c) 55 % HNO_3/ reflux/ 24 h	90
Figure 4.14	TEM images after functionalising of the CSs with (a) 55 % HNO_3/ 40 ^oC/ 24 h (b) 55 % HNO_3/ reflux/ 2 h (c) 55 % HNO_3/ reflux/ 24 h	91
Figure 4.15	FTIR of (a) as-synthesised CSs (b) 0.5 M $KMnO_4$/ 4 h/ 25 ^oC (c) 1 M $KMnO_4$/ 4 h/ 40 ^oC and (d) 2 M $KMnO_4$/ 4 h/ 70 ^oC	92
Figure 4.16	TGA profiles run in nitrogen gas: Effect of functionalising conditions of (a) 0.5 M $KMnO_4$/ 40 ^oC/ 4 h (b) 1 M $KMnO_4$/ 70 ^oC/ 4 h (c) 2 M $KMnO_4$/ 70 ^oC/ 4 h	93
Figure 4.17	TEM images after functionalising with (a) 0.5 M $KMnO_4$/ 40 ^oC/ 4 h (b) 1 M $KMnO_4$/ 70 ^oC/ 4 h (c) 2 M $KMnO_4$/ 70 ^oC/4 h	94
Figure 4.18	TEM image of CSs functionalised by (a) 0.5 M $KMnO_4$/ 40 ^oC/ 4 h (b) 2 M $KMnO_4$/ 70 ^oC/ 4 h	95

Figure 4.19	HRTEM image of CSs functionalised by 0.5 M $KMnO_4$/ 40 ^oC/ 4 h	95
Figure 5.1	TEM images of 2.5 % Co/CS $KMnO_4$ functionalised catalysts	104
Figure 5.2	TEM images of 2.5 % Co/CS $KMnO_4$ functionalised catalysts	105
Figure 5.3	TGA profile run in air of (a) 5 % Co/CS catalysts functionalised by $KMnO_4$. (b) $KMnO_4$ functionalised CSs, (c) HNO_3 functionalised CSs and (d) 5 % Co/CS catalysts functionalised by HNO_3	106
Figure 5.4	XRD patterns for (a) As-synthesised CSs, (b) 2.5% Co/CS HNO_3 functionalised CS, (c) 2.5% Co/CS $KMnO_4$ functionalised CS	108
Figure 5.5	TGA profile run in air on the (a) HNO_3 functionalised CSs, (b) 5 % Co/CS catalysts functionalised by HNO_3, (c) $KMnO_4$ functionalised CSs and (d) 5 % Co/CS catalysts functionalised by $KMnO_4$	109
Figure 5.6	H_2-TPR profiles of (a) As-synthesised CSs, (b) 5% Co/CS HNO_3 functionalised CS, (c) 5% Co/CS $KMnO_4$ functionalised CS, (d) 5% Co/ 0.05%K/ HNO_3 functionalised CS and (e) 5% Co/0.05%Mn/ HNO_3 functionalised CS	112
Figure 5.7	XRD patterns for (a) As-synthesised CSs, (b) 5% Co/CS HNO_3 functionalised CS, (c) 5% Co/CS $KMnO_4$ functionalised CS (d) 5% Co/0.05% K/CS HNO_3 functionalised CS, and (e) 5% Co/0.05% Mn HNO_3functionalised CS	113
Figure 5.8	TEM images of (a) 5% Co/CS $KMnO_4$ functionalised and (b) 5% Co/CS HNO_3 functionalised catalysts	115
Figure 5.9	EDS spectrum of 5% Co/CS $KMnO_4$	119
Figure 5.10	TEM images of (a) 10% Co/CS $KMnO_4$ functionalised catalyst (b) 10% Co/CS HNO_3 functionalised catalyst	119
Figure 5.11	TGA profile run in air on the (a) HNO_3 functionalised CSs, (b) 10 % Co/CS catalysts functionalised by HNO_3, (c) $KMnO_4$ functionalised CSs and (d) 10 % Co/CS catalysts functionalised by $KMnO_4$	120
Figure 5.12	ASF distribution for (a) 5% Co/CS $KMnO_4$, (b) 5% Co/CS HNO_3, (c) 0.05% Mn/ 5 % Co/CS HNO_3 and (d) 0.05% K/ 5 % Co/CS HNO_3	124
Figure 5.13	Olefin selectivity for 5% Co/CSs	125

Figure 5.14	TEM images and particle size distribution of $KMnO_4$ functionalised catalyst after 120 h on stream	126
Figure 5.15	TEM images and particle size distribution of HNO_3 functionalised catalyst after 120 h on stream	127
Figure 6.1	TEM images of as-prepared CS_{hydr} (a) low magnification and (b) high magnification (insert: particle size distribution bar chart)	136
Figure 6.2	TGA and DTG profiles of as-synthesised CS_{hydr} and sucrose under air	137
Figure 6.3	Effect of annealing temperature (a) 250, (b) 350, (c) 450, (d) 600 and (e) 800 ^oC for 2.5 h under N_2 gas and size distribution for (i) 250, (ii) 450 and 600 ^oC annealed CS_{hydr}	138
Figure 6.4	TGA profiles (under air) of as-synthesised and 300, 450 and 600 ^oC annealed CS_{hydr} samples (2.5 h heating)	139
Figure 6.5	Effect of annealing temperature on surface area and pore volume	140
Figure 6.6	Effect of annealing temperature on surface area and crystallinity of CS_{hydr}	142
Figure 6.7	Effect of annealing temperature on G-bands	143
Figure 6.8	Example of computer deconvoluted G and D bands [12]	145
Figure 6.9	Effect of annealing temperature on I_{Di}/I_G-bands	145
Figure 6.10	Effect of annealing temperature on S-bands	146
Figure 6.11	XRD patterns of annealed CS_{hydr}	147
Figure 6.12	TEM images of (a) $Co250CS_{hydr}$, (b) $Co450CS_{hydr}$ and (c) $Co600CS_{hydr}$ and Co particle size distribution of (i) $Co450CS_{hydr}$ and (ii) $Co600CS_{hydr}$ catalysts	149
Figure 6.13	TGA profiles of (a) $Co250CS_{hydr}$, (b) $Co450CS_{hydr}$ and (c) $Co600CS_{hydr}$ catalysts	150
Figure 6.14	ASF plot of Co/CS_{hydr} catalysts	152
Figure 7.1	TEM images of (a) NCS_{ver} (b)NCS_{hor} and (c) NCS_{hydr} and size distribution of (i) NCS_{ver} (ii)NCS_{hor} and (iii) NCS_{hydr}	164
Figure 7.2	Raman spectra of NCSs	165
Figure 7.3	C1s spectrum of (a) NCS_{ver} , (b) NCS_{hor} and (c) NCS_{hydr}	168
Figure 7.4	N1s spectrum of (a) NCS_{ver} , (b) NCS_{hor} and (c) NCS_{hydr}	169

Figure 7.5	Nitrogen-based species that and their XPS binding energies [15]	170
Figure 7.6	TGA profiles of as-synthesised (a) NCS_{ver} (b) NCS_{hor} and (c) NCS_{hydr} run in air	171
Figure 7.7	TGA profiles of NCS_{ver} (a) before and (b) after annealing at 250 ^{o}C for 2 ½ h in N_2 gas	172
Figure 7.8	TEM images and particle size distribution for 5 % Fe supported on (a) NCS_{ver}, (b) NCS_{hor} and (c) NCS_{hydr}	174
Figure 7.9	TGA profiles run in air of (a) as synthesised NCSs (b) 5% Fe catalyst supported on (i) NCS_{ver}, (ii) NCS_{hor} and (iii) NCS_{hydr}	176
Figure 7.10	XRD patterns of (a) 5 % Fe/NCS_{ver} (b) 5 % Fe/NCS_{hor} (c) 5 % Fe/NCS_{hydr}	177
Figure 7.11	TEM images of (a) 5 % Fe/NCS_{ver} (b) 5 % Fe/NCS_{hor} (c) 5 % Fe/NCS_{hydr} and size distribution of (i) 5 % Fe/NCS_{ver} (ii) 5 % Fe/NCS_{hor} (iii) 5 % Fe/NCS_{hydr} after 120 h of FTS	179
Figure B1	Adsorption isotherm of H_2 uptake during chemisorption analysis	191
Figure B2	TGA profile of 5 % Co/CS run for 6 h under (a) air at 250 ^{o}C, (b) oxygen at 250 ^{o}C, (c) air at 300 ^{o}C and (d) oxygen at 300^{o}C	192
Figure B3	In-situ XRD patterns of reduction of Co_3O_4 phases in 5 % Co/CS HNO_3 catalyst at 350 ^{o}C for 24 h in 5 % H_2 (balance N_2 gas)	193
Figure B4	In-situ XRD patterns of oxidation of Co^0 phases in 5 % Co/CS HNO_3 catalyst in air	193
Figure B5	Temperature programme for the oxidation of Co^0 phases in 5 % Co/CS HNO_3 catalyst in air	194
Figure B6	% CO conversion of 5 % Co/CS catalysts	195
Figure C1	Raman spectra of CS_{hydr} annealed at 250 ^{o}C under N_2 for 2.5 h	196
Figure C2	Raman spectra of CS_{hydr} annealed at 350 ^{o}C under N_2 for 2.5 h	196
Figure C3	Raman spectra of CS_{hydr} annealed at 400 ^{o}C under N_2 for 2.5 h	197
Figure C4	Raman spectra of CS_{hydr} annealed at 450 ^{o}C under N_2 for 2.5 h	197
Figure C5	Raman spectra of CS_{hydr} annealed at 600 ^{o}C under N_2 for 2.5 h	198
Figure C6	Raman spectra of CS_{hydr} annealed at 800 ^{o}C under N_2 for 2.5 h	198

LIST OF TABLES

Table 2.1	Effect of different operating parameters on product distribution [49]	24
Table 4.1	Effect of increasing reaction time and temperature during nitric functionalisation	88
Table 4.2	Effect of functionalising CSs with $KMnO_4$ for 4 h	93
Table 4.3	Effect of functionalising CSs with a 1:2 mixture of 1 M $KMnO_4$ and 55 % HNO_3 for 4 h	96
Table 5.1	N_2-physisorption results for CSs supports and 2.5% Co/CS catalysts	107
Table 5.2	Cobalt oxide crystallite particle size	109
Table 5.3	Cobalt oxide crystallite particle size	114
Table 5.4	N_2-physisorption results for CSs supports and 5% Co/CS catalysts	114
Table 5.5	Chemisorption results of 5% Co/CS catalyst	116
Table 5.6	N_2-physisorption results for CSs supports and 10 % Co/CS catalysts	121
Table 5.7	Summary of FTS catalytic performance of cobalt supported catalyst	124
Table 6.1	N_2-physisorption results of the prepared catalysts	151
Table 6.2	Summary of FTS catalytic performance of cobalt supported catalyst	152
Table 7.1	Shows NCSs size, N content and degree of graphitisation	165
Table 7.2	Summary of the elemental composition as determined by XPS	166
Table 7.3	Effect of NCSs on the iron oxide crystallite size	174
Table 7.4	FTS results of 5 % Fe/NCS catalysts	178

LIST OF SYMBOLS

ASF	Anderson-Schulz-Flory
BET	Brunauer-Emmett-Teller
C_2H_2	Acetylene
$CaCO_3$	Calcium carbonate
CaO	Calcium oxide
CCVD	Catalytic chemical vapour deposition
CVD	Chemical vapour deposition
CNFs	Carbon nanofibers
CNS	Carbon nitrogen sulfur analysis
CNTs	Carbon nanotubes
CO_2	Carbon dioxide
Co	Cobalt
CS	Carbon sphere
DWCNTs	Double walled carbon nanotubes
EDX	Energy dispersive X-ray spectroscopy
EM	Electron micscopy
Fe	Iron
FT	Fischer-Tropsch
FTS	Fischer-Tropsch synthesis
GC	Gas chromatography
GHSV	Gas hourly space velocity
h	Hour
H_2	Hydrogen
HNO_3	Nitric acid
H_2O_2	Hydrogen peroxide
$KMnO_4$	Potassium permanganate
mL/min	Millilitre per minute
N_2	Nitrogen
NCS	Nitrogen doped carbon spheres
nm	Nanometre
SBA	Mesoporous silica template
SWCNTs	Single walled carbon nanotubes
t	Time
TCD	Thermal conductivity detector
TEM	Transmission electron microscopy
TGA	Thermogravimetric analysis
TPR	Temperature programmed reduction
WGS	Water gas shift
wt. %	Weight percentage
α	Alpha value
Gb	Gigga barrels
Gbd	Gigga barrels per day

Chapter 1

Introduction

1.1 Overview

Crude oil derived fuels have for a long time dominated as a source of transport fuels [1]. Research has shown that crude oil is a finite and non-renewable resource, and in recent years there has been growing concern about the depleting global crude oil reserves [1].

Crude oil from currently producing fields, supplies approximately 85% of the global liquid fuel demand. However, estimates indicate a declining rate of 4.07 % per year of these reserves after the year 2010 (Fig. 1.1). Furthermore, the global fuel demand by the year 2030 is estimated at 45 Gigga barrels (Gb) per annum increasing from 31.2 Gb per annum in the year 2008 [1-2]. The additional increases are expected to come mostly from China and India [1].

The depleting crude oil reserves have in turn influenced the price increases of this commodity over recent years. Fig.1.2 shows a history of crude oil prices and price adjusted for USD inflation. These prices are expected to increase in the coming years; hence the age of cheap liquid fuels is coming to an end.

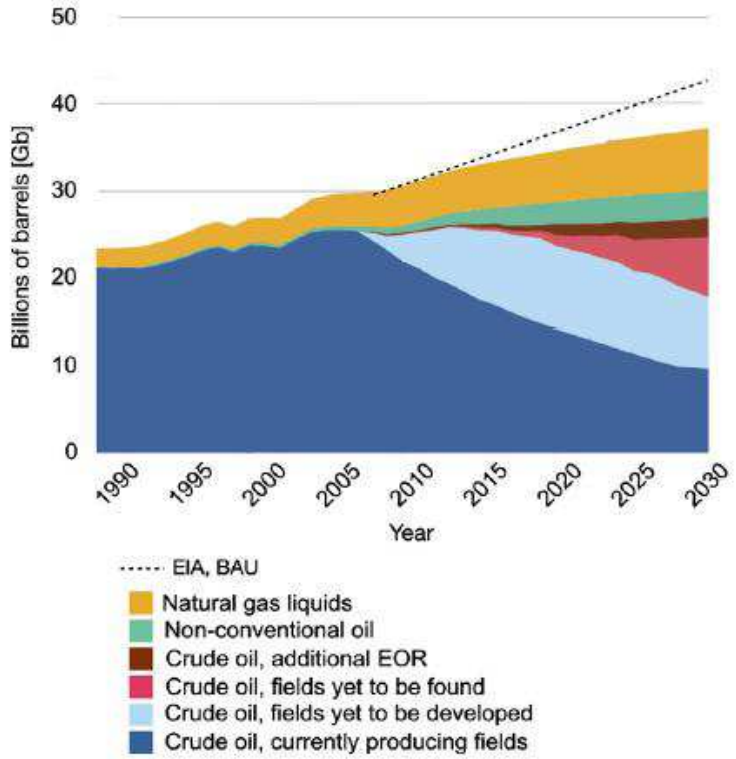


Figure 1.1: Projected world liquid fuels supply and demand [1]

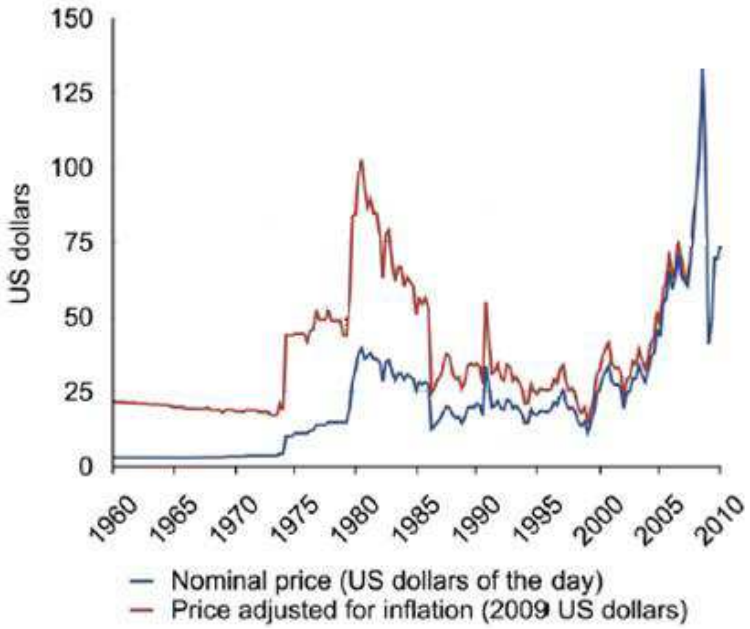


Figure 1.2: History of crude oil price [1].

The global demand for fuel will have to be met by alternative sources. Fischer-Tropsch synthesis (FTS) is one of the most promising routes for the production of liquid fuels and chemicals from the abundant natural gas, biomass and coal reserves. The Fischer-Tropsch reaction first discovered by Hans Fischer and Franz Tropsch in 1923 converts a mixture of H_2 and CO into hydrocarbons and oxygenates with a wide range of chain lengths and functional groups, over a metal catalyst [3]. Metals from group 8-10 of the periodic table especially cobalt, iron, nickel and ruthenium can catalyse this reaction. Co-based and Fe-based catalysts are the FT industrially preferred catalysts, due to their high activity, selectivity, availability, lower cost and longer life span [4].

Although Co and Fe are more abundant than other metals that catalyse the FT reaction, these metals are finite natural resources. Therefore, their use, by making the most of their physical properties in particle surface area needs to be maximised. One approach is to deposit small metal crystallites on a suitable support material. This also allows for cheaper catalysts to be produced. Many support materials have been used to support FT catalysts; these include silica, titinia, aluminia and carbon. A carbon support material has valuable properties not attainable by other conventional supports [5-6], these properties include: their chemically inert surface, thermal stability, relatively high mechanical strength and easy methods to tailor the pore sizes and the structure of carbon materials [5-6]. The metal phase can easily be recovered from the spent catalyst by simply burning off the carbon support.

Much research on the use of carbon materials as supports has been performed on carbon nanotubes (CNTs) [7-14], with few studies focusing on other shaped carbon materials such as carbon spheres (CSs). Although many similarities are expected when CSs are used as supports instead of CNTs, CSs are purer materials when produced by non-catalytic synthesis methods. Therefore CSs are novel model supports for studying metal-metal or metal-promoter interactions in the FT

reactions. In this study we have investigated carbon spheres (CSs) and nitrogen doped CSs (NCSs) as support materials for Co or Fe in FTS.

1.2 Aims and objectives of the study

(a) Synthesise carbon nano-spheres (CSs) by; (i) a non-catalytic chemical vapor deposition (CVD) method using acetylene gas as a carbon source. The synthesis of the CSs by the CVD method will be carried out using a horizontally aligned furnace; and (ii) a hydrothermal synthesis method in an autoclave using sucrose solution as a carbon source.

(b) Synthesise nitrogen doped carbon spheres (NCS) using three different synthesis methods; (i) a non-catalytic horizontally aligned furnace CVD method using acetylene as a carbon source and acetonitrile as a nitrogen source; (ii) a non-catalytic vertically aligned furnace CVD method using acetylene as a carbon source and acetonitrile as a nitrogen source; and (iii) a hydrothermal synthesis method in an autoclave using sucrose as a carbon source and urea as a nitrogen source. Their conditions were chosen to make CSs with a different range of diameters.

(c) Functionalise the CVD synthesised CSs using either; (i) 55 % HNO_3 or (ii) $KMnO_4$ functionalising agents and characterise the functionalised CSs. Characterisation techniques include: Transmission Electron Microscopy (TEM), Thermo-gravimetric analysis (TGA), alkalimetry, Raman spectroscopy, Fourier transform Infra Red spectroscopy (FTIR) and N_2 physisorption for surface area and pore volume (BET) measurements.

(d) Investigate the effect of annealing on the CS produced by a hydrothermal synthesis method in an autoclave.

(e) Deposit Co metal particles onto the functionalised CSs or annealed CSs using a deposition-precipitation method with urea as the precipitating agent (DPU). Characterise the synthesized catalysts by TEM, TGA, BET, H_2-Chemisorption and Temperature Programmed Reduction (TPR).

(f) Deposit Fe metal particles onto NCSs using a deposition-precipitation method with urea as the precipitating agent (DPU). Characterise the

synthesized catalysts by TEM, TGA, BET, H_2-Chemisorption and Temperature Programmed Reduction (TPR).

(g) Evaluate all synthesised catalysts for Fischer-Tropsch (FT) activity and selectivity.

1.3 Thesis outline

Chapter 2 presents a brief history of FTS and gives a general literature review of the FT process, the type of catalysts used, proposed FT reaction mechanisms, effects of metal precursor particle size on FTS etc. Chapter 3 describes the methodologies used to make the CSs and NCSs and the characterisation equipment and FT rig used in this work. Chapter 4 presents a study on the synthesis and functionalisation of CSs produced by a CVD method. Chapter 5 presents the use of the functionalised CSs as supports for Co catalysts. In Chapter 6, the hydrothermal synthesis of CSs using an autoclave is outlined. The effects of annealing on the as-synthesised CSs and their use as Co catalyst supports is also mentioned. Chapter 7: presents the study on the synthesis of NCSs and the use of NCSs as Fe supports for FTS. Chapter 8 gives the general conclusion deduced from the study and recommendations for further work.

The work reported in this thesis has been presented at a number of conferences and workshops (page vii). Studies reported in Chapter 4 and 5 have been published in the journal of Applied Catalysis A: General 413 (2012) p 223-229.

References

1. N.A Owen, O.R Inderwildi, D.A King, Energy Policy 38 (2010) 4743.
2. Energy Information Administration, International petroleum (oil) consumption: selected OECD countries, total OECD, and world total, years 1970–2007. (2009)
3. F. Fischer, H. Tropsch, Brennstoff Chem. 4 (1923) 276.
4. A.Y. Khodakov, W. Chu and P. Fongarland, Chem. Rev. 107 (2007) 1692.
5. G.M. Guldi, (2007) Nature 447 (2007) 7140.
6. F. Rodriguez-Reinoso, Carbon, 36 (1998) 159.
7. W. Chen, Z. Fan, X. Pan and X. Bao, JACS 130 (2008) 9414.
8. G.L. Bezemer, J.H. Bitter, H.P.C.E. Kuipers, H. Oosterbeek, J.E. Holewijn, X. Xu, F.Kapteijn, A. Jos van Dillen and K.P.de Jong. JACS 128 (2006) 3956.
9. J. Kang, S. Zhang, Q. Zhang, and Y. Wang, Angew. Chem. Int. Ed, 48 (2009) 2565.
10. M.C. Bahome, L.L. Jewell, K. Padayachy, D Hildebrandt, D Glasser, A.K. Datye, N.J. Coville, Appl. Catal. A: Gen. 328 (2007) 243.
11. M.C. Bahome, L.L. Jewell, D. Hildebrandt, D. Glasser, N.J. Coville, Appl. Catal. A: Gen. 287 (2005) 60.
12. M. Trépanier, A. Tavasoli, A.K. Dalai, N. Abatzoglou, Appl. Catal. A: Gen. 353 (2009) 193.
13. A. Tavasoli, R.M. Malek Abbaslou, M. Trépanier, A.K. Dalai, Appl. Catal. A: Gen. 345 (2008) 134.

14. R.M. Malek Abbaslou, A. Tavasoli, A.K. Dalai, Appl. Catal. A: Gen. 355 (2009) 33.

Chapter 2

History and Literature Review

2.1 Introduction

In this chapter both cobalt and iron catalysts are briefly discussed, although the main focus of this work is on cobalt FT catalysis.

2.2 History and Background

The history of catalytic hydrogenation reactions began in 1823 when Dobereiner discovered that finely divided platinum caused hydrogen to burn spontaneously in air [1]. Five decades later, scientists began investigating the catalytic properties of a wide range of metals which included palladium, iron, nickel, copper etc. They focused on hydrogenation reactions and hydrogen production from water and hydrocarbons. In 1902, Sabatier and Senderans, developed a number of catalysts for the hydrogenation of vapour phase organic compounds. These included the conversion of oleic to stearic acid and nitrobenzene to aniline. Most importantly they studied the synthesis of methane by the hydrogenation of CO and CO_2 over a cobalt or nickel catalyst at temperature of 180-200^{o}C and atmospheric pressure which can be thought of as a precursor of Fischer-Tropsch technology [2-3].

As early as 1923, Hans Fischer and Franz Tropsch who at the time worked at the

Wilhelm Institute in Germany, produced aliphatic oxygenated compounds from reacting syngas (CO and H_2) over alkalised iron chips at 400 ^oC and 150 bar pressure. They named this reaction the Fischer-Tropsch reaction (FT) and today the term "Fischer-Tropsch" applies to a range of similar reactions. The product from the FT reaction was transformed into "synthine", a mixture of hydrocarbons. One year later Fischer and Tropsch made an important breakthrough, when they discovered that heavy hydrocarbons could be synthesised from syngas over Fe/ZnO or Co/Cr_2O_3 at approximately 7 bar pressure [2].

A few years later Otto Roelen who had been working with Fischer and Tropsch at the Wilhelm Institute developed the homogeneously catalysed hydroformylation process for the industrial synthesis of aldehydes from alkenes and carbon monoxide [2].

After 1927 many chemical engineering problems associated with the FT reaction were tackled by scientists and a series of fixed bed reactors were developed for the FT process under Roelen's supervision. A FT process license was obtained in 1934 by Ruhrchemie and the FT process was commercialised two years later in Braunkohle-Benzin. During World War II, Germany used cobalt catalysts to produce liquid fuels from coal. The synthetic fuel capacity of Germany in early 1944 reached 124000 bpd. After World War II Arbeit-Gemeinschaft Lurgi and Ruhrchemie (ARGE) developed a large scale process using a fixed bed FT reactor, while Carthage Hydrocol Inc., developed a technology based on a circulating catalyst bed [4]. Both these processes were later adopted by Sasol in the 1950s when they built a plant (Sasol 1) at Sasolburg located in South Africa. This plant today uses a slurry phase reactor and synthesises liquid fuels from natural gas imported from Mozambique. The Sasolburg Natref was built in 1969 for the production of diesel from refined crude oil [5]. In the 1980s Sasol rapidly expanded by building Sasol 2 and 3 at Secunda in South Africa; these plants mainly specialise in the production of synthetic fuels from coal. Sasol plants in South Africa have been producing fuel and chemicals on a

commercial scale since the 1950s using the same technology, which is now better known as the Fischer-Tropsch synthesis. Sasol researchers have continued to carry out research work, on catalyst properties, reactor design and processes related to FT synthesis. Much of this research has been done at their plants in Sasolburg and in collaboration with a number of universities in South Africa, Scotland and the Netherlands amongst other countries [5].

In 1987 PetroSA was commissioned at Mossel Bay in South Africa after they discovered Mosgas, the first of South Africa's gas producing fields. They have since been producing synthetic fuels from these gas fields [6]. Many more plants (Table 2.1) have since been built around the world and the interest in GTL technology is still growing among research institutes, companies and individuals. The abundance of natural gas around the world has been a key factor attracting many companies to commission FT plants around the world in the last 25 years. This is an elegant solution to the environmentally unfriendly practice of flaring gas.

The growing market for FT products has resulted in the FT process being commercialised worldwide and many patents have been registered on the process since the early 1900s. Today FT synthesis has become a promising route for the synthesis of clean fuels. It also serves as a promising option for the environmentally friendly production of chemicals and fuels from coal, low value methane (natural gas) and biogas, since the reserves of crude oil are being depleted and the price of crude oil continues to rise.

2.3 Literature Review

2.3.1 Fischer-Tropsch Synthesis (FTS)

FTS is the backbone of coal-to-liquid (CTL) technologies and gas-to-liquid (GTL) technology. The world's large reserves of coal and natural gas (low value methane) makes FTS a promising route for the production of cleaner liquid transport fuels, aviation fuels and chemicals [7].

Industrial FT synthesis mainly involves three processes: syngas production, FTS and product workup and separation. The production of syngas is done by either converting coal or natural gas through gasification and steam reforming into a mixture of hydrogen and carbon monoxide (syngas) which is cleaned of unwanted impurities such as sulphur. The clean syngas is piped to the FT reactor for FT synthesis where a variety of catalytic reactions take place and a wide range of products are produced depending on temperature, pressure, flow rate, catalyst, type of support material used etc. The products are separated into methane and unreacted syngas which can be recycled, the gas fraction (C_2-C_4), gasoline (C_5-C_{11}), diesel (C_{12}-C_{18}), wax (C_{19+}) and chemicals that may include olefins and oxygenates. Further reactions, like isomerisation, may be done on specific fractions. The overall process is summarised in Fig. 2.1 below [8]. The range of products and the ability to influence these by changing the operating parameters of FT synthesis makes the process uniquely flexible amongst industrial processes; this has caught the interest of researchers, research institutions and companies.

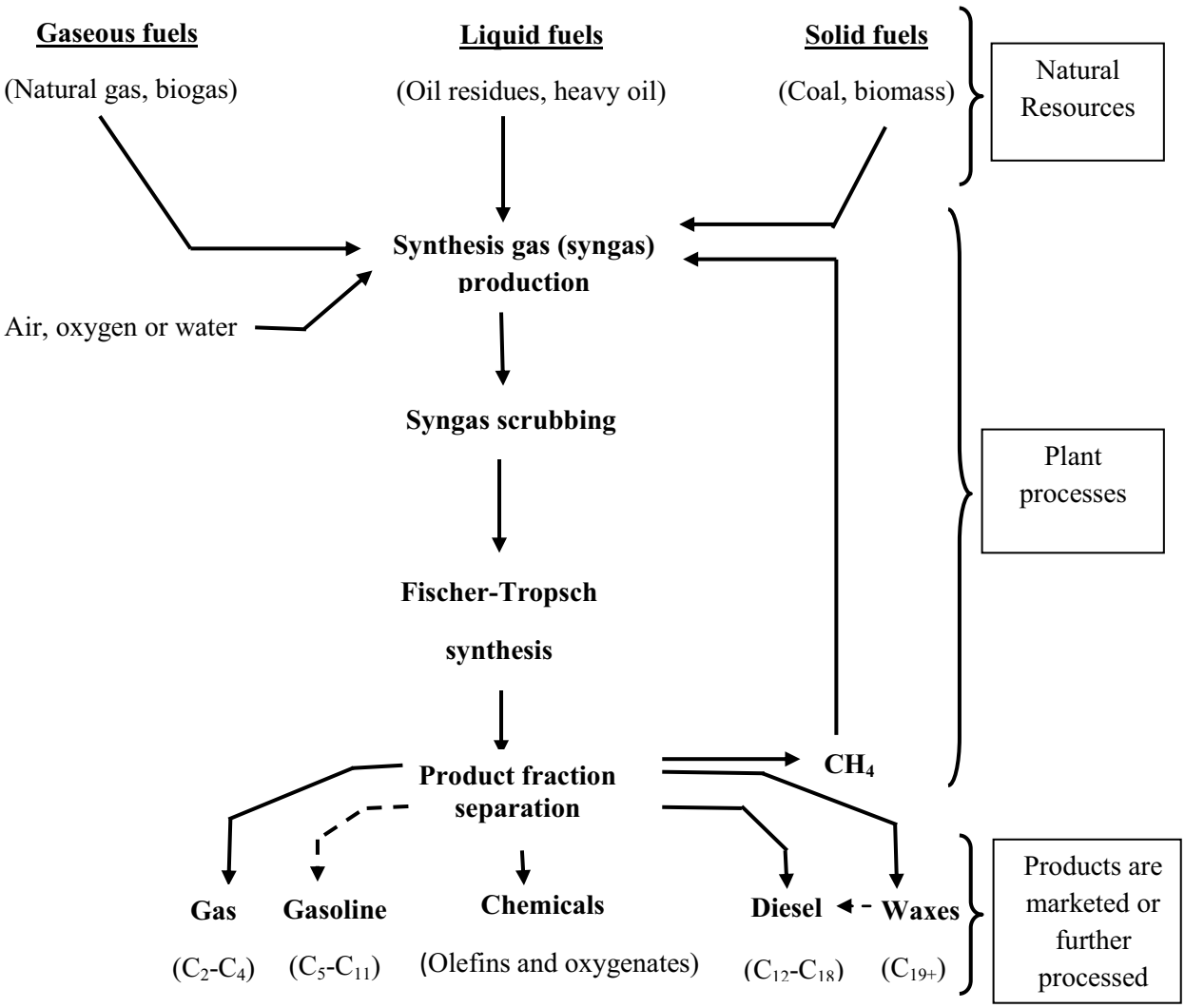


Figure 2.1: Industrial process overview for the production of fuels and chemicals by FTS [8].

2.3.2 Fischer-Tropsch reaction

The Fischer-Tropsch (FT) reaction is a highly exothermic, heterogeneous catalysed polymerisation reaction that converts syngas ($CO_{(g)}$ and $H_{2\,(g)}$) into hydrocarbons and

oxygenates with a wide range of chain lengths and functional groups, depending on the type of catalyst used [2].

The general stoichiometric equation for the reaction can be broken down into the following equations [10]:-

The hydrogenation of CO:-

$$CO + 2H_2 \longrightarrow --CH_2-- + H_2O \qquad \text{Equation 2.1}$$

$$\Delta H_{R,\,227°C} = -164.7 \text{ kJ/mol } (\textit{n-hexane})$$

The water gas shift (WGS) reaction also occurs in the Fischer-Tropsch reaction usually when a Fe based catalyst is used.

$$CO + H_2O \longrightarrow CO_2 + H_2 \qquad \text{Equation 2.2}$$

$$\Delta H_{R,\,227°C} = -39.7 \text{ kJ/mol}$$

The WGS reaction is the main source of carbon dioxide. It is however extremely limited for cobalt based catalysts.

Combining equations 2.1 and 2.2 gives the overall equation 2.3

$$2CO + 2H_2 \longrightarrow (--CH_2--) + CO_2 \qquad \text{Equation 2.3}$$

$$\Delta H_{R,\,227°C} = -204.4 \text{ kJ/mol } (\textit{n-hexane})$$

From equation 2.1, if CH_4 is formed instead of $--CH_2--$:

$$CO + 3H_2 \longrightarrow CH_4 + H_2O \qquad \text{Equation 2.4}$$

$$\Delta H_{R,\,227°C} = -214.4 \text{ kJ/mol}$$

In addition, most reactions associated with hydrocarbons encounter the problem of

carbon deposition by the Boudouard reaction as shown in equation 2.5

$$2CO \longrightarrow C + CO_2 \qquad \text{Equation 2.5}$$

$$\Delta H_{R,\,227^\circ C} = -133.8 \text{ kJ/mol}$$

From these equations it is evident that methane (an undesirable product of the FT synthesis) is most likely to form [9]. Reaction selectivity is therefore a key issue in FT synthesis.

The general Fischer-Tropsch reaction is;-

$$\chi CO + (1+2\chi)\, H_2 \xrightarrow{\text{catalyst}} C_\chi H_{(2\chi+2)} + \chi\, H_2O \qquad \text{Equation 2.6}$$

Where χ is an integer

The FT reaction does not proceed in the absence of a catalyst, although the impact of the catalyst in this particular reaction is not only in its capacity to facilitate the chemical reactions, but also in its propensity to improve the selectivity of the reaction. The most widely used and efficient FT catalysts contain a major proportion of a metal from group VIII-X of the periodic table especially cobalt, iron, nickel and ruthenium. Co-based and Fe-based catalysts are the FT industrial catalysts of choice, due to their high activity, selectivity and long life span [10].

A well-known property of cobalt-based FT catalysts is that they show no water gas shift activity, under conditions favouring the FT reaction, which is in contrast to the behaviour of the iron based FT catalysts. Other metals of group VIII-X catalyse this hydrogenation reaction to varying degrees [11].

The reaction mechanisms underlying FT synthesis are not fully understood, although a number of mechanisms have been proposed in the literature. The FT synthesis

involves several reaction sequences, including the primary hydrogenation of CO into *n*-alkanes and *n*-alkenes and methane. Subsequent reactions of the primary organic products generate additional product species in the FT reactor, for example reactions involving hydrogen migration, skeletal isomerisation, cyclisation and even sometimes hydrogenation and oxidation of the primary products [12].

A wide range of conditions such as temperature, hydrogen to carbon monoxide ratio, pressure etc, have been used to bring about the formation of many different products, including linear and branched chain hydrocarbons (alkanes and alkenes, including cyclic ones), oxygenates (such as methanol, ethanol and some higher alcohols) and amines [12-13].

2.3.3 Proposed molecular mechanisms for FT catalytic conversion of syngas

Molecular mechanisms have been a subject of investigation for many years. The exact details of the chemical steps that take place during FT synthesis are still a contentious topic. Several competing reactions with almost equal probabilities are likely to occur during FT synthesis, therefore reducing the selectivity of the desired products. Since FTS is a surface catalysed polymerisation reaction it may therefore involve some of the following steps: molecular chemisorptions, chain initiation, chain termination by both molecular desorption and re-adsorption of the reactive primary products leading to production of secondary products [8].

Most molecular mechanisms that have been proposed have been based on the assumption that multiple active sites exist on the catalyst metal crystallite [14]. Therefore metal hydrides, metal alkyls, metal clusters and cyclic formyl intermediates may be formed [15-22]. The oxygenate (enolic) mechanism is suggested to be more likely for iron catalysts, while the surface alkyl mechanism probably occurs on the cobalt catalysts [23].

The carbide and alkyl mechanisms

The original carbide mechanism postulates that CO is chemisorbed on the surface of the metal to form a carbide. The presence of hydrogen splits the double bond on the C=O chemisorbed forming aldehyde groups attached to the metal, followed by condensation and further hydrogenation and hence chain growth [23-24]. Kummer et al. [25] found that this mechanism was inconsistent with thermodynamic data for the formation of hydrocarbons by hydrogenation of the carbide studied at temperatures used for the synthesis reaction. Kummer et al. [25] also showed that carbide hydrogenation could be responsible for no more than 8-30 % of methane that was formed; the same conclusion was applied to the longer carbon chains when the % CO conversion was decreased [23].

The alkyl mechanism was later developed using the carbide–mechanism as a basis and has to date become the most widely accepted mechanism for chain growth; it suggests that the CH_x species are formed after the dissociation of chemisorbed CO species (Fig. 2.2). For the alkyl mechanism CH_2 is regarded as the monomer for chain growth [24, 26]. However, hydrogenating the surface carbon yields consecutively CH, CH_2 and CH_3 surface molecules [8, 27].

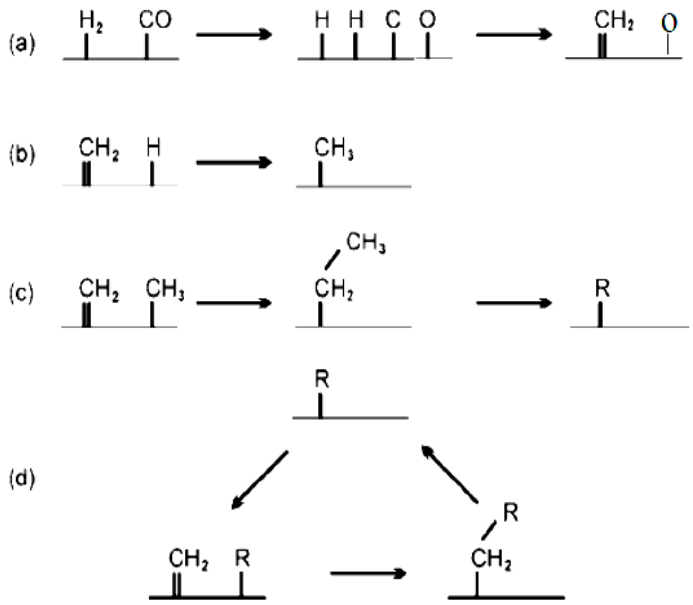


Figure 2.2: Schematic diagram of the alkyl mechanism showing (a) methylene formation, (b) chain initiation, (c) initial chain growth and (d) chain propagation [28].

The CO insertion mechanism

The CO insertion mechanism postulates that chemisorbed CO is the monomer although CH_2 can be involved in chain propagation [29-31]. CO insertion happens through the formation of a metal-alkyl bond and forms surface acyl species that can be hydrogenated (Fig. 2.3). Chain termination of oxygen containing species leads to the formation of oxygenates [32]. Oxygenates may also be formed by addition of OH species to surface alkylidene species [8, 33]. Condensation reactions of these species may form alkyl species. Hydrogenation and simultaneous water elimination of the COH_2 surface species is assumed to be the rate determining step for the insertion mechanism [23, 31, 34].

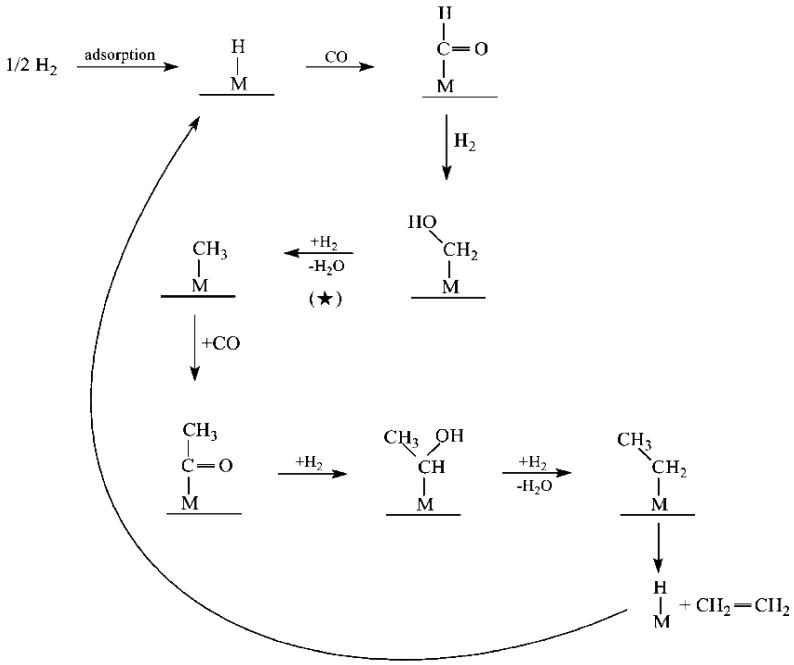


Figure 2.3: schematic diagram of the -CO insertion mechanism [23]

The oxygenate (enol) mechanism

The oxygenate (enol) mechanism (Fig. 2.4) was also proposed by Bureau of Mines workers in the 1950s [29-30]. This mechanism involves the chemisorption of CO, which reacts with hydrogen to form an enolic surface species that becomes both the chain initiator and monomer [30-31]. Chain growth was suggested to occur by condensation. Hydrogenation reactions led to chain termination and hence the formation of oxygenates or olefins and paraffins [23, 31].

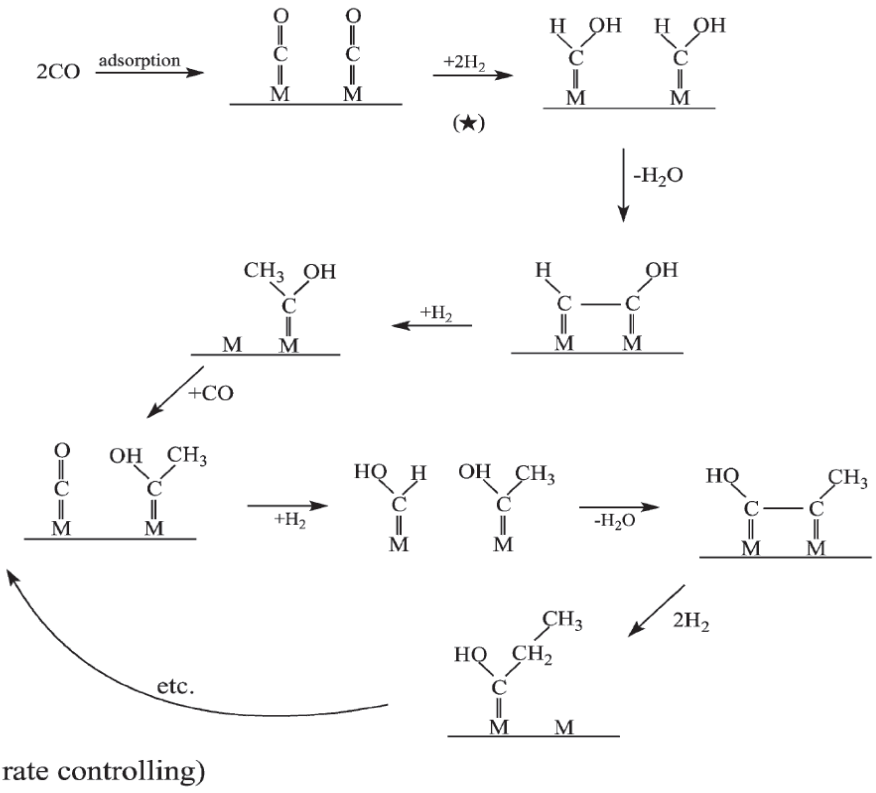


Figure 2.4: Schematic diagram showing the enol mechanism [23, 31]

The vinyl/alkenyl mechanism

The vinyl mechanism is similar to the alkyl mechanism and it explains the formation of branched hydrocarbons. In this mechanism the alkylidene and methyne surface species react to form a vinyl surface species which becomes the chain initiator, while methylene species are the monomers (Fig. 2.5). Chain growth leads to the formation of allyl species which can undergo isomerisation to form alkenyl species. Hydrogenation of alkenyl species leading to chain termination gives alkenes [27-28, 35-37]. Olefins such as propene which can possibly be re-adsorbed on carbon can react with methylene to form branched surface species. Desorption of these species yields branched hydrocarbon products [38-39].

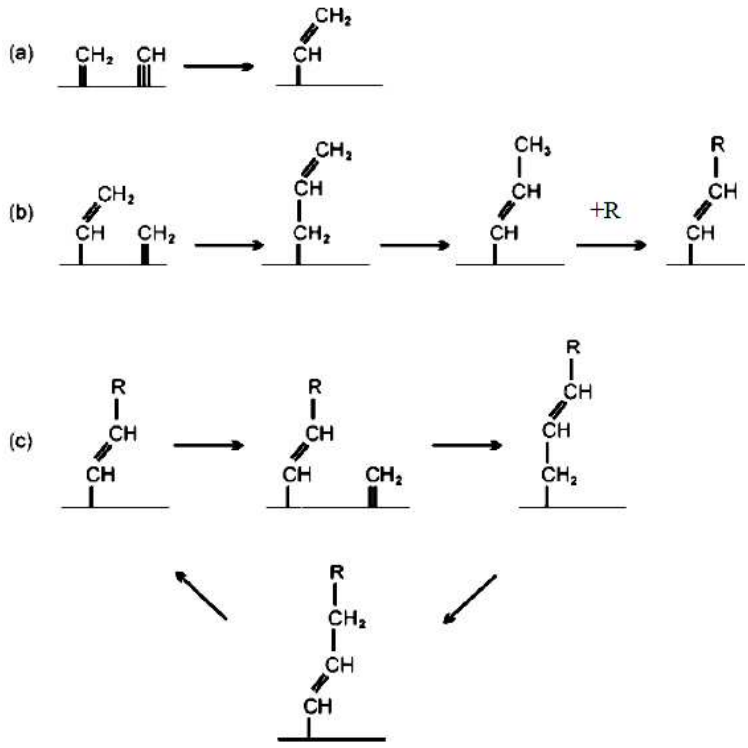


Figure 2.5: Schematic diagram of vinyl/alkenyl mechanism (a) chain initiation, (b) chain growth and methylene insertion, (c) chain propagation. [28]

2.3.4 FT product distribution

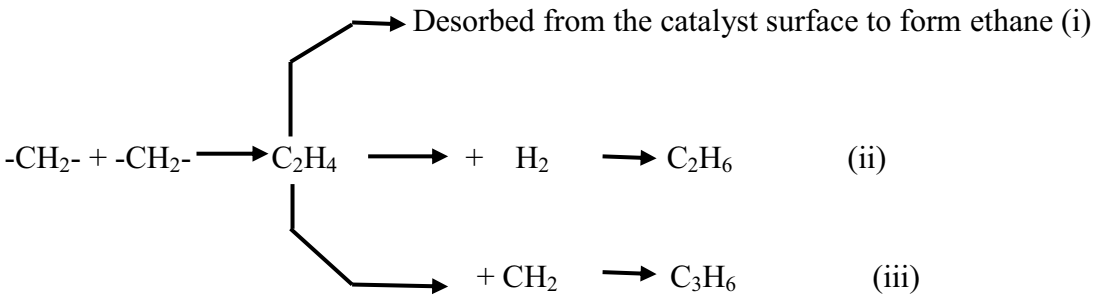
The Fischer-Tropsch reaction produces a wide range of hydrocarbons and oxygenated products via primary and/or secondary reactions. The selectivity for these various products appears to be controlled by mechanistic and kinetic factors of the various reactions occurring during FT synthesis [23]. The spread in carbon number products is dependent on the type of catalyst, the operating temperature and/or pressure, the type or amount of catalyst promoter, the feed gas composition or the type of reactor [40]. Although these parameters have a such a big influence in product selectivity all the proposed FT reaction mechanisms compare the FT synthesis to a conventional polymerisation process with the assumption that chain growth occurs by stepwise

insertion of the -CH_2- monomer chemisorbed on the catalyst surface into the chain [8, 27].

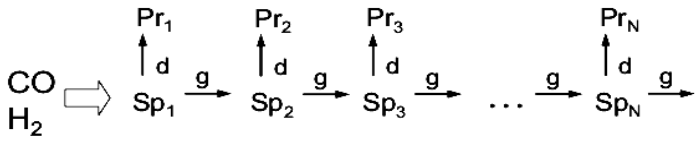
For example:-

$$H_2 + \text{-}CH_2\text{-} \longrightarrow CH_4$$

Or



Options (i) and (ii) are chain termination steps, whereas option (iii) is chain growth with its probability defined as alpha (α) and the probability of a chain terminating step defined as (1-α). The higher the α value the greater the probability of the hydrocarbon chain growing. If the formation of oxygenates and branched hydrocarbons is neglected by making an assumption that only one kind of product (Pr_N) desorbs (d) from the catalyst surface containing Sp_N surface species with N carbon number, the following chain growth kinetic model can be written [8, 27]



Such that

$$A = r_g/(r_g + r_d) \qquad \text{Equation 2.7}$$

Where:-

r_g = the rate of chain growth

r_d = the rate of desorption

A mathematical model based on the mass balance for the FT reaction showing the chain growth concept, assuming an α value independent of carbon chain length was developed by Herington [41], Anderson [42] and earlier by Flory [43] and today is known as the Anderson, Schultz, Flory (ASF) distribution.

$$\text{Log}\,(W_N/N) = N\,\text{Log}\,\alpha + \text{Log}\,[(1-\alpha)^2/\alpha] \qquad \text{Equation 2.8}$$

Where:-

W_N = the mass fraction of the species with carbon number N,

Plotting Log (W_N/N) versus N gives a straight line with a slope Log α, the value of α can then be calculated.

In practice, the C_1 point falls well above the Log (W_N/N) against N line and the C_2 point falls slightly below the C_3 point on an ASF plot show, this is due to the fact that C_2 olefins are much more reactive than other α-olefins. The carbon number range C_3

to C_{12} is usually linear implying a constant α value. When significant amounts of waxes are produced the ASF plot may shift to yield another alpha value (α_2) for the high boiling hydrocarbons. In this case, the C_3 to C_{12} alpha value is designated α_1. The existence of these two α values means that the value of alpha increases with chain length [44]. Since these higher boiling products are in the liquid phase at the pressure and temperature of the reactor they have been found to condense in the catalyst pores.

The existence of two alpha values may be due to diffusional restrictions of liquid products such as alkenes which become entrapped in the catalysts pores. Hence they spend longer in the reactor than the lighter vapour phase products resulting in alkene re-incorporation [45].

Diffusional restrictions of long chain products inside the catalyst particles may occur due to one of the following reasons; slower diffusion rates, higher solubility in the liquid phase and stronger physisorption of the longer chain products [46].

If the chain growth probability is assumed to be independent of hydrocarbon length and a single α value exists then an entire FT product spectrum can be calculated for a particular α value to give results shown in Fig. 2.6 [47-48].

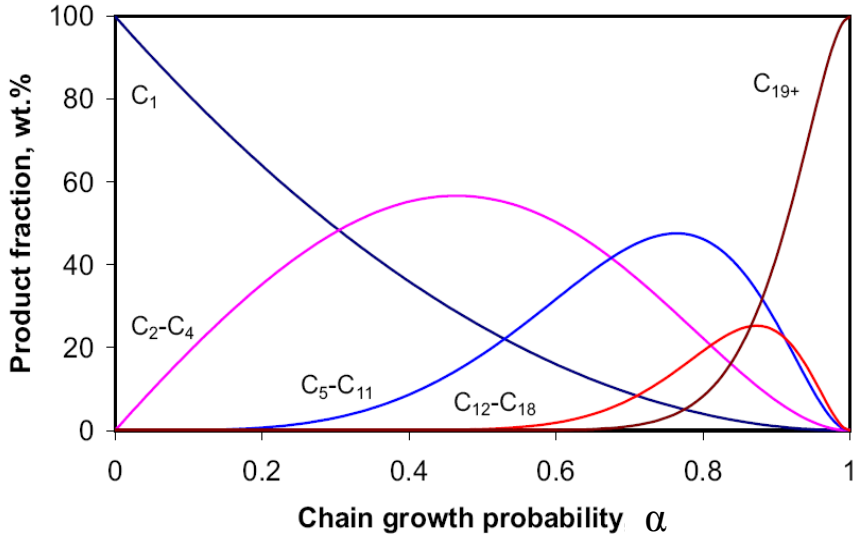


Figure 2.6: Theoretical product selectivity as a function of chain growth probability [47-48]

2.3.5 Factors affecting product selectivity

The distribution of FT products depends on the process operating conditions. The effect of operating conditions is listed in Table 2.1.

Table 2.1: Effect of different operating parameters on product distribution [49]

	Temperature	**Pressure**	**Syngas composition H_2/CO**	**Residence Time**
CH_4 selectivity	+	-	+	+
Chain growth	-	+	-	~
Olefin selectivity	~	~	-	-
Oxygenate selectivity	-	+	-	-
Carbon deposition	+	~	-	~
Chain Branching	+	-	~	~

+ increase with increase in parameter, - decrease with increase in parameter, ~ no clear effect

2.3.6 FT catalysts

All group VIII metals have been noted to show some FT activity [40]. It has been reported in the literature that the average molecular weight of hydrocarbons produced by FT synthesis decreased as follows: Ru > Co > Fe > Rh > Ni > Ir > Pt > Pd [50]. Therefore Fe, Ni, Ru and Co are possible industrial FT catalysts. The FT activity of these metals is as follows: Ru > Co > Fe > Ni and in terms of cost Fe: Ni: Co: Ru is 1:250:1000:50000. Although the cost of Ni is much lower than that of Co, Ni has been reported to have a high CH_4 selectivity [11, 40]. Although Ru has a higher FT activity than the other metals, its use is not economically viable due to its cost and availability as a natural resource, similarly for Rh. Thus Fe and Co have been determined to be the most viable catalysts for FT synthesis for industrial applications.

Cobalt catalysts are much more expensive than iron based catalysts but they possess some advantages over iron catalysts in that they show better product selectivity and they are more resistant to deactivation by water compared to iron catalysts. The WGS is more pronounced for iron based catalysts and very limited in cobalt based catalysts [40].

Cobalt catalysts are more sensitive to FT operating conditions such as pressure, H_2/CO ratio and temperature, whereas iron based catalysts are more tolerant to varying H_2/CO ratios. Iron catalysts are used to convert syngas derived from coal/biomass, which contains small amounts of hydrogen whereas cobalt catalysts are favourably used for converting syngas derived from natural gas which typically has higher levels of hydrogen in it [40].

Cobalt and iron based catalysts are deactivated by the presence of sulphur. Iron catalysts have a sulphur tolerance of less than 0.2 ppm sulphur while cobalt catalysts run for longer and therefore cannot tolerate more than 0.1 ppm sulphur [51-53]. Cobalt crystallites supported on metal oxides are more resistant to attrition than co-

precipitated iron catalysts; hence they are more suitably used in a slurry-phase reactor [51-53].

There are two widely known FT operating modes; the low temperature FT (LTFT) and the high temperature FT (HTFT). Cobalt based catalysts are suitable for the LTFT process (200-240 ^{o}C and 20-40 bar) either in a fixed bed or in a slurry phase reactor. Although iron catalysts can also be used under the same conditions, cobalt catalysts are preferred because of their higher catalytic performance, stability, higher per pass conversion and hydrocarbon productivity [40]. The LTFT process is most useful when the synthesis of C_{10}-C_{30} linear long chain hydrocarbons, waxes and paraffins is desirable. One advantage of this process is that it produces high quality fuels with very low sulphur concentrations while the disadvantage of the LTFT process is that it requires stoichiometric ratios of H_2: CO (1.7-2.15 : 1) as feed stocks. [40, 51-53].

The HTFT process is only suitable for iron based catalysts and it is most useful when C_1-C_{15} hydrocarbons, olefins and oxygenate products are most desired. This process is primarily used to produce liquid fuels and some valuable chemicals such as α-olefins and oxygenates that can be separated and purified into acetic acid, alcohols and ketones. The HTFT operating conditions are 300-350 ^{o}C and 20-40 bar in a fluidized bed reactor [40]. Since iron is more tolerant to varying ratios of H_2: CO it is used for the HTFT process which usually uses syngas derived from coal, with low ratios of H_2: CO (<<2:1) [40, 51-53]

2.3.7 Supported FT catalysts

FT catalysis occurs on the surface of the active metal. Therefore increasing the metal surface area by depositing small metal particles on a suitable support material maximises metal utilisation and in turn increases the specific metal activity.

Some of the advantages of supporting FT catalysts include:-

- producing large active metal surface areas
- limiting metal sintering during FTS
- allowing easy flow of feed gas through the reactor and catalyst pores
- the support material may act as a promoter to the supported metal
- producing cheaper catalysts
- limiting entrainment of small catalyst particles in fluidized bed reactors
- limiting unwanted pressure drops in fixed bed reactors during FTS

Supported FT catalysts often consist of all/or some of the following components: (1) a support material, which carries the active metal, (2) promoters, these may include Pt, Ru or Re for cobalt Fischer-Tropsch catalysts and Li, K, Rb and Na for iron Fischer-Tropsch catalysts and (3) the active catalytic metal [11, 40, 53]. The metal precursor surface area is inversely proportional to its crystallite size.

2.3.8 Effects of metal precursor crystallite size

Although high metal surface areas can be achieved by producing and supporting nano-sized metal particles, the physical, chemical and electrical properties of these particles may change with particle size [40].

Cobalt catalyst crystallite size effect

The following two points are noted for cobalt based catalysts:-

(1) Catalyst deactivation by oxidation under FT reaction conditions by water.

Holmen et al. [54-56] reported that smaller cobalt particles were more prone to be deactivated rapidly due to oxidation by water than larger cobalt particles, when the amount of water in the inlet stream was increased. Van Steen et

al. [57] also confirmed these findings from thermodynamic calculations that took account of surface energies in cobalt and cobalt oxide phases for small particles (d < 44Å). They reported small cobalt particles being more likely to be oxidised by water under FT reaction conditions than larger cobalt particles under the same conditions [57]. Other studies conducted to confirm these results are by Saib et al. [58] who used in-situ XANES experiments and Davis et al. [59-63] who have published numerous ex-situ data.

(2) Kinetic studies of elementary steps in the FT reaction on cobalt particles of different sizes.

Holmen et al. [64] reported the effects of varying cobalt particle sizes on the surface coverage of metal by reaction intermediates using steady-state isotopic transient kinetic analysis (SSTIKA). Their findings revealed that metal surface coverage with reaction intermediates was dependent on the cobalt particle sizes (2.6-16 nm). It was thought to be due to either quantum size effects of different sized cobalt crystallites that could influence the elementary steps of the FT reaction and/or cobalt phase composition which could have affected the catalytic performance of the cobalt particles.

Three possible crystalline cobalt phases may exist in supported cobalt catalysts:- the face centred cubic (fcc), the hexagonal close packed (hcp) and a novel phase [65]. It is suggested in the literature that cobalt catalysts with higher fractions of hcp phases would show higher FT activity than those containing higher fractions of the fcc phase [65].

On the contrary, studies by Iglesia et al. [66-68] have shown that FT activity is proportional to the number of active cobalt surface atoms when cobalt particles supported on aluminia, silica and titinia were studied. Their results also imply that cobalt site time yields are independent of the entire cobalt crystallite size [69-71].

However, when larger (8-15 nm) cobalt crystallites are considered slight changes in C_{5+} hydrocarbon selectivity can noted [72].

Cobalt particles (6-8 nm) supported on carbon nanofibres are reported in the literature to show higher specific catalytic activity than smaller or larger particles [73]. Little has been reported in the literature about the effects of metal crystallite size effects on FT product selectivity. Schultz et al. [74] proposed that some FT reactions may occur on low coordination sites (CO-insertion) while others may occur on high coordination sites (C-hydrogenation), which suggests possible variations in product selectivity with metal crystallite size in FTS.

Iron catalyst crystallite size effect

The effect of crystallite size on FTS has not received as much research interest for Fe as for Co. Fe based FT catalysts have also been shown to be size dependent. Mabaso et al. [8] showed that smaller Fe particles (< 7-9 nm) supported on carbon nanotubes were less active and also resulted in higher methane selectivity when compared to the bigger sized catalysts. Recent studies by Park et al. [75] on Fe supported Al_2O_3 catalysts showed that the optimum Fe particle size for FTS was 6.1 nm. Smaller Fe particle sizes (< 6.1 nm) formed strong-metal support interaction when the iron loading was lower than 10 % and became very difficult to reduce. It has been suggested in the literature that iron carbides are the FT active phase [76].

2.3.9 Deactivation of FT catalysts

FT catalysts may be deactivated by one or more of the following:-

- fouling of the catalyst by carbon deposition
- metal sintering
- oxidation of the FT active metal/carbide to the inactive oxide phase

- diffusion restrictions of feed gas by high molecular weight waxes trapped in the catalyst pores
- catalysts poisoning by feed gas impurities e.g. H_2S and organic sulphur compounds

The build up of liquid FT products on the catalyst surface and in pores has been reported as the cause of the rapid decreases in FT reaction rate on cobalt based catalysts during the first few hours of FTS [77-78]. These liquid products occupy and cover the metal active sites hence blocking adsorption of fresh syngas on these FT active metal sites. The non-porous nature of carbon spheres prevents this from occurring.

The deposition of foulants occurs when high reaction temperatures are used. The absence of CO_2 from the tail gas may suggest the absence of the Boudouard reaction, which produces carbon during FTS.

Water vapour produced as an FT product has been reported in the literature as a possible cause for the deactivation of FT catalysts by facilitating one or more of the following:-

- sintering of the metal particles
- surface or total oxidation of the metal particles
- formation of inactive FT metal-support compounds [79]

Sintering of metal particles due to the presence of water occurs when the highly electronegative adsorbed oxygen atoms associate with the positively charged cobalt atoms. The continuous cyclic oxidation and reduction of the surface cobalt atoms leads to the re-arrangement/movement of the metal particles along the surface of the support materials and hence they sinter [17, 79].

Thermodynamic studies, as reported in the literature suggest that bulk phase oxidation of cobalt particles by water under FT operating conditions (temperature and feed gas ratios) may not be possible, since the sub-surface atoms are co-ordinatively saturated. However, partial or temporary surface oxidation may occur [17, 79].

The reaction of cobalt with metal oxide supports such as titania, silica and alumina to form strong metal support interactions in cobalt titinates, silicates and aluminates respectively, requires that cobalt be in an oxidized state. Therefore the presence of water vapour during FTS operating conditions may oxidise a monolayer of surface cobalt atoms and facilitate the formation of strong metal support interactions that are not reducible and are FT inactive [79].

The effect of water on the FT reaction is largely dependent on the type of support used and the vapour pressure inside the FT reactor [80-82]. Detailed studies on the effect of water during FTS on Co/silica catalysts [83-84] and Co/titania catalysts [67, 85-87] can be found in the literature.

2.3.10 Catalyst preparation methods

FT catalysts can be prepared by one of the following methods [40]:-

- Impregnation methods
- Co-precipitation methods
- Sol-gel methods
- Deposition-precipitation methods
- Plasma methods
- Colloidal methods
- Microemulsion
- Solvated metal atom dispersion methods
- Chemical vapor deposition methods

The most common catalyst preparation methods are the precipitation or impregnation methods and to a lesser extent ion exchange, vapour phase deposition and synthesis from organometallic compounds [40].

Impregnation method

The impregnation method is also referred to as incipient wetness. The pore volume of the support material is determined by wetting the dry support with water, while recording the volume of water added. A salt solution containing the metal precursor is prepared so that the desired metal loading on the catalyst will be achieved when a volume of the solution equal to the pore volume is added to the support. The metal precursor is impregnated into the pores of the support by combining the support materials with the salt solution. The active metal precursor is transported to the interior of the support by capillary-type forces or by diffusional effects. The liquid is then removed by drying in an oven resulting in crystallization of the metal salt onto the pore walls and outer surface of the support [11, 40, 88]. After drying, the catalyst is calcined to form metal oxides in the pores of the support material

Deposition-precipitation method

During catalyst preparation by the deposition-precipitation method, the active metal source, usually in a salt form is dissolved in water with urea to form a homogeneous solution. The solution is then added slowly to the support material to form a slurry which is first stirred before being heated to 90 ^{o}C to hydrolyse the urea and form a precipitate of the metal on the support material. After drying and calcination the metal oxides are formed on the surface of the support material. In general this methods forms smaller metal crystallite sizes than catalysts prepared by impregnation methods, it may also give better metal dispersion and allow incorporation of higher loadings of the metal components in a one step synthesis [40].

2.4 Catalyst support materials

Catalyst support materials are the bulk components of catalysts that are either inert or may act as promoters for the supported metal precursor, they have multiple roles on the overall catalyst performance. The purpose of these materials is primarily to act as a base for dispersing and stabilising metal particles, therefore facilitating high catalytic phase surface areas. Catalyst support materials may affect the diffusion of reactants and/or products through the catalysts pores.

These materials may be selected based on their physical and chemical properties. Desirable properties for good catalyst support materials may include:-

- thermal stability under reaction conditions
- adequate mechanical strength
- high surface area
- appropriate physical morphology for a given reactor
- have narrow pore size ranges
- be chemically inert or act as a catalyst promoter

The most commonly used FT catalyst supports include silica, alumina, titania and carbon materials [40, 89]

2.4.1 Carbon

Carbon is a very useful element and forms the basis of organic chemistry because of its ability to exist in many possible electronic configurations i.e. sp, sp^2 and sp^3 hybridisation. The six best known allotropes of carbon include diamond, carbon nanotubes, amorphous carbon or carbon black, graphite, activated carbon and fullerenes. Carbon may also form carbon fibres, carbon onions etc [90-91].

Structure and properties of carbon materials

The surface chemistry of carbon materials used as catalyst supports affects for the overall catalyst performance: it governs the metal loading, metal dispersion and influences the catalyst activity and selectivity. In porous carbonaceous materials catalytic reactions occur in a confined nanospace. The dimensions of this nanospace significantly influence the chemical equilibrium [92-93], the activity and selectivity hence the efficiency of the reactor.

Spherical carbonaceous materials

There has been growing research interest in carbon materials since fullerenes and carbon nanotubes were discovered. Many other shaped carbon materials have been synthesised including the spherically shaped ones. These include materials such as carbon nanocapsules [94-95] carbon spheres [96-97] carbon onions [98] and carbon beads [99-100]. Inagaki and Serp have gone a step further by classifying them in two different ways: Inagaki [101-102] classified these materials based on the arrangement of the carbon layers while Serp et al. [103] classify them by size i.e. fullerenes (< 2nm) [104], carbon onions (2-20nm) [105] carbon spheres (50-1000nm) [106-108] and carbon beads (> 1μm) [99-100, 109].

Among these spherical carbonaceous materials, carbon spheres have similar properties to fullerenes and graphite and have many potential applications in addition to their use as catalyst support materials [110-113].

Carbon spheres can be synthesised by the following methods (1) high pressure carbonization [100, 114], (2) pyrolysis of carbon sources in the presence of transitional metals on a kaolin support [115, 116] (3) chemical vapour deposition method (CVD) [117] and (4) mixed–valent oxide catalytic carbonisation [118]. The

CVD method produces highly pure carbon spheres arising without any residual catalyst impurities. When transition metals are used as catalysts, catalyst-encapsulated carbon spheres may be formed resulting in difficulties of catalyst removal from the product. In most applications pure carbon spheres without impurities are required.

2.4.2 Mechanism of formation of carbon spheres

In general, carbon spheres are formed in a three step process:-

Carbon sphere precursor and particle nucleation

There are three possible routes for the formation of carbon particles,

(a) via polyacetylenes,

(b) via polyaromatic hydrocarbons (PAHs)

(c) via the formation of a carbon vapour as a result of dehydrogenation of a hydrocarbon source.

It has been reported in the literature that for pyrolytic or flame systems, PAHs are the most likely precursors of carbon nuclei [119, 121]. Bittner et al. [122] showed that a part of the benzene ring was destroyed to give an unsaturated aliphatic species, and that PAHs could form from aromatics and species derived from acetylene. Subsequent reactions may result in the formation of a benzyl type radical by substitution of a methyl radical at the α position of the naphthalene and the release of a hydrogen atom. The continuous addition of C_2H_2 leads to cyclisation.

Fullerene formation in flames is a molecular growth analogous to the formation of PAH and carbon blacks [123] but it is not a possible nucleus for carbon spheres. Detailed studies on carbon black inception can be found in the literature [124-130].

Agglomeration of nuclei into particles and of particles into aggregates

During inception a large number of particles are produced, which may collide and form larger spherical particles, these particles can aggregate to form carbon black clusters as the final product. Regardless of the use of either pyrolysis or flame methods the final number density of the aggregates is normally similar, typically $10^{16}/m^3$ [131-132]. The rate of change of particle number density N with time on stream *t* during a sticking collision can be expressed as:-

$$dN/dt = N^o_i - N^o_c \qquad \text{Equation 2.9}$$

Where:-

N^o_i = is the inception rate

N^o_c = the coagulation rate

The inception rate makes a significant contribution to the formation of the carbon material only at the early stages of the process, while the coagulation rate controls to a larger extent. Therefore the very rapid change of the number density can be expressed by the Smoluchowski equation, assuming that the system is in the free molecular regime (i.e Knudsen number >10) [133]

$$N = N_o[1 + 9.03 \times 10^{13} N_o^{5/6} T^{1/2} f_v^{1/6} t]^{-6/5} \qquad \text{Equation 2.10}$$

Where:-

N_o = the initial particle number density

N = the final particle number density after time *t*

T = the operating temperature in Kelvin

f_v = the volumetric flow rate

Surface growth

About 10 % of the carbon spheres mass may be produced at inception. However, the remaining ca. 90 % is formed due to surface growth on the particles. The surface grows on both individual and aggregated particles and it is believed that acetylene radicals are the main hydrocarbons responsible for carbon sphere growth [133].

2.4.3 Carbon materials as catalyst supports

Carbon based materials are unique supports in heterogeneous catalysis because of their highly controllable surface properties [134-135], which can be manipulated by functionalising the carbon atoms surface monolayer. Carbon materials have the following advantages which make them suitable metal supports:-

- they are chemically inert and are resistant to acidic and basic media
- they are thermally stable at high temperatures
- they are cheaper materials to produce than most conventional support materials e.g. silica, titinia and aluminia.
- the metal phase can easily be recovered from the spent catalyst by simply burning off the carbon support
- they exhibit relatively high mechanical strength
- it is easy to tailor the pore sizes and the structure of carbon materials [134-135]

Carbon based catalysts cannot be used above 430 ^{o}C in the presence of hydrogen or above 230^{o}C in oxygen due to methanation and oxidation respectively of the carbon support [136].

The non-porous nature of carbon spheres has advantages over the conventional support materials when they are used as FT catalyst support materials. Conventional oxide supports allow liquid product to condense in the pores under the reaction conditions, which may result in catalyst deactivation and increased diffusion resistance. The CS support material does not allow this to happen.

References

1. http://www.eoht.info/page/Johann+Dobereiner, retrieved 9 Jul 2011
2. F. Fischer, H. Tropsch, Brennstoff Chem. 4 (1923) 276
3. H. Schulz, Appl. Catal. A: Gen. 186 (1999) 3–12
4. http://www.fischer-tropsch.org, "Historical Development of Cobalt-slurry Fischer-Tropsch Reactor Systems", retrieved 29 July 2008.
5. www.sasol.co.za fact sheet, retrieved 29 July 2008
6. www.petrosa.co.za, retrieved 29 July 2008
7. M.E. Dry, in: G. Ertl, H. Knozinger, F. Schuth and J. Weitkamp (Eds.), Handbook of Heterogeneous Catalysis, Wiley-CVH-Weinheim, (2008) 2965.
8. E.I. Mabaso, "Nanosized iron crystallites for Fischer-Tropsch synthesis" PhD. thesis, University of Cape Town, Rondebosch, Cape Town, (2005).
9. C. Wang, L. Xu, Q. Wang, Journal of Natural Gas Chemistry 12 (2003) 10-16
10. J. G. Price PhD Thesis," An investigation into novel bimetallic catalysis for use in the FT reaction", University of Witwatersrand, (1994).
11. M.E. Dry, J .R. Anderson, M Boudart (Eds), Catalysis Science and Technology, vol1,Springer, New York (1981) 159.
12. P.M. Maitlis, J. Organomet. Chem. 689 (2004) 4366.
13. Q. Zhang, J. Kang and Ye Wang, ChemCatChem, 2 (2010) 1030.
14. M.E. Dry, Ind. Eng. Chem., Product Res. Dev. 15 (1976) 282.
15. R.S. Armstrong, T. Bell, A.F. Masters, M.A. Williams, A.L. Chaffee, Polyhedron 9 (1990) 282.
16. J.W. Rathke, H.M. Feder, J. Am. Chem. Soc. 100 (1978) 623.
17. M.E. Dry, Catalysis — Science and Technology (Chap. 4), J.R. Anderson, M. Boudart (Ed.), Springer, New York, (1980).
18. M.E. Dry, Catal. Today 6 (3) (1990) 623.
19. J.J. Boor, Polym. Sci., Part D 2 (1967) 115.
20. P.M. Maitlis, H.C. Long, R. Quyoum, M.L. Turner, Z.-Q.Wang, Chem.

Commun. (1996) 1–8.
21. Masters and Van Doorn UK Patent Application No. 40322-75 (1975).
22. H. Pichler, H. Schultz, Chem. Ing. Tech. 12 (1970) 1160.
23. B. H. Davis, Fuel Process. Technol. 71 (2001) 157.
24. F. Fischer, H. Tropsch, Brennst.-Chem. 7 (1926) 97.
25. P.H. Emmett, J. Am. Chem. Soc. 74 (1952) 1680.
26. S.R. Craxford and E. Rideal, Brennstoff-Chem. 20, (1939) 263.
27. M. Claeys, E. Van Steen, in: A. Steynberg and M. Dry (Eds.), Stud. Surf. Sci Catal., 152 (2004) 601.
28. M.L. Turner, P.K. Byers, H.C. Long, P.M. Maitlis, J. Am. Chem. Soc. 115 (1993) 4417.
29. O. Evans, A. Nash, Nature 118 (1954) 1926.
30. H.H. Storch, N. Golumbic, R.B. Anderson, The Fischer–Tropsch and Related Synthesis. Wiley, New York (1951).
31. M.E. Dry, Catal. Process., Proc. S. African Catal. Soc. Meeting, October. (1993).
32. J.P. Hindermann, G. J. Hutchings and A. Kiennemann, Cat. Rev. Sci. Eng. 35 (1993) 1.
33. O. Johnstonand R. Joyner, Stud. Surf. Sci. Catal., 75 (1993) 165.
34. I. Wender, S. Friedman, W.A. Steiner, R.B. Anderson, Chem. Ind. (London) (1958) 1694.
35. H.C. Long, M.L. Turner, P. Fornasiero, J. Kapar, M. Graziani, P.M. Maitlis, J. Catal. 167 (1997) 172.
36. A. Guerrero-Ruiz, I. Rodriguez-Ramos, in: J.A. Anderson and M.F. Garcia (Eds.), Supported Metals in Catalysis, Imperial College Press, London (2005)
37. P.M. Maitlis, R. Quyoum, H.C. Long, M.L. Turner, Applied Catalysis A: General 186 (1999) 363.
38. Schulz, H., E. Erich, H. Gorre, and E. van Steen, Catal.Lett. 7 (1990) 157.

39. H. Schulz, K. Beck and E. Erich, Stud. Surf. Sci. Catal. 36 (1988) 457.
40. A.Y. Khodakov, W. Chu and P. Fongarland, Chem. Rev. 107 (2007) 1692.
41. E.F.G. Herington, Chem. Ind, London (1946).
42. B. Anderson and R.A. Friedel, J. Amer Chem. Soc. 2 (1950) 2307.
43. P.J Flory. J. Am. Chem. Soc., 58 (1936) 1877
44. I. Puskas and R.S. Hurlbut, Catalysis Today 84 (2003) 99.
45. C. M. Masuku, D. Hildebrandt, D. Glasser The Role of Vapour–Liquid Equilibrium in Fischer–Tropsch Product Distribution. To be published.
46. F. Fischer and H. Pichler, Brennst. Chem. 20 (1939) 41.
47. R.C. Everson, E.T. Woodburn and A.R. Kirk, J. Catal. 53 (1978) 186.
48. F. Martins, Chem. Fabrik. 12 (1939) 233.
49. M. Claeys, 'Selektivit¨at, Elementarschritte und Kinetische Modellierung bei der Fischer-Tropsch-Synthese'. Ph.D. thesis, Universit¨at Fridericiana Karlsruhe (1997).
50. M.A. Vannice, J. Catal., 37, (1975) 449.
51. R.L. Espinoza, A.P. Steynberg, B. Jager and A.C. Vosloo, Appl. Catal. A, 186 (1999), 13.
52. B. Jager and R. Espinoza, Catal. Today, 23 (1995) 17.
53. J. Haggin, 'Several issues drive research for new catalysts for methane conversion'.Chem. Eng. News 22 (1991).
54. O. Borg, S. Storsaeter, S. Eri, H. Wigum, E. Rytter and A. Holmen, Catal.Lett. 107 (2006) 95.
55. S. Storsaeter, O. Borg, E.A. Blekkan and A. Holmen, J. Catal. 231 (2005) 405.
56. S. Storsaeter, O. Borg, E.A. Blekkan, B.Totdal and A.Holmen, Catal. Today 100 (2005) 343.
57. E.van Steen, M. Claeys, M.E. Dry, J.van de Loosdrecht, E.L. Vilkoen and J.L Visagie, J.Phys.Chem.B 109 (2005) 3575.
58. A.M. Saib, A. Borgna, J.van de Loosdrecht, P. J. van Berge, J.W. Geus and

J.W. Niemantsverdriet, J. Catal. 239 (2006) 326.

59. T.K. Das, G.Jacobs and B.H.Davis, Catal.Lett. 101 (2005) 187.
60. G. Jacobs, J.A. Chaney, P.M. Patterson, T.K. Das, J.C. Maillot and B.H. Davis, J. Synchrotron Radiat. 11 (2004) 414.
61. G. Jacobs, P.M. Patterson, T.K. Das, M. Luo and B.H. Davis, Appl.Catal. A. 270 (2004) 65.
62. T.K. Das, W. Conner, G. Jacobs, J. Li, K. Chaudhari and B.H. Davis, Stud. Surf. Sci. Catal. 147 (2004) 331.
63. G. Jacobs, T.K. Das, P.M. Patterson, J. Li, L. Sanchez and B.H.Davis, Appl. Catal. A 247 (2003) 335.
64. P.B. Radstake, J.P. den Breejen, G.L. Bezemer, J.H. Bitter, K.P. deJong, V. Frøseth and A. Holmen, Stud. Surf. Sci. Catal. 167 (2007) 85
65. D.I. Enache, B.Rebours, M. Roy-Auberger and R. Revel, J. Catal. 205 (2002) 346
66. E. Iglesia. S.C. Reyes, R.J. Madon and S.l. Soled, Adv. Catal. 39 (1993) 221.
67. E. Iglesia, Appl. Catal. A 161 (1997) 59.
68. S. L. Soled, E. Iglesia, R. AFiato, J.E. Baumgartner, H. Vroman, S. Miseo, Top. Catal. 26 (2003) 101.
69. A.Y. Khodakov, Catalysis Today, 144 (2009) 251.
70. G. Haddad, B. Chen and J.G. Goodwin, J. Catal.161 (1996) 274.
71. M. Rothaemel, K.F. Hanssen, E.A .Blekkan, D.Schanke and A.Holmen, Catal. Today 38 (1997) 79.
72. O. Borg. S.Eri, E.A. Blekkan, S.Storsæter, H. Wigum, E.Rytter and A. Holmen, J. Catal 248 (2007) 89.
73. G.L. Bezemer, J.H. Bitter, H.P.C.E. Kuipers, H. Oosterbeek, J.E. Holewijn, X. Xu, F. Kapteijn, A.J. van Dillen and K.P de Jong, J. Am. Chem. Soc. 128 (2006) 3956.
74. H. Schulz, Z. Nie and F. Ousmanov: Catal. Today 71 (2002) 351.

75. J. Park, Y Lee, P. K. Khanna, K. Jun, J. W. Bae, Y. H. Kim, J. Mol. Catal.323 (2010) 84.
76. D.B. Bukur, L. Nowicki, R.K. Manne, X.S. Lang, J. Catal. 155 (1995) 366.
77. P.J. van Berge and R.C. Everson, Natural gas conversion IV, Studies Surface Sci. Catal., 107 (1997) 207.
78. M.K. Niemela and A.O. Krause, Catal. Letters, 42 (1996) 161
79. A. Kogelbauer, J.C. Weber and J.G. Goodwin, Catal. Letters, 34 (1995) 259
80. D. Schanke, A.M. Hilmen, E. Bergene, K. Kinnari, E. Rytter, E. Adnanes, A. Holmen, Catal Letters 34 (1995) 269.
81. A.M. Hilmen, D. Schanke, K.F. Hanssen and A.Holmen, Appl.Catal. A: Gen, 186 (1999) 169.
82. A.M. Hilmen, O.A. Lindvag, E. Bergene, D. Schanke, S. Eri and A. Holmen, Stud. Surf. Sci Cat, 136 (2001) 295.
83. S. Krishnamoorthy, M. Tu, M.P. Ojeda, D.Pinna and E. Iglesia, J. Catal., 211 (2002) 422.
84. J. Li, Y. Chang, G. Jacobs, T. Das and B.H. Davis, Appl. Catal. A: Gen., 236 (2002) 67.
85. C.J. Bertole, C.A. Mims and G. Kiss, J. Catal, 210 (2002) 84.
86. C.J. Kim, European Patent No. 339, 923 (1989).
87. J. Li, G. Jacobs, T. Das and B. H. Davis, Appl. Catal. A: Gen., 233 (2002) 255.
88. A.A. Adesina, Appl. Catal A: Gen., 138 (1996) 345.
89. D. Yu, E. Nagelli, F. Du and L. Dai, J. Phys. Chem. Lett. 1 (2010) 2165.
90. A.A. Deshmukh, S.D. Mhlanga, N.J. Coville, Mater. Sci. Eng., R 70 (2010) 1.
91. P. Serp, J. L. Figueiredo, “Carbon Materials for Catalysis”, John Wiley & Sons, Inc, New Jersey (2009) 1-34
92. K. Kaneko, N. Fukuzaki, K. Kakei, T. Suzuki and S. Ozeki, Langmuir 5 (1989) 960.

93. J. Imai, M. Souma, S. Ozeki, T. Suzuki and K. Kaneko, J. Phys. Chem. 95 (1991) 9955.
94. R.S. Ruoff, D.C. Lorents, B. Chan, R. Malhotra and S. Subramoney, Science 259 (1993) 346.
95. T.C. Liu and Y.Y. Li, Carbon 44 (2006) 2045.
96. Y.Z. Jin, C. Gao, W.K. Hsu, Y.Q. Zhu, A. Huczko, M. Bystrzejewski, M. Roe, C.Y. Lee, S. Acquah, H. Kroto and D.R.M. Walton, Carbon 43 (2005) 1944.
97. Z.S. Lou, C.L. Chen, D.J. Zhao, S.L. Luo and Z.C. Li, Chem. Phys. Lett. 421 (2006) 584.
98. N. Sano, H. Wang, M. Chhowalla, I. Alexandrou and G.A.J. Amaratunga, Nature 414 (2006) 506
99. K. Kamegawa and H.Yoshida, Carbon 35 (1997) 631.
100. V.G. Pol, M. Motiei, A. Gedanken, J. Calderon-Moreno, M. Yoshimura, Carbon 42 (2004) 111.
101. M. Inagaki, Solid State Ion. 86-88 (1996) 833.
102. M. Inagaki, Carbon 35 (1997) 711.
103. P. Serp, R. Feurer, P, Kaick, Y. Kihn, J. L. Faria and J. L. Figueiredo, Carbon 39 (2001) 621.
104. H.W. Kroto, J. R. Heath, S.C. Obrien, R. F. Curl and R. E.Smalley, Nature 318 (1985) 162.
105. S. Lijima, J. Cryst. Growth, 50 (1980) 675.
106. P. Serp, R. Feurer, P, Kaick, Y. Kihn, J. L. Faria and J. L. Figueiredo, Carbon 39 (2001) 621.
107. Z.C. Kang and J.N. Wang, J. Phys.Chem. 100 (1996) 5163.
108. H.S. Qian, F. M. Han, B. Zhang, Y. C. Guo, J. Yue and B. X. Peng, Carbon 42 (2004) 761.
109. H.S Qiu, Y. F. Li, Y. P. Wang, C. H. Liang, T. H. Wang and D .wang, Carbon

41 (2003) 767.
110. E. Auer, A. Freud, J. Pietsch and T. Tacke, Appl. Catal. A-Gen. 173 (1998) 259.
111. Y. C. Liu, X. P. Qiu, Y. Q. Huang and T. Zhu, Carbon 40 (2002) 2375.
112. F. B. Li, J. Huang, J. Zou, P.L Pan and G.Q. Yuan, Carbon 40 (2002) 2871.
113. Y.Z. Jin, Y.J. Kim, C. Gao, Y.Q. Zhu, A.Huczko, M. Endo and H.W. Kroto, Carbon 44 (2006) 724.
114. V.G. Pol, S.V. Pol, J.M.C. Moreno and A. Gedanken, Carbon 44 (2006) 3285.
115. J. Y. Miao, D.W. Hwang, C.C. Chang, S.H. Lin, K.V. Narasimhulu and L.P. Hwang, Diamond Relat, Mater. 12 (2003) 1368.
116. Z.X. Xu, J.D. Lin, V.A.L. Roy, Y. Ou and D.W. Liao, Mater, Sci. Eng, B-Solid State Mater, Adv. Technol. 123 (2005) 102.
117. P. Serp, R. Feurer, P, Kaick, Y. Kihn, J. L. Faria and J. L. Figueiredo, Carbon 39 (2001) 621.
118. Z.L. Wang and Z.C. Kang, J. Phys. Chem. 100 (1996) 17725.
119. J. Lahaye, Carbon 30, 309 (1992).
120. G. Prado, A. Garo, A. K, and A. Sarofim, In 20th symp. (Int.) on combustion, page. 989. The Combustion Institute, Pittsburg, PA (1984).
121. A. Garo, J. Lahaye, and G. Prado, 21th Symp. (Int.) on combustion,. The Combustion Institute, Pittsburg, PA (1986) 1023.
122. J.D. Bittner, J.B. Howard, and H.B. Palmer, In soot in Combustion Sysems and its Toxic Properties (Edited by J. Lahaye and G. Prado), Plenum Press, New York (1983) 95.
123. J.B. Howard, In 24th Symp. (Int) on Combustion. The Combustion Institute, Pittsburg, PA (1992).
124. M. Frenklach, D.W. Gardiner, Jr., and S.E. Stein, In 21th Symp. (Int.) on Combustion, The Combustion Institute, Pittsburg, PA (1986) 695.
125. J. Lahaye, G. Prado, and J.B. Donnet, Carbon 12 (1974) 27.

126. J.B. Donnet, J. Lahaye, A. Voet, and G. Prado, Carbon 12 (1974) 214.
127. K. H. Homan, In Soot Formation in Combustion: An International Round Table Discussion (Edited by H. Jander and H. Gg. Wagner), Vandenhoeck and Ruprecht, Gottingen (1990) 101.
128. J.T McKinnon and J.B. Howard, In 24th Symp. (Int.) on Combustion, The Combustion Institute, Pittsburg, PA (1992) 695.
129. F. Beretta, A. D'Alessio, A. D'Orsi, and P. Minutolo, Comb. Sc. Techn. 85 (1992) 455.
130. A. D'Alessio, A. D'Anna, A. D'Orsi, P. Minutolo, R. Barbella, and A. Ciajolo, In 24th Symp. (Int.) on Combustion, The Combustion Institute, Pittsburg, PA (1992) 973.
131. G. Prado, I.J. Jagoda, K. Neoh, and J. Lahaye, In 18th Symp. (Int.) on Combustion, The Combustion Institute, Pittsburg, PA (1981) 1127.
132. G. Prado, J. Lahaye, and G. S. Haynes, In Soot in Combustion Systems and its Toxic Properties (Edited by J. Lahaye and G. Prado), Plenum Press, New York (1983) 95.
133. R.J. Grow, Carbon nanotubes (2006) 187.
134. G.M. Guldi, (2007) Nature 447 (2007) 7140.
135. F. Rodriguez-Reinoso, Carbon, 36 (1998) 159.
136. R.B. Anderson, in catalysis, P.H. Emmett (ed) Reinhold, New York (1956).

Chapter 3

Experimental Methods

3.1 Introduction

This chapter describes the experimental equipment that was used in this work. Carbon spheres (CSs) were synthesised by three methods i.e. the horizontal furnace chemical vapour deposition (CVD), vertical furnace CVD method and the hydrothermal synthesis method.

CSs synthesised by CVD method are hydrophobic and need to be functionalised to allow them to be miscible in water for metal loading. The functionalisation of CVD synthesised CSs is described in chapter 4 and the catalyst preparation and characterisation methods has been detailed in Chapter 4, 5, 6, 7 and 8. The catalytic performance of the prepared catalysts was tested in a Fischer-Tropsch (FT) micro reactor system.

3.2 Synthesis of carbon spheres (CSs)

3.2.1 Chemical vapour deposition method (CVD) in a horizontally aligned furnace

The CVD horizontal furnace equipment used for synthesising carbon spheres (CSs) and nitrogen doped carbon spheres (NCSs) is shown in Fig. 3.1. In this method a quartz tubular reactor with a heat tolerance of 1200 ^{o}C was used. Acetylene gas was used as the carbon source and acetonitrile was used as the nitrogen source. The gas flow rates were controlled by means of a needle valve

and the flow rates were measured by a flow meter. The furnace temperature was ramped at 10 ^{o}C/min until the desired temperature was reached in all experiments. The products were deposited on the inner walls of the quartz tubular reactor.

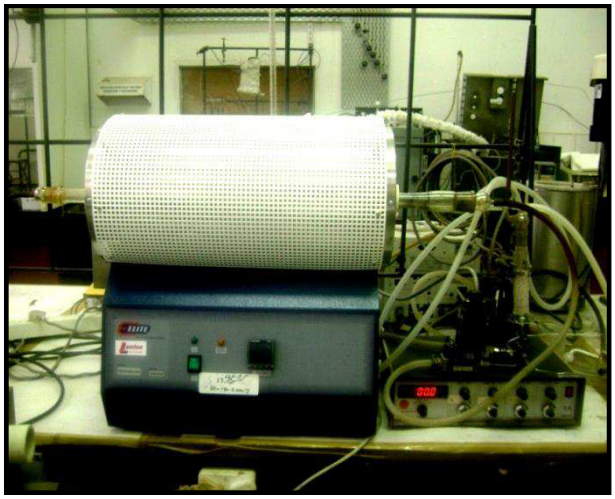


Figure 3.1: Image of horizontal furnace equipment.

The gases used were supplied by AFROX (African oxygen Ltd) and were accompanied by a certificate of analysis i.e. nitrogen gas (UHP 99.99 %) and acetylene gas (99.99 %).

3.2.2 Chemical vapour deposition method (CVD) in a vertically aligned furnace

Fig. 3.2 shows the equipment used for synthesising NCSs using the vertical furnace CVD method. A quartz tubular reactor with a heat tolerance of 1200 ^{o}C was used in this method. The gas flow rate was controlled by means of a needle valve and the furnace was heated at 10 ^{o}C/min. Acetylene gas was used as the carbon source while acetonitrile was used as the nitrogen source. The products were deposited on the inner walls of the quartz tubular reactor and also in adjoining cylones.



Figure 3.2: Image of CVD vertical furnace equipment

3.2.3 Hydrothermal synthesis of carbon spheres

The hydrothermal synthesis of CSs or NCSs at low temperatures was carried out in a 60 mL autoclave, which was heated by an element at a heating rate of 10 ^{o}C/min. Sucrose was used as a carbon source and urea was used as the nitrogen source for NCS synthesis. All chemicals used were ACS reagents supplied by Sigma Aldrich.

3.3 Catalyst characterisation equipment

3.3.1 TEM

A FEI Tecnai G^2 Spirit (Fig. 2.3) at 120 kV was used for transmission electron microscopy studies. All samples were ultrasonically suspended in ethanol and a

drop of the suspension was transferred to a copper grid and allowed to dry before analysis.

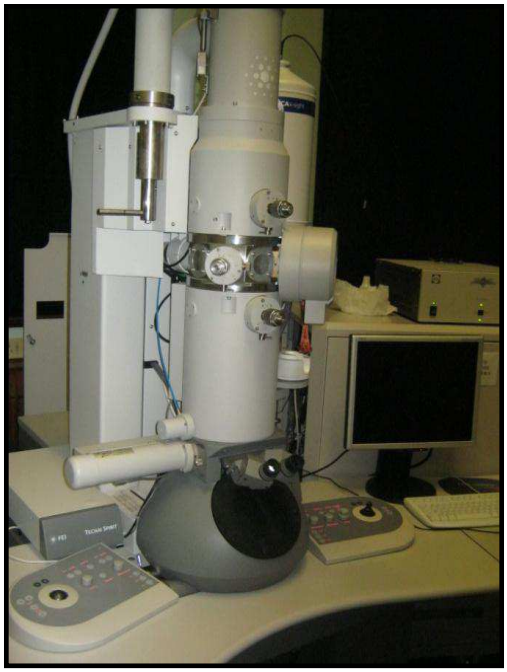


Figure 3.3: Image of FEI Tecnai G^2 Spirit TEM instrument

3.3.2 Thermo-gravimetric analysis (TGA)

A Perkin Elmer TGA 4000 Thermo-gravimetric analyzer (Fig. 3.4) was used for thermal analysis of all samples in air or nitrogen, at a constant heating rate of 10 °C/min from 25 ^{o}C up to 850 ^{o}C. The sample mass used was approximately 0.01 g and the gas flow rate was 20 ml/min.

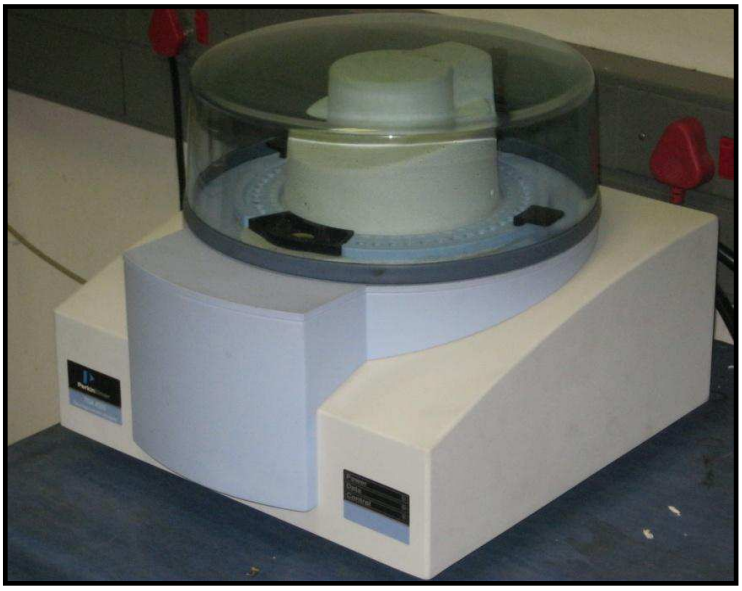


Figure 3.4: Image of PerkimElmer TGA 4000 instrument

3.3.3 Brunnet Emmett Teller (BET) analysis

The surface area, pore volume, and average pore diameter of the CSs were measured on an ASAP-2000 Tristar analyser from Micromeritics (Fig. 3.5). Approximately 0.2 g sample was degassed in N_2 at 120 ^oC for 12 h prior to analysis using a Micromeritics flow Prep 060, sample degas system.



Figure 3.5: Image of ASAP-2000 Tristar analyser BET instrument

3.3.4 Temperature programmed reduction (TPR)

Temperature programmed reduction of ~0.2 g degassed samples was carried out using a Micromeritics Autochem II TPR instrument (Fig. 3.6) in a 5 % hydrogen gas (flow rate of 50 mL/min) at 1 bar pressure while the temperature was raised to 800 ^{o}C at a heating rate of 10 ^{o}C/min.



Figure 3.6: Image of Micromeritics Autochem II TPR instrument

3.3.5 Chemisorption

H_2-chemisorption analysis was performed with a Micromeritics ASAP 2020 (Fig. 3.7), surface area and porosity analyser. Calcined pre-weighed samples (~0.5 g) were degassed using He at 130 ^oC prior to chemisorption analysis. The catalysts were reduced in pure H_2 at 330 ^oC for 18 h and O_2 titration was performed at 300 ^oC.



Figure 3.7: Image of Micromeritics ASAP 2020 Chemisorption instrument.

3.3.6 Raman spectroscopy

Raman spectroscopy measurements were carried out using a micro-Raman attachment of a Jobin-Yvon T64000 Raman spectrometer (Fig. 3.8). The spot size on the sample was ~1.5 μm in diameter and the excitation wavelength was 514.5 nm from an Ar ion laser. A grating with 600 grooves/mm was used to disperse the spectrum onto a charge coupled detector (CCD).

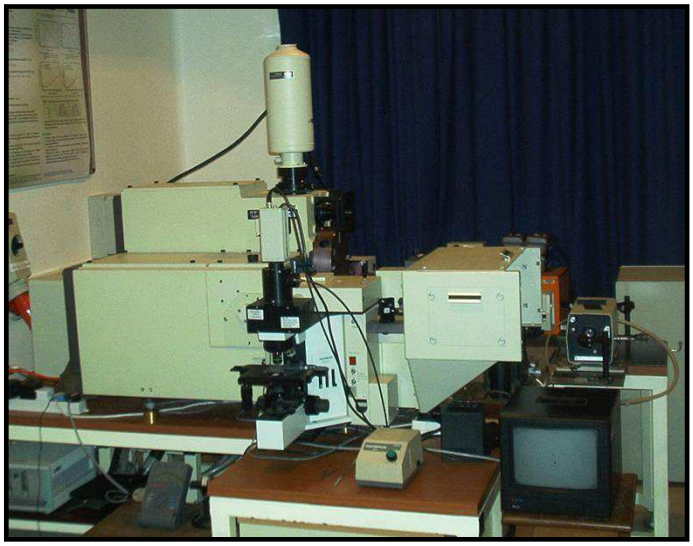


Figure 3.8: Image of Jobin-Yvon T64000 Raman spectrometer.

3.3.7 X-ray diffraction (XRD)

The phase compositions of the support and catalysts were determined by means of XRD analysis on a Brüker D2 phaser in Bragg Brentano geometry with a Lynxeye detector using Cu-K_α radiation at 30 kV and 10 mA (Fig. 3.9). The scan range was $5\ ^{o} < 2\theta < 90\ ^{o}$ in 0.040 steps, using a standard speed with an equivalent counting time of 1 second per step. The diffraction peaks were then compared with those of standard compounds reported in the $Diffrac_{plus}$ evaluation package using the EVA (V11.0, rev.0, 2005) software package.

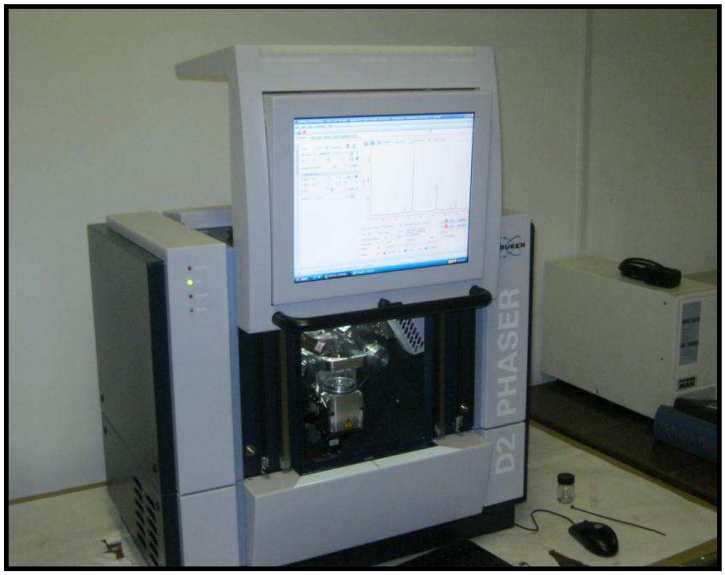


Figure 3.9: Image of Bruker D2 phaser XRD instrument

3.3.8 Fourier Transform Infra Red spectroscopy (FT-IR)

A Brüker Tensor 27 Fourier Transform Infrared spectrometer (Fig. 3.10) was used for qualitative analysis of functional groups on carbon spheres.

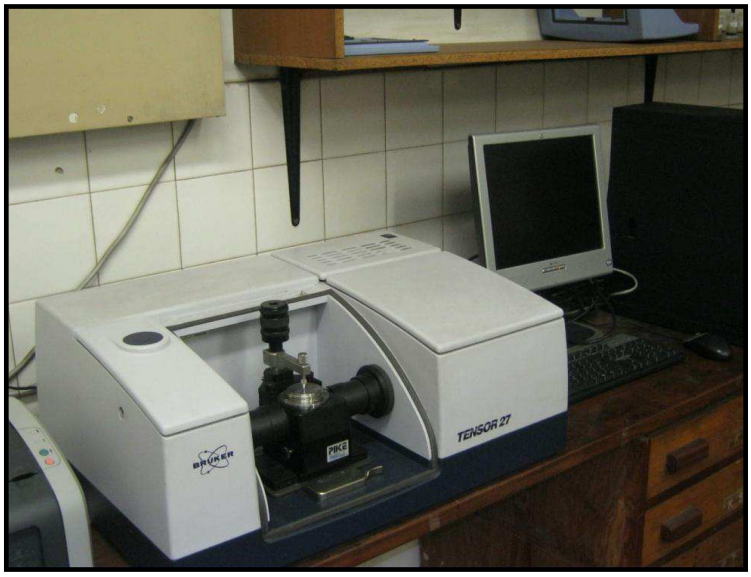


Figure 3.10: Image of Bruker Tensor 27 IR instrument

3.3.9 X-ray photoelectron spectroscopy

An X-ray photoelectron spectroscopy (XPS) physical Electronics Quantum 2000, Al K-Alpha spectrometer (at CSIR, Pretoria) was used to characterise surface nitrogen functional groups and the elemental composition of NCSs.

3.3.10 Elemental analysis (C,H and N)

The nitrogen content in NCSs was determined by C,H and N elemental analysis using a Carlo Erba NA1500 analyzer (at the soil institute, Pretoria).

3.4 Reactor studies

3.4.1 Gases

All gases used for Fischer-Tropsch experiments were supplied by AFROX (African Oxygen) Ltd and were accompanied by a certificate of analysis. Prior to the FT synthesis Ultra high purity (UHP) grade Hydrogen gas (99.997% purity) was used for catalyst reduction and syngas cylinders containing H_2/CO/Ar mixtures (0.60/0.30/0.1 vol; Purity: 99.99%) were used as the feed gas. N_2 was used as an internal standard in order to ensure accurate mass balances and Ar gas was used as carrier gas for the gas chromatograph (GC).

3.4.2 Catalyst evaluation

Equipment setup

The equipment setup for the Fischer-Tropsch synthesis is shown schematically in Fig. 3.11.

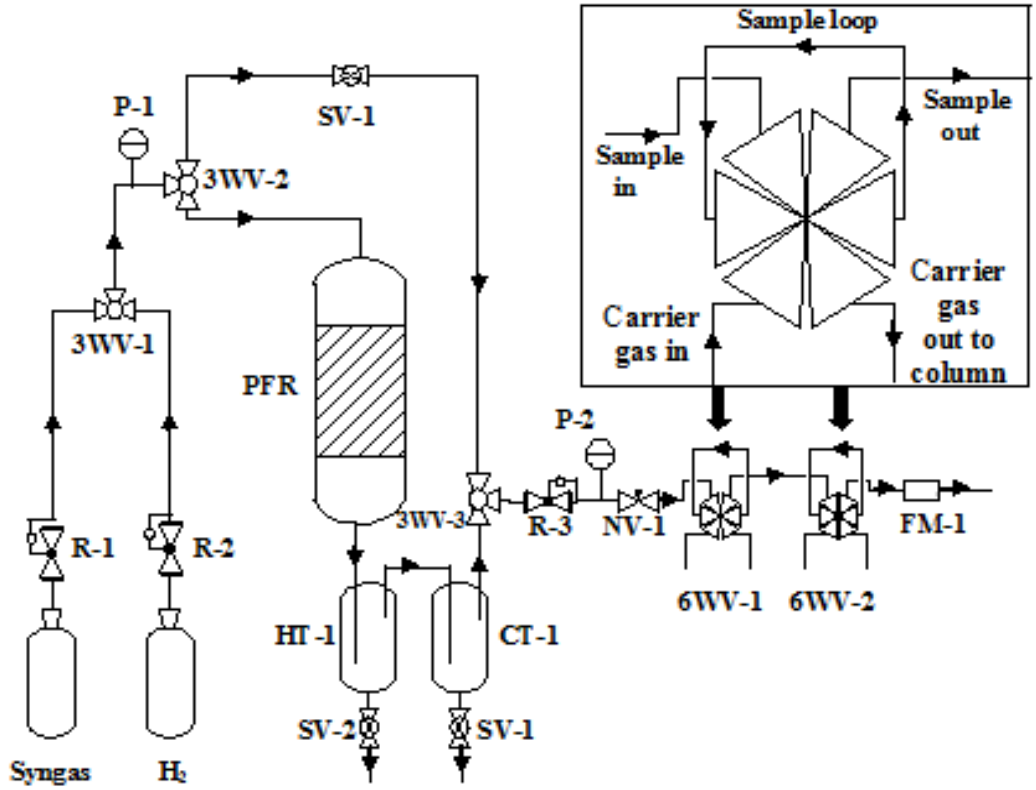


Figure 3.11: Flow sheet diagram of FT rig set up (insert: 6 way valve connecting to GC-FID and GC-TCD.)

R- regulator, **P**- pressure gauge, **3WV**- three way valve, **6WV**- six wave valve, **NV-** needle valve, **SV-** shut off valve, **HT/CT**- hot /cold trap, **FM**-flow meter, **FBR**- plug flow reactor.

The system consisted of a single tubular fixed bed reactor (FBR), with all gases supplied from gas cylinders fitted with pressure regulators to control the gas pressure output (R-1,R-2 and R-3). The system was also equipped with two pressure gauges (P-1 and P-2): one between the shut off valve (SV-1) and the reactor that indicated the pressure of gas entering the reactor, while the other one was installed between the cold trap (CT-1) and the Gas chromatographs (GC-FID and GC-TCD) and indicated the pressure entering the GCs (set at 1 atm). The

volumetric gas flow rates were monitored by a soap bubble meter (FM-1) connected to the FID-GC bypass line.

All gas lines after the reactor were kept at 150 ^{o}C. Three product traps were installed after the reactor; a hot trap which was heated to 130 ^{o}C was used to collect wax while two cold traps kept at ambient temperatures were used to collect liquid products (oil and water). The gaseous products were directed to the GC's which were connected in series (on-line) for analysis. The reactor temperature and line temperatures were controlled by using programmable electronic temperature controllers connected to the system.

All the gas lines used in the system consisted of 1/4" and 1/8" stainless steel tubing and the fittings used were Swagelock stainless steel fittings. The shut off valves were SS Valco valves with Viton ® seals and the needle valves were Whitey valves. The data signal from both the FID and TCD detectors was captured means of Clarity ® software programme.

Fixed bed reactor design

A single tubular fixed bed reactor (FBR) was used for all FT synthesis experiments. The schematic diagram of the FB reactor is shown in Fig. 3.12. The micro-reactor was made of stainless steel, with a total height of 250 mm, internal diameter of 50 mm and filled with 2 mm stainless steel balls above a sieve plate with pore diameters of 0.5 mm placed 88 mm above the bottom of the reactor. The FBR was heated by an element with a 700 Watt rating placed in a heating jacket covered with fiber-glass insulation. The micro reactor used can be divided into three zones, (1) the gas pre-heating zone where the feed gas was heated as it passed through a bed of 2 mm stainless steel balls packed to a height of 160 mm,

(2) the catalyst chamber where the catalyst is packed and the FT reaction occurs and (3) the bottom of the reactor.

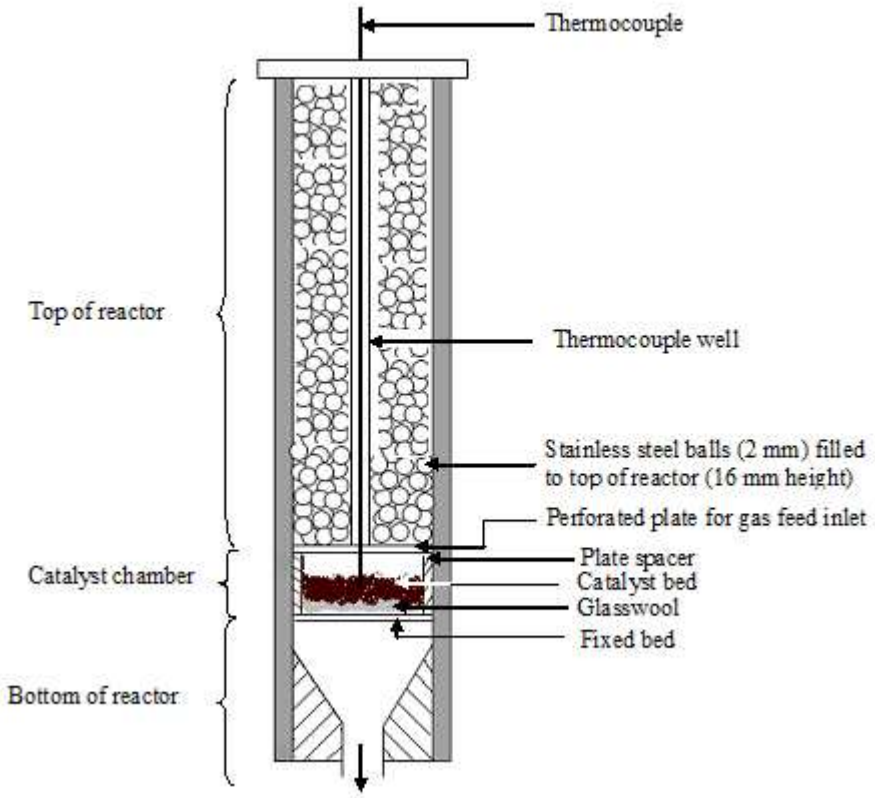


Figure 3.12: Schematic diagram of fixed bed reactor

Catalyst reduction and FT synthesis

All catalysts samples (0.5 g) were reduced *in-situ* prior to FT synthesis. The 3WV was switched to open H_2 gas through the reactor at 2 bar pressure while the reactor containing the catalyst was heated to 330 ^{o}C for 18 h, a gas flow rate of 45 ml/min was maintained throughout the reduction step and during reactor cooling

After the catalyst reduction step, the reactor was cooled under H_2 gas to room temperature before the 3WV was switched to select syngas. The pressure on the syngas gauge was set to 1 bar, the reactor temperature was kept at room temperatures and the syngas (H_2/CO = 2) was analysed to determine the amount

of syngas entering the reactor. This analysis was continued until consistent areas of H_2, N_2 and CO were obtained. Then the syngas pressure was slowly raised to 8 bar and maintained while the FBR was heated at 3 ^{o}C/min to 220 ^{o}C and maintained at this temperature throughout the FT reaction.

The gas pressure after the FBR was dropped to 1 bar on the second regulator (P-2) and a gas flow rate of 75 mL/min (space velocity = 2100 h^{-1}) was controlled by a needle valve (NV-1).

3.4.3 Gas chromatography calibration and product analysis

Gas chromatography (GC) calibration

Prior to all FTS experiments, the GCs were calibrated using two calibration gases: (1) a calibration gas mixture which consisted of CH_4 (2.5%), C_2H_4 (0.2%), C_2H_6 (0.5%), CO (10.0%), CO_2 (5.0%) and balance of Ar, a typical trace is shown in Fig. 3.13. (2) Syngas with a gas composition of H_2 (60%), N_2 (10%) and CO (30%), a typical trace is shown in Fig. 3.14. The peak area corresponding to each molecule detected was taken to correspond to the number of moles of that molecule passing through the detector.

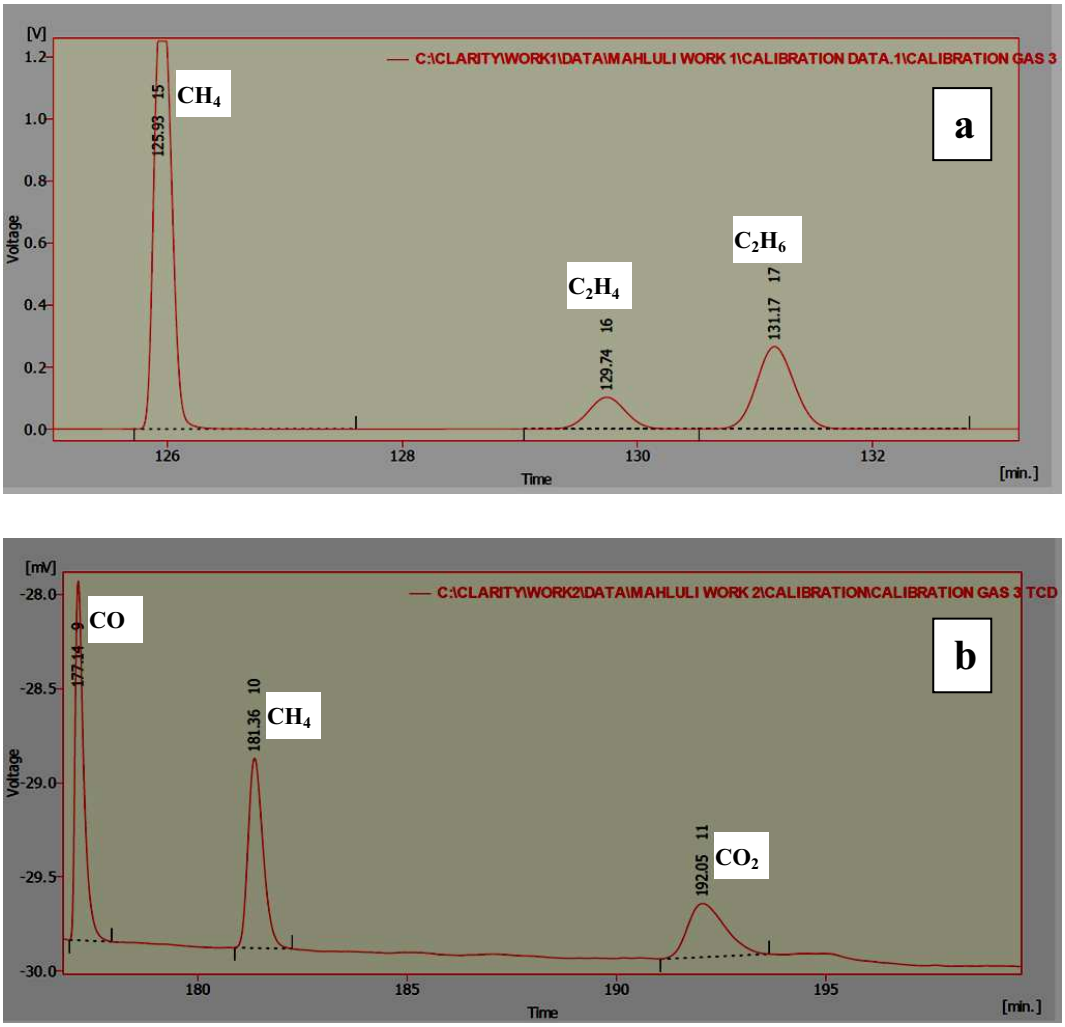


Figure 3.13: (a) GC-FID and (b) GC-TCD trace of calibration gas with CH_4 (2.5%), C_2H_4 (0.2%), C_2H_6 (0.5%), CO (10.0%), CO_2 (5.0%) and balance of Ar gas composition.

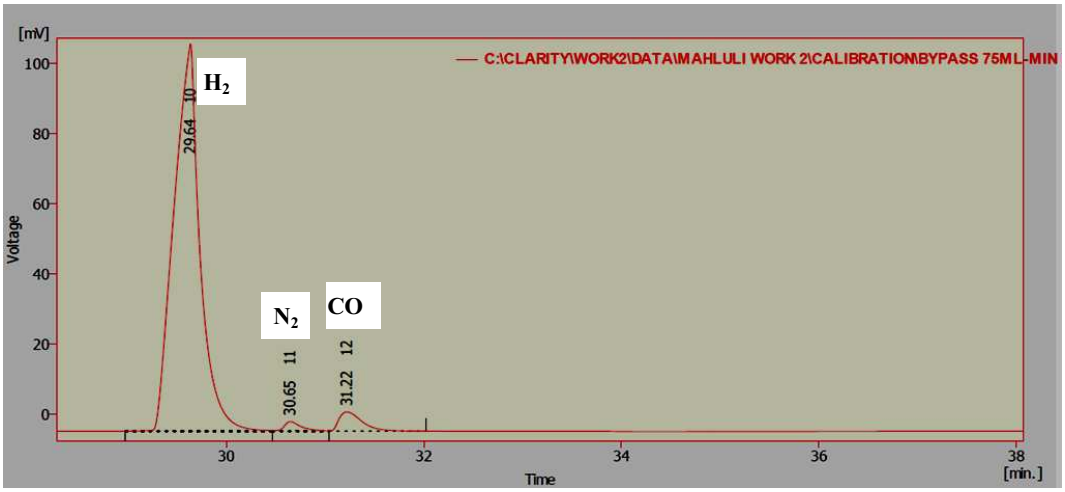


Figure 3.14: GC-TCD trace of syngas calibration H_2 (60%), N_2 (10%) and CO (30%)

Product analysis

The analysis of the product spectrum was divided into two parts.

(i) Online analysis which involved analysis of the tail gas using two gas chromatographs one fitted with a TCD detector and the other with a FID detector. Unreacted syngas, N_2 internal standard, CO_2 and methane from the product stream were analysed using a GC-TCD instrument fitted with a Carbosieve S-II (1.50 m x 1/8 inch, stainless) packed column. The low boiling FT products were analysed by a GC-FID instrument fitted with a Porapak Q packed column.

(ii) Offline analysis which involved analysis of the wax and oil fractions collected from the knockout traps (HT-1and CT-1). The offline analysis was carried out using a GC-FID instrument. Approximately 0.2 µL sample was injected into an offline GC-FID instrument using a syringe.

The analysis conditions are detailed in Appendix A.

3.4.4 Mass balance calculations

Before carrying out FTS, the amount of syngas in the inlet stream was determined as outlined in the section 3.4.3. During FTS the amount of un-reacted syngas and the low boiling FT products from the outlet stream were analysed. After FTS the oil fraction and wax fraction were analysed off-line.

The % CO conversion was calculated as follows:-

$$\% CO = \left[\frac{N_{co,in} - N_{CO,out}\ x\ Gas\ contraction}{N_{CO,in}}\right] x\ 100 \qquad \text{Equation 3.1}$$

Where:-

$N_{co,\ in}$ = mole fraction of CO in the inlet stream

$N_{co,\ out}$= mole fraction of CO in the outlet stream

Gas contraction = N_{in}/N_{out} (where N_{in}= the moles of nitrogent from bypass

N_{out} = moles of nitrogen during reaction)

The mass balance calculations used are similar to those described by Nijs and Jacobs [1], Mokoena [2], Duvenhage [3] and Price [4]. The mass balances were performed on carbon and oxygen. The analysis of feed gas and products at steady state by the two gas chromatographs at steady state was recorded as integrated peak areas by means of Clarity ® software installed on a computer. The gas flow rate and mass balance time was noted for the period at steady state. The wax and liquid fractions were collected separately from the hot and cold traps respectively

and weighed. From the liquid fraction the oil was separated from water before analysis on the offline GC. Peak areas for each component were converted to molar compositions using peak percentages.

The feed inlet flow rate to the reactor was determined using N_2 gas detected by GC-TCD before and after reaction and was calculated using the equation below:-

$$F_{in} = \left[\frac{X_{N_2,in}}{X_{N_2,out}}\right] x\ F_{out} \qquad \text{Equation 3.2}$$

Where:-

F_{in} = the total feed flow rate in mol/s,

$X_{N_2,in}$ = the mole fraction of N_2 in the feed (syngas)

$X_{N_2,out}$ = the mole fractions of N_2 in the reactor exit stream

F_{out} = the reactor exit stream flow rate in mol/s.

The number of moles of carbon in the feed stream in the total mass balance period was calculated by:

$$N_{C,in} = F_{in}.t.X_{CO,in} \qquad \text{Equation 3.3}$$

Where:-

$N_{C,in}$ = the moles of carbon in the feed

F_{in} = the total feed flow rate in mol/s

t = the total mass balance time

$X_{CO,\,in}$ = the mole fraction of CO in the feed gas.

The number of moles of product for each of the components present in the gas phase was calculated using the following equation:

$$N_{c,out} = \left[\frac{A_C}{A_{C,cal}}\right].X_{c,cal}.F_{out}.t \qquad \text{Equation 3.4}$$

Where:-

A_c = the integrated peak area for component c,

$A_{c,\,cal}$ = the peak area for the component c in the calibration gas

$X_{c,cal}$ = the mole fraction of component c in the calibration gas.

The hydrocarbon product areas were corrected relative to C_2H_4 (olefins) and C_2H_6 (paraffins) by using the response factors based on those presented by Dietz [5], and Scanlon and Willis [6]. The mole fraction of hydrocarbon *i*, $X_{HC,\,i}$ was calculated using the equation below:

$$X_{HC,i} = \frac{RF_i.A_{HC,i}}{A_{C_2,cal}}.X_{C_2,cal} \qquad \text{Equation 3.5}$$

Where:-

RF_i = the response factor for carbon number *i*

$A_{HC,i}$ = the integrated peak area for a hydrocarbon with carbon number *i*

$A_{C_2,cal}$ = the peak area of the C_2 hydrocarbon in the calibration gas

$X_{C_2,cal}$ = the mole fraction of the C_2 hydrocarbon in the calibration gas [2-3]

The mole fraction of the individual hydrocarbons with *i* carbon atoms from the oil and wax analysis was calculated in the same manner and added to the gas fraction. The molar response factors for the hydrocarbons are presented in Table. 3.1. The molar response factors of carbon number greater than 15 were assumed to be 1.00 [7]. The mass fractions of these hydrocarbons (i > 15) were therefore determined directly from the GC integrated areas using the following equation:

$$m_i = \frac{A_{HC,i}}{\sum A_{HC}} . \textit{[mass of oil or wax product]} \qquad \text{Equation 3.6}$$

Where:-

$A_{HC,i}$ = the integrated peaks area of hydrocarbon *i*

$\sum A_{HC,}$ = summation of the integrated peak areas of all hydrocarbons analysed present in the oil or wax fraction

Table 3.1: Molar response factors for hydrocarbon [4-5, 8]

Carbon Number	Olefin	Paraffin
1	-	1.00
2	1.00	1.00
3	0.70	0.74
4	0.78	0.55
5	0.47	0.47
6	0.40	0.40
7	0.35	0.35
8	0.32	0.32
9	0.28	0.28
10	0.24	0.24
11	0.21	0.21
12	0.19	0.19
13	0.18	0.18
14	0.17	0.17
15	0.15	0.15

Carbon and oxygen mass balances were determined using the information obtained from the above analysis and calculations:

$$\%\ Mole\ balance = 100\ x\ [\frac{Total\ C_{out}}{Total\ C_{in}}] \qquad \text{Equation 3.7}$$

Where:-

C_{in} = the moles of carbon that enter the reactor

C_{out} = the moles of carbon that exit the reactor

The mass balance was acceptable at +/- 5 % error.

Product selectivity

The product selectivity for hydrocarbons S_i was calculated for component x_i as follows:

$$S_i = \left[\frac{N_i}{r_{co} \,.\, t}\right] X\ 100\ \% \qquad \text{Equation 3.8}$$

Where:-

N_i = moles of hydrocarbon containing *i* carbon atoms

r_{co} = rate of CO conversion

t = mass balance time

Rates of reaction

The individual rates of reaction for FTS (r_{FTS}) and water gas shift WGS (r_{WGS}) were calculated from experimentally obtained quantities as follows:

$$r_{WGS} = r_{CO_2} \qquad \text{Equation 3.9}$$

$$r_{FTS} = r_{CO} - r_{CO_2} \qquad \text{Equation 3.10}$$

Where:-

r_{CO_2} = the rate of carbon dioxide formation

r_{CO} = the rate of carbon monoxide conversion [2-3, 9-10].

Olefin to paraffin ratio

The olefin to paraffin ratio of product i was calculated as follows:

$$Olefin\ to\ paraffin\ ratio\ i\ = \frac{N_i^=}{N_i^= + N_i^-} \qquad \text{Equation 3.11}$$

Where:

$N_i^=$ = moles of olefin containing *i* carbon atoms

N_i^- = moles of paraffin containing *i* carbon atoms

References

1. H.H. Nijs, P.A. Jacobs, J. Chrom. Sci. 19 (1981) 40.

2. E. M. Mokoena, “Synthesis and use of silica materials as support for the Fischer-Tropsch reaction”, PhD Thesis, University of the Witwatersrand, Johannesburg, 2005.

3. D.J. Duvenhage, “The preparation, Characterization and Evaluation of Titania Supported Fe:Co Bimetallic Catalysts for the Hydrogenation of CO”, PhD Thesis, University of the Witwatersrand, Johannesburg, 1994.

4. J.G. Price, “An Investigation into novel bimetallic catalysts for use in the Fischer-Tropsch reaction”, PhD Thesis, University of the Witwatersrand, Johannesburg, 1994.

5. A.W. J. Dietz, Gas Chrom. (1967) 62.

6. J.T. Scanlon, D.E. J. Willis, Chrom. Sci. 23 (1985) 333.

7. M.C. Bahome, "Synthesis and use of carbon nanotubes as a support for the Fischer-Tropsch Synthesis", PhD thesis, University of the Witwatersrand, Johannesburg 2008.

8. A.M.M Motchelaho, “Iron and cobalt catalysts supported on carbon nanotubes for use in the Fischer-Tropsch synthesis”, PhD thesis, University of the Witwatersrand, Johannesburg, 2011.

9. K. Jalama, "Fischer Tropsch synthesis over supported cobalt catalysts: effect of ethanol addition, precursors and gold doping", PhD thesis, University of the Witwatersrand, Johannesburg, 2008.

10. W.M. Hexana, "A systematic study of the effect of chemical promoters on the precipitated Fe-based Fischer-Tropsch synthesis catalyst", PhD thesis, University of the Witwatersrand, Johannesburg 2009.

Chapter 4

Synthesis, functionalisation and characterisation of carbon spheres

4.1 Synthesis of carbon spheres

4.1.1 Introduction

Carbon spheres (CSs), produced by a chemical vapour deposition method (CVD), are comprised of randomly dispersed graphene flakes that form a ball of carbon, these materials have a different structure from that of the C_{60} (fullerene) cage as well as that of carbon onions which comprise of graphene layers. Research has shown that carbon spheres exhibit similar physical and chemical properties to graphite and fullerenes. These properties can be exploited to allow the spheres to be used to fabricate diamond films, and be used as lubricating materials and as special rubber additives [1].

Carbon spheres have also been shown to be useful as catalyst support materials because of chemical inertness, high thermal stability and lower cost of production compared to conventional supports such as alumina and silica. They have a very high mechanical strength, high purity and it is relatively easy to tailor the pore structure of these materials [2]. Based on these properties carbon spheres have very valuable characteristics which are not attainable with any other support material.

4.1.2 Experimental

Carbon spheres were synthesised by a chemical vapour deposition (CVD) method at 900 ^{o}C in the absence of a catalyst, using acetylene gas as a carbon source [3]. A schematic diagram of the experimental setup is shown in Fig. 4.1. In this method nitrogen gas was flowed through a quartz tubular reactor at a flow rate of 60 mL/min while the furnace was heated to 900 ^{o}C at a heating rate of 10 ^{o}C/min. When the furnace temperature reached and stabilised at 900 ^{o}C, the nitrogen gas flow was cut off and replaced with acetylene gas at a flowrate of 100 mL/min for 1 h. After 1 h the acetylene gas flow was cut off and nitrogen gas was once again flowed through the reactor at a flow rate of 60 mL/min while the furnace wa cooled to room temperature.

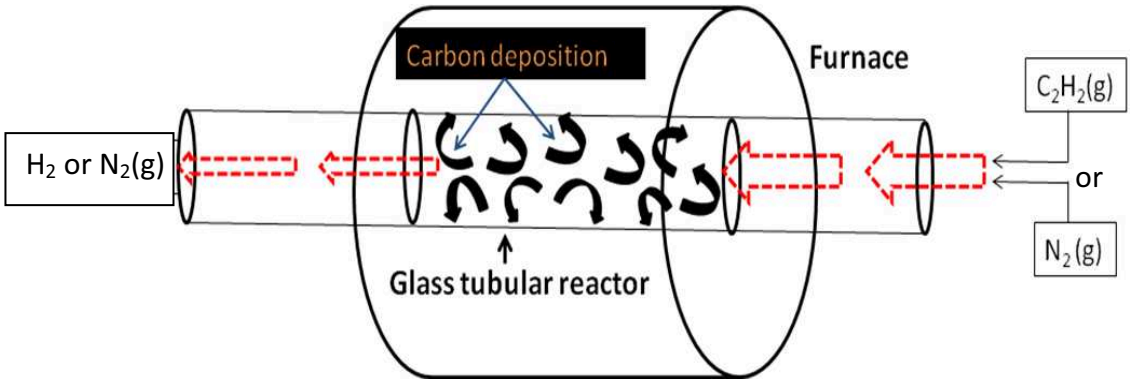


Figure 4.1: Schematic diagram of the chemical vapour deposition equipment and reaction.

At room temperature the CSs that had deposited on the inner walls of the quartz tubular reactor were then scraped out with a spatula and collected (Fig. 4.2). The product (yield 2.1 g) was characterised by TEM, Raman spectroscopy and TGA.



Figure 4.2: Image of the bulk carbon spheres products

4.1.3 Results and discussion

When the soot like product shown in Fig. 4.2 was analysed using TEM. The images revealed that the crude product consists of a solid carbon material with a spherical shape (Fig. 4.3a), which can accrete to form carbon beads as shown in Fig. 4.3b.

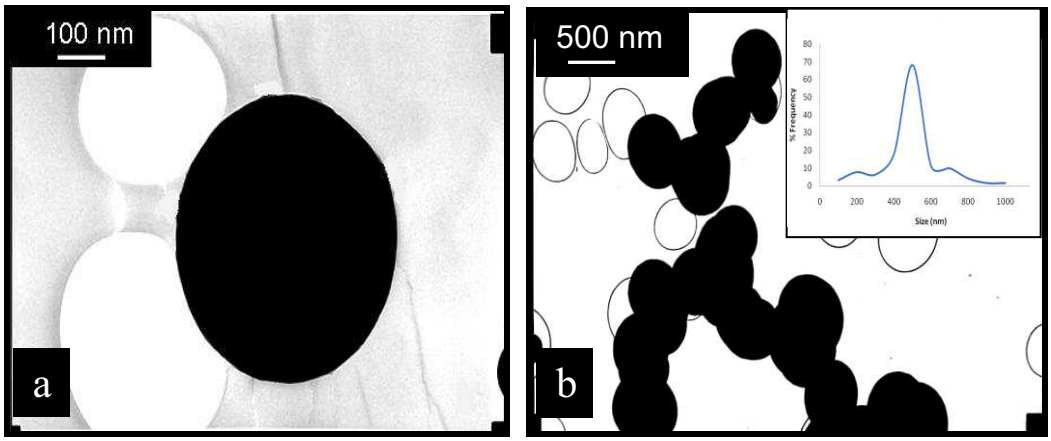


Figure 4.3: TEM images of as-synthesised CSs (a) single sphere and (b) accreted spheres (insert showing CSs diameter distribution).

Carbon spheres form when carbon nucleates and then deposits on itself. If the CSs are close together, the carbon can deposit on top of both CSs to yield the necklace like structure. CSs can also be attracted to each other by van der Waals forces. These beads still retain the non-graphitic nature of the individual CSs. Under the reaction conditions employed the as-synthesised CSs were of a uniform size with an average diameter of 480 nm (inset in Fig. 4.3b). It is believed that the carbon flakes that make up the CSs tend to rearrange themselves forming a much more orderly structure if annealed above 600 ^{o}C under inert conditions as illustrated in Fig. 4.4. The resulting carbon material becomes more graphitic.

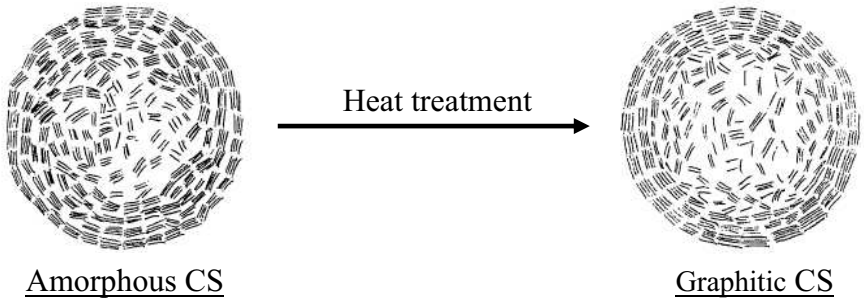


Figure 4.4: Cartoon illustration of heat treatment of CSs

The SEM image of the as-synthesised CSs is shown in Fig. 4.5 below. Although the CSs appear spongy and fluffy, these materials are in fact hard, solid, carbonaceous materials.

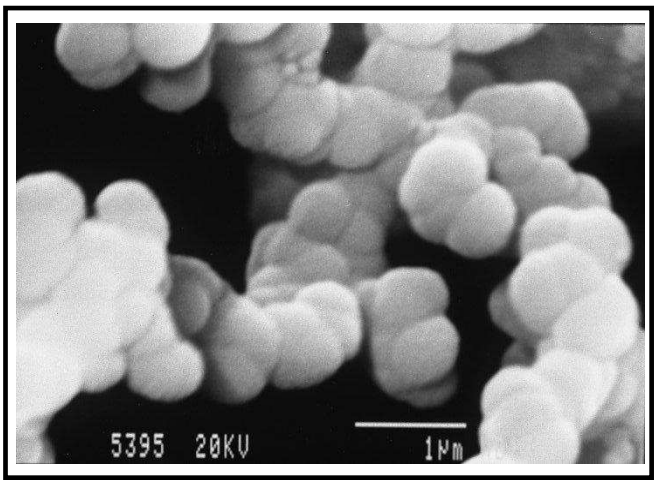


Figure 4.5: Shows SEM image of as-synthesised CSs.

TGA results (Fig. 4.5) of the as–synthesised CSs show that these materials are thermally stable up to a temperature of 560 ^{o}C in air. More importantly, at temperatures between 200 and 300 ^{o}C, no evidence of mass loss was observed by TGA, implying that CSs should be capable of maintaining their spherical morphology under FT synthesis conditions. The rapid and complete (100 %) weight loss at 560 ^{o}C confirms that the as-synthesised CSs are made entirely of carbonaceous compounds.

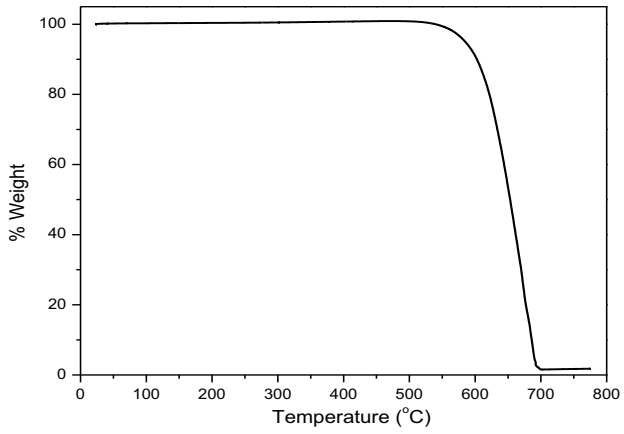


Figure 4.6: TGA of as-synthesised CSs run in air

Raman spectroscopy was used to determine the crystallinity of the as-synthesised CSs. The set back with this technique is in its inability to effectively analyse carbon materials with very low amorphous content. Fig 4.7 shows the Raman spectra of the as-synthesised CSs. Two characteristic peaks can be noted in Fig. 4.7 i.e at ~1350cm^{-1} corresponding to the disorder-induced band (D-band) and the other at ~1590cm^{-1} corresponding to the tangential mode (G-band). The D-band is due to the disorder features present in the CSs while the G-band is due to the more ordered graphitic nature of the CSs. The ratio of I_D/I_G = 1.4 for the as-synthesised CSs implying that the as-synthesised materials contains a high level of sp^3 hybridised carbon atoms. Graphitisation of the CSs is directly proportional to the residence time of the CSs during synthesis. Therefore the reaction time of 1 hour was sufficient to produce the materials required for further study.

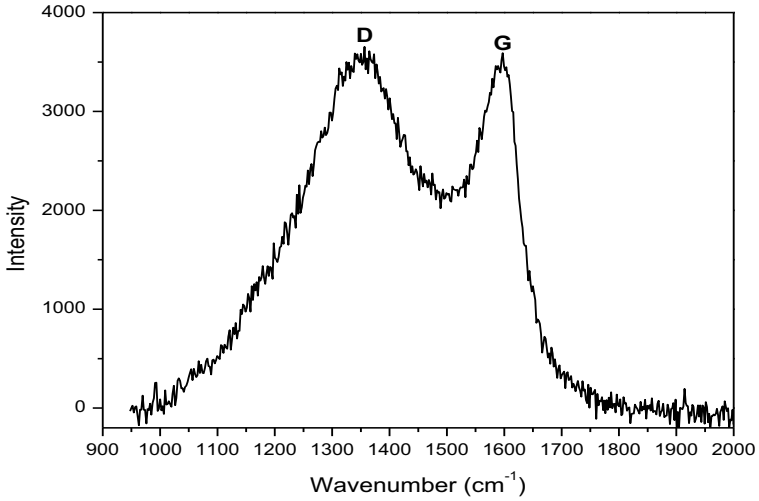


Figure 4.7: Raman spectra of the synthesised CSs

4.2 Functionalisation of the carbon spheres

4.2.1 Introduction

Carbon spheres can show basic or acidic pH values in aqueous dispersions [6-12]. The carbon spheres exposed to dry oxygen after synthesis possess a basic surface

whereas an acidic surface is introduced through functionalisation using various functionalising agents [6-12]. The correlation between pH and oxygen content of carbon materials is: the more acidic the surface of carbon spheres the higher the oxygen content. CSs with a high acid content have more cation exchange properties, while those with a low oxygen or acid content show basic surface properties and are prone to anion exchange behaviour. The basic properties of carbon materials are ascribed to the presence of basic surface oxides [4].

The reactivity of carbon spheres is relatively low in the absence of functional groups and carbon spheres are immiscible in polar solvents like water before functionalisation. Functionalisation introduces hydrophilic sites on the hydrophobic CS surface. The dissociation of carboxylic surface groups that are introduced facilitates the dispersion of the CSs by creating a negative surface charge [5]. In catalysis the introduction of surface acidic groups enhances the reactivity of the CS surface and determines the ion exchange properties that are important for metal loading onto the CS support.

Carbon materials can be functionalised using HNO_3, H_2SO_4, ozone, $KMnO_4$, H_2O_2 or a mixture of $KMnO_4$ and HNO_3. Other functionalising methods can also be found in the literature [6-12]. After functionalisation several different kinds of functional groups can be formed on the surface of the CSs. These may include carboxylic acid groups which are formed by incorporating O and H atoms into the surface structure. In the event that these carboxylic acid groups are in close proximity they can form carboxylic anhydrides or lactones. In place of carboxylic acid groups, hydroxyl groups may attach to the surface carbon atom or an oxygen atom may attach to one of the surface atoms to form an isolated carbonyl group. These carbonyl groups may arrange themselves to form quinones. The other possibility is that an oxygen atom may be included in a six membered graphene ring [6].

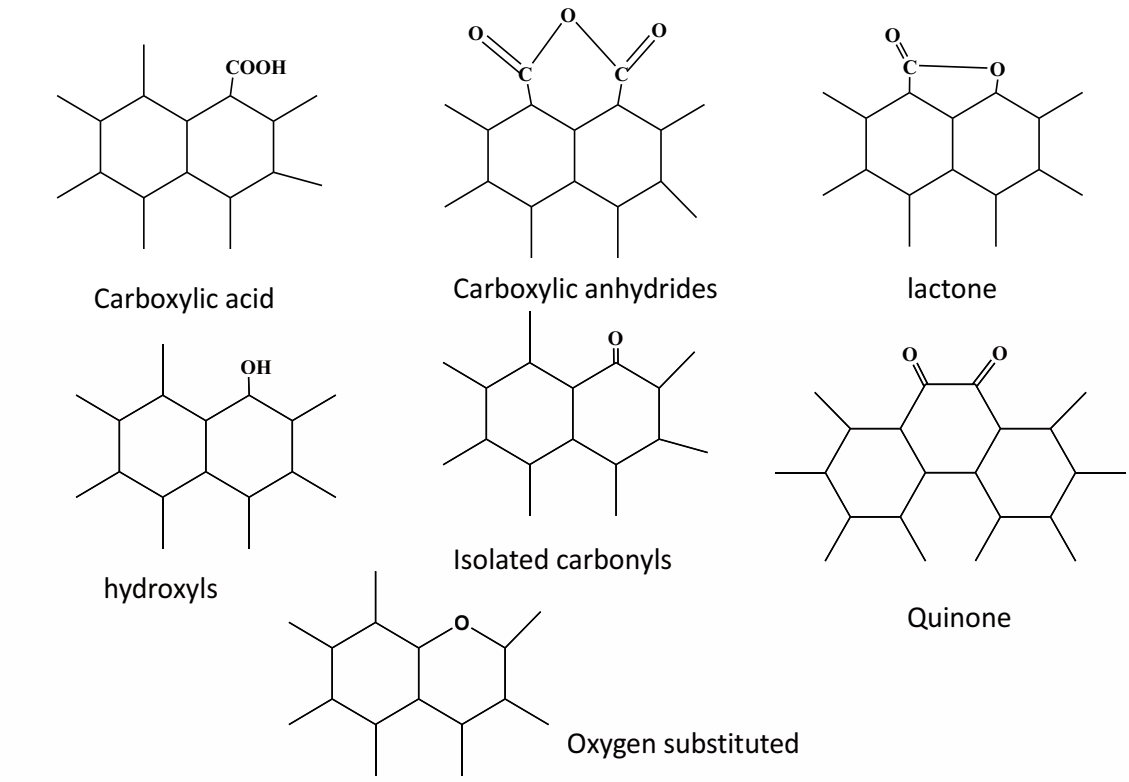


Figure 4.8: Possible surface functional groups found on CSs [6]

The carboxylic acid, carboxylic anhydride, lactone, lactol or single hydroxyl groups attached to the surface of the CSs are all weakly acidic groups of which some are stronger than others. These groups can be used to bind metal particles to the CS.

The surface compounds found on the carbon spheres can be easily removed by simply heating the material under inert gas conditions to *ca.* 400 °C. However, it has been shown that when this material is exposed to dry oxygen after cooling to room temperature, some oxygen is re-chemisorbed forming basic functional groups such as pyrones and chromenes [13-16]. If immersed in aqueous acids, the same quantity of oxygen lost during heat treatment can be regained by chemical reaction [6, 17].

4.2.2 Experimental

Functional groups were introduced onto the CSs by three methods (a) 55 % HNO_3 (b) various concentrations of $KMnO_4$ and (c) a mixture of $KMnO_4$ and HNO_3.

(a) CSs were immersed in an aqueous solution of 55 % HNO_3 under the following conditions:-

- 2, 12, 24, 48 and 96 h at room temperature.
- 2, 24 and 48 h at 40 ^oC.
- 2 and 24 h under reflux (83 ^oC).

After the reaction the CSs were slurried, filtered and washed with deionised water until the filtrate was neutral. The residue was then dried in an oven at 120 ^oC for 12 h.

(b) In this method functional groups were introduced onto the surface of CSs by immersing CSs into a solution of:-

- 0.5, 1 and 2 M $KMnO_4$ solutions at room temperature for 4 h.
- 0.5 and 2 M $KMnO_4$ solutions at 40 ^oC for 4 h.
- 1 M and 2 M $KMnO_4$ solutions at 70 ^oC for 4 h.

After the potassium permanganate treatment all samples were washed with hot deionised water. The CSs were then immersed in a 4 M HCl (aq) solution for 17 h at room temperature with continuous stirring to introduce H ions to the oxygen containing functionalities. After the HCl treatment the CSs were washed to neutrality and then dried in an oven for 12 h at 120 ^oC.

(c) A mixture of 1M $KMnO_4$ and 55 % HNO_3 solutions in the ratio of 1:2 was used to functionalise carbon spheres for 4 h at 40 ^oC. The functionalised CSs were then washed with hot deionised water to neutrality followed by immersion in 4 M HCl solution for 17 h at room temperature. After the HCl

treatment the CSs were washed to neutrality and then dried in an oven for 12 h at 120 ^{o}C.

Acids group characterisation

A qualitative study of the acid sites on the surface of the carbon spheres was carried out using FTIR and TGA described in chapter 3. However, the quantity study of the functional groups on the CSs was determined carried out using the Boehm's titration method using a 0.05 M standardised solution of $NaHCO_3$ as the titrant.

In this method approximately 1 g of functionalised CSs were immersed in 100 mL of 0.1 NaCl solution and stirred for 30 min before titrating with 0.1 mL portions of a 0.05 M standard solution of $NaHCO_3$. The titrant was added in 30 seconds intervals while N_2 gas was bubbled through the sample to remove CO_2; pH Readings were taken 30 seconds after the addition of each titrant portion.

4.2.3 Results and discussion

Alkalimetry

The alkalimetric method was first validated to establish reproducibility when sample size and volume of titrant increments were varied.

End point determination

A typical titration curve for CSs suspended in a 0.1M NaCl electrolyte solution is shown in Fig. 4.9. The titration curve is a result of a potentiometric back titration of hydrogen ions evolved due to an ion exchange between the electrolyte cations and the active hydrogen ions on the surface of the carbon spheres. This neutralisation reaction only occurs in the bulk of the solution. The pH of the

suspension gradually increases in response to the addition of the titrant. This is due to the progressive dissociation of surface acid groups. As can be observed from Fig. 4.9 the titration curves were smooth throughout the pH range, however the titration curves do not show any distinct points of inflection.

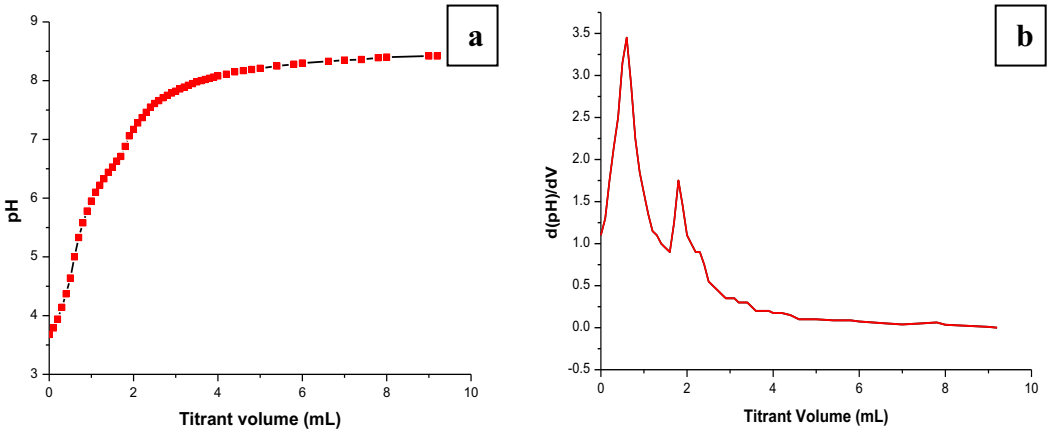


Figure 4.9: (a) Typical potentiometric titration curve of functionalised CSs and (b) the derivative graph.

The raw data was therefore differentiated using Origin 6.0 software to obtain a d(pH)/dV vs titrant volume graphs as shown for example, in Fig. 4.9b. The end point titrant volume was determined from the peak positions on the derivative graph Fig. 4.9b.

Validation of the titration method

The effect of mass of CSs used on the potentiometric titration was investigated by doubling the mass of CSs from ca. 0.2 g while maintaining other variables constant i.e. titrant portions (0.01 mL) and the equilibrium time (30 seconds). The equilibrium time is defined here as the time taken between the addition of the titrant portion and the recording of the pH of the solution. It was noted that varying the sample weight from ca. 0.2 g to 0.8 g shifted the titration curve to the

right, implying that a larger portion of $NaHCO_3$ was required for the neutralisation of the surface acid groups.

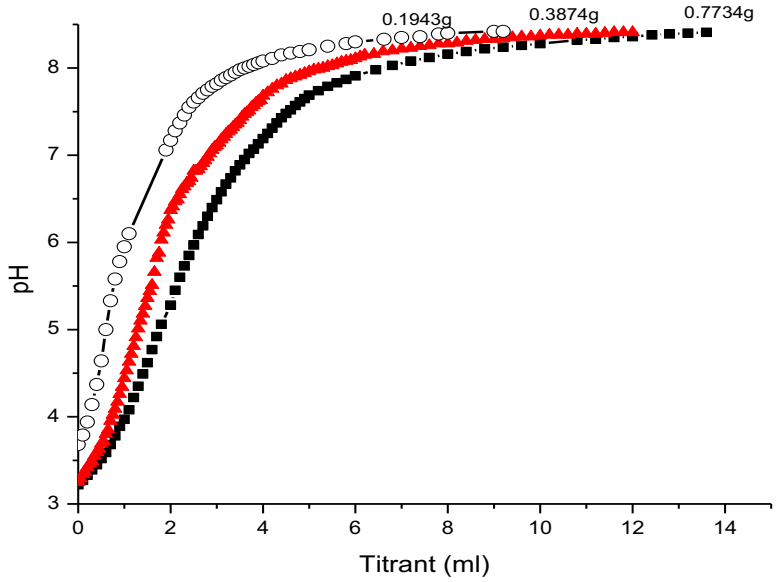


Figure 4.10: Effect of sample size on the determination of end point

From Fig. 4.10 it can also be noted that the initial pH of the suspension decreased with an increase in sample weight. This result was due to an increase in the number of active hydrogen ions dissociated from the functional groups into the electrolyte with an increase in sample size. However a final pH of 8.31 was achieved for the three samples, since this is the pH value associated with 0.05 M $NaHCO_3$. The same amount of carboxylic groups per gram of CSs was determined for each sample, implying that varying sample size between 0.2 g and 0.8 g had no effect on the end point.

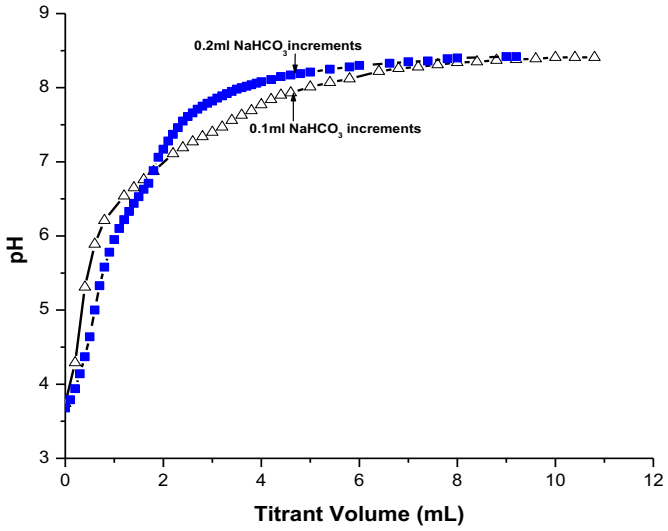


Figure 4.11: Effect of increasing volume

The effect of titrant portion size was investigated by changing the volume additions of the titration portions from 0.1 mL to 0.2 mL while keeping the equilibrium time constant at 30 seconds and sample size constant at 0.4 g. From Fig. 4.11 the initial and final pH values were the same in both samples, titrant volume only affected the shape of the titration curve. An increase in the titrant volume steepens the curve hence eliminating some data points. Any further increase in titrant volume will result in a further loss of data points from the titration curve and hence change the endpoint. Decreasing the titrant volumes increases the number of data points resulting in more accurate data being generated from the experiment. The disadvantage with this is that it increases the experimental time significantly. The addition of 0.1 mL portions of $NaHCO_3$ was therefore selected as a suitable volume for adding titrant when carrying out potentiometric titrations.

4.3 Characterisation of active acid sites

4.3.1 Carbon spheres functionalisation by 55 % HNO_3

Fourier Transform Infra-Red (FTIR) analysis shows advantages over dispersive IR spectroscopy in signal-to-noise (S/N) ratio and the accuracy of the frequency scale. The intensity of the bands obtained during analysis of carbon materials can be affected by the presence of peripheral functional groups at the edges of the carbon surfaces. Although FTIR spectroscopy does not provide quantitative information about the carbon surface chemistry, it can be used for the qualitative analysis of surface functional groups of CSs during functionalisation. The FTIR spectrum of the as-synthesised and nitric acid functionalised CSs are shown in Fig. 4.12.

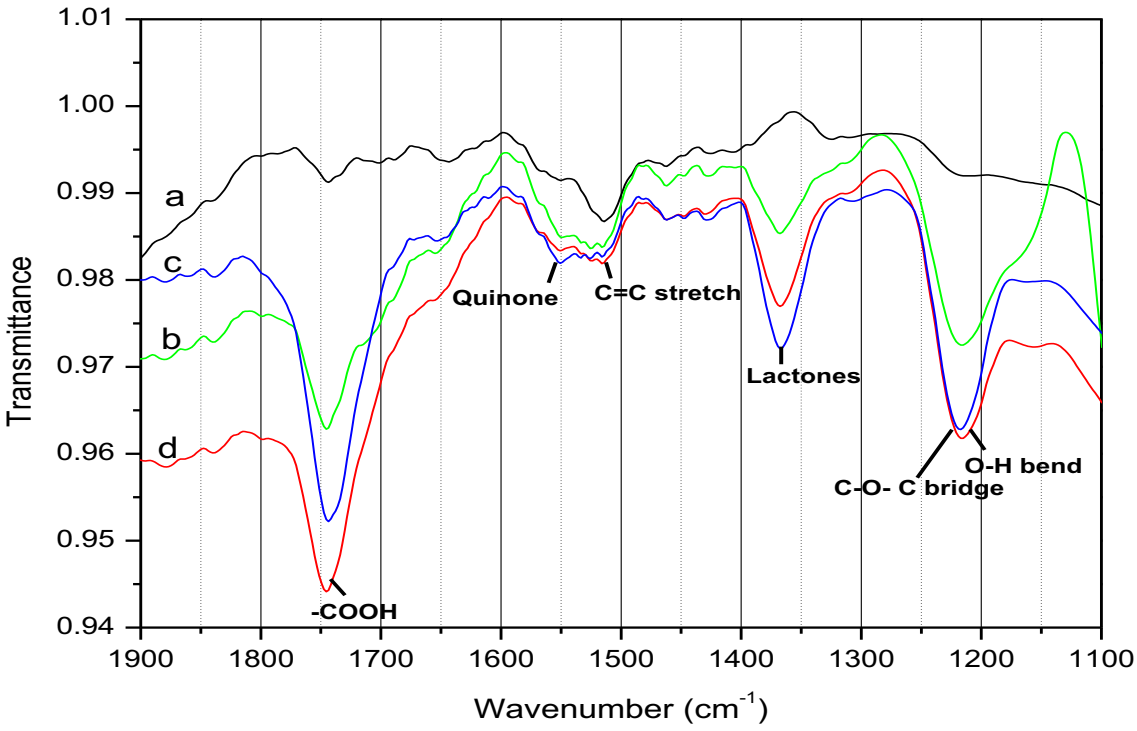


Figure 4.12: FTIR of (a) as-synthesised, CSs and 55 % HNO_3 functionalised CSs for (b) 96 h at room temperature (c) 24 h at 40 ^{o}C and (d) 2 h under reflux.

From Fig. 4.12 It can be noted that the as-synthesised CSs have small amounts of oxygen containing functional groups even before functionalisation. This observation has been reported in the literature [6, 17] and is thought to be due to oxygen chemisorption on the surface of CSs immediately after synthesis to satisfy the valence of the surface carbon atoms. Functionalisation of CSs with nitric acid increases the amount of functional groups such as -COOH and -OH among others. In Fig. 4.12 the peak at 1745 cm^{-1} is assigned to the C=O stretch in carboxylic acid groups, at 1550 cm^{-1} to C=O in the quinone structure, at 1516 cm^{-1} to the C=C stretch, at 1369 cm^{-1} to lactones and 1216 cm^{-1} is thought to be due to an overlap of both COC and the -OH bending mode. The peak intensity of the carboxylic acids was observed to increase significantly as the functionalising conditions were changed from 96 h at room temperature to 2 h under reflux. This is due to an increase in the amount of carboxylic acid groups introduced onto the surface of CSs as the functionalising conditions are changed to harsher conditions. Lactone structures could have been formed due to an O-H group collapsing from a carboxylic acid group such that an oxygen atom remains attached to the surface carbons. The -OH functional groups were also noted to increase as the functionalising conditions were changed. Quinones could have been formed due to the breakage of -OH groups forming carbonyl groups on the surface of CSs. However, as mentioned earlier, FTIR spectroscopy was not used to quantify the functional groups. The technique was only used for the qualitative analysis of functional groups after CSs functionalisation.

Table 4.1 shows the amount of active hydrogen ion (-COOH) groups as quantified using a potentiometric titration first designed by Boehm [18]. This method is limited to the detection of carboxylic acid groups, phenols and lactones. It has been proposed that $NaHCO_3$ (pKa = 6.37) can only be used to quantify carboxylic acids, Na_2CO_3 (pKa = 10.25) can be used to quantify both carboxylic acids and lactones and NaOH (pKa = 15.74) can be used to quantify carboxylic acids,

lactones and phenols [19-21]. The carboxylic acid groups were of interest in this study because the dissociation of these groups facilitates the dispersion of the CSs in aqueous media by creating a negative surface charge, this plays a crucial role in achieving well dispersed metal particles during catalyst preparation.

The FTIR spectrum of as-synthesised CSs showed that carboxylic acid groups are present on the surface of CSs after exposure to air (see Fig. 4.12). However, as seen in Table 4.1, carboxylic acid groups could not be detected on CSs functionalised with 55 % HNO_3 for 2 or 12 h at room temperature. An increase in the amount of carboxylic acid groups was observed when the reaction time was increased from 24 h to 96 h at room temperature. A similar trend was also observed when the reaction time was increased at a temperature of 40 ^{o}C. Furthermore, increasing the reaction temperature from 25 ^{o}C to 83 ^{o}C (reflux) while other parameters were kept constant increased the amount of carboxylic acid groups on the surface of CSs.

Table 4.1: Effect of increasing reaction time and temperature during nitric functionalisation

25 ^{o}C		**40 ^{o}C**		**Acid reflux (83 ^{o}C)**	
Time (h)	Concentration of carboxylic groups mmol (H^+)/g	Time (h)	Concentration of carboxylic groups mmol (H^+)/g	Time (h)	Concentration of carboxylic groups mmol (H^+)/g
2	a	2	0.060	2	0.612
12	a	12	0.113	24	0.580
24	0.008	24	0.151		
48	0.021	48	0.278		
96	0.039				

a - were not detected by titrimetry

Under refluxing conditions, increasing the reaction time from 2 h to 24 h showed a decrease in functional groups. This is believed to be due to the reaction of carboxylic acid groups attached in close proximity to each other, forming

carboxylic anhydrides or their collapse to lactone-like structures. The carboxylic anhydrides and the lactones are undetectable using $NaHCO_3$ as a titrant. A maximum of 0.612 mmol/g of carboxylic acid groups was detected on CSs after functionalisation for 2 h in HNO_3 at reflux. The trend observed here is similar to that reported in literature [22]. The quantities of the carboxylic groups reported here are lower than those in the literature reported for CSs, due to the low surface area of the CSs (3.1 m^2/g).

TGA and TEM studies of the functionalised CSs were used to characterise the effect of functionalising conditions on the thermal stability and morphology of the CSs. Fig. 4.13 shows the TGA profiles recorded under nitrogen of CSs that were functionalised with 55 % HNO_3 solution at (a) 40 ^oC for 24 h (Fig. 4.13a) (b) at reflux for 2 h (Fig. 4.13b) and (c) at reflux for 24 h (Fig. 4.13c). The mass loss observed at ca. 300 ^oC was due to the decomposition and loss of functional groups. This mass loss increased as the degree of functionalisation was increased implying again that functionalising conditions are directly proportional to the number of functional groups introduced on the surface of CSs. The trend observed from these TGA profiles at ca. 300 ^oC is similar to that observed from the titration data.

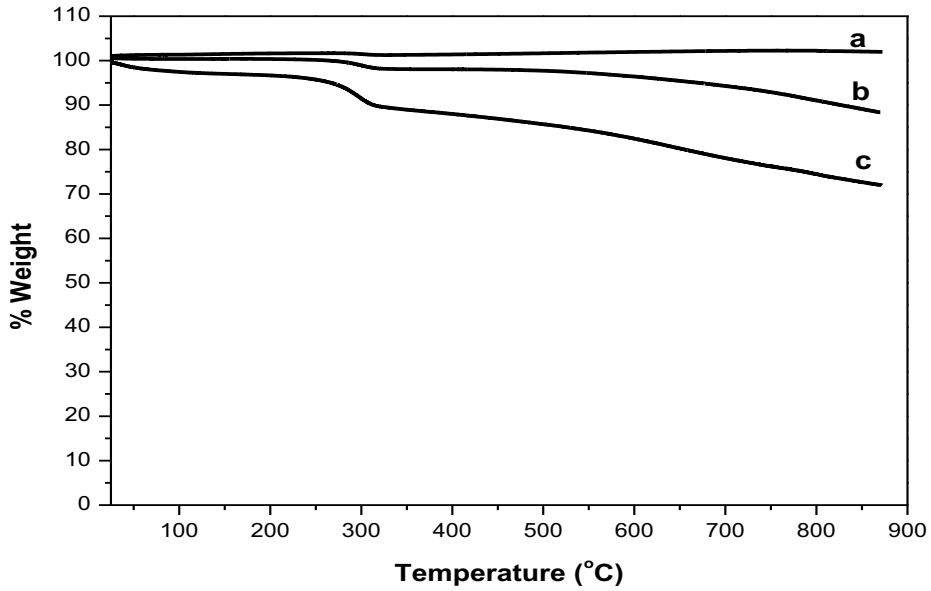


Figure 4.13: TGA profiles run in nitrogen: Effect of functionalising conditions: (**a**) 55 % HNO_3/ 40 ^oC/ 24 h (**b**) 55 % HNO_3/ reflux/ 2 h (**c**) 55 % HNO_3/ reflux/ 24 h.

TGA profiles also revealed that shifting functionalising conditions from relatively mild conditions to harsher conditions compromised the thermal stability of the CSs as shown by a greater weight loss at temperatures above 300 ^oC. A good correlation is therefore observed between the functionalising conditions and the thermal stability of the functionalised CSs. TEM images (Fig. 4.14) of these samples showed that by changing the functionalising conditions from relatively mild to hasher conditions destroyed the spherical morphology of the CSs. This effect has also been reported in the literature CSs [19,23]

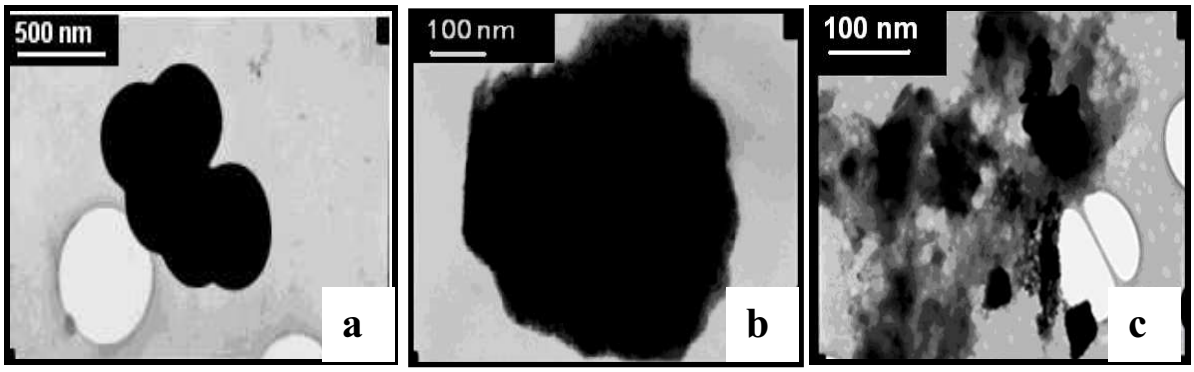


Figure 4.14: TEM images after functionalising of the CSs with (**a**) 55 % HNO_3/ 40 ^oC/ 24 h (**b**) 55 % HNO_3/ reflux/ 2 h (**c**) 55 % HNO_3/ reflux/ 24 h.

5.3.2 Carbon spheres functionalisation by $KMnO_4$

It is interesting to note that oxidation with $KMnO_4$ significantly changed the surface chemical nature of the CSs. FTIR spectra of the potassium permanganate functionalised CSs are presented in Fig. 4.15.

Functionalisation of CSs using $KMnO_4$ produced carboxylic acids, quinones, lactones and hydroxyl groups. The peaks assigned to each of these functional groups have been discussed in the preceding section. From Fig. 4.12b the quinone peak shifted to higher wave-numbers (cm^{-1}). Generally it can be concluded that functionalising CSs with either $KMnO_4$ or HNO_3 introduces similar functional groups on the surface of CSs.

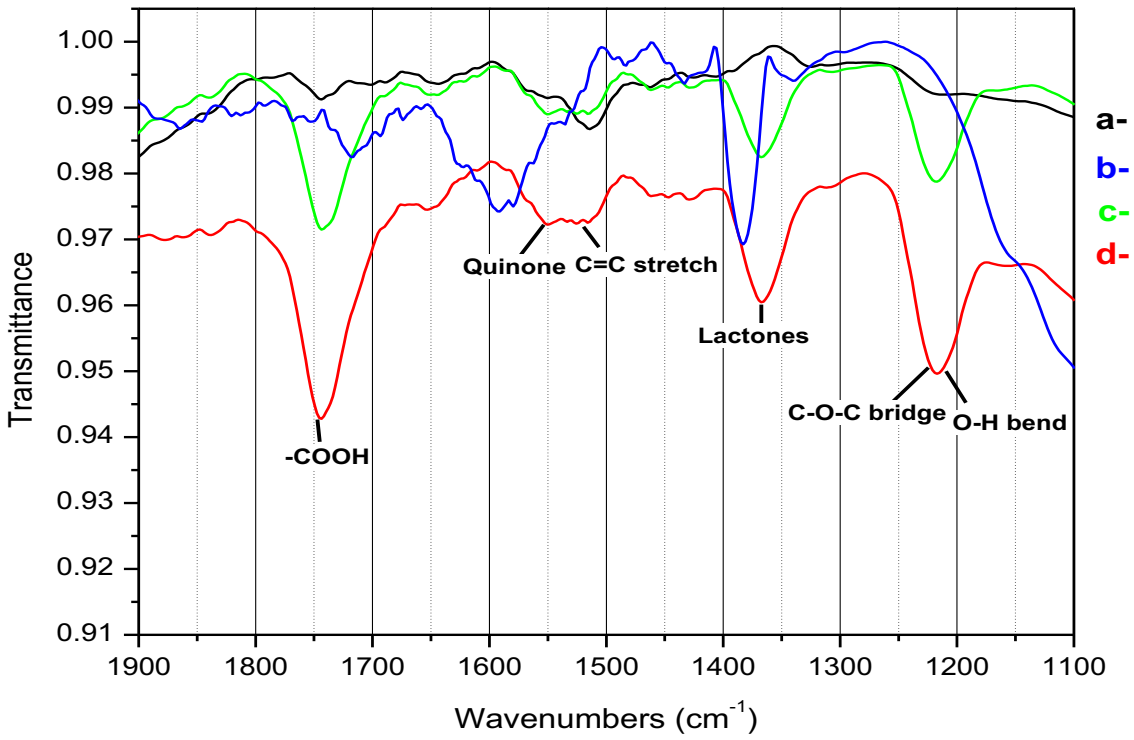


Figure 4.15: FTIR of (a) as-synthesised CSs (b) 0.5 M $KMnO_4$/ 4 h/ 25 ^oC (c) 1 M $KMnO_4$/ 4 h/ 40 ^oC and (d) 2 M $KMnO_4$/ 4 h/ 70 ^oC.

From Table 4.2 it was observed that the amount of carboxylic acids on the surface of the CSs can be increased by either increasing the concentration of $KMnO_4$ or the reaction temperature. The saturation point of CSs with acid groups was not reached when $KMnO_4$ was used mainly because of the relatively mild conditions used in all the experiments. Since $KMnO_4$ is a very strong oxidising agent, a similar amount of carboxylic acid groups as was introduced by 55 % HNO_3 using harsher reaction conditions can be achieved with $KMnO_4$ using relatively mild reaction conditions. Indeed the maximum amount of acid groups obtained (0.438 mmol/g) is about 70 % of the maximu value obtained fom the HNO_3 reactions (0.612 mmol/g). The brownish appearance of $KMnO_4$ functionalised CSs may

suggest that residual K and Mn ions remained on the surface of the CSs after washing. The catalytic effect of these ions is discussed in chapter 6 of this thesis.

Table 4.2: Effect of functionalising CSs with $KMnO_4$ for 4 h.

	25 ^oC	**40 ^oC**	**70 ^oC**
$KMnO_4$ Concentration	Concentration of carboxylic groups mmol (H^+)/g	Concentration of carboxylic groups mmol (H^+)/g	Concentration of carboxylic groups mmol(H^+)/g
0.5 M	0.028	0.098	0.245
1 M	0.061	0.201	0.324
2 M	0.083	0.224	0.438

TGA profiles of CSs functionalised with a 0.5 M $KMnO_4$ solution at 40 ^oC for 4 h and 1 M and 2 M $KMnO_4$ solutions at 70 ^oC for 4 h carried out under N_2 are presented in Fig. 4.16. It was observed from Fig. 4.16 that by changing the functionalising conditions from relatively mild to more harsh conditions (Fig. 4.16a to c) the thermal stability of the CSs under N_2 is compromised.

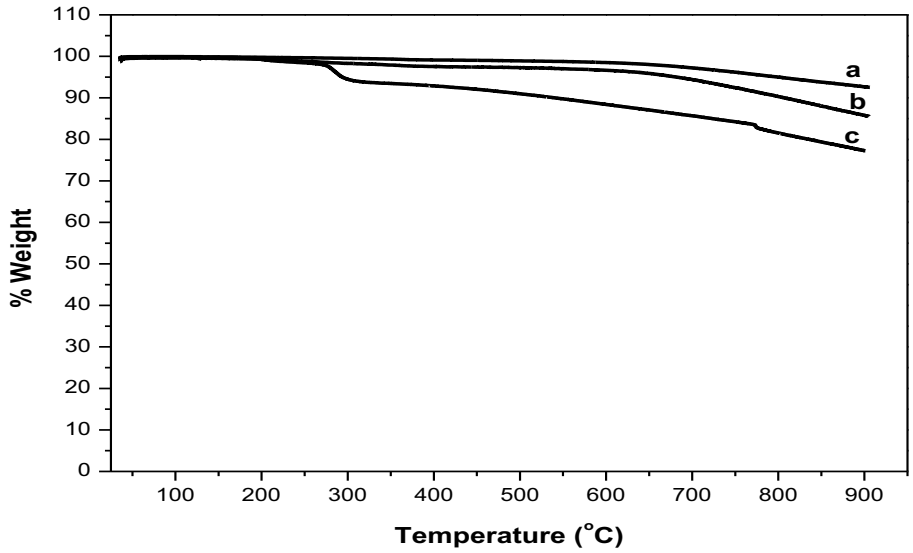


Figure 4.16: TGA profiles run in nitrogen gas: Effect of functionalising conditions of (a) 0.5 M $KMnO_4$/ 40 ^oC/ 4 h (b) 1 M $KMnO_4$/ 70 ^oC/ 4 h (c) 2 M $KMnO_4$/ 70 ^oC/ 4 h.

Again, the weight loss observed at 290 ^{o}C due to the decomposition of functional groups increased with a change of functionalising conditions from mild to harsher conditions. This increase in weight loss is due to the increasing number of functional groups on the surface of CSs as the functionalising conditions are changed. The trend noted from the TGA results agrees well with that observed from the titration data.

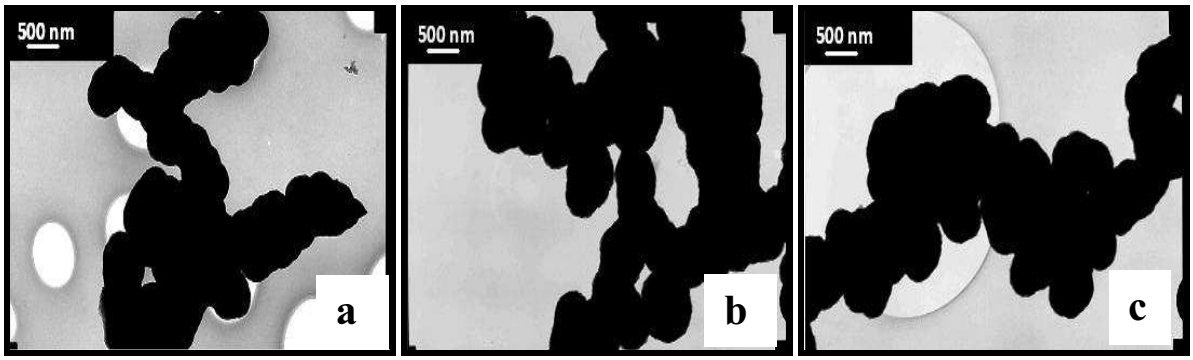


Figure 4.17: TEM images after functionalising with **(a)** 0.5 M $KMnO_4$/ 40 ^{o}C/ 4 h **(b)** 1 M $KMnO_4$/ 70 ^{o}C/ 4 h **(c)** 2 M $KMnO_4$/ 70 ^{o}C/ 4 h.

TEM images of these functionalised CSs are presented in Fig. 4.17. They showed that the above mentioned functionalising conditions had little to no effect on the overall spherical morphology of the CSs but the TEM analysis at higher magnification (Fig 4.18) showed that by increasing the concentration of $KMnO_4$ from 0.5 M to 2 M the surface of the CSs became rougher. HRTEM images of CSs functionalised under 0.5 M $KMnO_4$/ 40 ^{o}C/ 4 h conditions showed that the carbon graphitic layers became broken and were randomly arranged on the surface of the CS (Fig. 4.19). It is proposed that the carbon atoms in these broken edges of the graphite sheets are attached to the oxygen containing functionalities and would act as metal anchoring sites when these materials are used as catalyst supports.

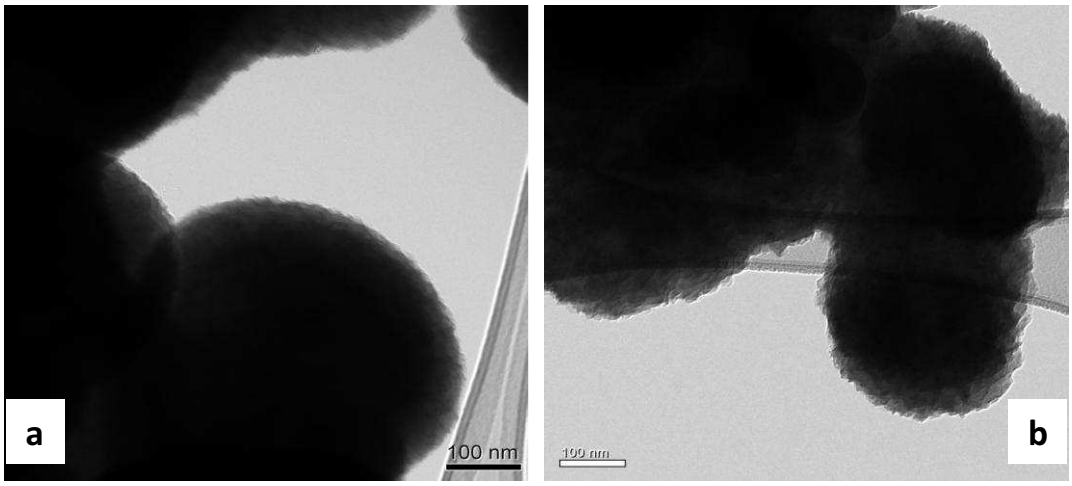


Figure 4.18: TEM image of CSs functionalised by (a) 0.5 M $KMnO_4$/ 40 ^oC/ 4 h (b) 2 M $KMnO_4$/ 70 ^oC/ 4 h.

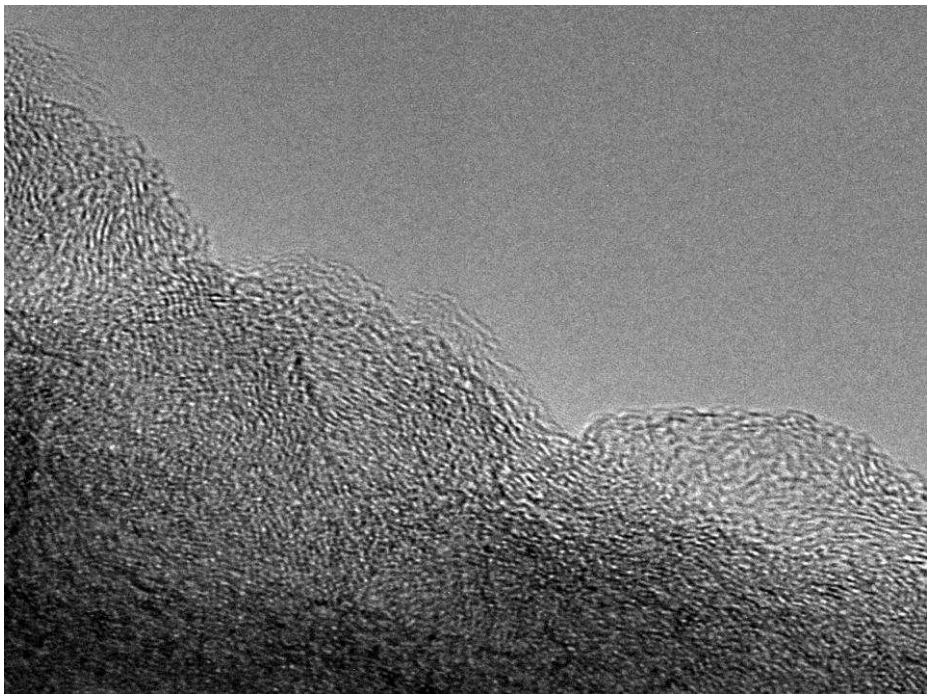


Figure 4.19: HRTEM image of CSs functionalised by 0.5 M $KMnO_4$/ 40 ^oC/ 4 h

4.3.3 CSs functionalisation by 1M $KMnO_4$ and 55 % HNO_3 in the ratio 1:2

Table 4.3: Effect of functionalising CSs with a 1:2 mixture of 1 M $KMnO_4$ and 55 % HNO_3 for 4 h.

Functionalising conditions	Concentration of carboxylic groups mmol (H^+)/g
25 ^oC	0.071
40 ^oC	0.258
70 ^oC	0.495

More carboxylic acid groups were introduced when a mixture of 1 M $KMnO_4$ and 55 % HNO_3 in the ratio 1:2 was used than when 1M $KMnO_4$ was used on its own at the same conditions. At room temperature, the amount of carboxylic acid groups introduced by $KMnO_4/HNO_3$ mixture was similar to that introduced by using1M $KMnO_4$. It can be noted from Table 4.3 that increasing the reaction temperature also increase the amount of carboxylic groups introduced onto the surface of the CSs.

4.4 Conclusions

CSs with a narrow size range (200-500 nm) were successfully synthesized in our laboratory. The synthesized materials showed properties not attainable with other materials previously studied as supports for FT catalysts. These properties include: high purity, inert surface chemical nature, absence of pores, metal precursor recovery by combustion of CSs support and chemical modification of the CSs surface. The surface chemistry of the CSs was successfully altered using two functionalizing agents i.e. $KMnO_4$ and HNO_3. It was observed from FTIR spectroscopy that similar functional groups can be introduced onto the surface of

CSs when either functionalising agent is used. Functional groups introduced onto the surface of carbon spheres using 55% HNO_3 under harsh reaction conditions could be achieved by using $KMnO_4$ under relatively mild conditions. The advantage or disadvantage of using $KMnO_4$ as a functionalising agent is that residual K and Mn ions may be present on the surface of CSs even after washing. TGA, TEM and alkalimetry results allowed us to choose the best reaction conditions for functionalizing our catalyst support materials, which were 55 % HNO_3/ 40 ^oC/ 24 h and 0.5 M $KMnO_4$/ 40 ^oC/ 4 h. These conditions introduced similar amounts of functional groups without destroying the morphology of the CSs.

References

1. J. Miao, D. W. Hwang, K. V. Narasimhulu , P. Lin , Y.T. Chen , S. Lin and L. Hwang, Carbon 42 (2004) 813.
2. Y.Yan. F. Zhang, Y. Meng, B Tu, & D Zhao, Chem. Commun (2007) 2867.
3. F. Rodriguez-Reinoso, Carbon 36 (1998) 159.
4. M. L. Studebaker, Rubber Chem. Technol. 30 (1957) 1400.
5. J. B. Donnet, Carbon 6 (1968) 161.
6. H.P. Boehm, Carbon 32 (1994) 759.
7. J.S. Noh, J.A. Schwarz, Carbon 28 (1990) 675.
8. J.M. Solar, F.J. Derbyshire, V.H.J. de Beer, L.R. Radovic, J. Catal. 129 (1991) 330.
9. C. Moreno-Castilla, M.V. L´opez-Ram´on, F. Carrasco-Marin, Carbon 38 (2000) 1995.
10. T.J. Bandosz, J. Jagiello, J.A. Schwarz, Anal. Chem. 64 (1992) 891.
11. I. Salame, T.J. Bandosz, J. Colloid Interface Sci. 240 (2001) 252.
12. C.A. Leon y Leon, L.R. Radovic, in P.A. Thrower, Ed., Chemistry and Physics of Carbon, Vol. 24, Marcel Dekker, New York, (1990) 212.
13. V.V. Strelko, V.S. Kuts, P.A. Thrower, Carbon 38 (2000) 1499.
14. J.A. Men´endez, L.R. Radovic, B. Xia, J. Phillips, J. Phys. Chem. 100 (1996) 17243.
15. J.A. Men´endez, J. Phillips, B. Xia, L.R. Radovic, Langmuir 12 (1996) 4404.
16. A. Contescu, C. Contescu, K. Putyera, J.A. Schwarz, Carbon 35 (1997) 83.
17. M. Voll and H. P. Boehm, Carbon 8 (1970) 741.
18. H.P. Boehm, in D.D. Eley, H. Pines, P.B. Weisz, Eds., Advances in Catalysis, Vol. 16, Academic Press, New York (1966) 179.
19. T.J. Bandosz, J. Jagiello, J.A. Schwarz, Anal. Chem. 64 (1992) 891.
20. S. Neffe, Carbon 25 (1987) 441.

21. Y. Matsumura, S. Hagiwara, H. Takahashi, Carbon 14 (1976) 163.
22. K. Amine, M. Mizuhata, K. Orguro and H. Takenaka, J. Chem Soc. Faraday Trans., 91 (1995) 4451.
23. I. Salame, T.J. Bandosz, J. Colloid Interface Sci. 240 (2001) 252.
24. V.V. Strelko, V.S. Kuts, P.A. Thrower, Carbon 38 (2000) 1499.

Chapter 5

Preparation and characterisation of cobalt supported on carbon spheres (Co/CS) as Fischer-Tropsch catalysts

5.1 Introduction

Fischer–Tropsch synthesis (FTS) is a promising catalytic route for the industrial production of cleaner liquid fuels from syngas (CO and H_2), which may be produced from non-petroleum resources, such as (i) gaseous fuels e.g. natural gas, coal-bed gas and biogas, (ii) liquid fuels e.g. heavy oils and oil residues and (iii) solid fuels e.g. biomass and coal [1-4]. Co and Fe based catalysts are the industrially preferred catalysts for FTS. Although Fe is much cheaper than Co, Co based catalysts are the preferred catalysts for industrial application when high FT activity, long chain hydrocarbon selectivity, low water-gas shift activity and good stability towards deactivation by water are required [5-10]. Due to the high cost of cobalt, high surface area cobalt particles are required in FTS. This is achieved by dispersing cobalt crystallites on a suitable support material such as SiO_2, TiO_2, Al_2O_3 or C [11-12]. Research work has shown that the support material significantly influences the preparation of well dispersed cobalt crystallites with a high surface area of catalytically active cobalt phases. Therefore the support material plays a vital role in stabilising these active phases against loss of surface

area by sintering. This positively influences the feed gas adsorption onto the surface Co monolayer atoms of the metal precursor, thus changing the overall catalyst activity and product selectivity [13-15].

Much recent work on carbon materials as catalyst supports has focused on the use of carbon nanotubes (CNTs) and carbon nanofibers (CNFs) [16-23] with little study of other shaped carbons such as carbon spheres (CSs) being reported. Indeed many similarities might be expected when either CNTs, CNFs or CSs are used to support metals, and the numerous advantages that apply to CNTs and CNFs as supports should apply to CSs as well. CSs are readily produced by many synthetic procedures including numerous chemical vapour deposition (CVD) methods [24].

CSs also possess other advantages over CNTs and CNFs that include: high purity; no metal residue and simplicity of synthesis. Previous research studies have shown that CSs are useful as catalyst supports [25]. While, FTS studies have been reported on N-doped CSs [26], no studies on Co/CS supported catalysts have been noted.

The original intention of this work was to evaluate the effect of two commonly used oxidising agents (HNO_3, $KMnO_4$) on the functionalisation of the CS surface. To our surprise we noted that the different procedures gave CSs with chemical/physical properties and FT synthesis data that could not be reconciled with the acidity behaviour of the CS and Co/CS catalysts.

To further explore this behaviour small amounts of potassium and manganese were added to the HNO_3 functionalised 5 % Co/CS catalysts. The results indicated that the $KMnO_4$ treated CSs contained small amounts of K and Mn ions, even after copious washings with water to remove the contaminants. The results from

our study as reported below reveal the effect of different functionalising agents on Co/CS FT catalysts.

The promoter effect of manganese oxide on cobalt based FT catalysts has been studied on support materials such as TiO_2 and carbon nanofibres (CNFs). Bezemer et. al [27] showed that small amounts of manganese (0.03-0.13 wt%) on Co/CNF catalysts improved olefin product selectivity with no effect on the FTS activity at 1 bar pressure. Previous studies [28-32] have also shown that addition of small amounts of manganese to Co/TiO_2 catalysts improved FT product selectivity by suppressing methane production as well as giving a higher olefin to paraffin ratio in the product stream.

Previous studies by Trépanier et al. [21] on the promoter effects of K on Co/CNT showed that the addition of very small amounts of potassium (0.0016 wt %) decreased the % CO conversion and FTS rate but increased olefin to paraffin selectivity. In other FT studies, Colley et al. investigated the promoter effects of potassium on a cobalt supported manganese oxide catalyst [33]. Their data showed that the K promoted Co catalysts give (i) low selectivity towards C_1, (ii) a high olefin to paraffin ratio, (iii) high selectivity towards long-chain alkanes and (iv) alcohol formation.

5.2 Preparation and characterisation of Co/CS catalyst

5.2.1 Experimental

Cobalt metal loading on CSs

Co metal was loaded onto the CSs by a deposition-precipitation method (DPU) using urea. This method was preferred over the wetness impregnation method due to the fact that CSs have a negligible pore volume. The DPU method allows control over particle size unlike in the wetness impregnation method.

In a typical DPU method, $Co(NO_3)_2 .6H_2O$ (7.21 g) and urea (1.61 g; 1.5 moles urea per mole of cobalt) were dissolved in de-ionized water (18 ml) and added to 10 g of functionalised carbon spheres (CSs) support to give a 10 % Co/CS loading. After allowing sufficient time (at least two hours) for the hydrolysis of urea, the sample was dried by evaporating the water under vacuum at 90 °C for 40 minutes. Urea was added to facilitate the uniform formation of metal hydroxides onto the surface of the CSs support.

5.2.2 Characterisation of Co/CS catalysts

2.5, 5 and 10 % Co catalysts were prepared and characterised by TEM, TGA, XRD, TPR and H_2-chemisorption. The characterisation results presented below are separated according to the percentage Co metal loadings. K (0.05 %) and Mn (0.05 %) promoter effects were investigated on 5 % Co/CS catalysts.

2.5 % Co/CS catalysts

CSs are good models for studying carbon supported Co catalysts because of their high purity and ease in evaluating the supported cobalt metal particles. TEM studies were used to characterise the cobalt particle sizes on $KMnO_4$ and HNO_3 functionalised CSs. TEM images (Fig 5.1) showed that cobalt particles of size 3-15 nm (insert Fig 5.1b) were successfully deposited on to the $KMnO_4$ functionalised CSs. These particles were evenly distributed across the surface of the CS implying that functionalisation by $KMnO_4$ created evenly dispersed metal anchoring sites in the form of acidic functional groups discussed in chapter 4.

The cobalt particle size was controlled by the DPU method. Fig 5.1b reveals that $KMnO_4$ functionalised CSs became pitted during functionalisation creating a rough surface which limits the extent to which metal particles sinter during FTS.

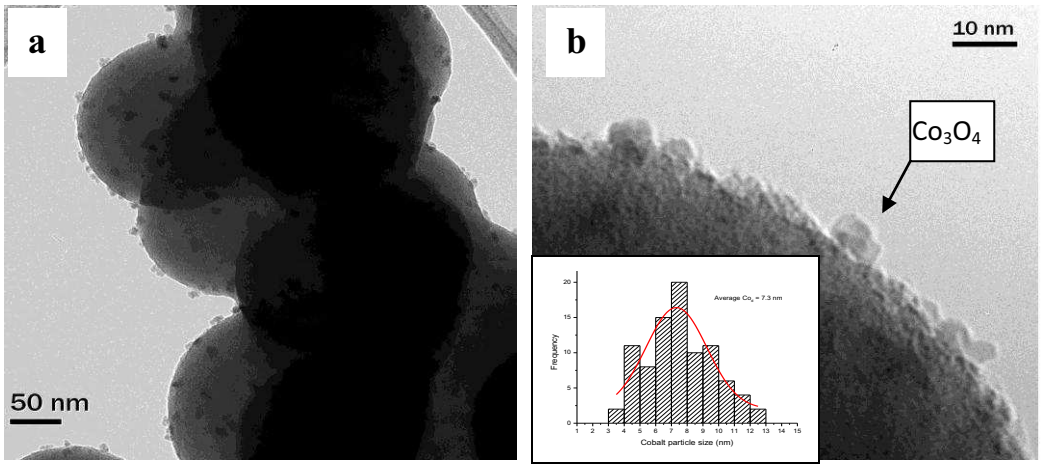


Figure 5.1 TEM images of 2.5 % Co/CS $KMnO_4$ functionalised catalysts

Fig 5.2 shows TEM images of 2.5 % Co/CS HNO_3 functionalised catalysts. From Fig 5.2a it can be noted that cobalt particles were only attached to selected areas on the surface of the CSs. This was due to the distribution of the functional groups on the CSs surface after functionalising with HNO_3. It is thought that when HNO_3 is used as a functionalising agent, the acid attacks the edges of the flakes of CS. Similar amounts of active hydrogen ions were detected (0.098 and 0.151 mmol/g) between the $KMnO_4$ and HNO_3 functionalised CS. The Co particles were distributed differently on the CS surfaces implying that the functional groups introduced by HNO_3 are grouped on small areas of the CS. Fig 5.2 shows that the cobalt particles loaded on the HNO_3 catalysts formed clusters of cobalt particle size range of 3-15 nm (insert 5.2b).

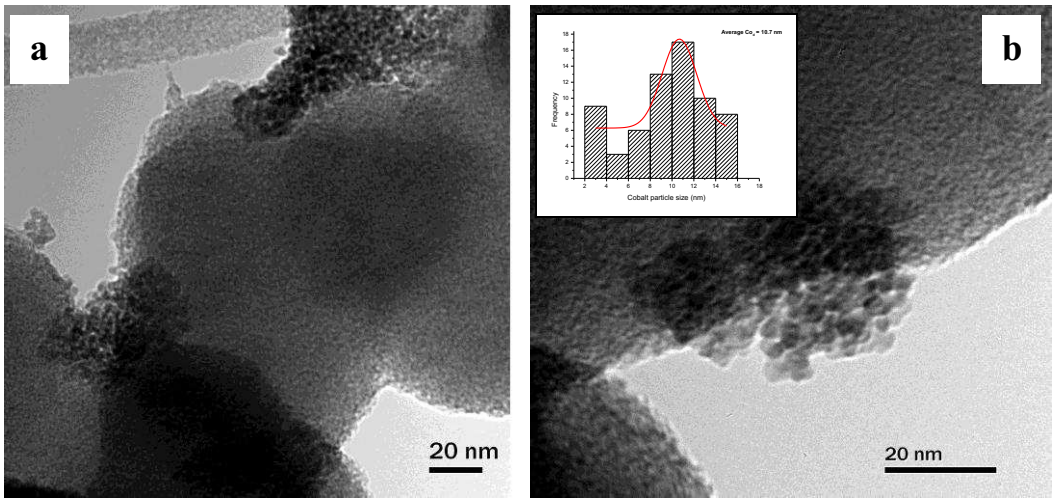


Figure 5.2 TEM images of 2.5 % Co/CS $KMnO_4$ functionalised catalysts

The metal loading of the catalysts was confirmed from TGA data recorded in air (Fig. 5.3). From Fig. 5.3a and b the decomposition of nitrates was not observed at a temperature of ~ 250 ^oC implying that pre-heating the catalysts at 230 ^oC under

N_2 for 2.5 h was sufficient to remove all nitrates in the catalysts. Furthermore it was noted from Fig 5.3a and b that after oxidation of the catalysts residual Co_3O_4 (2.8 %) is observed. The onset oxidation temperature of CSs was noted to decrease from ca. 560 ^oC to ca. 400 ^oC for the HNO_3 functionalised catalyst and to ca. 350^oC for the $KMnO_4$ functionalised catalyst. This was due to the catalytic effect of Co on the oxidation of carbon. The CSs functionalised with $KMnO_4$ oxidised at a lower temperature than those functionalised with HNO_3, this is thought to be due to residual manganese oxide phases aiding the Co catalysed oxidation of CSs (see later).

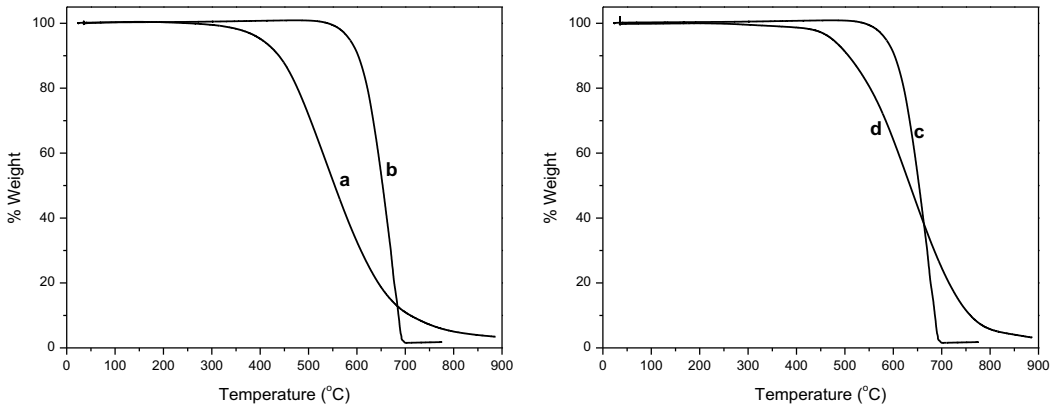


Figure 5.3: TGA profile run in air of (a) 5 % Co/CS catalysts functionalised by $KMnO_4$. (b) $KMnO_4$ functionalised CSs, (c) HNO_3 functionalised CSs and (d) 5 % Co/CS catalysts functionalised by HNO_3,

The rate of oxidation of the CS supports (Fig.5.3a and d) was noted to be uniform compared to that shown by the 5 % Co/CS catalysts (Fig. 5.10). The TGA profiles were smooth and different to the TGA profiles of the 5 % Co/CS and 10 % Co/CS catalysts due to the presence of very low metal content in the 2.5 % Co/CS catalysts (see later).

Table 5.1 shows the N_2-physorption results of the functionalised CSs and the 2.5 % Co/CS catalysts. The addition of 2.5 % weight cobalt showed no effect on the surface area of the functionalised catalysts. These results were expected because of (i) the absence of pores in the CS support, which could have been filled or blocked resulting in a decrease in catalyst surface area and (ii) the very low metal loading on the surface of the CSs which resulted in small changes in the catalyst surface area *(catalyst surface area is defined here as equal to the sum of support surface area and metal particles surface area)*.

Table 5.1: N_2-physisorption results for CSs supports and 2.5% Co/CS catalysts

Sample	**S.A support (m^2/g)**	**S.A of 2.5 % Co/CS catalyst (m^2/g)**
$KMnO_4$ functionalised CSs	3.1	2.7
HNO_3 functionalised CSs	2.9	3.0

X-ray diffraction patterns of the support and calcined 2.5 % Co/CS catalysts are presented in Fig. 5.4. From the XRD spectrum of the CS support and those of the catalysts, the peaks at 2θ values of 25 ° and 43 ° correspond to the carbon spheres, while the other peaks at 2θ values of 18^o, 31.5^o, 36.8^o, 43.8 °, 59.3^o and 65.2 ° in the spectrum of the catalysts are related to the different crystal planes of Co_3O_4 [34].

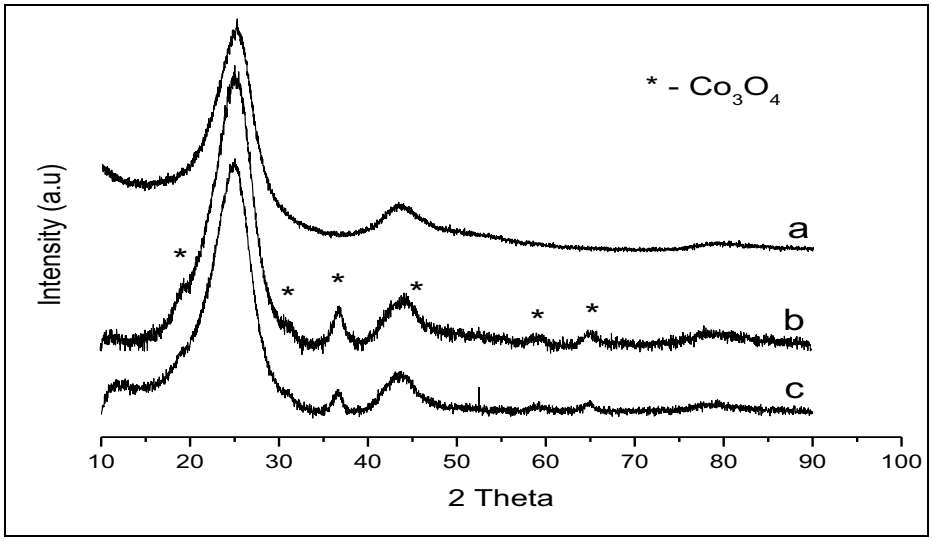


Figure 5.4: XRD patterns for (**a**) As-synthesised CSs, (**b**) 2.5% Co/CS HNO_3 functionalised CS, (**c**) 2.5% Co/CS $KMnO_4$ functionalised CS.

The peak at 36.8^0 was the most intense peak of Co_3O_4 in the XRD patterns of all the catalysts. From Fig. 5.4c, no peaks were observed indicating diffraction lines of manganese oxide or potassium oxides due to the small amounts of these residual ions being present in the $KMnO_4$ functionalised catalyst. A comparison of the average Co_3O_4 particle size of the catalysts calculated from the XRD spectrum using the Scherer equation on the peak at $2\Theta = 36.8^o$ and that calculated from TEM are presented in Table. 5.2. There was good agreement in the particle sizes determined by TEM and XRD.

Table 5.2 Cobalt oxide crystallite particle size

Catalyst	XRD particle size (nm)	TEM particle size range (nm)
2.5%Co/CS $KMnO_4$	7.0	3-12 (average = 7.3)
2.5%Co/CS HNO_3	8.3	3-15 (average = 10.7)

5 % Co/CS catalysts

TGA studies of the 5 % Co/CS catalysts run in air showed that supported cobalt phases catalysed the oxidation of CSs, reducing the temperature of the onset of oxidation from ca. 560 ^{o}C in the absence of cobalt to ca. 350 ^{o}C in the presence of cobalt (Fig. 5.5) [26].

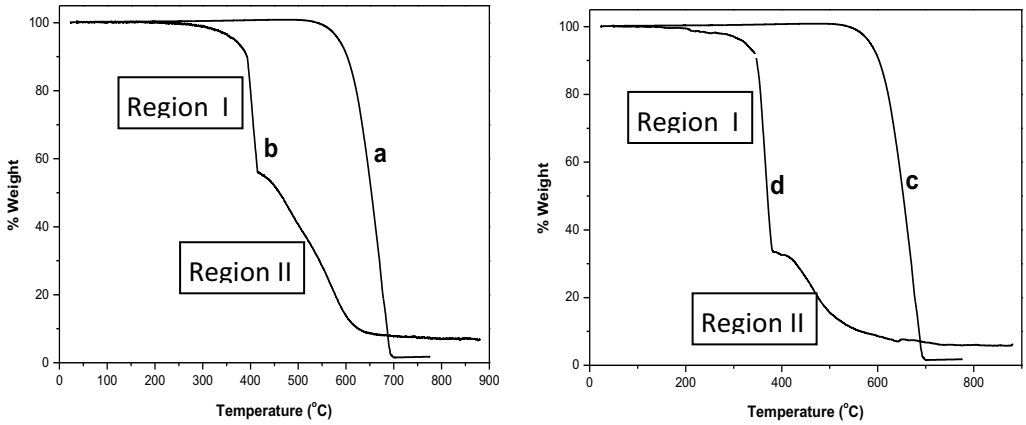


Figure 5.5: TGA profile run in air on the (a) HNO_3 functionalised CSs, (b) 5 % Co/CS catalysts functionalised by HNO_3, (c) $KMnO_4$ functionalised CSs and (d) 5 % Co/CS catalysts functionalised by $KMnO_4$.

Two distinct regimes for the oxidation of 5 % Co/CS catalysts were observed: (i) from 200 ^{o}C to ca. 400 ^{o}C and (ii) from ca. 400 ^{o}C to 650 ^{o}C. It is proposed that for the Co/CS materials, the reaction $C + O_2 \rightarrow CO_2$ is catalysed by Co and during this reaction cobalt becomes reduced [26]. The slower oxidation of carbon in region II is due to the noncatalysed oxidation reaction of carbon. The TGA profiles also reveal that the carbon is more easily oxidised after HNO_3 treatment than by $KMnO_4$ treatment. Another interesting feature observed in the TGA curves relates to the differences in the transition between regions I and II of Fig. 5.5b and d. For the HNO_3 treated catalyst (Fig. 5.5b) this occurs after ca. 45 % carbon removal and is complete by > 700 ^{o}C (6.7 % residue). For the $KMnO_4$ treated catalyst (Fig. 5.5d) the transition occurs after 65 % carbon loss and is complete by < 700 ^{o}C (7.2 % residue). This would suggest that residual MnO_x species may also assist in the oxidation reaction of carbon. Assuming that Co_3O_4 is the only phase present in the TGA residue of the catalysts, one can calculate a loading 4.92 % of cobalt metal on the HNO_3 functionalised catalyst.

The reduction behavior of the catalysts (after heating at 220 ^{o}C under nitrogen gas) is presented in Fig. 5.6. It is noted from Fig. 5.6a that the as-synthesised CSs undergo a methanation reaction with hydrogen at ca. 600 ^{o}C followed by a negative peak as opposed to a baseline drift. This negative peak occurs due to the emission of the methane gas from the system. The TCD detector responds to the release of methane gas in an opposite response to when hydrogen gas is being absorbed during Co reduction hence showing a negative peak. The HNO_3 functionalised catalyst shown in Fig. 5.6b, shows three peaks in the TPR profile. The peaks centered at *ca*. 297 ^{o}C and 342 ^{o}C correspond to the two step reduction process of Co_3O_4 as shown in the equations below [26]. The third peak (T > 550 ^{o}C) is due to the hydrogenation and gasification of CSs to form methane [35].

This peak is also followed by a negative peak due to the emission of methane gas from the system similar to the TPR profile of the blank (Fig. 5.6a).

$$Co_3O_4 + H_2 \rightarrow 3CoO + H_2O \qquad \text{Equation 5.1}$$

$$3CoO + 3H_2 \rightarrow 3Co + 3H_2O \qquad \text{Equation 5.2}$$

The potassium permanganate functionalised catalyst showed four peaks in the TPR profile (Fig. 5.6c). The first two peaks are due to the reduction of Co_3O_4 to CoO and CoO to Co^0. The third peak is proposed to be due to the presence of manganese species [36]. The Mn also appears to broaden the second peak associated with the reduction of CoO to Co^0. This effect on the reduction of Co by Mn has also been reported in the literature [27]. The fourth reduction peak is due to the methanation reaction of the CSs. This peak occurs at a higher temperature (*ca.* T = 740 ^oC) than for the non-manganese containing catalysts (c*a.* T = 580 ^oC) suggesting that Mn inhibits the methanation reaction [27, 29-33]

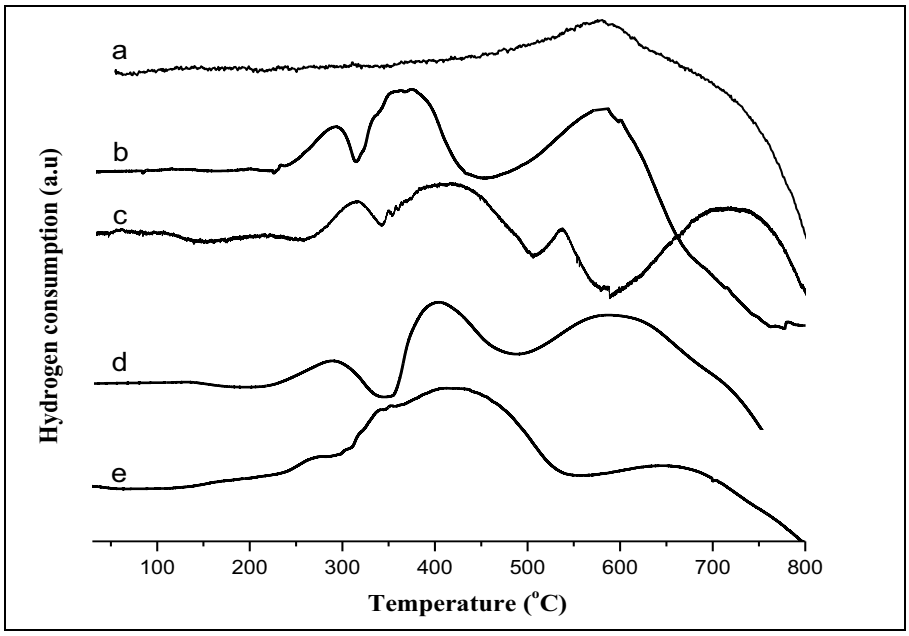


Figure 5.6: H_2-TPR profiles of (**a**) As-synthesised CSs, (**b**) 5% Co/CS HNO_3 functionalised CS, (**c**) 5% Co/CS $KMnO_4$ functionalised CS, (**d**) 5% Co/ 0.05%K/ HNO_3 functionalised CS and (**e**) 5% Co/0.05%Mn/ HNO_3 functionalised CS.

X-ray diffraction studies were used to characterise the cobalt oxide phases of the Co/CS materials after removal of nitrates at 220 ^oC for 2.5 h under nitrogen.

The diffraction peaks at 2θ values of 25 ° and 43 ° correspond to the carbon spheres as seen from the XRD pattern of the as-synthesised CSs (Fig. 5.7a). These diffraction peaks are readily distinguished from those of Co_3O_4 at 36.8 °, 59 ° and 66 ° (Fig. 5.7) in the XRD patterns of the 5 % Co/CS catalysts. Fig.5.7b and c showed similar XRD patterns suggesting that functionalising conditions had no significant effects on the cobalt phases present in these samples. Cobalt carbide phases were not identified by XRD in any of the Co/CS catalysts studied. The diffraction peaks present for cobalt from the studied catalysts were either for

Co_3O_4 or CoO phases, with the most intense peak at 36.8 ° which is for Co_3O_4 phase.

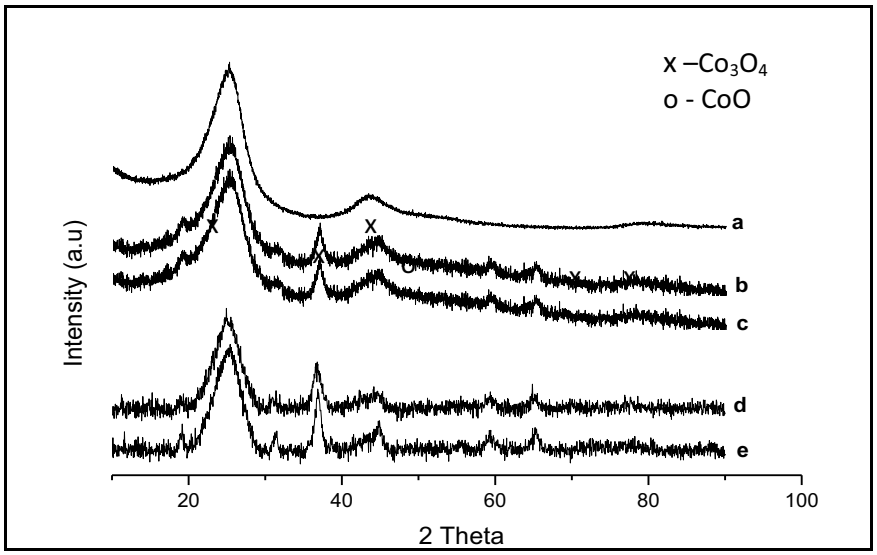


Figure 5.7: XRD patterns for (**a**) As-synthesised CSs, (**b**) 5% Co/CS HNO_3 functionalised CS, (**c**) 5% Co/CS $KMnO_4$ functionalised CS (**d**) 5% Co/0.05% K/CS HNO_3 functionalised CS, and (**e**) 5% Co/0.05% Mn HNO_3functionalised CS.

The average cobalt oxide crystallite sizes calculated from the XRD diffraction patterns using the Scherrer equation at peak 2Θ = 36.8 ° agreed well with those determined from TEM. These results are presented in Table 5.3.

Deposition of Co on functionalised CSs resulted in an increase in surface area (Table 5.4). These results agree with TEM results (Fig. 5.2) showing that Co particles are deposited on the surface of the CSs.

Table 5.3: Cobalt oxide crystallite particle size

Catalyst	XRD particle size (nm)	TEM particle size range (nm)
5%Co/CS $KMnO_4$	8.8	3-10
5%Co/CS HNO_3	7.6	3-10
0.05%Mn/5%Co/CS HNO_3	7.3	3-10
0.05%K/5%Co/CS HNO_3	9.5	3-10

Table 5.4: N_2-physisorption results for CSs supports and 5% Co/CS catalysts

Sample	S.A support (m^2/g)	S.A of 5 % Co/CS catalyst (m^2/g)
$KMnO_4$ functionalised CSs	3.1	4.7
HNO_3 functionalised CSs	3.0	4.1

High magnification TEM images of cobalt loaded on the functionalised CSs (after heating under nitrogen gas) illustrates the importance of the surface active functional groups on the loading of cobalt. The particle sizes of the cobalt crystallites ranged from 3-10 nm as shown in the insert to Fig. 5.8b. Although the $KMnO_4$ functionalised CSs have less functional groups (0.098 mmol./g) than the HNO_3 functionalised CSs (0.15 mmol./g) (Table 4.1 and 4.2), cobalt particles loaded on $KMnO_4$ functionalised CSs appeared to be more evenly spread out on the surface of the carbon spheres than the cobalt particles loaded on HNO_3 functionalised CSs. On the HNO_3 treated CSs the Co particles formed clusters of

cobalt particles with a size range of 3-10 nm. It is proposed that due to the relatively weak oxidizing effect of HNO_3, the HNO_3 tends to attack the weaker and more acid susceptible areas of the CS surface that lie between the carbon flakes making the surface of the CS. This results in a few reactive areas being created on the CS surface. $KMnO_4$ is a strong oxidizing agent and attacks the CS surface uniformly resulting in more spread functional groups on the CS surface. This creates a larger reactive surface area on the CSs for loading cobalt metal than when HNO_3 is used.

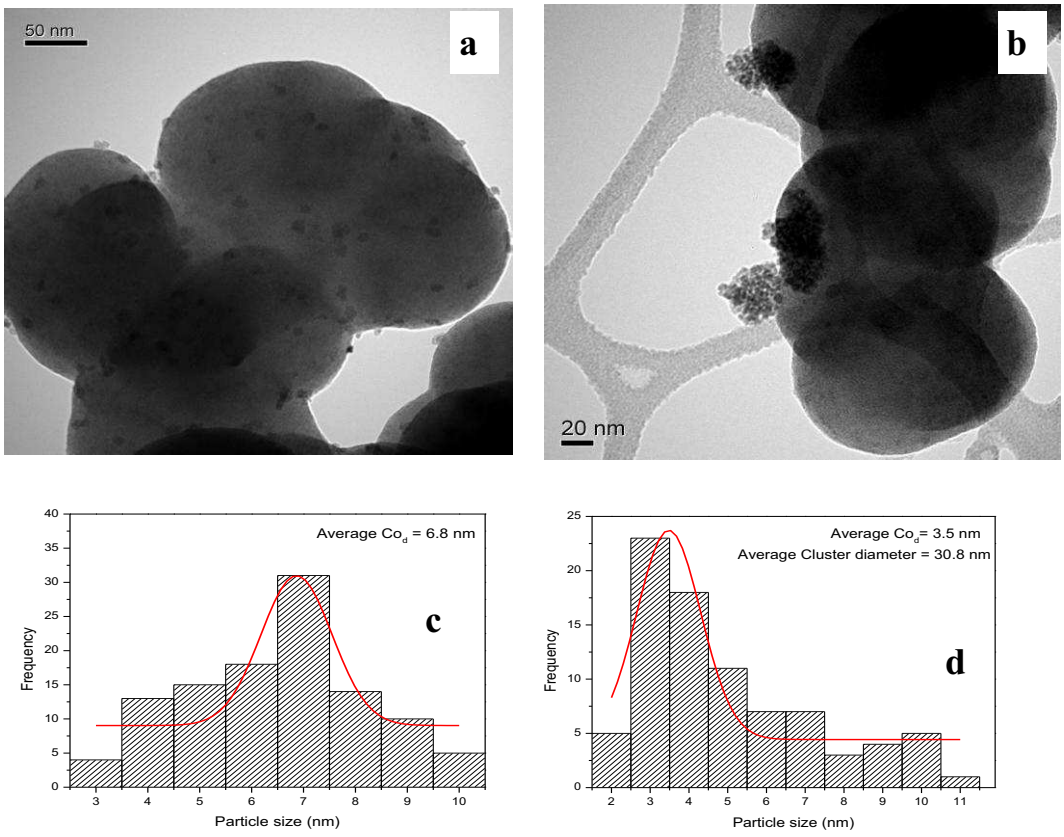


Figure 5.8: TEM images of (**a**) 5% Co/CS $KMnO_4$ functionalised and (**b**) 5% Co/CS HNO_3 functionalised catalysts.

Chemisorption results in Table 5.5 show the cobalt metal dispersions on CSs. The degree of reduction measured by chemisorption (64-76 %) as determined by oxygen titration is suspected to be higher than the real degree of reduction. This could be due to the cobalt catalysed oxidation reaction of CSs at relatively low temperatures as shown by TGA data (Fig. 5.5b and d).

Table 5.5: Chemisorption results of 5% Co/CS catalyst

Sample	**H_2 Uptake (mmol/g)**	**% reduction**	**% dispersion**[a]	**% dispersion**[b]
5% Co/CS ($KMnO_4$)	0.013	76	4.0	10.9
5% Co/CS (HNO_3)	0.010	64	3.7	12.7

[a]*-determined by chemisorption*
[b]*-determined using TEM and XRD particle*

From the TGA profiles (Fig. 5.5) it can be noted that approximately 3-4 % weight is lost at 300 ^oC due to the oxidation of CSs. This implies that during oxygen titration some oxygen is used to re-oxidise Co^0 to Co_3O_4 while some oxygen is used to oxidise CSs to CO_2 or CO. Due to the oxidation of C the oxidation results of Co tend to be incorrect. Further results confirming this reaction can be found in Appendix B. The interference of CSs in determining the degree of reduction results in higher values of oxygen uptake assigned to oxidation of Co hence lower percentage metal dispersion and larger average cobalt particle sizes are calculated from the chemisorption data.

K and Mn promoter effects on a 5% Co/CS catalyst

5 % cobalt loading on CSs was observed to be the optimum metal loading for these CSs supports based on the distribution of metal particles shown by TEM studies. Therefore Mn and K promoter effects were investigated on a 5% Co/CS catalyst.

The 5 % Co/CS HNO_3 functionalised catalyst provides the standard for studying the promotion of K^+ and MnO_4^- ions on the FT reaction. The promoter effect of Mn or K on the FT activity and selectivity of the Co/CS catalysts prepared by HNO_3 functionalised CSs was studied by adding 0.05 wt % Mn or 0.05 % K to the Co/CSs HNO_3 treated catalyst. This amount corresponds to the estimated amount of the residual Mn thought to be present in the $KMnO_4$ functionalised catalyst.

The amounts of K and Mn used in the promoted catalysts were estimated taking note of the following points:-

(i) From TGA (Fig. 5.5) the difference in the residual material between the HNO_3 and $KMnO_4$ treated 5 % Co/CS catalyst is about 0.05 %. Although this method is not an accurate way to determine amounts of K and Mn due to inaccuracies in Co loading. TGA gives an indication that the amounts of residual ions (already known to be present from EDS) are less than 1% wt/wt of catalyst.

(ii) Mn promotion of Co catalysts in the ratio range of Mn/Co of 0 to 0.014 does not result in changes in FT activity but change the FT product selectivity reported by B.L Bezemer [29]. Presence of K in quantities as little as 0.0016 % decreased FT activity but improved o/p ratios reported by Trépanier et al. [21].

(iii) EDS shows K and Mn peak presence. However intensities could not be used to get a quantitative % presence.

(iv) ICP analysis. The amounts present – error bar suggests 0.05 +/- 0.02. So absolute amount is not known with great accuracy.

Based on these points we know the following, the weight of both K and Mn residual ions should be less than 1% of the mass of the catalyst (TGA) and Mn/Co ratio should lie between 0 to 0.014 since K in very small quantities reduces the FT activity (see later), hence a good estimate would be 0.05 % wt/wt of the catalyst for each promoter.

The addition of the promoters Mn or K to the 5 % Co/CS catalyst functionalised by HNO_3 gave similar XRD patterns as found for the un-promoted catalysts (Fig. 5.7d and e). For the Mn promoted catalysts the presence of cobalt-manganese complexes was not detected by XRD due to the very low Mn loadings. The effect of adding potassium to the HNO_3 functionalised catalyst had a minor effect in shifting the second peak of the TPR profile of the cobalt oxide species to a higher temperature (Fig. 5.6d). However the addition of small amounts of manganese to the HNO_3 functionalised catalyst gave a shoulder peak of MnO_2 at *ca.* 344 ^{o}C [29, 31, 36]. The presence of the manganese oxide species also broadened the reduction peak of CoO to Co similar to the TPR profile of the $KMnO_4$ functionalised catalyst (Fig. 5.6c), This suggests that manganese oxide species hinder the second reduction stage for cobalt (Fig. 5.6c and e). The peak due to the methanation of CSs at *ca.* T = 650 ^{o}C was also shifted to a higher temperature (Fig. 5.6e) relative to the samples that did not contain Mn (Fig. 5.6b and c). The presence of K and Mn was confirmed by EDS on a 5 % Co/CS $KMnO_4$ functionalised catalyst (Fig. 5.9).

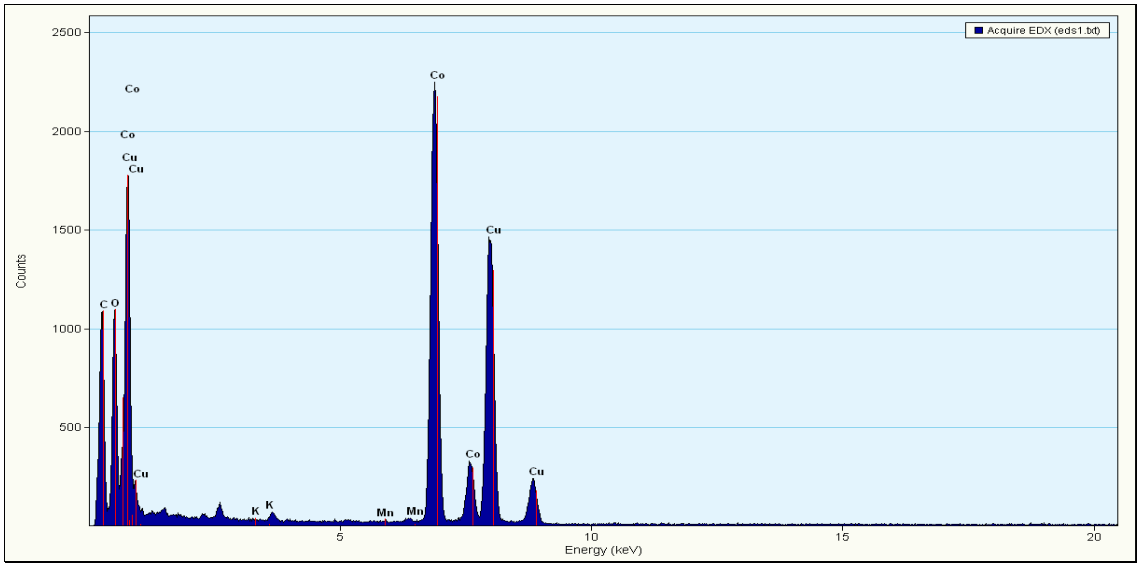


Figure 5.9: EDS spectrum of 5% Co/CS $KMnO_4$.

10 % Co/CS catalysts

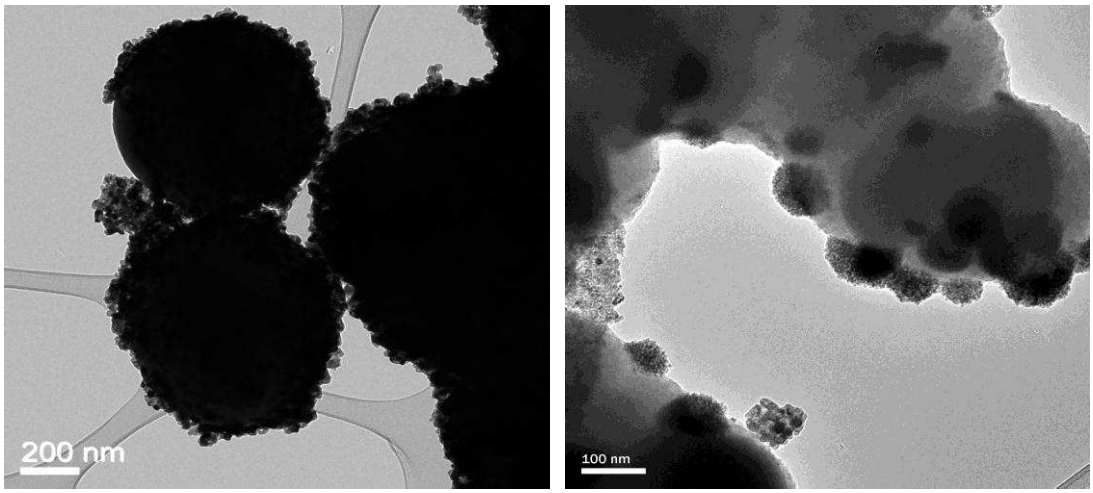


Figure 5.10: TEM images of (**a**) 10% Co/CS $KMnO_4$ functionalised catalyst (**b**) 10% Co/CS HNO_3 functionalised catalyst.

TEM studies of the 10 % Co/CSs catalysts are presented in Fig. 5.10a and b. From Fig.5.10a it can be seen that cobalt particles agglomerated forming large cobalt clusters which were densely packed on each of the CS. These results show that at 10 % wt/wt metal loading, CSs had reached a metal loading saturation point. The cobalt particle sizes of these catalysts could not be measured by TEM because they formed multiple layers of Co metal around the CSs.

The cobalt metal loading on 10 % Co/CS sample was confirmed by TGA run in air. A residual weight of ca. 12.4 % and 13.9 % ascribed to Co_3O_4 phases was noted from the HNO_3 and $KMnO_4$ functionalised catalysts (Fig. 5.11a and b) respectively. The cobalt catalysed CS oxidation reaction, discussed for the 5 % Co/CS catalysts, was also observed with the 10 % Co/CS catalysts.

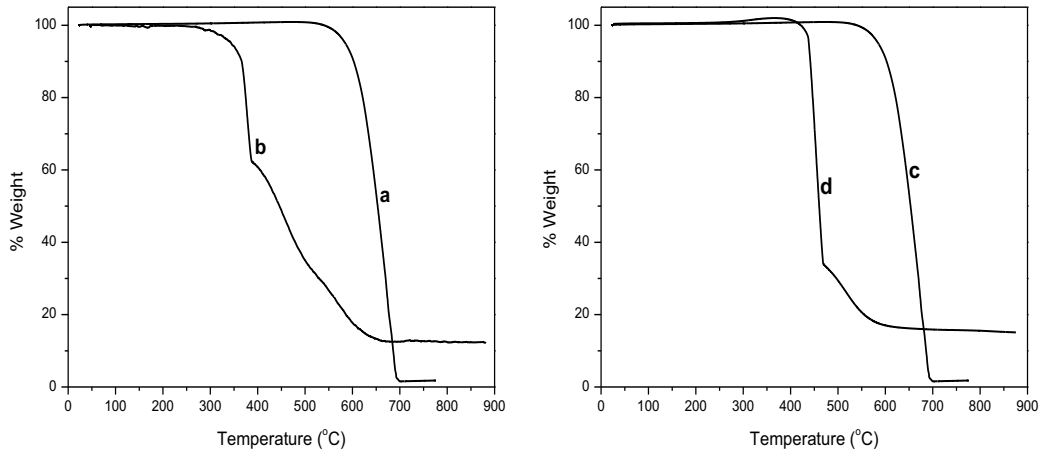


Figure 5.11: TGA profile run in air on the (a) HNO_3 functionalised CSs, (b) 10 % Co/CS catalysts functionalised by HNO_3, (c) $KMnO_4$ functionalised CSs and (d) 10 % Co/CS catalysts functionalised by $KMnO_4$.

Similar to the 5 % Co/CS TGA, the 10 % Co/CS catalysts run in air showed that supported cobalt phases catalysed the oxidation of CSs, reducing the temperature of the onset of oxidation from ca. 560 ^{o}C in the absence of cobalt to ca. 400 ^{o}C in the presence of cobalt (Fig. 5.11). The two distinct regimes for the oxidation of CS observed with the 5 % Co/CS catalysts is also noted with the 10 % Co/CS catalysts: From Fig. 5.11 the following is noted (i) the Co catalysed oxidation of CS from 200 ^{o}C to ca. 400 ^{o}C and (ii) the non-catalysed oxidation of CS from ca. 400 ^{o}C to 650 ^{o}C. The transition between regions I and II from Fig. 5.11b and d showed that for the HNO_3 treated catalyst (Fig. 5.11b) this occurs after ca. 40 % carbon removal and is complete by > 600 ^{o}C, but for the $KMnO_4$ treated catalyst (Fig. 5.11d) the transition occurs after 65 % carbon loss and is complete by < 600 ^{o}C. These results are similar to those shown by 5% Co/CS materials.

It can be noted from Table 5.6 that the addition of 10 % wt/wt cobalt on CS increases the surface area. These results confirm that cobalt particles are deposited on the surface of a non-porous CS.

Table 5.6: N_2-physisorption results for CSs supports and 10 % Co/CS catalysts

Sample	**S.A support (m^2/g)**	**S.A of 10 % Co/CS catalyst (m^2/g)**
$KMnO_4$ functionalised CSs	3.1	7.9
HNO_3 functionalised CSs	3.0	5.4

5.3 Catalyst evaluation for Fischer-Tropsch synthesis

5.3.1 Experimental

FT synthesis was carried out in a fixed bed reactor (FBR) (internal diameter of 50 mm, height 250 mm) filled with 2 mm stainless steel balls above a sieve with pore diameters of 0.5 mm. The catalyst (0.5 g) was reduced at 330 ^{o}C and 1 bar pressure for 18 h under 100 % H_2 gas before carrying out FTS. The average FTS results reported were collected at 220 ^{o}C, 8 bar pressure and GHSV 2100 h^{-1} under steady state conditions. The FBR was connected to two on-line GCs, one with a flame ionization detector (FID) and the other with a thermal conductivity detector (TCD). A Poropak-Q (PPQ) column was used to separate hydrocarbons from C_1 to C_{10} while a *ZB*-1 capillary column fitted into an offline GC-FID was used to separate C_7 to C_{30} hydrocarbons collected as wax and oil fractions from the hot and cold traps respectively.

Before FT synthesis was carried out, all catalysts were reduced with pure hydrogen (T = 330 ^{o}C, 18 h, 1 bar pressure, flow rate 45 mL/min and STP exit conditions). After the reduction step the FBR was cooled and the hydrogen gas flow was cut off and replaced with synthesis gas (H_2:CO ratio of 2, 10 % N_2 as internal standard for mass balance calculations). Two traps were mounted after the reactor; one maintained at T = 150 ^{o}C for wax collection, while the other was kept at ambient temperature for collecting oil and water. At steady-state the knock out pots were emptied and the period of the mass balance calculation commenced.

5.3.2 Results and Discussion

All catalysts reached steady state after approximately 26 h of reaction time. Table 5.7 summarises the catalysts performance for FTS and Fig. 5.13 shows the olefin to paraffin selectivity. The 5 % Co/CS HNO_3 and 5 % Co/CS $KMnO_4$ functionalised catalysts surprisingly showed similar % CO conversions although they showed significant differences in their Co particle sizes after 120 h of reaction time (Fig. 5.14 and 5.15). This result initially appears to be in contradiction to the known Co particle size and FT activity relationship [6, 15, 17]. TEM images recorded for the Co/CS catalysts at the end of the FT reaction (120 h) and are shown in Fig 5.14 and 5.15. It is clear that the Co particles on the $KMnO_4$ treated Co/CS have undergone little sintering while the HNO_3 treated Co/CS sample have undergone severe sintering.

From Table 5.7 the $KMnO_4$ functionalised catalysts showed relatively lower CH_4 and C_2-C_4 selectivity but higher C_{5+} selectivity compared to the HNO_3 functionalised catalyst. However, as is discussed below, this effect is actually due to residual promoter ion effects, which confirms the presence of K or MnO_4^- ions on the Co/CS catalysts.

Table 5.7: Summary of FTS catalytic performance of cobalt supported catalyst

Catalyst	% CO Conversion	Activity ($\mu mol/sec.g_{Co}$)	% Mol Selectivity				[a]α-value
			C_1	C_2 - C_4	C_{5+}	CO_2	
5 % Co/CS $KMnO_4$	14.4	35.4	17.6	24.1	58.4	0	0.79
5 % Co/CS HNO_3	15.1	37.3	29.2	26.6	44.1	0	0.66
0.05% Mn/5 % Co/CS HNO_3	13.8	34.0	20.9	27.8	51.3	0	0.73
0.05% K/5 % Co/CS HNO_3	6.6	16.3	29.0	43.1	27.9	0	0.65

[a]-determined from ASF plot (Fig. 5.12)

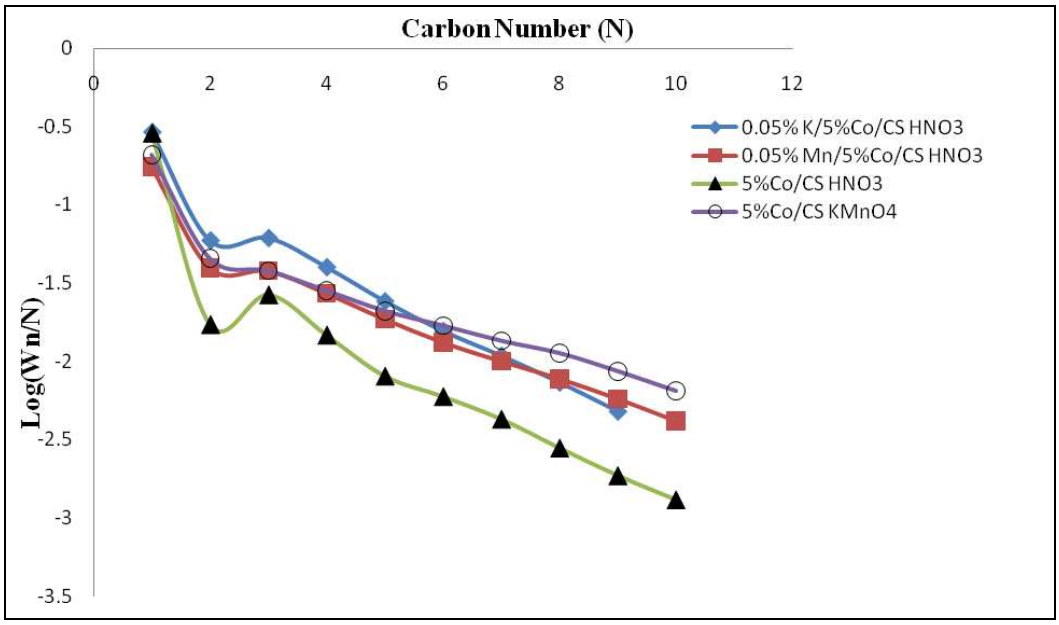


Figure 5.12: ASF distribution for (a) 5% Co/CS $KMnO_4$, (b) 5% Co/CS HNO_3, (c) 0.05% Mn/ 5 % Co/CS HNO_3 and (d) 0.05% K/ 5 % Co/CS HNO_3.

The Mn addition showed little effect on the FT activity but significantly changed the product selectivity to yield (i) less C_1 and more C_{5+} products (Table 5.7) and (ii) more olefin products when compared to the Co/CS HNO_3 functionalised catalysts (Fig. 5.13). These results agree with previously reported literature data by Bezemer et. al on the effect of Mn on a Co/C catalyst [27]. Their studies, using a Co/CNF catalyst, showed that increasing Mn/Co ratios from 0 to 0.08 had little or no effect on FT activity but increased the olefin to paraffin ratios. Our studies were conducted at a Mn/Co ratio of 0.01.

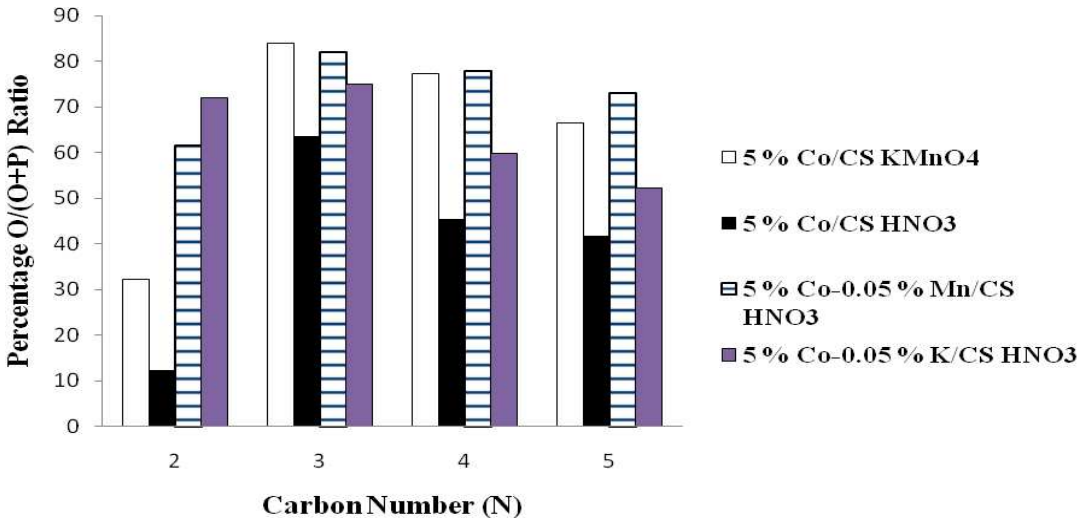


Figure 5.13: Olefin selectivity for 5% Co/CSs.

The presence of K in the HNO_3 functionalised Co catalysts increased the low molecular weight olefin selectivity (Fig. 5.13) but decreased the FT activity from ca. 14 % to ca. 7 % (Table. 5.7). This effect has been previously reported in the literature [21]. A comparison of the $KMnO_4$ treated Co/CS with the K and Mn

promoted HNO_3 functionalised catalysts reveals (i) the activity of the Mn promoted material is similar to that of the $KMnO_4$ treated sample (ii) the C_1, C_2-C_4 and C_{5+} products are less hydrogenated than found for the Mn and K promoted materials and (iii) the olefin/paraffin ratios are in general more similar to the Mn than the K promoted material. The data suggest that the residual ions left behind on the $KMnO_4$ treated sample are likely to be MnO_4^- ions. This will need to be confirmed by surface characterisation techniques e.g. SIMS.

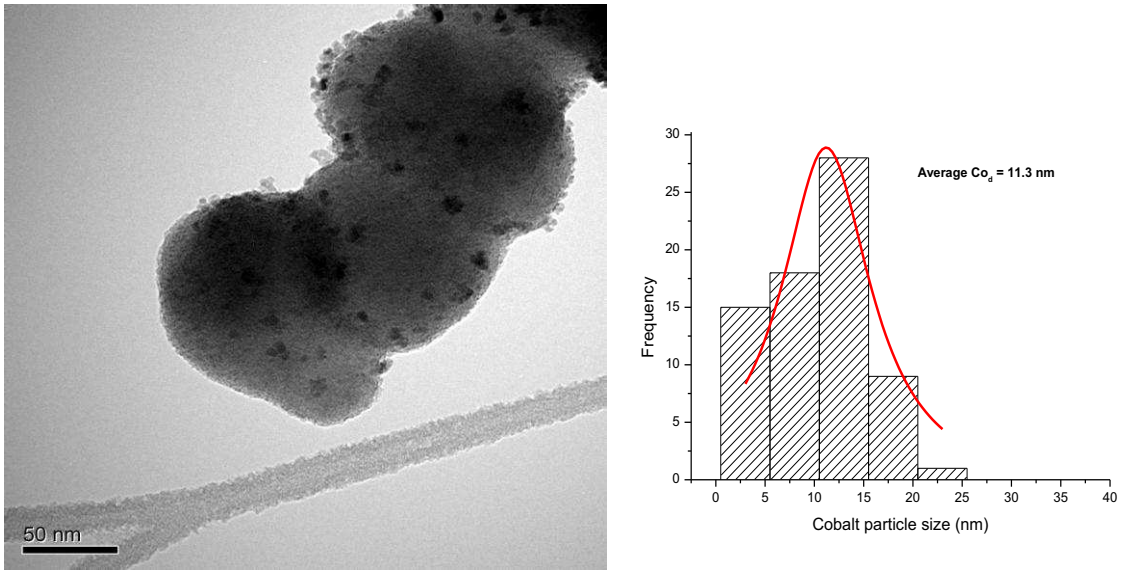


Figure 5.14: TEM images and particle size distribution of $KMnO_4$ functionalised catalyst after 120 h on stream.

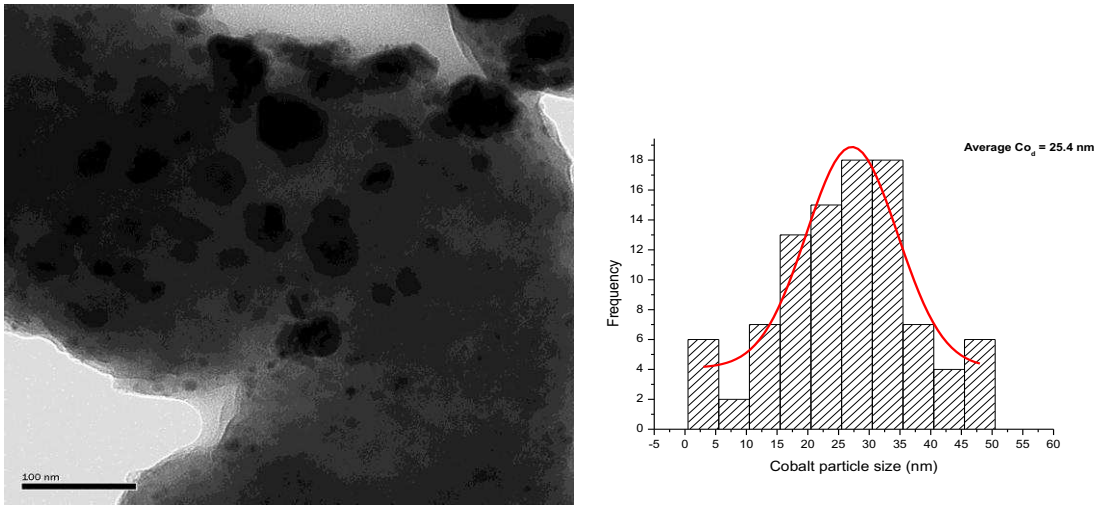


Figure 5.15: TEM images and particle size distribution of HNO_3 functionalised catalyst after 120 h on stream.

General discussion

The effect of adding Mn to the HNO_3 treated Co/CS catalyst confirmed that the residual Mn present in the $KMnO_4$ functionalised catalyst had a minimal effect on FT activity but decreased the C_1 content and increased the α-values of this catalyst (Fig. 5.12). This implies that the remaining Mn in the $KMnO_4$ functionalised catalyst had created a less hydrogenating catalyst even after a thorough washing procedure. It is clear that water washing procedures to remove MnO_4^- ions was not successful. Thus, functionalised carbons have an ability to bind strongly to small amounts of metal ions. The presence of these ions can be detected by physical techniques (TPR, TGA, EDS) or chemical reactions (FT product distribution). This represents the second example of residual ions trapped on a carbon support playing a role in the activity of FT catalysts. We recently reported that Ca ions could be detected, after acid washing of CNTs made from $Fe/Co/CaCO_3$ catalysts [37]. Clearly, the impact of residual surface ions on carbon

surfaces is widespread and impacts significantly on the catalytic behaviour of FT catalysts. This phenomenon will need further investigation.

5.4 Conclusions

Co particle sizes of 3-15 nm for 2.5 and 5 % metal loadings were successfully produced by both HNO_3 and $KMnO_4$ treatment of CSs, followed by Co addition to the CSs. The deposition of these particles onto the surface of CSs was largely dependent on the dispersion of the active sites on the surface of CSs. The use of 0.5 M $KMnO_4$ as a functionalizing agent for CSs is more advantageous than the use of 55 % HNO_3. These advantages include: (i) $KMnO_4$ produces more highly dispersed functional groups than HNO_3, (ii) $KMnO_4$ produced the same amount of functional groups under milder reaction conditions than did HNO_3 using harsher reacting conditions.

An increase in cobalt loading from 2.5 to 5 % resulted in an increased number of agglomerated cobalt particles that formed clusters greater than 20 nm in diameter for HNO_3 functionalised catalysts. The $KMnO_4$ functionalised catalysts showed well distributed cobalt particles on a CS support. An increase in metal surface area coverage was observed when the metal loading was increased from 2.5 to 5 %. A further increase in metal loading from 5 to 10 % resulted in a more highly covered surface for both $KMnO_4$ and HNO_3 functionalised CSs. As a result the Co particle sizes could not be measured by TEM. Therefore 5 % metal loading was determined to be the optimum conditions for preparing Co/CS catalysts.

TGA profiles of all Co/CS catalysts show that cobalt phases catalyse the oxidation of CSs. The 5 % and 10 % cobalt loaded catalysts showed two regimes for the oxidation of CS, these were due to (i) catalysed oxidation of CS and (ii) the non-catalysed oxidation of CSs. However the 2.5 % cobalt loaded catalysts did not

show any effect of the Co catalyst on the TGA profiles. For the 5 and 10 % cobalt loaded catalysts similar trends for the catalysed oxidation of CSs were observed i.e. for $KMnO_4$ functionalised catalysts this reaction was complete after ca. 65 % carbon weight loss below 700 ^oC, whereas for the HNO_3 functionalised catalysts this reaction was complete after ca. 45 % carbon weight loss but above 700 ^oC. These results imply that residual manganese oxide species on the surface of the CSs promote the cobalt catalysed oxidation reaction of carbon.

However residual Mn (and possibly K) ions remain on the surface of CSs even after washing. These ions may act as catalyst promoters or inhibitors. The effect of adding Mn to HNO_3 functionalised Co/CSs in the ratio Mn/Co = 0.01 produced FT catalysts with high olefin and C_{5+} products but with no effect on FT activity. Addition of K in the ratio K/Co = 0.01 increased olefin products but significantly reduced the % CO conversion.

The study reveals that CSs are very good catalyst support materials for studying the effects of promoters on the active metal precursor even in low concentrations.

References

1. Q. Zhang, J. Kang and Y. Wang, ChemCatChem 2 (2010) 1030.
2. M.E. Dry, in: J.R. Anderson, M. Boudart (Eds.), Catalysis Science Technology, vol. 1, Springer, New York, (1981) 159–319.
3. F. Fischer, H. Tropsch, German Patent 4,843,371,925.
4. B. Jager, R. Espinoza, Catal. Today 23 (1995) 17.
5. R. Oukaci, A.H. Singleton, J.G. Goodwin, Appl. Catal. A: Gen. 186 (1999) 129.
6. E. Iglesia, Appl. Catal. A: Gen., 161 (1997) 59.
7. R. Bechara, D. Balloy, D. Vanhove, Appl. Catal. A: Gen. 207 (2001) 343.
8. E. van Steen, F.F. Prinsloo, Catal. Today 71 (2002) 327.
9. P.J. van Berge, J. van de Loosdrecht, S. Barradas, A.M. van der Kraan, Catal. Today 58 (2000) 321.
10. G. Jacobs, T. Das, Y. Zhang, J. Li, G. Racoillet, B.H. Davis, Appl. Catal, A: Gen. 233 (2002) 263.
11. C.H. Bartholomew, in: L. Guczi (Ed.), New Trends in CO Activation, Elsevier, Amsterdam, (1991) 225.
12. N.E. Tsakoumis, M. Ronning, O. Borg, E. Rytter, A. Holmen, Catal. Today 154 (2010) 162.
13. S. Bessell, Appl. Catal. A. 96 (1993) 253.
14. R.C. Reuel, C.H. Bartholomew, J. Catal. 85 (1984) 78.
15. E. Iglesia, S. Soled, R.A. Fiato, J. Catal. 137 (1992) 212.
16. W. Chen, Z. Fan, X. Pan and X. Bao, JACS 130 (2008) 9414.
17. G.L. Bezemer, J.H. Bitter, H.P.C.E. Kuipers, H. Oosterbeek, J.E. Holewijn, X. Xu, F.Kapteijn, A. Jos van Dillen and K.P.de Jong. JACS 128 (2006) 3956.

18. J. Kang, S. Zhang, Q. Zhang, and Y. Wang, Angew. Chem. Int. Ed, 48 (2009) 2565.
19. M.C. Bahome, L.L. Jewell, K. Padayachy, D Hildebrandt, D Glasser, A.K. Datye, N.J. Coville, Appl. Catal. A: Gen. 328 (2007) 243.
20. M.C. Bahome, L.L. Jewell, D. Hildebrandt, D. Glasser, N.J. Coville, Appl. Catal. A: Gen. 287 (2005) 60.
21. M. Trépanier, A. Tavasoli, A.K. Dalai, N. Abatzoglou, Appl. Catal. A: Gen. 353 (2009) 193.
22. A. Tavasoli, R.M. Malek Abbaslou, M. Trépanier, A.K. Dalai, Appl. Catal. A: Gen. 345 (2008) 134.
23. R.M. Malek Abbaslou, A. Tavasoli, A.K. Dalai, Appl. Catal. A: Gen. 355 (2009) 33.
24. A.A. Deshmukh, S.D. Mhlanga, N.J. Coville, Mater. Sci. Eng., R 70 (2010) 1.
25. S. Tang, Y. Tang, S. Vongehr, X. Zhao, X. Meng, App. Surf. Sci. 255 (2009) 6011.
26. H. Xiong, M. Moyo, M.K. Rayner, L.L. Jewell, D.G. Billing, N.J. Coville, ChemCatChem. 2 (2010) 514.
27. G.L. Bezemer, P.B. Radstake, U. Falke, H. Oosterbeek, H.P.C.E. Kuipers, A.J. van Dillen, K.P. de Jong, J. Catal. 237 (2006) 152.
28. F. Morales, E. de Smit, F.M.F. de Groot, T. Visser, B.M. Weckhuysen, J. Catal. 246 (2007) 91.
29. F. Morales, F.M.F. de Groot, O.L.J. Gijzeman, A. Mens, O. Stephan, B M. Weckhuysen, J. Catal. 230 (2005) 301.
30. F. Morales, D. Grandjean, A. Mens, F.M.F. de Groot, B M. Weckhuysen, J. Phys. Chem. B 110 (2006) 8626.
31. T.E. Feltes, L. Espinosa-Alonso, E. de Smit, L. D'Souza, R.J. Meyer, B.M. Weckhuysen, J.R. Regalbuto, J. Catal. 270 (2010) 95.

32. F. Morales, F.M.F. de Groot, P. Glatzel, E. Kleimenov, H. Bluhm, M. Havecker, A. Knop-Gericke, B.M. Weckhuysen, J. Phys. Chem. B 108 (2004) 16201.
33. S.E. Colley, M.J. Betts, R.G. Copperthwaite, G.J. Hutchings, N.J. Coville, J. Catal. 134 (1992) 186.
34. G.L. Bezemer, A. van laak, A.J. van Dillen, K.P. de Jong, Stud. Surf. Sci. Catal. 147 (2004) 259.
35. F. Rodriguez-Reinoso, Carbon 36 (1998) 159.
36. E.R. Stobbe, B.A. de Boer, J.W. Geus, Catal. Today. 47 (1999) 161.
37. U.M. Graham, A. Dozier, R.A. Khatri, M.C. Bahome, L.L. Jewell, S.D. Mhlanga, N.J. Coville, B.H. Davis, Catal. Lett. 129 (2009) 39.

Chapter 6

Cobalt supported on hydrothermally synthesised carbon spheres (Co/CS_{hydr}) for Fischer-Tropsch synthesis.

6.1 Facile hydrothermal synthesis of carbon spheres (CS_{hydr}).

6.1.1 Introduction

Carbon spheres have mainly been synthesised by two procedures: (i) high temperature procedures that involve decomposition of a carbon source under inert conditions and (ii) low temperature procedures that involve pyrolytic and/or catalytic decomposition of organic compounds such as disaccharides, often at high pressures. These high temperature procedures include arc-discharge, chemical vapour deposition (CVD) and laser ablation processes, while the low temperature procedures include hydrothermal methods in an autoclave. [1].

The hydrothermally synthesised CSs formed in an autoclave show several advantages over CVD synthesised CSs. These advantages include: the introduction of oxygen functionalities during synthesis, a variable surface area, as well as pore volume and structural properties that result from annealing the CSs under inert conditions.

The hydrothermal synthesis of CSs has numerous challenges that arise from the use of the low reaction temperatures used. These limitations are overcome by the high pressure employed in the autoclave during the reaction. In this approach the

reactants in the autoclave are heated to various (typically low) temperatures [1] and the boiling liquid in the autoclave builds the high reaction pressure. The assumption made in this method is that the material of construction of the autoclave does not affect the reaction. This is not always true for all reactions. There are some reports where the reactor walls have had an impact on the reactions [2-3].

Carbon spheres in general have received growing attention that relates to their applications due to their unique physical and chemical properties [1]. They can be used as molecular sieves [4], photonic band gap crystals [5-6.], and electrode materials for lithium ion batteries [7-8]. Hydrothermally synthesised carbon spheres have also been shown to be very good catalyst supports [9]. Although these materials have been used as catalyst supports for various reactions, in this chapter we report the first study conducted of cobalt catalysts supported on hydrothermally synthesised CSs in the FT reaction.

6.1.2 Experimental

Hydrothermal synthesis of carbon spheres (CS_{hydr})

CS_{hydr} were synthesized using a hydrothermal synthesis method from a sucrose precursor [9]. In a typical experiment the 0.3 M aqueous sucrose solution was added into a teflon cup (90 % filled) with a total volume of 58 mL. This was placed into a stainless steel autoclave which was heated to 190 ^{o}C. The reaction was allowed to proceed for 4 h once the temperature in the autoclave reached 190 ^{o}C. After 4 h the autoclave was allowed to cool to room temperature and the suspension was centrifuged 5 times using water and 5 times using ethanol at 5000 rpm for 10 min. The products were then dried in an oven at 70 ^{o}C overnight.

Annealing of CS_{hydr}

The as-prepared material was then annealed at different temperatures under N_2. In a typical experiment 2.5 g of as-prepared CS_{hydr} was loaded into a quartz boat which was placed in a quartz tube and placed at the middle of a furnace. Nitrogen gas was allowed to flow at 20 mL/min through the quartz tube while the furnace was heated to the desired annealing temperature i.e. 250, 350, 400, 450, 600 or 800 ^{o}C. The annealing was allowed to proceed for 2.5 h before the furnace was cooled to room temperature. Both the as-prepared and annealed samples were characterised by transmission electron microscopy (TEM), X-ray diffraction (XRD) and Fourier transform infrared (FTIR) measurements, Raman spectroscopy, thermogravimetric analysis (TGA), and Brunnet- Emmett Teller (BET) surface analysis. Further details on the equipment used are to be found in Chapter 2.

6.1.3 Results and Discussion

TEM studies were used to gain an understanding of the morphology of the CS_{hydr}. Fig. 1 shows TEM images of the as-prepared material at different magnifications. It can be noted that the as-prepared material consists of spherical particles, with a size distribution of 700-1200 nm. The physical surface characteristics of these spherical particles were clearly noted in the high magnification TEM image (Fig. 6.1b). These particles have bare surfaces which look rough (Fig. 6.1b).

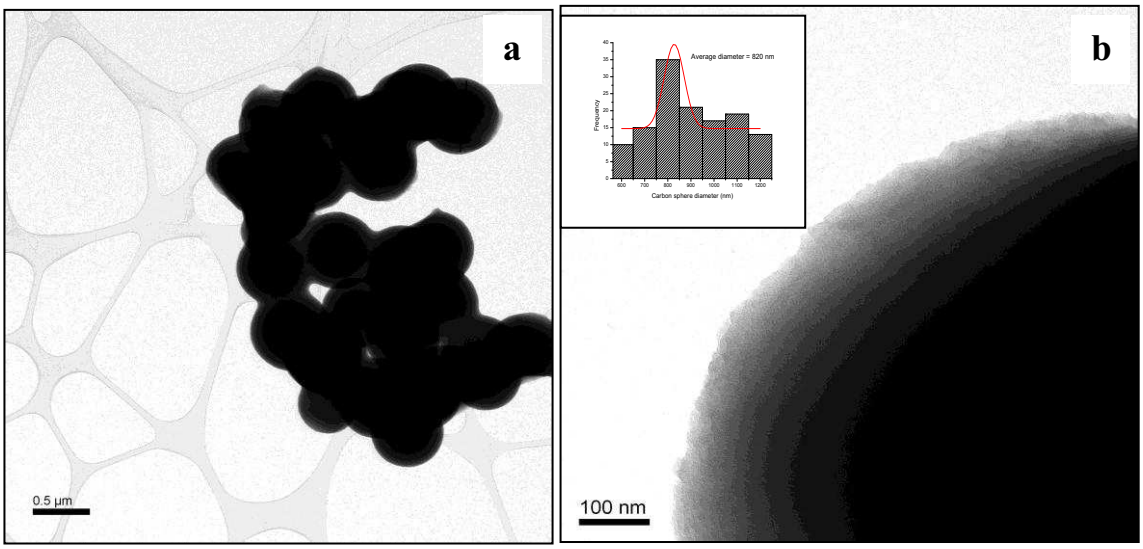


Figure 6.1: TEM images of as-prepared CS_{hydr} (a) low magnification and (b) high magnification (insert: particle size distribution bar chart).

Fig. 6.2 shows DTG profiles of the as-synthesised CS_{hydr} materials and sucrose. The thermal degradation of sucrose follows the following reaction:

$$C_{12}H_{22}O_{11} \longrightarrow 12C + 11\ H_2O$$

A DTG analysis of this reaction showed three weight loss peaks (Fig. 6.2). The first peak (i) represents the condensation reaction resulting in the formation of oligomers and polymeric products, the second peak (ii) represents reactions that lead to the formation of a black aerated charlike solid [10-11] and the third peak (iii) represents the volatilisation of the charlike solids. A detailed study of the thermal degradation of sucrose can be found in the literature [10-11]. The DTG of the as-synthesised CS_{hydr} showed three negative peaks, the first peak observed below 100 ^{o}C was due to loss of moisture in the sample, the second peak observed at 300 ^{o}C is similar to the second peak observed in the thermal degradation of sucrose and the third peak is due to the oxidation of the carbon spheres at 540 ^{o}C.

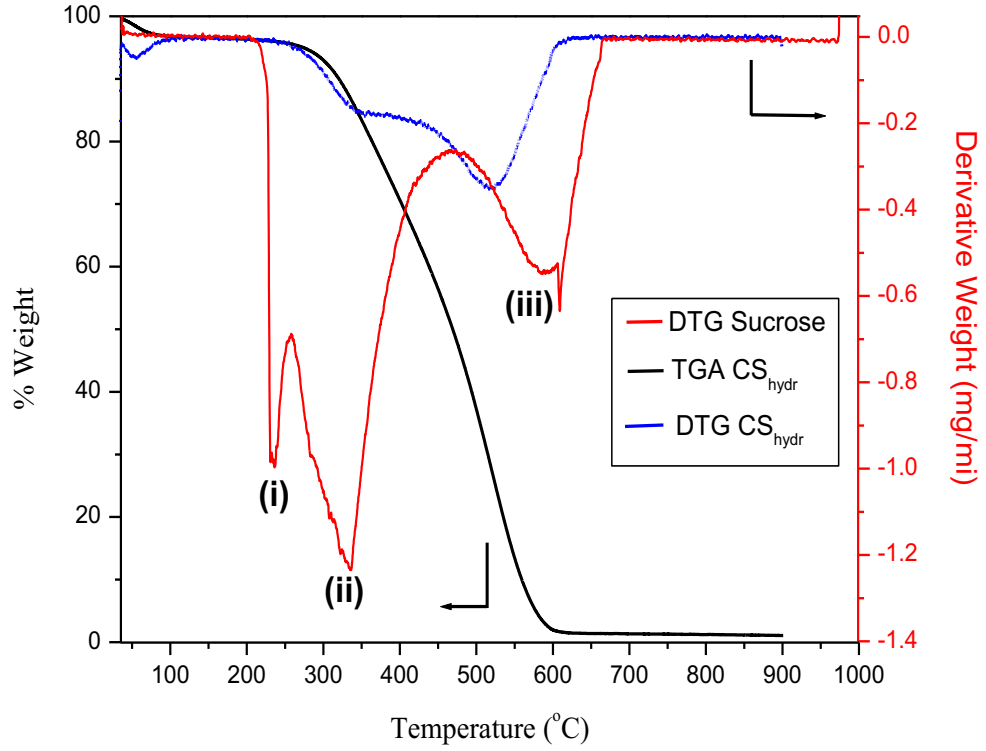


Figure 6.2: TGA and DTG profiles of as-synthesised CS_{hydr} and sucrose under air.

Annealing the as-synthesised CS_{hydr} at 250, 350, 450, 600 or 800 ^{o}C for 2.5 h under nitrogen gas had little effect on the morphology of the CSs, as shown in Fig. 6.3. However the annealing process removes the volatile oligomeric and polymeric products and also amorphous carbon on the CSs which formed during the CS_{hydr} synthesis reaction. The CS_{hydr} materials annealed at temperatures greater than 350 ^{o}C appear to have been stripped of amorphous carbon materials (Fig. 6.3d to e) compared to those annealed at a temperatures less than or equal to 350 ^{o}C (Fig. 6.3a to c).

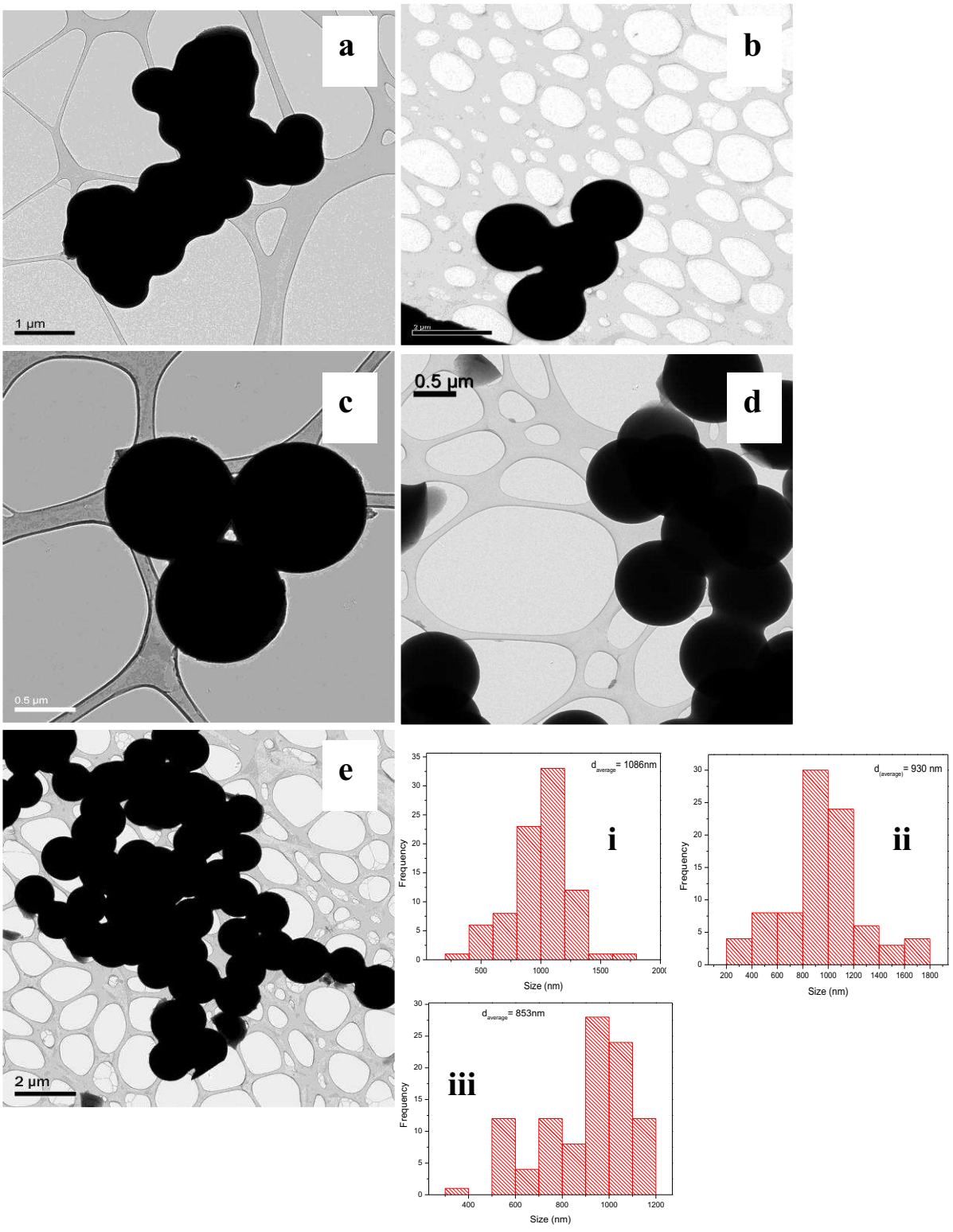


Figure 6.3: Effect of annealing temperature (a) 250, (b) 350, (c) 450, (d) 600 and (e) 800 ^{o}C for 2.5 h under N_2 gas and size distribution for (i) 250, (ii) 450 and 600 ^{o}C annealed CS_{hydr}.

Fig. 6.4 shows the relation between annealing temperature and thermal stability of CS_{hydr}. It can be noted that increasing the annealing temperature under N_2 increased the thermal stability of the CS_{hydr} as reflected by the shift of the onset of weight loss to higher temperatures in the TGA profiles. This is due to the decomposition and removal of the thermally unstable compounds during the annealing process. The effects of annealing temperature on the chemical properties of the CS_{hydr} are discussed below.

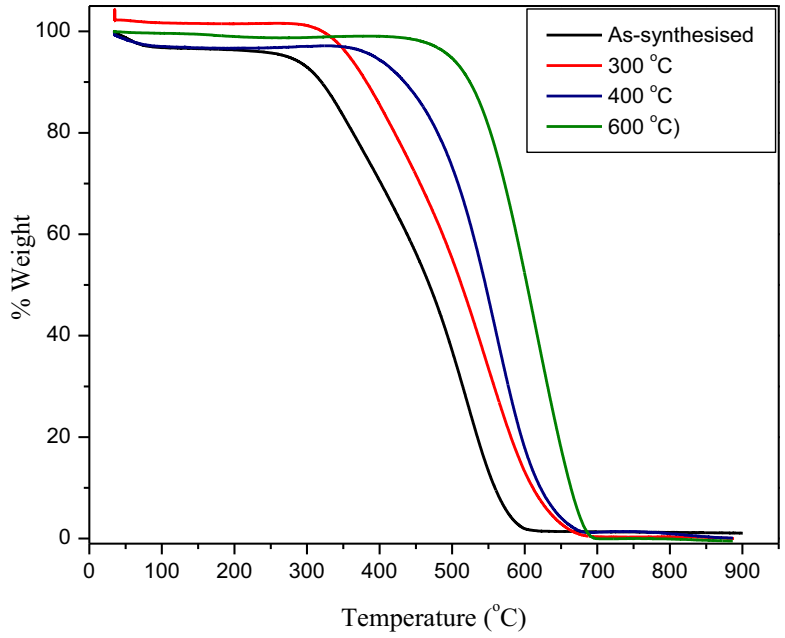


Figure 6.4: TGA profiles (under air) of as-synthesised and 300, 450 and 600 °C annealed CS_{hydr} samples (2.5 h heating).

From Fig. 6.5, an increase in annealing temperature from 250 to 450 °C under N_2 gave CS_{hydr} with slightly higher surface areas and pore volumes. This is thought to be due to the decomposition of oligomeric and polymeric products formed during the synthesis of the CS_{hydr} [10-11]. A further increase of annealing temperature from 450 to 600 °C resulted in a rapid increase in surface area and pore volume. This is thought to be due to the opening of pore channel networks within the

CS_{hydr} matrix resulting from the thermal decomposition and removal of polymeric and polymeric products shown by TGA studies (Fig. 6.2).

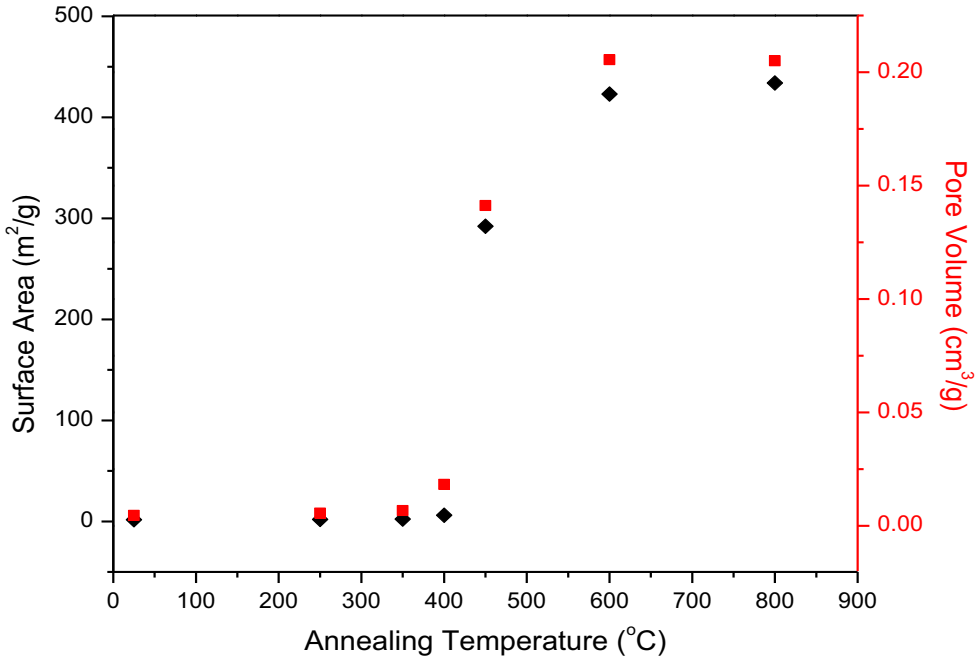


Figure 6.5: Effect of annealing temperature on surface area and pore volume.

Raman spectroscopy is a type of vibrational spectroscopy that is frequently used to identify and quantify chemical compounds. Carbon has several allotropes and it can exist in a variety of disordered forms [12]. Raman spectroscopy has historically been applied in the structural characterisation of carbonaceous materials [13] and graphitic systems i.e carbon fibers, pyrolytic graphite, nanographite ribbons, fullerenes and carbon nanotubes [12], due to its high sensitivity to structural changes that perturb translational symmetry in carbon materials [13]. However, Raman spectroscopy was used in this study to gain further understanding of the effects of annealing temperature on the CS_{hydr}.

The Raman spectrum of carbonaceous materials is usually divided into two regions that depend on the degree of crystallinity of the material. These regions include (i) the first and (ii) the second order regions.

The first-order Raman spectrum is sensitive to the extent of the two-dimensional ordering and contains structural information on carbonaceous materials. It is the spectral region between 1000 and 1800 cm^{-1}. A graphitic lattice would have a hexagonal symmetry that belongs to a prismatic D^4_{6b} point group. Therefore this symmetry has vibrational modes of the type $2E_{2g}$, $2B_{2g}$, E_{1u} and A_{2u} [14] as seen in equation 6.1 below. The E-symmetry modes exhibit in-plane atomic modes whereas the A-symmetry modes exhibit out of plane displacements. The B-modes are optically inactive.

$$\mathbf{r_{vib}} = \mathbf{2E_{2g}}\ \textit{(Raman active)} + \mathbf{2B_{2g}}\ \textit{(optically inactive)} + \mathbf{E_{1u}}\ \textit{(IR active)} + \mathbf{A_{2u}}\textit{(IR active)}$$

Equation 6.1

In the case where a perfectly symmetric molecule such as hexagonal graphite is analysed for Raman spectral modes, an in plane C=C bond in the aromatic stretching vibrational mode with a E_{2g} symmetry will be observed in the first order spectra as a single band around 1582 cm^{-1} . This is commonly known as the G-band. However if this material's structure is disturbed by, for example acid treatment, a second band at around 1330 cm^{-1} known as the D-band will appear due to the lowering of molecular symmetry. New vibrational modes with A_{1g} symmetry become Raman active due to the disorder in the sp^2 carbon network [12]. Previous researchers have also explained the D-band in carbonaceous materials to be due to the existence of specific vibrations at the edges due to functional groups [15]. However, all studies of pyrolised or hydrothermally synthesised carbon materials conclude that the D-band corresponds to structural disorder. It should be noted that in these materials there is a continuum from graphite (pure sp^2) to diamond (pure sp^3), where materials in between consist of both sp^2 and sp^3 hybridised carbon atoms. As the degree of sp^3 hybridization

increases in a material which is largely sp^2 carbonaceous material the G-band tends to broaden and shift to higher wave-numbers [15-17]. In such cases the G-band denotes that the material contains sp^2 carbon networks that are not necessarily graphitic.

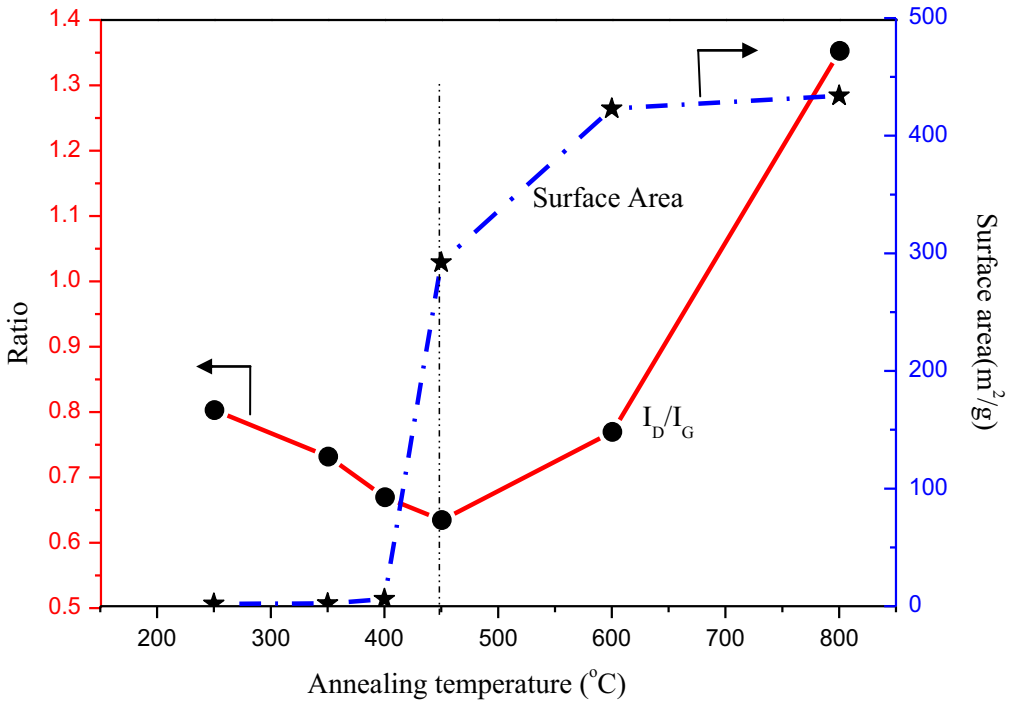


Figure 6.6: Effect of annealing temperature on surface area and crystallinity of CS_{hydr}.

Fig. 6.6 shows the effect of annealing temperature on the I_D/I_G ratio and surface areas of the CS_{hydr}. The I_D/I_G ratio was used to determine the degree of disorder in the CS_{hydr} materials. As the annealing temperature was increased from 250 to 450 ^oC the I_D/I_G ratio is noted to decrease gradually. However, the surface area increased slightly up to 400 ^oC before a rapid increase was noted from 400 ^oC to 450 ^oC. This result implies that the as-synthesised CS_{hydr} material initially contains amorphous material which leads to the Raman data implying a high degree of disorder due to the presence of oligomeric and polymeric by-products produced during CS_{hydr} synthesis. These by-products are Raman active and

contribute towards the degree of disorder in the material. Heating the CS_{hydr} to 400 ^{o}C facilitates decomposition of some of these materials. When the annealing temperature was increased from 400 to 450 ^{o}C the oligomeric and polymeric are decomposed (see Fig. 6.2) resulting in a sharp increase in surface area while the I_D/I_G ratio continues to decrease due to the newly formed charlike compounds [12].

The surface area increase when the temperature is raised from 450 to 600 ^{o}C is proposed to be due to the opening of pore channels, when the newly formed charlike compounds are decomposed (see Fig. 6.2). From 600 to 800 ^{o}C most of the pore channels have been opened resulting in a slight increase in surface area. Raman spectra analysis of I_D/I_G ratios from 450 to 800 ^{o}C confirms decomposition of the volatile by products formed during CS_{hydr} synthesis and these results completely agree with the TGA results (Fig. 6.2)

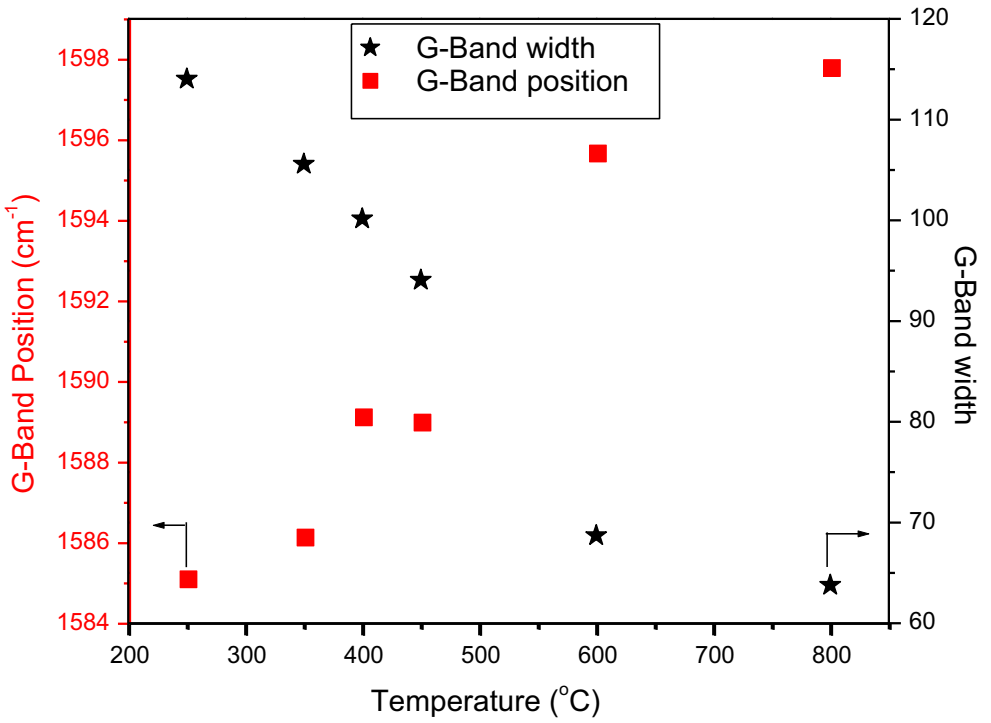


Figure 6.7: Effect of annealing temperature on G-bands

From Fig. 6.7 it can be seen that the G-band position shifts to higher wave-numbers while the G-band width decreases linearly. These results imply that there is a decrease in bond structure disorder with an increase in annealing temperature [18]. The G-band width was observed to decrease with annealing temperature as expected. This is attributed to graphene layers becoming larger with an increase in annealing temperature due to the carbon deposition on these layers as a result of the thermal degradation of the polymeric and oligomeric products; hence a decrease in band width is noted [19]. Graphene layers become larger due to carbon deposition resulting in the thermal degradation of oligomeric and polymeric products. This result also confirms the relationship of the G-band to crystalline components in CS_{hydr}.

The G- and D-bands in the spectra obtained in this study can be computer deconvoluted into five component bands that can be resolved into Gaussian or Lorentzian bands (Fig. 6.8) [12, 16]. These are (i) **D2** due to the disordered sp^2 lattice (ca. 1615 cm^{-1}), (ii) **G** due to the in-plane C=C in an aromatic ring stretching vibrational mode with E_{2g} symmetry (ca. 1598 cm^{-1}), (iii) **D3** due to amorphous carbon (ca. 1545 cm^{-1}), (iv) **D1** due to the A_{1g} symmetry that becomes Raman active to the existence of a disordered sp^2 carbon network and **D4** due to sp^3 bonds or due to C-C and C=C stretching vibrations of polyene like structures (ca.1215 cm^{-1}) [12, 16].

The second-order Raman bands which are found in the spectrum of isolated carbon materials arise from (i) overtone scattering (appear at 2 x 1360 cm^{-1}= 2735cm^{-1}, 2 x 1620 = 3240 cm^{-1}) and (ii) combination scattering (1620 + 830 = 2450 cm^{-1}, 1580 + 1355 = 2935 cm^{-1}). These bands appear due to three dimensional structural ordering. When carbon materials acquire a triperiodic structure a characteristic S band (2700 cm^{-1}) may split into a doublet of G'_1 and G'_2 (2695 and 2735 cm^{-1} respectively) bands [12, 17].

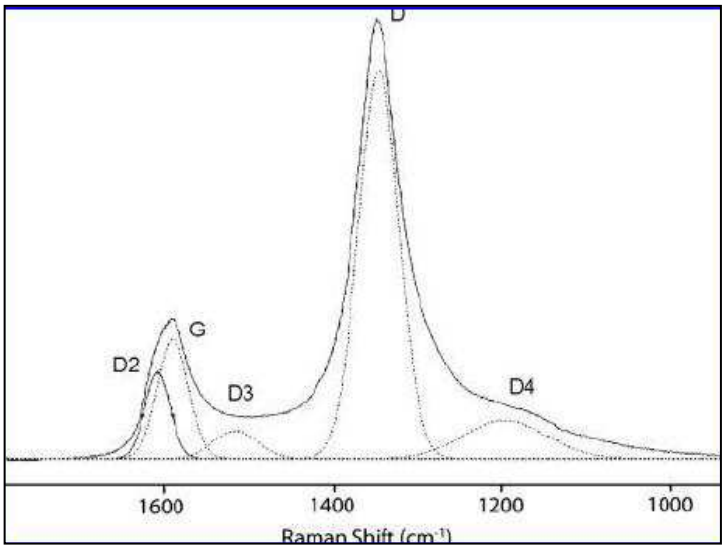


Figure 6.8: Example of computer deconvoluted G and D bands [12].

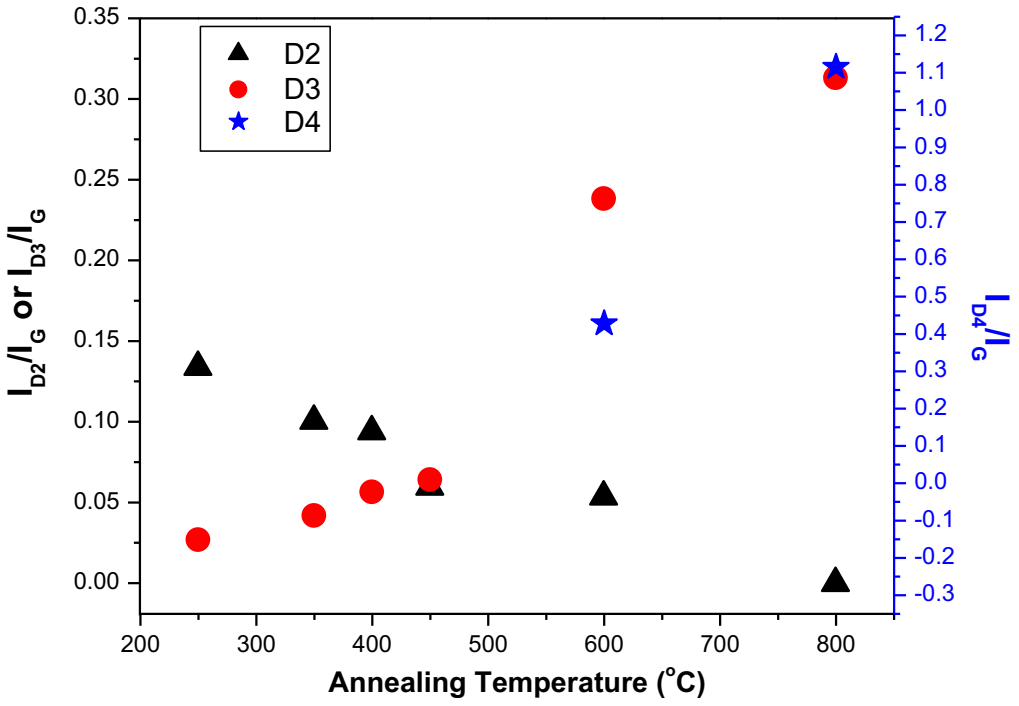


Figure 6.9: Effect of annealing temperature on I_{Di}/I_G-bands

The I_{D3}/I_G ratio also increases monotonically with an increase in annealing temperature from 250 to 800 ^oC (Fig. 6.9), indicating an increase in amorphous

carbon content compared to graphitic carbon. This is a result of C formation from the thermal degradation of polymeric and oligomeric products. The I_{D2}/I_G ratio decreased with an increase in annealing temperature suggesting a decrease in the ratio of the disordered sp^2 lattice compared to the ordered carbon network. This decrease occurs at the expense of an increase in sp^3 bonds or C-C and C=C stretching vibrations of polyene like structures as shown by the appearance of the D_4-band at 600 °C and higher temperatures [12]. An increase in the I_{D4}/I_G ratio from 600 to 800 °C is also observed.

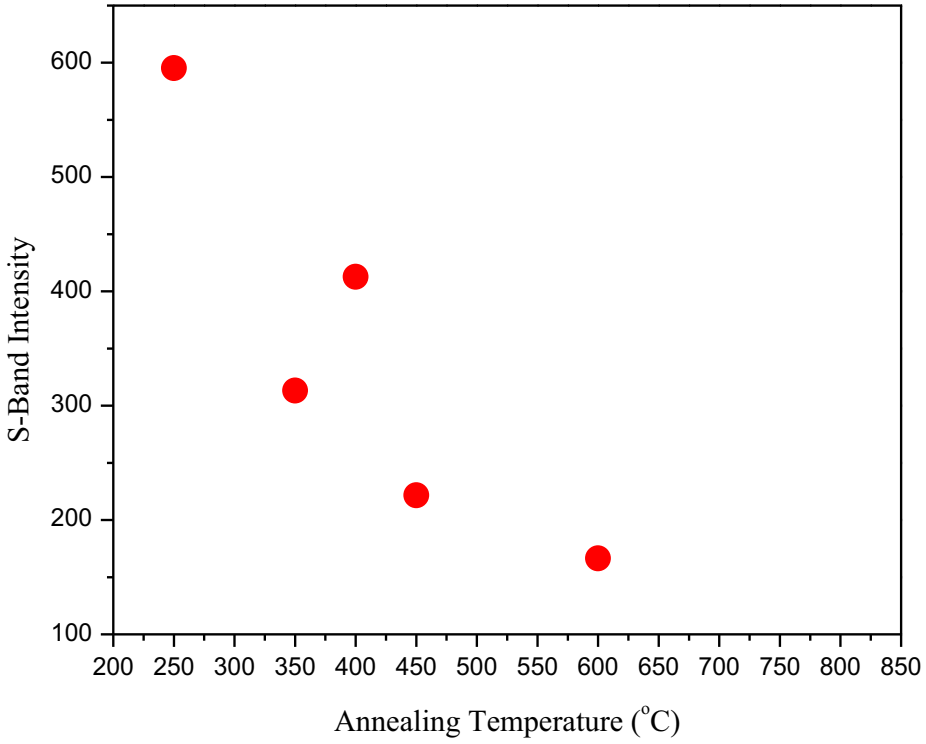


Figure 6.10: Effect of annealing temperature on S-bands

The S-band ($2700cm^{-1}$) in the second-order Raman band arises as a result of isolated carbon materials [12]. The presence of this band in the as-synthesised CS_{hydr} (Fig. 6.10) implies that these materials have a three dimensional ordering before annealing. Increasing the annealing temperature from 250 to 800 °C results in a decrease in the S-band intensity due to a loss in the three dimensional

ordering of the CS_{hydr}. An increase in S-band intensity at 400 ^{o}C was due to the formation of the black aerated charlike compounds from the oligomeric and polymeric compounds present after CS_{hydr} materials synthesis revealed by TGA studies (Fig. 6.2). Detailed studies of this reaction can be found in [10-11]. Annealing the CS_{hydr} materials at 450 ^{o}C decomposes some of the formed charlike compounds. These compounds are further decomposed by increasing the annealing temperature to 600 ^{o}C. Annealing the CS_{hydr} completely removes all volatile compounds as shown by the absence of the S-band. These results agree well with an increase observed in the I_{D3}/I_G ratios (Fig. 6.9) [17].

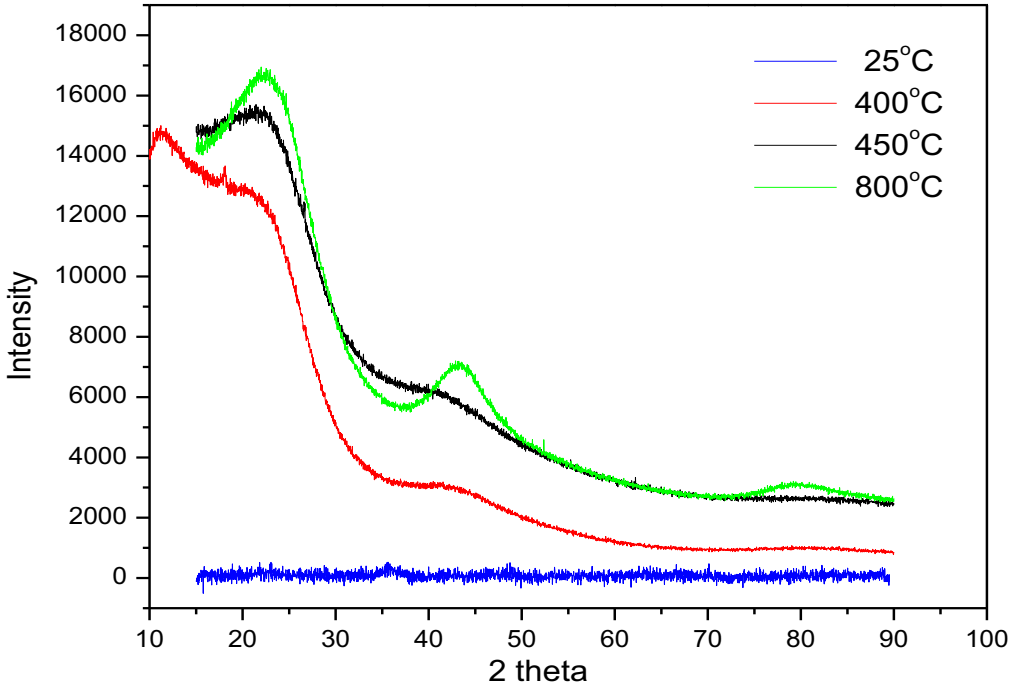


Figure 6.11: XRD patterns of annealed CS_{hydr}

In addition to the Raman data, XRD was also used to analyse the structures of the annealed CS_{hydr}. The results of the XRD analysis of the as-synthesised and annealed CS_{hydr} are presented in Fig. 6.11. The XRD patterns show that the structure of the as-synthesised CS_{hydr} are completely amorphous as shown by data

recorded at 25 ^{o}C, Fig. 6.11 [20-21]. For carbon materials, the degree of developed graphitic structure is inversely proportional to the interlayer spacing but proportional to the crystallite size [22]. The typical appearance of the two carbon peaks at 2Θ values of 26.2° and 43.8°, characteristic of (002) and (100) planes, were found in the XRD patterns of the 400 ^{o}C and 450 ^{o}C (Fig. 6.11) [23]. This suggests a degree of graphitization of the CS_{hydr} samples is enhanced by heat treatment. These results are in complete agreement with results obtained from Raman spectroscopy (Fig. 6.7) and TGA studies (Fig. 6.2). The diffraction intensity of the (002) peak (Fig. 6.11) increased with annealing temperature. Further, the (002) peaks of the annealed CS_{hydr} are located at 26.2°, a value which is larger than that of CS (Fig. 5.7), implying a decreased interlayer spacing $d_{(002)}$ when compared with materials produced in the horizontal furnace [24]. The intensities of the (100) peak also increased with annealing temperature of CS_{hydr}, and these results show improved in-plane and interlayer graphitic structure [22] after annealing up to 800^{o}C.

Seemingly, discrepancies between Raman and XRD are noted when the samples are annealed from 450 ^{o}C to 600 ^{o}C, XRD results show an increase in graphitisation (Fig. 6.11) while a comparison of the intensity of the D and G band from Raman spectra shows an increase in amorphous carbon (Fig. 6.6). This is due to the presence of charlike compounds formed during the annealing of CS_{hydr} materials, these materials are Raman active but do not diffract X-rays.

6.2 Cobalt supported on CS_{hydr} Fischer-Tropsch catalysts.

6.2.1 Results and Discussion

CS_{hydr} annealed at 250 ^{o}C, 450 ^{o}C and 600 ^{o}C temperatures were selected to be used as supports for Co FT catalysts for the following reasons:-

(i) From 250 ^{o}C to 450 ^{o}C: to investigate the effect of decomposing oligomeric and polymeric compounds but in the presence of black aerated charlike compounds on the CS_{hydr}.

(ii) From 450 ^{o}C to 600 ^{o}C: to investigate the effect of removing the black aerated charlike compounds on the CS_{hydr} (Fig. 6.2)

The 5 % Co loaded catalysts are coded $Co250CS_{hydr}$, $Co450CS_{hydr}$ and $Co600CS_{hydr}$ for the 250, 450 and 600 ^{o}C annealed CS_{hydr} supports.

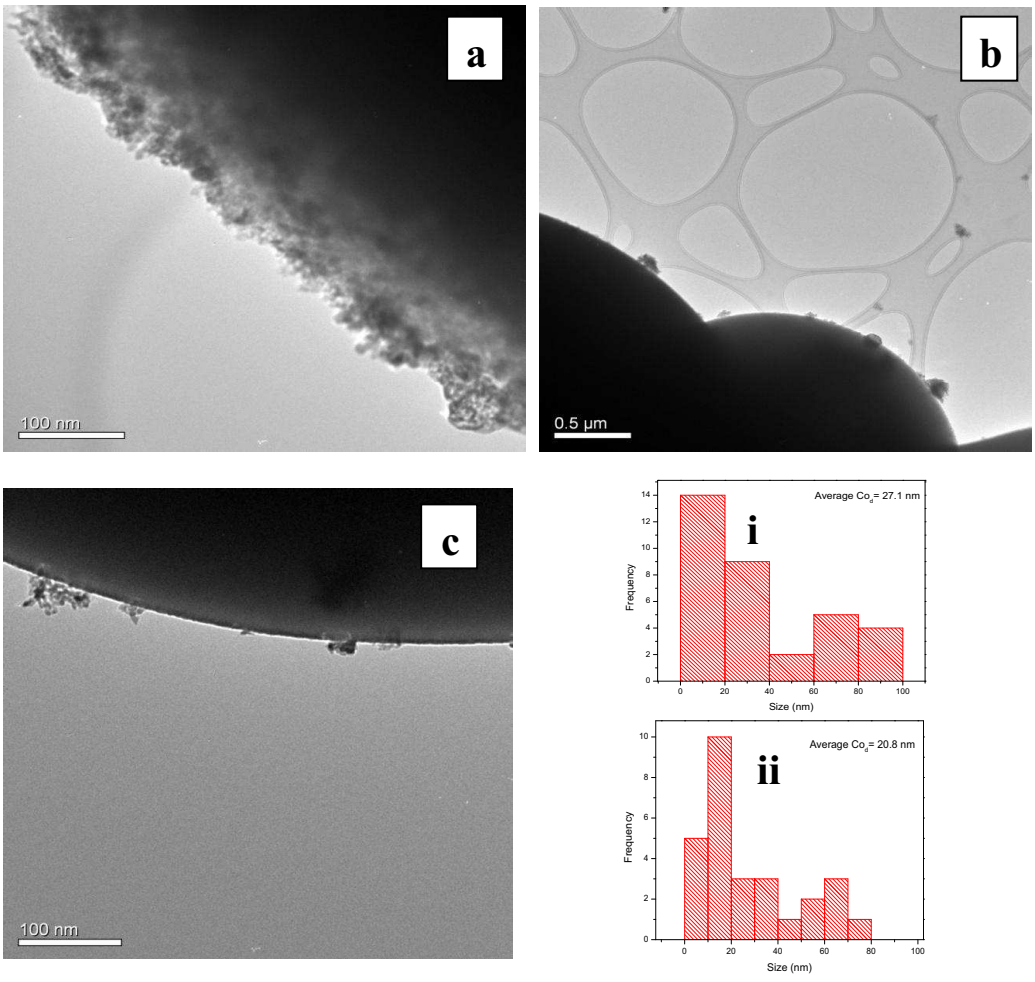


Figure 6.12: TEM images of (a) $Co250CS_{hydr}$, (b) $Co450CS_{hydr}$ and (c) $Co600CS_{hydr}$ and Co particle size distribution of (i) $Co450CS_{hydr}$ and (ii) $Co600CS_{hydr}$ catalysts.

Co particles in the $Co250CS_{hydr}$ catalyst (Fig. 6.12a) could not be detected.TEM studies on $Co450CS_{hydr}$ (Fig. 6.12b) showed dispersed cobalt particles deposited on the $450CS_{hydr}$ support. Although it is well known that oxygen functionalities are decomposed at 300-350 ^{o}C (Chapter 4), most of these functional groups are replaced when the CS_{hydr} are re-exposed to air. This then suggests that Co dispersion on CS_{hydr} and particles size was largely dependent on support surface area. $Co450CS_{hydr}$ and $Co600CS_{hydr}$ (Fig. 6.12 b and c respectively) catalysts showed similar Co particle size distributions.

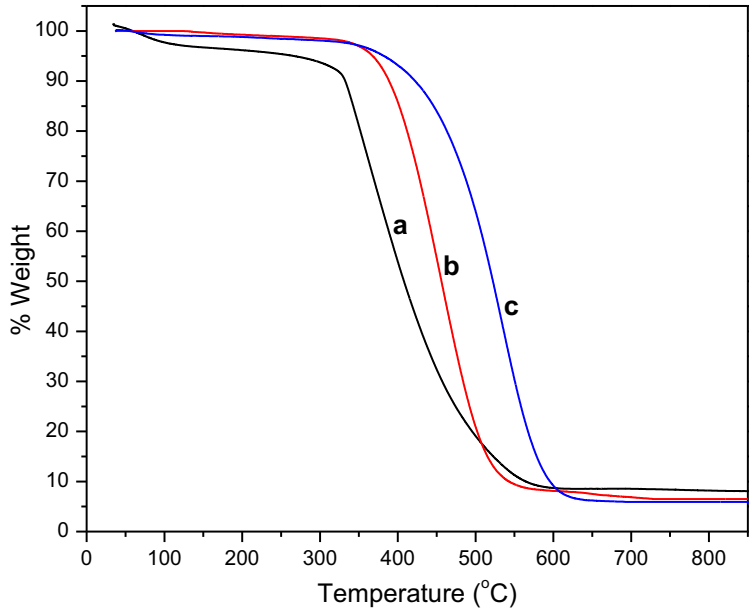


Figure 6.13: TGA profiles of (a) $Co250CS_{hydr}$, (b) $Co450CS_{hydr}$ and (c) $Co600CS_{hydr}$ catalysts

TGA profiles of the catalysts (Fig. 6.13) confirmed the amount of Co metal present in the catalysts. The $Co600CS_{hydr}$ catalyst is the most thermally stable catalyst because of the high annealing temperatures used compared to the other catalysts. From the TGA profiles one can calculate approximately 5.7, 5.3 and 5.2 % Co metal loading for $Co250CS_{hydr}$, $Co450CS_{hydr}$ and $Co600CS_{hydr}$ catalysts respectively, assuming that the ash obtained from TGA is entirely Co_3O_4.

Table 6.1: N_2-physisorption results of the prepared catalysts

Sample	Support surface area m^2/g	Catalyst surface area m^2/g
$Co250CS_{hydr}$	2.1	5.6
$Co450CS_{hydr}$	292.2	301.7
$Co600CS_{hydr}$	423.0	431.4

The surface area of $Co250CS_{hydr}$ catalysts increase slightly when Co was deposited on the support material. A larger increase between the catalyst and the support surface area was noted when Co was deposited on $450CS_{hydr}$ and $600CS_{hydr}$ support materials. The difference in surface area between the catalyst and support was largely affected by Co metal particle size of the catalysts. An increase in surface area in the $Co450CS_{hydr}$ and $Co600CS_{hydr}$ catalysts suggests that most Co particles were deposited on the surface of the support materials rather than within the pores. These results agree with TEM results (Fig. 11). The Co particles on the surface of the support could be seen from TEM images.

The synthesised catalysts were evaluated for FT activity and selectivity. All FT experiments were carried out at 220 ^oC, 8 bar and GHSV 1800 h^{-1}. The instrumentation setup has been detailed in Chapter 3. The effect of annealing temperature on the support material affected the catalytic properties of the Co/CS_{hydr} catalyst (Table 6.2). The chain growth probability (α-value) of each catalyst was determined from the slope of the plot log W_n/N vs N (Fig. 6.14). The $Co250CS_{hydr}$ catalyst showed the lowest % CO conversion due to the presence of large Co metal deposits on the support material. This catalyst also showed the highest selectivity towards C_1 and the lowest C_{5+} selectivity due to the presence of the large metal particle sizes. Although the support material was annealed at a temperature higher than the FTS operation conditions, C_1 selectivity could have also been contributed to by the decomposition of the volatile compounds present in the support material (see Fig. 6.2).

Table 6.2: Summary of FTS catalytic performance of cobalt supported catalyst

Catalyst	% CO Conversion	Activity (µmol/sec.g_{Co})	% Mol selectivity				[a]α-value
			C_1	C_2 - C_4	C_{5+}	CO_2	
$Co250CS_{hydr}$	9.8	17.4	37.8	33.3	27.6	1.3	0.48
$Co450CS_{hydr}$	18.7	32.1	30.8	25.6	44.0	1.6	0.64
$Co600CS_{hydr}$	23.1	39.7	25.9	19.7	53.6	0.9	0.75

[a]-determined from ASF plot (Fig. 6.13)

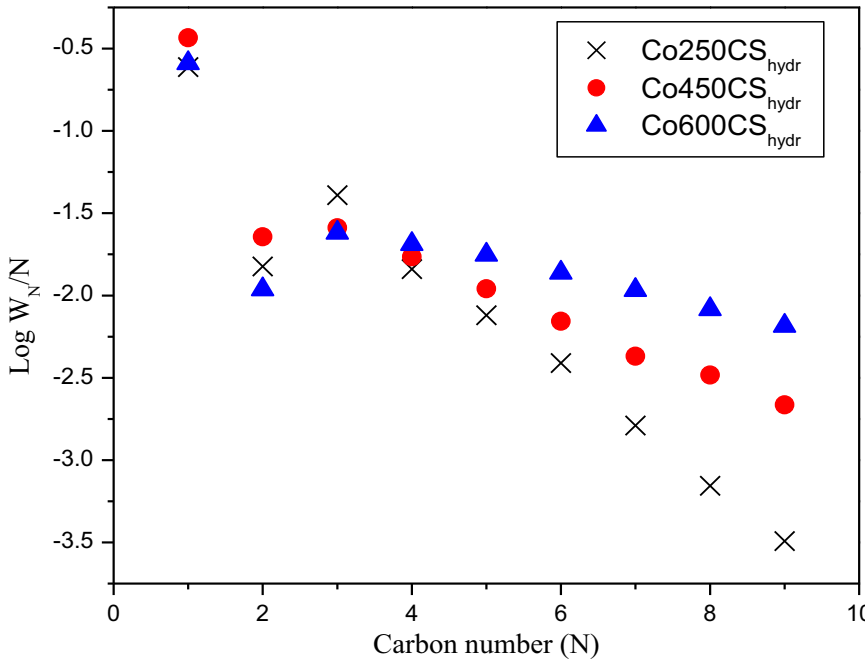


Figure 6.14: ASF plot of Co/CS_{hydr} catalysts

The $Co450CS_{hydr}$ catalyst showed a higher % CO conversion than the $Co250CS_{hydr}$ catalyst, but lower than the $Co600CS_{hydr}$ catalysts. The fresh $Co450CS_{hydr}$ catalyst contained black aerated charlike compounds which were absent from the $Co600CS_{hydr}$ catalyst. It is thought that the presence of these compounds in the $Co450CS_{hydr}$ catalyst could melt under FT reaction conditions

and partially cover the surface of the metal crystallites hence affecting the catalyst activity.

6.3 Conclusions

CS_{hydr} materials were successfully synthesised from a sucrose substrate by a low temperature hydrothermal synthesis method using an autoclave. Even after centrifuging the as-synthesised material with water and ethanol several times, many volatile by-products remain on the CS_{hydr}, which may also be removed by soxlet extraction with toluene. These volatile compounds are completely removable by simply annealing the as-synthesised CS_{hydr} above 450 ^{o}C in N_2 gas, shown by a constant surface area when CS_{hydr} are annealed between 600 and 800 ^{o}C. Annealing CS_{hydr} also increases the surface area and changes the chemical properties of these materials. The presence of these volatile by-products affects the catalytic properties of the supported Co particles. It is thought that volatile compounds present in CS_{hydr} may partially cover the surface of the FT active Co particles when they melt under FT operating conditions. However, further characterisation studies need to be conducted to verify this.

A more active FT Co/CS_{hydr} catalyst was produced when all volatile by-products, produced during CS_{hydr} synthesis were completely decomposed by annealing the CS_{hydr} at 600 ^{o}C in N_2 gas.

References

1. A.A. Deshmukh, S.D. Mhlanga, N.J. Coville, Mater. Sci. Eng. R 70 (2010) 1.
2. C.H. Bartholomew, Catal. Rev. Sci. 16 (1982) 67.
3. N.M. Rodriguez, J. Mater. Sci. 8 (1993) 3233.
4. H.T. Wang, B.A. Holmberg and Y.S. Yan, J. Am. Chem. Soc. 125 (2003) 9928.
5. Y.N. Xia, B. Gates, Y.D. Yin and Y. Lu, Adv. Mater. 12 (2000) 693.
6. F. Caruso, Top. Curr. Chem. 227 (2003) 145.
7. M. Endo, C. Kim, K. Nishimura, T. Fujimo and K. Miyashita, Carbon 38 (2000) 183.
8. Q. Wang, H. Li, L.Q. Chen and X.J. Huang, Solid State Ionics 152 (2002) 43
9. S. Tang, Y. Tang, S.Vongehr, X. Zhao and X. Meng. Appl. Surf. Sci. 255 (2009) 6011.
10. G. Eggleston, B.J Trask-Morrell and J.R Vercellotti, J. Agric. Food Chem. 44 (1996) 3319.
11. G.N Richards and F. Shafizadeh, Aust. J. Chem. 31 (1978) 1825
12. G. P. Marshall, H.G.M. Edwards and J. Jehlicka, Astrobiology 10 (2010) 230.
13. M.S. Dresselhaus and G. Dresselhaus, Light scattering in graphite intercalated compounds. In Light scattering in Solids III (1982) 187.
14. F. Tuinstra and J.L. Koenig, J. Chem. Phys. 53 (1970) 1126.
15. T.P. Mernagh, R.P. Cooney and R.A. Johnson, Carbon 22 (1984) 39.
16. A.C. Ferrari and J. Robertson, Phys. Rev. B Condens. Matter Mater. Phys. 61 (2000) 14095.
17. P. Lespade, R. Al-Jishi and M.S. Dresselhaus, Carbon 5 (1982) 427.
18. M. Neuhaeuser, H. Hilgers, P. Joeris, R. White, J. Windeln, Diamond Relat. Mater. 9 (2000) 1500.
19. Z. Ni, Y. Wang, T. Yu, and Zexiang Shen, Nano. Res. 1 (2008) 273.
20. M. Kang, Y. Bae and C. Lee, Carbon 43 (2005) 1512.
21. L. Ci, H. Zhu, B. Wei, C. Xu, D. Wu, Appl. Surf. Sci. 205 (2003) 39.

22. Q. Gong, Z. Li, Y. Wang, B. Wu, Z. Zhang, Ji Liang, Mater. Res. Bull. 42 (2007) 474.
23. H. Pang, X. Wang, G. Zhang, H. Chen, G. Lv, S. Yang, Appl. Surf. Sci. 256 (2010) 6403.
24. Y.Z. Jin, Y.J. Kim, C. Gao, Y.Q. Zhu, A. Huczko, M. Endo, H.W. Kroto, Carbon 44 (2006) 724.

Chapter 7

Preparation and characterisation of iron supported on N-doped carbon spheres (Fe/NCSs) as Fischer-Tropsch catalysts

7.1. Introduction

Gas-to-liquid (GTL) and coal-to-liquid (CTL) technologies have become increasingly important in the future of synthetic fuels, as crude oil reserves have been estimated to be decreasing at a rate of 4.07 % per year from the current producing fields [1].

The Fischer-Tropsch (FT) process first discovered in 1923 is a proven alternative technology for the production of liquid fuels and chemicals from non-petroleum feed stocks [2-3]. This process produces a wide range of hydrocarbons and oxygenates over a metal catalyst. Co and Fe metals are the industrially preferred catalysts because of their cost and availability [4].

Supported FT catalysts have numerous advantages over bulk catalysts in that they possess high active metal surface areas and have a lower cost of production. Co or Fe particles may be supported on materials such as TiO_2, MgO_2, Al_2O_3, C etc. Carbon nano-materials are reported in the literature to constitute a set of versatile materials with valuable chemical and physical properties not attainable with metal oxides [5-6]. Carbon spheres (CS) prepared from a non-catalytic synthesis method have a higher purity than the much researched carbon nanotubes (CNTs) and

carbon nanofibers (CNFs). Although similarities are expected when CNTs, CNFs or CSs are used, CSs have advantages over CNTs for their application as catalysts supports for the same reasons.

Functional groups on CSs play pivotal roles in the preparation of carbon supported catalysts, by altering the acid-base and hydrophilic character of the carbon surface [7-9]. Many research studies have focused on the effects of oxygen containing functional groups on Co [10-11] or Fe [12-14] metal precursor particle size and dispersion, amongst other metals studied. Little research work has been reported on the applications of nitrogen doped carbons especially nitrogen doped carbon spheres (NCSs).

Nitrogen functionalities may occur as pyridinic, pyrrolic or quartenary groups [15] and their presence can be determined by X-ray photoelectron microscopy (XPS) analysis. Nitrogen functional groups are introduced to a carbon matrix either from a liquid or gaseous nitrogen source, these may include urea, melamine, acetonitrile, ammonia etc [16]. The presence of nitrogen functionalities affects the polarity of the surface of the carbon material [16-18]. Pyrolle and pyridine nitrogen groups are basic in nature and hence their heterogeneity on carbon surfaces may determine the basic or acidic nature of the carbon surface [19].

The effect of nitrogen functionalities on carbon supports largely depends on their application. Recently, we reported our studies on the auto-reduction of cobalt oxide phases by NCSs, these studies also showed that NCSs are potentially good metal supports for FT, with advantages over conventional metal oxide supports in that the metal precursor is easily characterised by microscopic techniques such as TEM [20].

Active Fe/C catalysts prepared by pre-nitriding the carbon support have been reported in the literature [21]. Matter et al. [22] reported the presence of highly active Fe/C catalysts for use in the oxygen reduction reaction. These catalysts

were reported to contain large amounts pyridinic nitrogen groups. In other recent studies, Fe/N-CNTs catalysts prepared from post doped CNTs were investigated for FT activity, the results showed that post-doping CNTs gives poor FT catalysts with a broad Fe particle size range. However, more active catalysts were obtained by doping the CNTs during their synthesis [23].

The synthesis method used to prepare NCSs may give different physical and chemical properties of the carbon materials prepared. For example the reagent used as a carbon source may affect the reactivity of the carbon matrix formed and hence the type of nitrogen functional groups attached to the carbon framework. In addition, the reaction temperature used may also affect the surface chemistry of NCSs owing to the fact that some nitrogen functional groups are not stable at high temperatures.

In this chapter, we investigate the effect of chemical and physical properties of NCSs induced by different synthesis methods on the activity and selectivity of NCS supported Fe FT catalysts. The NCSs were synthesised by three different methods; (i) a vertical furnace CVD method, which employed short reaction times (30 min) at 900 ^{o}C, giving smaller NCSs, (ii) a horizontal furnace CVD method, which employs longer reactions times (60 min) at 950 ^{o}C, giving larger spheres. In both these methods acetylene gas was used as a carbon source and acetonitrile as a nitrogen source. (iii) a hydrothermal method in an autoclave using sucrose as a carbon source and urea as a nitrogen source. In this method NCSs are produced for 4 h at 190 ^{o}C giving even larger NCSs compared to those produced by a CVD method. The synthesis methods employed allowed us to investigate the effect of preparation conditions on the chemical properties of NCSs. Furthermore, the effect of these chemical properties and the size of NCSs on Fe/NCSs FT activity and selectivity are investigated.

7.2. Experimental

7.2.1 Synthesis of N-doped CSs

(a) Synthesis of N-doped carbon spheres by a chemical vapour deposition method in a vertically aligned furnace

NCSs were prepared by decomposing CH_3CN and C_2H_2 in a vertically aligned quartz tubular reactor in the absence of a catalyst. The mid section of the reactor was placed in a furnace and the base connected to a 500 mL round bottom flask to collect the synthesised material. The furnace was heated to 900 °C at 10 °C/min under flowing Ar gas. Once the desired temperature was reached, Ar (300 mL/min) and C_2H_2 (200 mL/min) gases were simultaneously bubbled through CH_3CN (80 °C) before being passed through the reactor for 30 min. After 30 min the gas flow was shut off and the furnace was allowed to cool down to room temperature under Ar (40 mL/min). Approximately 1.5 g of black soot was collected and heated under nitrogen at 300 ^oC to remove excess PAHs. The as-synthesised materials will be referred to as NCS_{ver} .

(b) Synthesis of N-doped carbon spheres by chemical vapour deposition method in a horizontally aligned furnace

NCSs were prepared by a chemical vapour deposition method in a horizontally aligned quartz tubular reactor [9]. The experiment was carried out at atmospheric pressure in a 19 mm internal diameter and 510 mm length reactor. The reactor was placed horizontally into a furnace. The front end of the tube was connected to a glass manifold which allowed for the free flow of acetylene and nitrogen gases into the reactor. The rear end of the tube was connected to an exhaust pipe. The furnace temperature was raised to 950 ^oC at a heating rate of 10 ^oC/min while the N_2 gas was allowed to flow at 60 mL/min. When the furnace temperature reached 950 ^oC the N_2 gas flow was switched to acetylene gas at a flow rate of 100 mL/min. Acetylene gas was first bubbled through a warm acetonitrile solution

(kept at 80 ^{o}C) before entering the reactor. The carbonization was allowed to continue for 1 h before the acetylene gas flow was disconnected and nitrogen gas was allowed to pass through the furnace as it was cooled to room temperature. After this, the system was cooled to room temperature and the carbon materials produced were scraped out of the reactor using a spatula; approximately 2 g of material was collected. The as-synthesised materials will be referred to as NCS_{hor}.

(c) Hydrothermal synthesis of N-doped carbon spheres

NCSs were synthesized by a hydrothermal synthesis procedure using a solution containing 0.9 moles sucrose and 0.1 moles urea. The aqueous mixture was placed in a teflon cup (90 % filled) with a total volume of 58 mL and then placed into a 60 mL stainless steel autoclave which was heated to 190 ^{o}C. The reaction was allowed to proceed for 4 h once at 190 ^{o}C. The autoclave was then allowed to cool to room temperature and the suspension was centrifuged 5 times using water and 5 times using ethanol at 5000 rpm for 10 min each, i.e. a total of 100 mins. The products were then dried in an oven at 70 ^{o}C overnight. The product is referred to as NCS_{hydr}. Approximately 3 g of product was collected.

7.2.2 Fe metal loading on N-doped CSs

A deposition-precipitation method (DPU) using urea was used to load 5% Fe onto the surface of the N-doped carbon spheres. In this method, $Fe(NO_3)_2.6H_2O$ (3.605 g) and urea (0.805 g; 1.5 moles urea per mole of iron) were dissolved in de-ionised water (18 mL) and added to 10 g of a CS support at room temperature. After allowing at least 2 h for the hydrolysis of the urea at 90 ^{o}C, the sample was dried under vacuum at 90 °C for 40 minutes.

7.2.3 Characterisation of NCS and 5 % Fe/NCS catalysts

BET

The surface area, pore volume, and average pore diameter of the CSs were measured on an ASAP-2000 Tristar analyser from Micromeritics. Approximately 0.2 g of sample was degassed in N_2 at 393 K for 12 h prior to analysis using a Micromeritics flow Prep 060, sample degas system.

TGA

A Perkin Elmer TG/DTA Thermogravimetric analyzer was used to measure weight changes of samples heated in air at a constant heating rate of 10 °C/min. The sample mass used was varied between 0.01 and 0.02 g.

CHN elemental analysis

The nitrogen content in NCSs was determined by CHN elemental analysis using a Carlo Erba NA1500 analyzer (Agricultural Research Council, Pretoria).

TEM

A JEM 100s and a FEI Tecnai G^2 Spirit were used for transmission electron microscopy studies. All samples were ultrasonically suspended in ethanol and a drop of the suspension was transferred to a copper grid and allowed to dry before analysis.

Raman spectroscopy

Raman spectroscopy measurements were carried out using a micro-Raman attachment of a Jobin-Yvon T64000 Raman spectrometer. The spot size on the sample was ~1.5 μm in diameter and the excitation wavelength was 514.5 nm from an Ar ion laser. A grating with 600 grooves/mm was used to disperse the spectrum onto a charge coupled detector (CCD).

XPS

X-ray photoelectron spectroscopy (XPS) (Physical Electronics Quantum 2000, Al K-Alpha spectrometer) was used to investigate the surface nitrogen functional groups and the elemental compositions of NCSs. Analysis were performed at the CSIR, Pretoria.

7.2.4 Catalysts evaluation in FTS

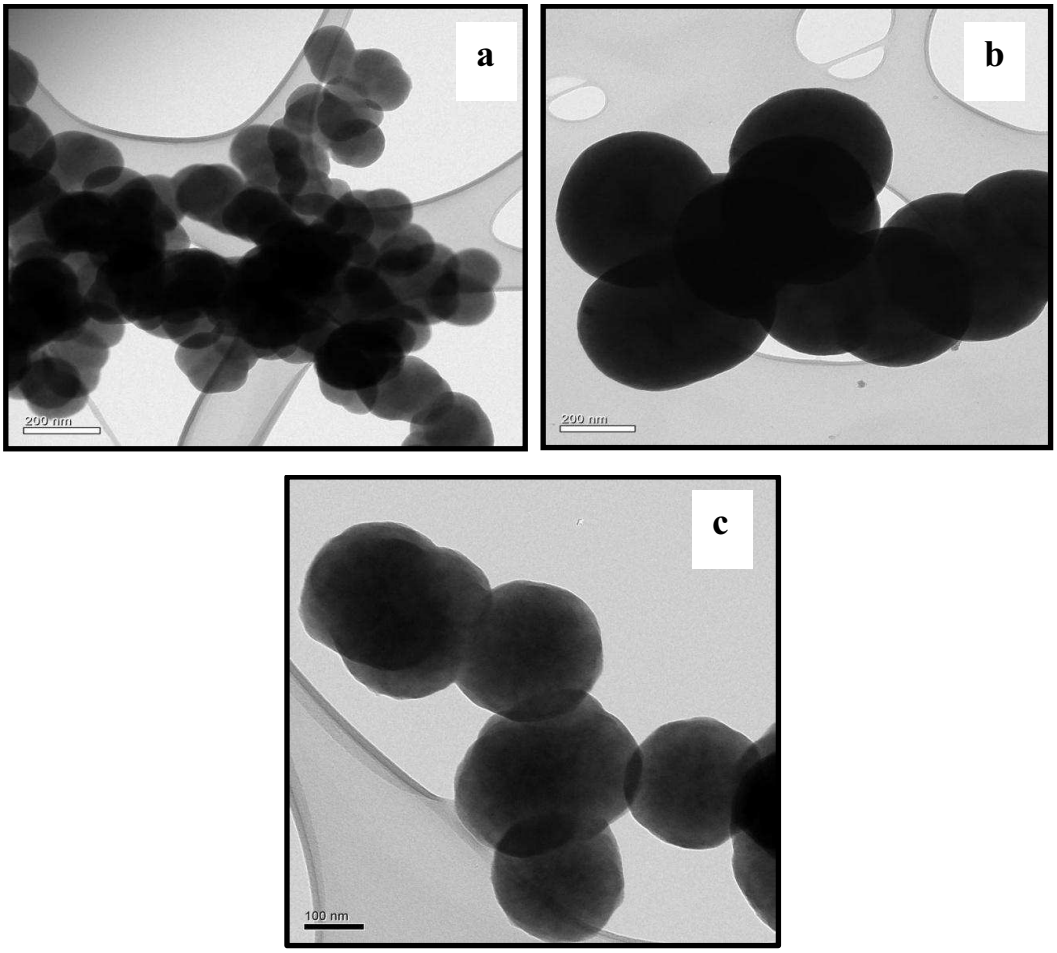
FT synthesis was carried out in a fixed bed reactor (FBR) with an internal diameter of 50 mm, height 250 mm and was filled with 2 mm (diameter) stainless steel balls above a sieve with a mesh size of 0.16 mm. The catalyst (0.5 g) was reduced at 350 ^{o}C and 1 bar pressure for 18 h under 100 % H_2 gas before carrying out FTS. The FTS results were collected at 275 ^{o}C, 8 bar pressure and a GHSV 2700 h^{-1} at steady state conditions. The FBR was connected to two on-line GCs, one with a flame ionization detector (FID) and the other with a thermal conductivity detector (TCD). A Poropak-Q (PPQ) column was used to separate hydrocarbons from C_1 to C_{10} while a *ZB*-1 capillary column fitted into an offline GC-FID was used to separate C_7 to C_{30} hydrocarbons collected as wax and oil fractions from the hot and cold traps respectively.

Before FT synthesis was carried out, all catalysts were reduced with pure hydrogen (T = 350 ^{o}C, 18 h, 1 bar pressure, flow rate 45 mL/min). After the reduction step the FBR was cooled and the hydrogen gas flow was cut off and replaced with synthesis gas (H_2 : CO ratio of 2, 10 % N_2 as internal standard for mass balance calculations). Two traps were mounted after the reactor; one maintained at T = 150 ^{o}C for wax collection, while the other one was kept at ambient temperature for collecting hydrocarbons and water. At steady-state the knock out pots were emptied and the period of the mass balance calculation commenced [24].

7.3 Results and Discussion

7.3.1 Synthesis of NCSs

NCSs were successfully synthesised in our laboratory in (i) a CVD vertical furnace method at 900 ^{o}C for 30 mins, (ii) a CVD horizontal furnace method at 950 ^{o}C 1 h and (iii) a hydrothermal autoclave synthesis method at 190 ^{o}C for 4 h as outlined in the experimental section. TEM studies (Fig. 7.1) on the synthesised NCS materials showed that the synthesised materials were all solid carbon spheres.



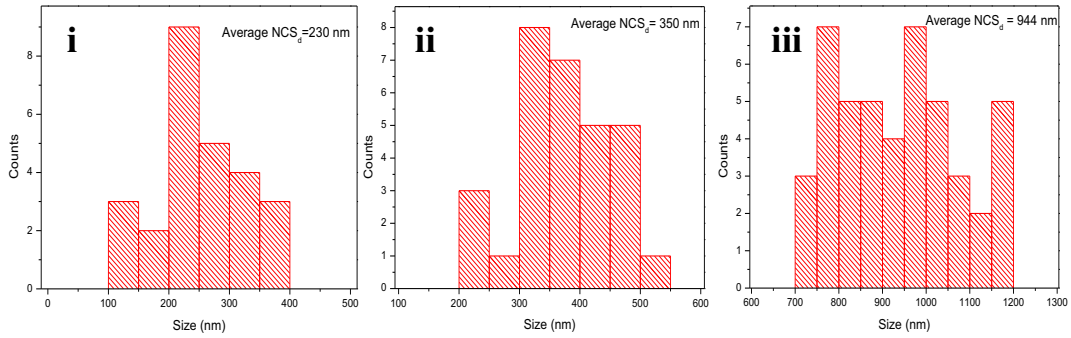


Figure 7.1: TEM images of (a) NCS_{ver} (b)NCS_{hor} and (c) NCS_{hydr} and size distribution of (i) NCS_{ver} (ii)NCS_{hor} and (iii) NCS_{hydr}

The synthesised NCS particle sizes were in the order NCS_{hydr} > NCS_{hor} > NCS_{ver} as determined by TEM and shown in Table 7.1. The N content determined by CHN elemental analysis was 4.0 % and for NCS_{ver}, 2.4 % for NCS_{hor} and 2.0 % for NCS_{hydr} (Table 7.1). The N content was also determined by XPS and was found to be 3.1, 2.4 and 1.5 % for the NCS_{ver}, NCS_{hor} and NCS_{hydr} respectively.

It can be noted from Table. 7.1 that the nitrogen concentration decreases in the order NCS_{ver}>NCS_{hor}>NCS_{hydr}. The results obtained by XPS showed a slightly lower percentage concentration of N than those obtained from CHN elemental analysis, except for NCS_{hydr} for which it was the same. However, the trends are the same. The difference relates to the two different techniques used. Even though XPS is a surface technique and the values reported correspond to the surface nitrogen and CHN elemental analysis is a bulk technique and the values reported correspond to the total nitrogen contained in the sample, the slight differences found in terms of the values measured imply that there is homogeneous distribution of N groups within each NCS.

Raman spectroscopy results (I_D/I_G) showed that the disorder in the samples decreased in the order NCS_{ver} > NCS_{hor} > NCS_{hydr} (Table. 7.1). This order was largely influenced by carbon sphere residence time in the synthesis step. The

source of the carbon may also have an effect, with sucrose seemingly giving more graphitic spheres than acetylene. This however is an aspect of the method used which yields large amounts of polymeric and oligomeric compounds (see chapter 6).

Table 7.1: Shows NCSs size, N content and degree of graphitisation

Sample	[a] NCSs size (nm)	[b] % N-content	[c] % N-content	[d] I_D/I_G
NCS_{ver}	100-400 nm	4.01	3.1	1.52
NCS_{hor}	200-500 nm	2.40	2.4	1.02
NCS_{hydr}	800-1200 nm	2.01	1.5	0.82

[a]determined by TEM, [b]determined by C, H and N elemental analysis, [c]determined by XPS and [d]determined by Raman spectroscopy.

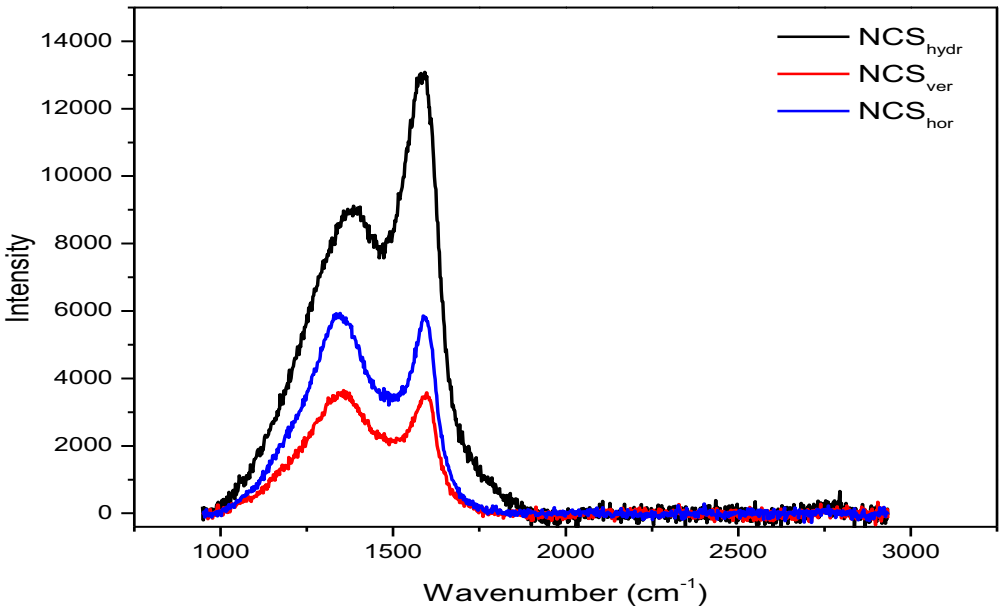


Figure 7.2: Raman spectra of NCSs.

The XPS measurements are presented in more detail in Table. 7.2. In this table the N atomic concentration (of different N types) in the NCSs was estimated from the area ratio of the nitrogen peaks to the sum of carbon and oxygen (and silica). The presence of the Si peak in the NCS_{hor} relates to the method used to scrape the carbon spheres from the quartz reactor. This peak was absent from the NCS_{ver} because these materials drop down from the vertical quartz reactor due to gravity as they are synthesised. High amounts of Si were also noted from the NCS_{hydr} which is suspected to be due to a result of scrapping these materials from the walls of a beaker after drying in the oven. This was not, however, confirmed.

Table 7.2: Summary of the elemental composition as determined by XPS.

Sample	Element	Atomic Concentration (%)	Binding Energy (eV)	Probable Bond(s)/Compound(s)
NCS_{ver}	C	93.3	284.9 (90.3%) 286.6 (8.8%) 288.0 (0.6%) 289.1 (0.3%)	C-C C-O C=O O-C=O
	N	3.1	398.9 (61.7%) 400.7 (38.3%)	N-(C,H,O)
	O	3.6	533.0	O-(C,H,N)
NCS_{hor}	C	91.0	284.9 (88.5%) 286.6 (10,2%) 288.0	C-C C-O C=O O-C=O

			(0.4%) 289.1 (0.9%)	
	N	2.4	398.5 (50%) 400.9 (50%)	N-(C,H,O)
	O	5.9	532.6	O-(C,H,N,Si)
	Si	0.6	102.6	Si-(O,H)
NCS_{hydr}	C	70.5	284.8 (78.0%) 286.5 (16.3%) 287.9 (3.0%) 289.0 (2.7%)	C-C C-O C=O O-C=O
	N	1.5	400.1	N-(C,H,O)
	O	24.3	532.3	O-(C,H,N,Si)
	Si	3.6	102.2	Si-(O,H)

Fig. 7.3 shows the C1s spectra of the NCSs. The C1s peak at 285 eV corresponds to the energy of the sp^2 C-C bond in a C1s spectrum of pyrolytic graphite [25]. In all the three samples the main C1s line is positioned at 284.9 eV +/- 0.1 which confirms the graphitic structure of the NCSs [26].

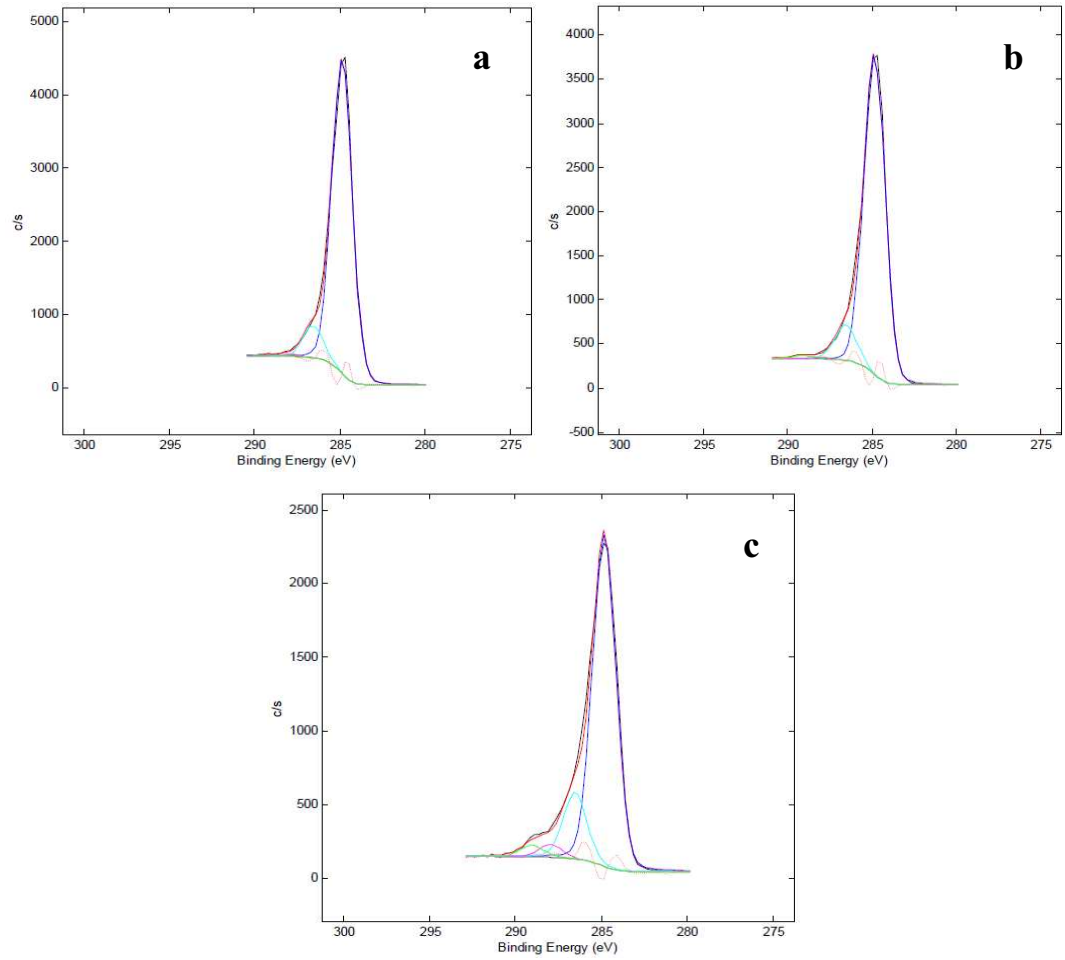


Figure 7.3: C1s spectrum of (a) NCS_{ver} , (b) NCS_{hor} and (c) NCS_{hydr}

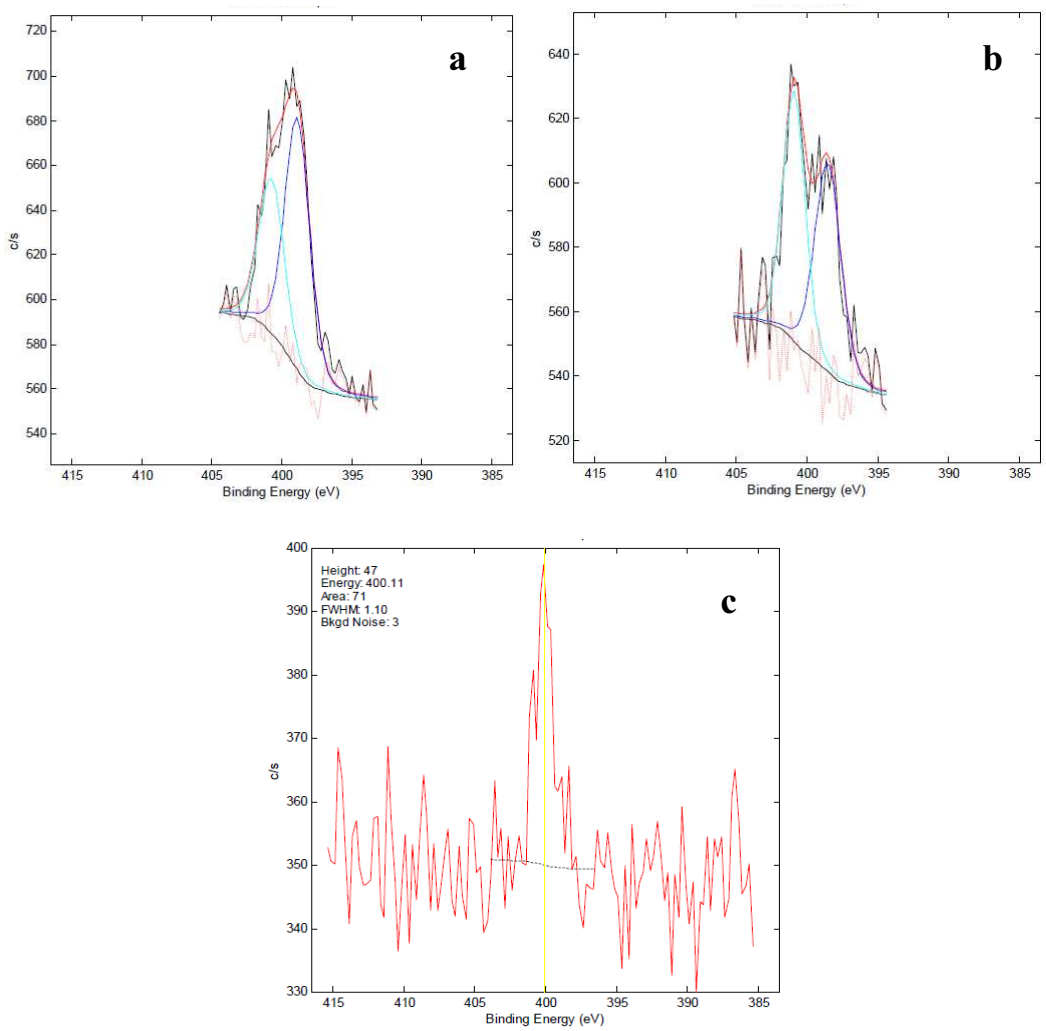


Figure 7.4: N1s spectrum of (a) NCS_{ver} , (b) NCS_{hor} and (c) NCS_{hydr}

The N1s spectra (Fig. 7.4) were de-convoluted to gain an understanding of the type of nitrogen containing functional groups present and details on the chemical bonding configurations of N in the samples. The N1s spectral data of the as-synthesised NCS_{ver}, NCS_{hor} and NCS_{hydr} samples are summarised in Table 7.2. In the N1s spectra the following were detected: (i) pyridinic nitrogen (398.3–399.8 eV) in which N atoms contribute to the *p*-system with one electron, (ii) pyrolic nitrogen (400.1–400.5 eV)) where N atoms contribute to the *p*-system with two electrons such as lactam and pyrrol species and (iii) quaternary nitrogen (401.0–

401.4 eV) including protonated pyridine and substitutional nitrogen where the N replaces a C atom in the graphitic structure [26-29].

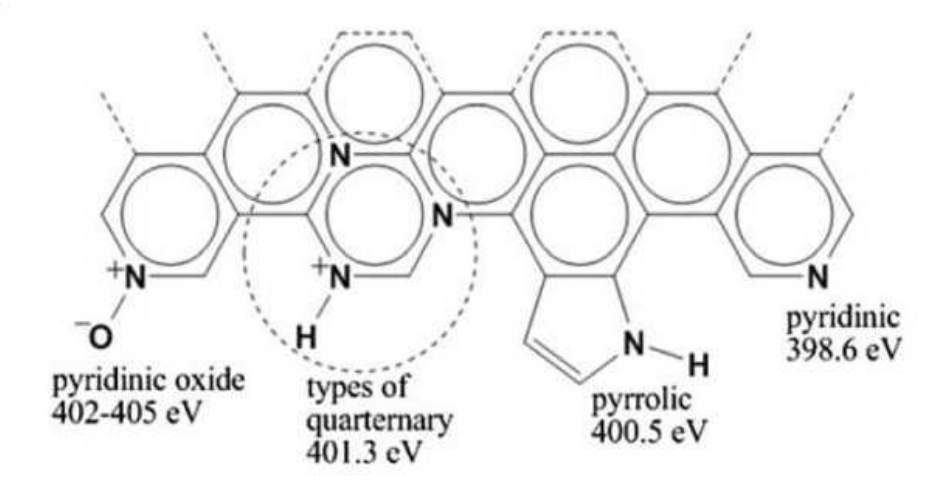


Figure 7.5: nitrogen-based species that and their XPS binding energies [15]

NCS_{ver} with the highest N concentration contained 62 % pyridinic and 3 % pyrolic nitrogen, while the NCS_{hor} sample contained 50 % pyridinic nitrogen and 50 % quaternary nitrogen. NCS_{hydr} contained 100% of pyrolic nitrogen. The oxygen content in the samples was in the order NCS_{hydr}>NCS_{hor}>NCS_{ver}. NCS_{hydr} had a high oxygen concentration (Table 7.2) presumably related to the use of sucrose as the carbon sources in this sample. In the NCS_{hor} and NCS_{ver}, oxygen was absorbed onto the NCS surface when the samples were exposed to air. This has been previously reported in the literature [7-9]. These oxygen and nitrogen containing functional groups may act as metal binding sites on NCS.

TGA profiles were recorded in air and the derivative curves are plotted in Fig. 7.6 (see Fig. 7.9 for TGA curves). For the as prepared NCS_{ver} material there are two negative peaks corresponding to two weight loss steps (Fig. 7.6a). The negative peak at ca. 200 ^{o}C was due to the decomposition of low boiling compounds

believed to be moisture and poly-aromatic hydrocarbons (PAHs). PAHs are formed as a precursor in the formation of carbon flakes which make up the carbon sphere structure [30]. The NCS_{ver} sample has a short residence time during synthesis and hence the final product contains large amounts of PAHs. The second negative peak at ca. 700 ^{o}C is due to the oxidation of NCS_{ver}. PAHs were removed by heating the as-synthesised NCS_{ver} at 220 ^{o}C for 2.5 h under N_2. NCS_{hor} showed only one peak due to the oxidation of the carbon material at ca. 700 ^{o}C (Fig. 7.6b). Fig 7.6c showed three negative peaks for NCS_{hydr}, these peaks were due to (i) the evaporation of moisture at ca. 84 ^{o}C (ii) the decomposition of the numerous oxygen containing functionalities ca. 370 ^{o}C and (iii) the oxidation of NCS_{hydr} at ca. 532 ^{o}C.

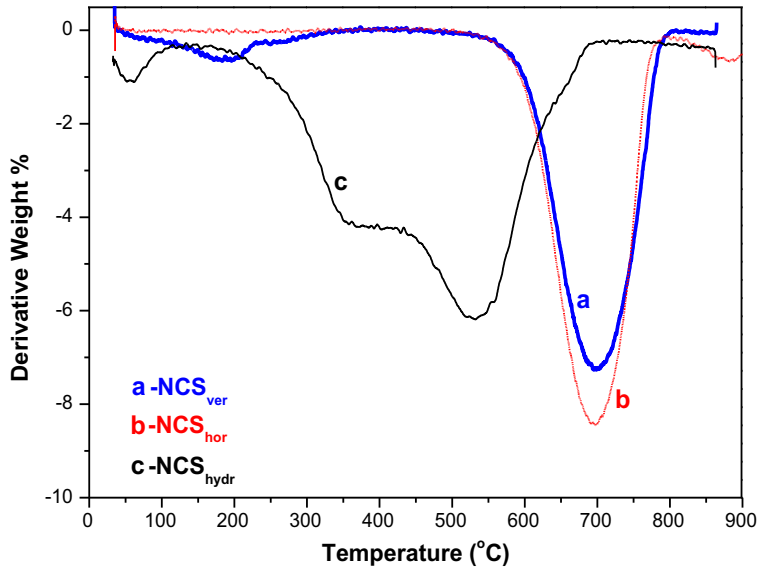


Figure 7.6: TGA profiles of as-synthesised (a) NCS_{ver} (b) NCS_{hor} and (c) NCS_{hydr} run in air

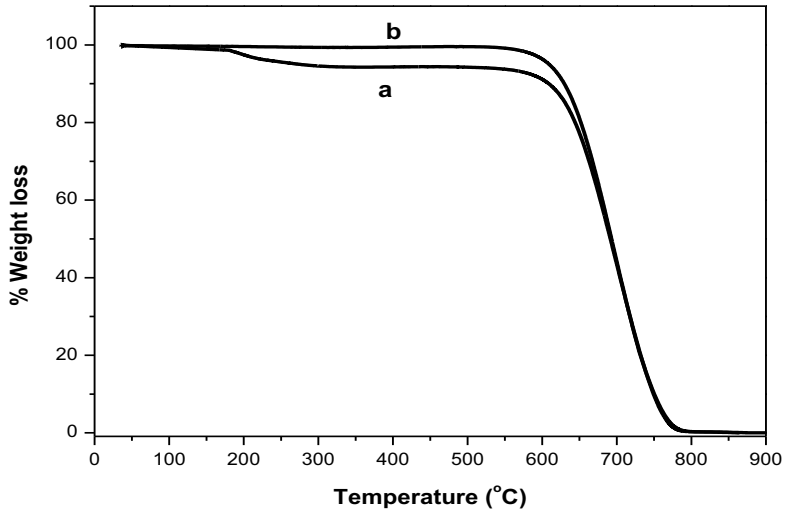


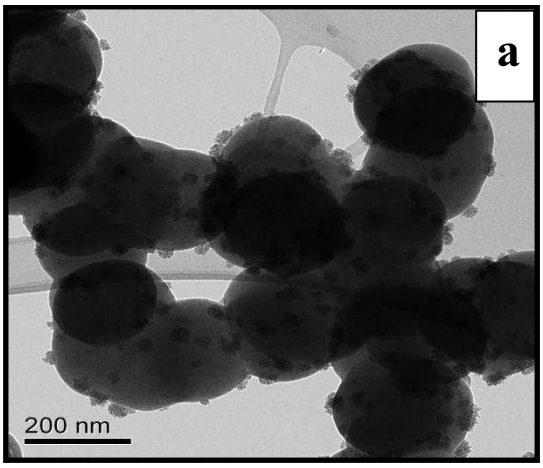
Figure 7.7: TGA profiles of NCS_{ver} (a) before and (b) after annealing at 250 °C for 2 ½ h in N_2 gas.

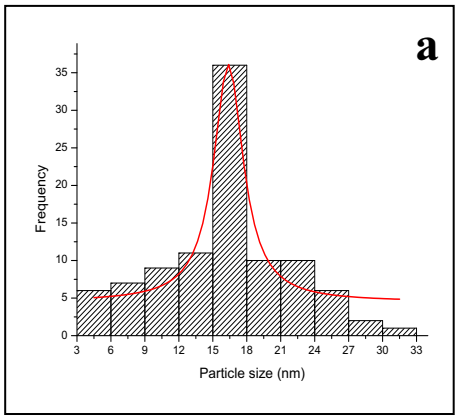
The PAHs were removed by heating the NCS_{ver} at 250 °C for 2.5 h under nitrogen gas. TGA results showed that NCS_{ver} were clean after this heat treatment (Fig. 7.7)

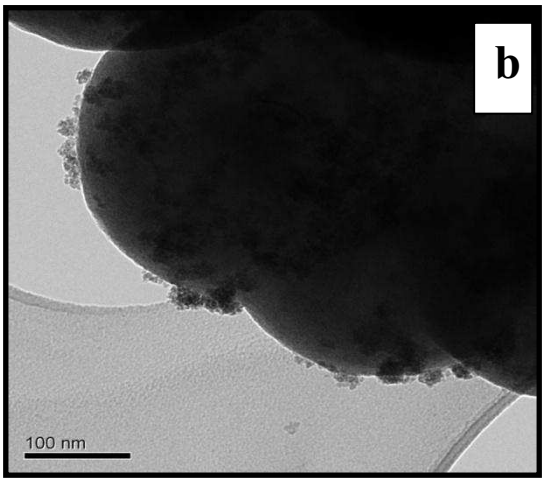
7.3.2 Fe supported on N-doped CSs catalysts

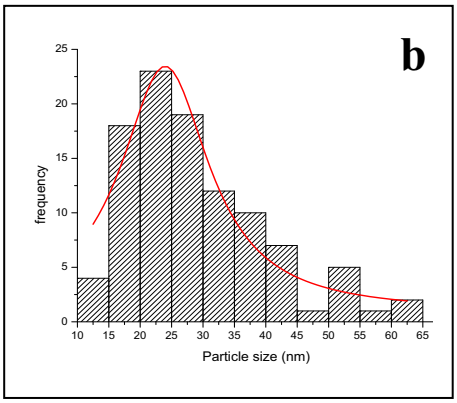
Fe (5 wt %) was added to the NCSs by a deposition-precipitation method. Fig. 7.8 shows the TEM images and particle size distribution of the three Fe supported NCS catalysts. The Fe particles deposited on NCS_{ver} were well dispersed and relatively smaller (average diameter of about 15 nm) compared to those deposited on NCS_{hor} (average diameter of about 25 nm) and NCS_{hydr} (average diameter of about 19 nm) presented in Figs. 7.8a to c respectively. The difference in iron particle size between NCS_{ver} and NCS_{hor} supported catalysts can be accounted for in part by the difference in surface area of the support material (Table. 7.3). NCS_{ver} sample has a surface area of 6.8 m^2/g and NCS_{hor} has a surface area of 4.0 m^2/g (+/- 1 % error), so that NCS_{ver} has a greater surface than NCS_{hor} on which the particles can be deposited.

The degree of carbon graphitisation of the support (Table. 7.1 where the I_D/I_G values for NCS_{ver} > NCS_{hor}), affects the dispersion of surface N containing functional groups on the NCS surface. The surface N content (NCS_{ver} > NCS_{hor} as given in Table 7.1) also presumably provides an explanation as to why the Fe crystallites on NCS_{ver} are smaller. These functionalities act as anchoring sites for Fe particles and their presence affects the dispersion of the Fe precursor particles. NCS_{hydr} contains a surface abundant in carboxylic functionalities (Table. 7.2) [31] in addition to the nitrogen containing functionalities the surface contains numerous sites for iron deposition.









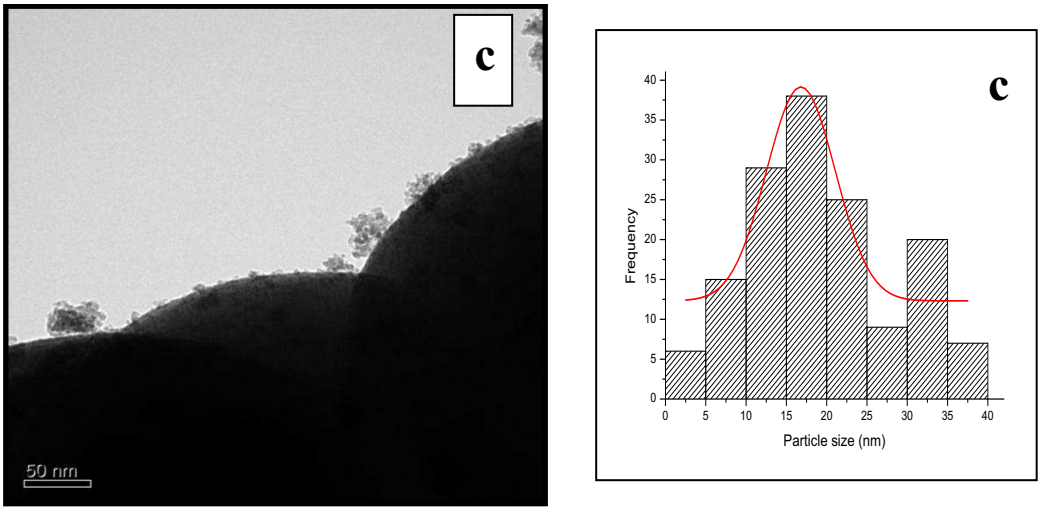


Figure 7.8: TEM images and particle size distribution for 5 % Fe supported on (a) NCS_{ver}, (b) NCS_{hor} and (c) NCS_{hydr}

N_2-physisorption results for all three catalysts (Table. 7.3) gave data that showed an increase in surface area when iron particles were deposited on the NCSs. These results imply that iron particles are deposited on the surface of the NCS.

Table 7.3: Effect of NCSs on the iron oxide crystallite size

Sample	[a] Fe_2O_3 average size	[b] S.A support (m^2/g)	[b] S.A catalyst (m^2/g)	Increase in S.A. when Fe is loaded (m^2/g)
NCS_{ver}	15 nm	6.8	18.2	11.6
NCS_{hor}	26 nm	4.0	8.1	4.1
NCS_{hydr}	18 nm	1.8	7.4	5.6

[a] – determined by TEM, [b]– determined by BET

The difference noted in the surface areas of the catalyst and support follow the order NCS_{ver}>NCS_{hydr}>NCS_{hor}. The surface area of the catalyst is a summation of the surface area of the support and the supported metal particles. A bigger increase in catalyst surface area compared to that of the support suggests smaller

iron particles are deposited on the surface of the support. This result provides an explanation of the sizes of the different iron particles determined by TEM (Table. 7.3).

TGA studies of the as-synthesised NCSs and the iron catalysts (recorded in air) are presented in Fig. 7.9i to iii. As can be seen from the weight loss graphs of NCS_{ver} and NCS_{hor} presented in Fig. 7.3i and ii respectively, these materials decompose at ca. 700 ^{o}C in air. However, in the presence of iron (Fig. 7.9i and ii) the oxidation onset temperature is lowered to ca. 430 ^{o}C. This is due to the catalytic effect of the iron on the oxidation of carbon spheres. This effect has been previously reported in the literature [32-34]. The same catalysed oxidation reaction was not clearly observed on the NCS_{hydr} because of the simultaneous decomposition of the oxygen-containing functional groups which starts at ca. 370 ^{o}C (Fig. 7.3iii) and the low oxidation temperature associated with these materials. The percentage iron loading was confirmed by noting the residual weight from the TGA profiles (Fig. 7.9i to iii). A residual percentage weight of ca. 7 % was observed for all catalysts after completely oxidising the NCSs in air (Fig. 7.9i to iii). Then this corresponds to a 5 % Fe^{0} loading for all three catalysts if the assumption is made that the residual material is entirely Fe_2O_3.

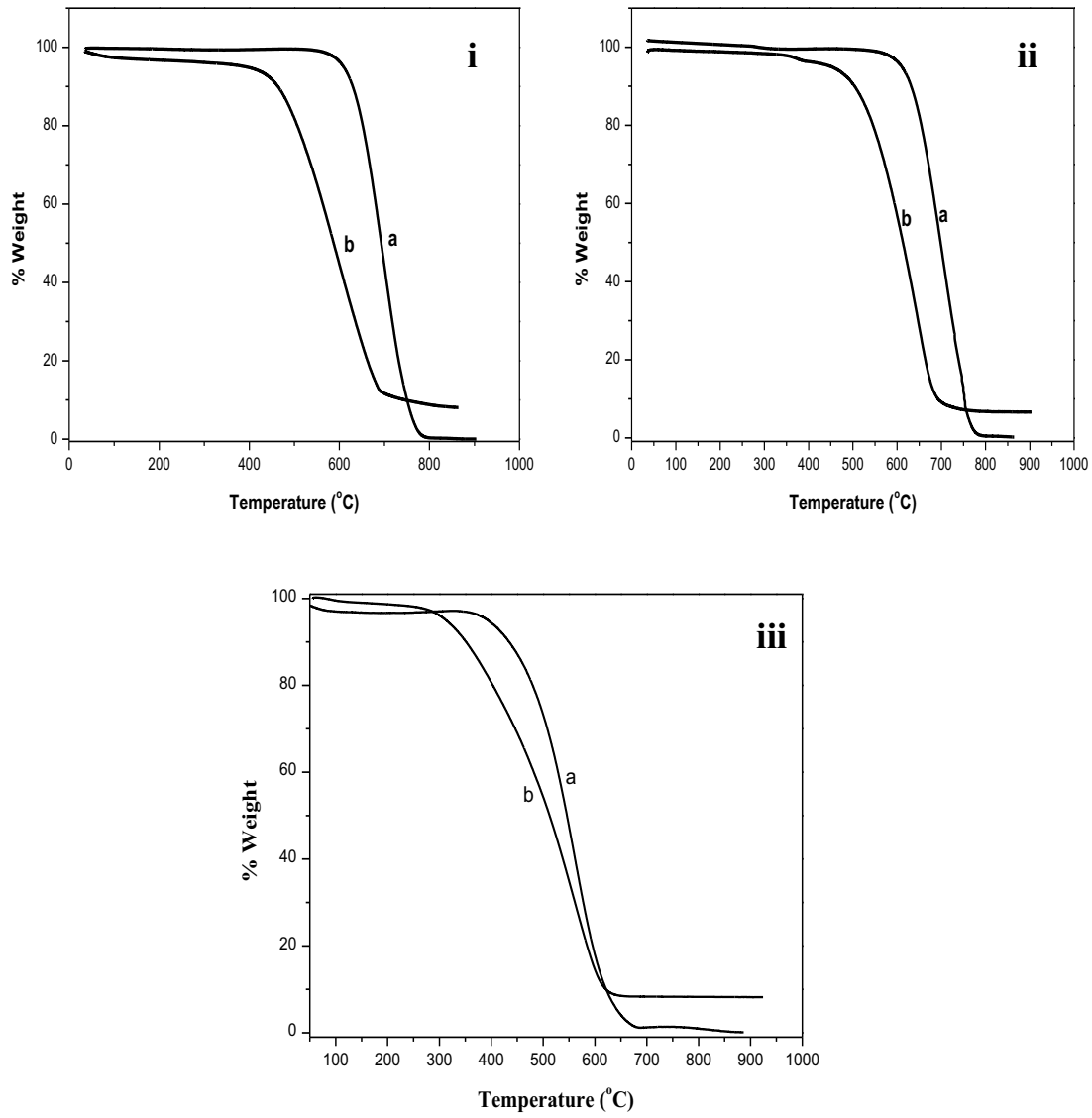


Figure 7.9: TGA profiles run in air of (a) as synthesised NCSs (b) 5% Fe catalyst supported on (**i**) NCS_{ver}, (**ii**) NCS_{hor} and (**iii**) NCS_{hydr}.

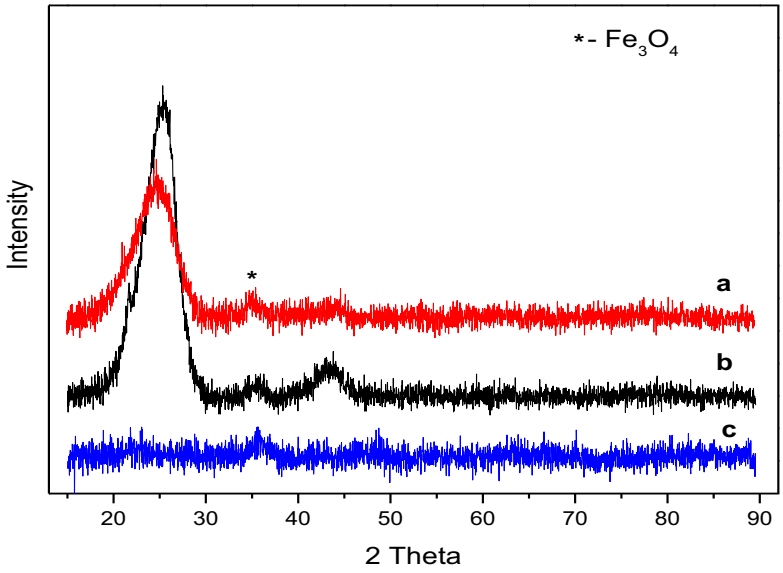


Figure 7.10: XRD patterns of (a) 5 % Fe/NCS_{ver} (b) 5 % Fe/NCS_{hor} (c) 5 % Fe/NCS_{hydr}

Fig. 7.10 shows the XRD patterns of the 5 % Fe catalysts. The peaks due to iron oxide are shown at ca. 36 ^{o} and carbon peaks were seen for NCS_{ver} and CS_{hor}. However carbon peaks could not be noted for NCS_{hydr} due to the amorphous nature of the carbon. The Fe sizes determined for XRD were 13, 29 and 21 nm for 5 % Fe/NCS_{ver} , 5 % Fe/NCS_{hor} and 5 % Fe/NCS_{hydr} respectively.

TPR and H_2-chemisorption experiments were not performed because fine materials tend to cause instrument blockage.

7.3.3 Fischer Tropsch synthesis over 5 % Fe/NCSs catalysts

Prior to FTS, all catalysts were reduced in 99.99 % H_2 at 330 ^{o}C for 18 h. FTS experiments were carried out under a set of similar conditions (275 ^{o}C, 8 bar and H_2/CO = 2). Table 7.4 summarises the FTS results of the 5 % Fe loaded carbon sphere catalysts. All three catalysts reached steady activity state after 30 h on stream. The activity (% CO conversions) was in the order NCS_{ver} > NCS_{hydr} > NCS_{hor} for the 5 % Fe loaded catalysts. The activity of the catalysts was

influenced by the Fe crystallite sizes and hence Fe dispersion. NCS_{ver} materials showed the highest surface area and the biggest I_D/I_G ratios (Table. 7.1) implying that they exhibited the most amorphous surface. The relatively large reactive surfaces of NCS_{ver} allowed for smaller and well dispersed FT active Fe phases to be deposited on them. It was expected that NCS_{hor} would show higher FT activity than NCS_{hydr} for those reasons. However, NCS_{hydr} materials contain abundant C=O and OH groups attached to their surfaces [31]. These functional groups act as additional anchoring sites for Fe metal particles deposited on the surface of the NCS_{hydr}. Due to the larger number of sites available for metal loading on NCS_{hydr}, a larger number of FT active Fe particles were available on NCS_{hydr} than on NCS_{hor} support materials although a broad Fe metal particle size range was achieved on NCS_{hydr} support material influenced by the wide size range of NCS_{hydr}.

The CO_2 selectivity followed the same trend as the catalyst's activity. This is because the rate of the WGS reaction, responsible for CO_2 production depends on the water partial pressure in the reactor which is influenced by the FTS rate.

Table 7.4: FTS results of 5 % Fe/NCS catalysts.

		% Mol selectivity						[a] Fe size after
Support	**% CO Conv.**	**CO_2**	**C_1**	**C_2-C_4**	**C_{5+}**	**$C_{2=}$**	**α-value**	**120 h FTS (nm)**
NCS_{Ver}	49.3	13.3	22.3	26.1	51.6	6.1	0.71	5-20
NCS_{Hor}	40.2	6.3	27.9	33.8	38.3	4.8	0.54	20-40
NCS_{hydr}	43.7	9.4	25.8	32.9	41.3	7.9	0.67	5-30

[a]*-determined by TEM after 120 h FTS*

The 5 % Fe/NCS_{hor} catalyst showed the highest selectivity towards methane and C_2-C_4 and had the lowest selectivity towards C_{5+} and CO_2 products due to the large Fe particle size effects (Table 7.4) [35]. The effect of Fe crystallite size and dispersion on the FT activity and hydrocarbon selectivity is noted when the

NCS_{ver} and NCS_{hydr} supported catalysts are compared (Table 7.4). The smaller spheres of NCS_{ver} may lead to gas and product diffusion restrictions which facilitates re-adsorption and reaction of primary FT products in spaces between the NCSs lead to the formation of longer hydrocarbon chains.

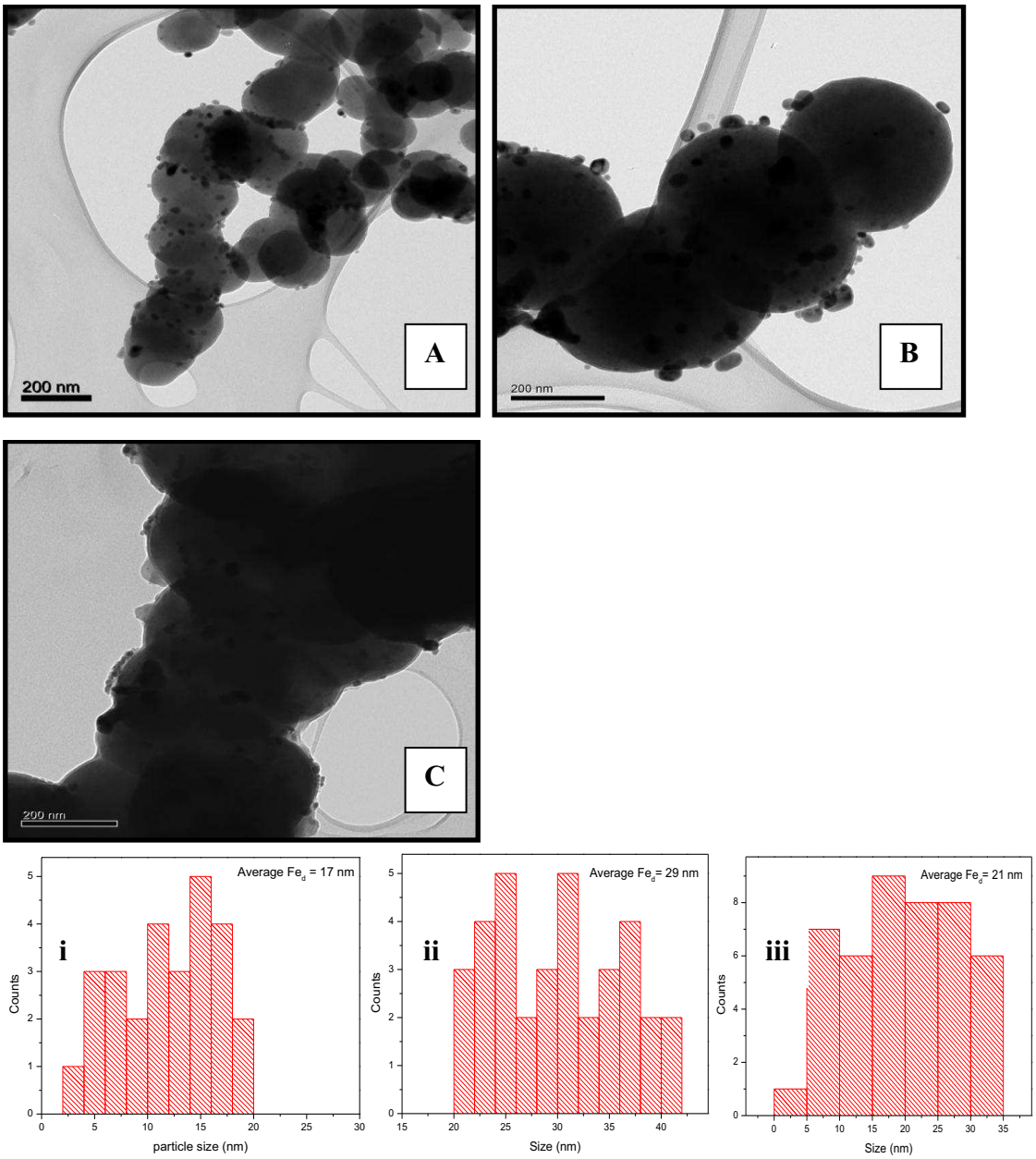


Figure 7.11: TEM images of (a) 5 % Fe/NCS_{ver} (b) 5 % Fe/NCS_{hor} (c) 5 % Fe/NCS_{hydr} and size distribution of (i) 5 % Fe/NCS_{ver} (ii) 5 % Fe/NCS_{hor} (iii) 5 % Fe/NCS_{hydr} after 120 h of FTS.

TEM studies of the Fe catalysts after 120 h of reaction time (Fig. 7.11) revealed that the same particle size order of 5 % Fe/NCS_{ver} > 5 % Fe/NCS_{hydr} > 5 % Fe/NCS_{hor} was still valid. Very little metal sintering was noted in all catalysts, implying that nitrogen functionalities are thermally stable under FT reaction conditions and their presence creates stable sites for Fe particles to attach on, thereby limiting metal sintering.

7. 4 Conclusions

NCSs were successfully synthesised in our laboratory using three different methods (i) a vertical furnace CVD method; (ii) a horizontal furnace CVD method and; (iii) a hydrothermal method in an autoclave. The synthesised NCSs showed different chemical and physical properties. NCS_{ver} contained mainly pyridinic nitrogen groups, while the NCS_{hor} sample contained equal ratios of pyridinic and quaternary nitrogen. NCS_{hydr} contained entirely pyrolic nitrogen. The oxygen content in the NCSs was shown to largely depend on the synthesis method used, NCS_{hydr} sample had the highest oxygen concentration as a result of the use of sucrose as a carbon source in this sample. The small quantities of oxygen observed in the NCS_{hor} and NCS_{ver} samples were as result of oxygen uptake from the atmosphere when these materials were exposed to air. This has been previously reported in the literature [7-9].

The effect of the properties of NCSs resulting from different synthesis methods was investigated when these materials are used as supports for Fe catalysts. The NCS synthetic methods outlined in this study affected the size, degree of graphitisation and reactivity of the carbon spheres. Although NCS_{hydr} possess large amounts of oxygen and nitrogen functionalities, which act as anchoring sites for Fe particles, their very low surface area and presence of polymeric and oligomeric compounds formed during NCS_{hydr} synthesis (see chapter 6), led to larger and less dispersed particles than those supported on NCS_{ver}. The amount of

defects on a carbon material is shown to play a crucial role in dispersing metal particles. FT results revealed that NCS_{ver} had the best FT results because of the higher surface area and the presence of defects on the surface. NCSs make potentially good support materials for studying Fe catalysts when it is desirable not to have any residual impurities since they are synthesized without a catalyst.

References

1. N.A Owen, O.R Inderwildi, D.A King, Energy Policy 38 (2010) 4743.
2. M.J. Gradassi, Stud. Surf. Sci. Catal. 119 (1998) 35.
3. C.H. Bartholomew, Stud. Surf. Sci. Catal. 64 (1991) 158.
4. A.Y. Khodakov, W. Chu and P. Fongarland, Chem. Rev. 107 (2007) 1692.
5. F. Rodr´ıguez-Reinoso, in J.W. Patrick, Ed., Porosity in Carbons: Characterization and Applications, Edward Arnold, London (1995).
6. A.A. Deshmukh, S.D. Mhlanga, N.J. Coville, Mater. Sci. Eng., R 70 (2010) 1.
7. C. Prado-Burguete, A. Linares-Solano, F. Rodr´ıguez-Reinoso, C. Salinas-Mart´ınez de Lecea, J. Catal. 115 (1989) 98.
8. C. Prado-Burguete, A. Linares-Solano, F. Rodr´ıguez-Reinoso, C. Salinas-Mart´ınez de Lecea, J. Catal. 128 (1991) 397.
9. F. Rodr´ıguez-Reinoso, Carbon 36 (1998) 159.
10. M. Trépanier, A. Tavasoli, A.K Dalai, N. Abatzoglou, Fuel Process. Technol. 90 (2009) 367.
11. H. Xiong, M.A.M. Motchelaho, M. Moyo, L.L. Jewell, N. J. Coville, J. Catal. 278 (2011) 26.
12. E. van Steen, F.F Prinsloo, Catal. Today 71 (2002) 327.
13. R.M.M Abbaslo, A. Tavasoli, A.K. Dalai, Appl. Catal. A: Gen. 355 (2009) 33.
14. M.C. Bahome, L.L Jewell, D. Hildebrandt, D. Glasser, N.J Coville, Appl. Catal. A: Gen. 287 (2005) 60.
15. E.J Biddinger, D. von Deak, U. S. Ozkan, Top. Catal. 52 (2009) 1566.
16. Ed. P. Serp, J.L. Figueiredo, carbon materials for catalysis, John Wiley & Sons, Inc, New Jersey (2009) 50.
17. J. Lahaye, G. Nanse, A. Bagreev, V. Strelko, Carbon 37 (1999) 585.
18. Y. Tomastubara, S. Ida, H. Fujitsu, H. Mochida, Fuel 63 (1984) 1738.
19. Y. Elsayed, T.J. Bandosz, Langmuir 18 (2002) 3213.
20. H. Xiong, M. Moyo, M.K Rayner, L.L Jewell, D.G Billing, N.J Coville, Chemcatchem, 2 (2010) 514.

21. A. Guerrero-Ruiz, I. Rodr´ıguez-Ramos, F. Rodr´ıguez-Reinoso, C. Moreno-Castilla, J.D. L´opez-Gonz´alez, Carbon 26 (1988) 417.
22. P.H. Matter, L. Zhang, U.S. Ozkan, J. Catal. 239 (2006) 83.
23. A.M.M Motchelaho, PhD Thesis, Iron and cobalt catalysts supported on carbon nanotubes for use in the Fischer-Tropsch synthesis, University of the Witwatersrand (2011) 203.
24. D.J. Duvenhage, The Prepapration, Characterization and Evaluation of Titania Supported Fe:Co Bimetallic Catalysts for the Hydrogenation of CO, PhD Thesis, University of the Witwatersrand, Johannesburg, 1994.
25. J.R Pels, F. Kapteijn, J.A.Moulijn, Q. Zhu, K.M Thomas, Carbon 33 (1995) 1641.
26. T.X. Tao, X.B. Zhang, F.Y. Sun, J.P. Cheng,F. Liu, Z.Q. Luo, Diamond. Relat. Mater. 16 (2007) 425.
27. P. Ayala, A. Gruneis, T.Gemming, D. Grimm, C. Kramberger, M.H. Rummeli, J. Phys. Chem. C 111 (2007) 2879.
28. H. Liu, Y. Zhang, R. Li, X. Sun, S. Desilets, H. Abou-Rachid, M. Jaidann, L. Lussier, Carbon 48 (2010) 1498.
29. Z. Chen, D. Higgins, Z. Chen, Carbon 48 (2010) 3057.
30. S. Maldonado, S. Morin, K.J Stevenson, Carbon 44 (2006) 1429.
31. X.M Sun, Y.D Li. Angew. Chem., Int. Ed. 43 (2004) 597.
32. H. Xiong, M. Moyo, M. A.M Motchelaho, L.L. Jewell, N. Coville, Appl. Catal A: Gen. 388 (2010) 168.
33. G. S. Szymanski, T. Grzybek, H. Papp, Catal. Today 90 (2004) 51.
34. H. Juntgen, in P. Thrower, Ed., Chemistry and Physics of Carbon, Vol. 22, Marcel Dekker, New York, (1989) 145.
35. J. Park, Y Lee, P. K. Khanna, K. Jun, J. W. Bae, Y. H. Kim, J. Mol. Catal. 323.

Chapter 8

Conclusions

Carbon spheres (CSs) with a narrow size range were successfully synthesized using a horizontal furnace CVD method in our laboratory. Although these materials showed low surface areas (by BET analysis) they possessed interesting properties that outweighed this disadvantage when used as support materials for catalysts. These properties, not attainable with other previously studied conventional metal oxide supports include: high purity, inert surface chemical nature, absence of micro pores and the metal precursor can be recovered easily by simply burning off the CSs. With these properties, CSs are potentially good model supports for studying promoter effects with little interference of the support material.

The as-synthesized CSs have an inert surface and they are hydrophobic and immiscible in polar solvents. Therefore, oxygen containing functional groups e.g. OH, COOH etc were introduced to the surface of the CSs by treating these materials with $KMnO_4$ and HNO_3 functionalizing agents. TGA, TEM and alkalimetry studies showed that the best reaction conditions for functionalizing CSs with HNO_3 were 55 % HNO_3/40 ^oC/24 h. These conditions introduce detectable amounts of oxygen functionalities without altering the morphology of the CSs. A 0.5M $KMnO_4$/40 ^oC/4 h acidification was selected for $KMnO_4$ functionalised CSs because these conditions gave similar amounts of acid groups when compared to those treated with HNO_3. Furthermore, the morphology of the CSs is maintained using this functionalisation procedure. FTIR results showed

that similar functional groups were introduced onto the surface of the CSs when either HNO3 or $KMnO_4$ were used as a functionalizing agent. This allowed for the study of the effect of the two functionalizing agents to be compared when Co particles are deposited onto the CSs.

After functionalisation of the CSs, Co metal particles were successfully deposited onto the surface of the CSs using a deposition precipitation method. The use of TEM studies were used to compare different cobalt loadings (2.5, 5 and 10 %) on the functionalised CSs and revealed that the 5 % Co loading was the preferred metal loading on these CSs. A 2.5 % metal loading was shown to be too low whereas 10 % metal loadings gave large metal particles.

Co crystallites of a size range 3-10 nm were successfully deposited onto the functionalised CSs in the 5 % Co loaded catalysts. The effect of functionalizing agents was indicated by the dispersion of the Co particles on the functionalised CSs. TEM studies on the 5 % Co/CS catalysts showed that, the HNO_3 functionalised catalysts formed clusters of Co particles while the $KMnO_4$ functionalised catalyst formed better dispersed Co particles. The dispersion of the Co particles was influenced by the functionalizing conditions and the oxidizing strength of the functionalizing agent used. HNO_3 is a weaker oxidizing agent than $KMnO_4$ hence it oxidizes the weaker areas of the CSs located in between the carbon flakes. $KMnO_4$ is a stronger oxidizing agent and oxidizes the CSs surface much more uniformly. The functionalised areas on the CSs act as anchoring sites for Co metal loading.

The use of $KMnO_4$ as a functionalizing agent results in residual Mn and K ions remaining on the surface of the CSs (as determined by EDS). The presence of these ions changed the final catalyst product selectivity to higher olefins and C_{5+} when these catalysts were evaluated for FTS. In an attempt to understand the role of each residual ion, the 5 % Co/CS HNO_3 functionalised catalyst was promoted

with Mn and K in the ratios of Mn/Co = 0.01 and K/Co = 0.01. The FT product selectivity of the $KMnO_4$ functionalised catalyst was compared to the promoted catalysts. The results revealed that the product selectivity of the $KMnO_4$ functionalised catalysts was much more similar to the Mn promoted catalyst.

To enhance the surface area of the CSs, a low temperature hydrothermal method in an autoclave was used to synthesize high surface CS_{hydr} materials from a sucrose substrate. CS_{hydr} materials of diameter range 800-1200 nm were successfully synthesised from a sucrose substrate by a low temperature hydrothermal synthesis method using an autoclave. After several centrifugal steps of these materials in water and ethanol, TGA studies revealed that volatile by-products (oligomeric and polymeric compounds) remain entrapped on the CS_{hydr}. The effect of annealing temperature was investigated on the as-synthesised CS_{hydr}. BET and TEM studies showed that an increase in the annealing temperature from 250 ^oC to 800 ^oC increased the surface area from 1.8 to 433 m^2/g of CS_{hydr} without changing the morphology of these materials. These trapped compounds were completely removed by simply annealing the as-synthesised CS_{hydr} above 450 ^oC in N_2 gas.

The effect of the presence of the oligomeric and polymeric compounds on Co/CS_{hydr} catalysts was investigated by depositing Co particles on the CS_{hydr} materials after annealing them at different temperatures. The results showed that the presence of oligomeric and polymeric products resulted in formation of large Co particles (which could not be measured) being deposited onto the CS_{hydr} due to the very low surface area of the support. Removal of these by-products at 600 ^oC gave smaller Co particles (average size = 20 nm) deposited onto the CS_{hydr}. The synthesised Co/CS_{hydr} catalysts were then tested for FT activity and selectivity. FTS results showed that the presence of oligomeric and polymeric compounds resulted in a low % CO conversion (9.8 %), but removal of the polymeric and

oligomeric materials by annealing the CS_{hydr} at 600 ^{o}C before metal loading gave Co/CS_{hydr} catalysts with higher % CO conversion (23.1 %) under identical FT reaction conditions. The $Co250C_{hydr}$ catalyst showed the highest selectivity for C_1 (37.8 %) and lowest C_{5+} (27.6 %) while the $Co600C_{hydr}$ catalyst showed the lowest selectivity towards C_1 products (25.9 %) and the highest selectivity towards C_{5+} products (53.6 %). Similarly the chain growth probability (α) increased with increasing the CS_{hydr} annealing temperature. Clearly, hydrocarbon product selectivity for these catalysts can be correlated to CS_{hydr} annealing temperature. In addition the highest CO_2 percentage mole selectivity was observed on the $Co450CS_{hydr}$ catalysts (1.6 %) while the lowest CO_2 selectivity was observed on the $Co600C_{hydr}$ catalyst (0.9 %).

Nitrogen doped carbon spheres (NCSs) were successfully synthesized using three different methods; (i) CVD in a horizontal furnace (NCS_{hor}); (ii) CVD in a vertical furnace (NCS_{ver}); and (iii) hydrothermal synthesis in an autoclave (NCS_{hydr}). The as-synthesized NCSs showed different chemical and physical properties. XPS results showed that NCS_{ver} contained mainly pyridinic nitrogen groups, while the NCS_{hor} sample contained equal ratios of pyridinic and quaternary nitrogen. NCS_{hydr} contained entirely pyrolic nitrogen. Varying amounts of oxygen functionalities were detected in all samples. The oxygen content in the NCSs was shown to largely depend on the synthesis method used; NCS_{hydr} showed the highest oxygen concentration (24.3 %) as a result of the use of sucrose as a carbon source in this sample. The small quantities of oxygen observed in the NCS_{hor} (5.9 %) and NCS_{ver} (3.6 %) samples arise from oxygen uptake from the atmosphere when these materials were exposed to air.

Fe crystallites were successfully deposited onto the NCS surface using a deposition-precipitation with urea (DPU) method. The Fe particle sizes were dependent on the size, graphitization and functional groups on the NCSs. The Fe/NCS_{ver} catalyst which had the smallest Fe particle size showed a higher % CO

conversion (49.3 %) than its counterparts (NCS_{hor} = 40.1 % and NCS_{hydr} = 43.7 %) under similar FT reaction conditions. The presence of oxygen functional groups introduced during NCS_{hydr} synthesis and the surface area of the support facilitated the dispersion of Fe particles, improving the FT activity of this catalyst compared to the Fe/NCS_{hor} catalyst. Fe/NCS_{hor} catalysts showed the highest selectivity towards C_1 products and the lowest selectivity towards C_{5+} products, while the Fe/NCS_{ver} showed the lowest selectivity towards C_1 products and the highest C_{5+} products. Hydrocarbon product selectivity could be correlated to Fe particle sizes. There was no clear correlation between N-type groups and Fe/NCS catalytic performance. Fe/NCS_{ver} showed the highest CO_2 selectivity due to the relatively high FT activity when compared to its counterparts.

In general CSs are good supports to study metal precursor and promoter interactions on FT catalysts. Some of the numerous advantages of using a CS support over a metal oxide support such as TiO_2, is that the metal precursor is easily characterized by microscopy techniques e.g. TEM or SEM. Although CSs synthesized by a CVD method possess a low surface area, the surface area of the carbon spheres can be improved by annealing the as-synthesised CS_{hydr} above 350 ^{o}C.

Recommendations

When large amounts of functional groups are desired without altering the morphology of the CSs oxidizing agents such as ozone, peroxides and/or stronger acids or bases would be investigated for functionalizing CVD synthesized CSs. For example the advantage of using H_2O_2 over $KMnO_4$ would be that highly pure functionalised CSs would be achieved. In this case these materials could be used as novel supports to study the catalytic and promoter effects of metals.

APPENDIX

APPENDIX A

GC analysis conditions

Online Analysis

GC- TCD

Detector:	TCD, T = 220 ^{o}C
Column type:	Packed, stainless steel, 2m x 2.2mm, O.D = 1/8"
Stationary phase:	Carbosieve S-II, 60-80 mesh
Sample valve temperature:	150 ^{o}C
Carrier gas:	Argon
Flow rate:	20 mL/min
Oven temperature:	250 ^{o}C
Products analysed:	H_2, N_2, CO, CH_4, CO_2

GC-FID

Detector FID:	T = 220 ^{o}C
Column type:	Packed, stainless steel, 1.5 m x 2.2 mm, O.D = 1/8"
Stationary phase:	ZB-5, 80/100 mesh
Sample valve temperature:	150 ^{o}C
Carrier gas:	Argon
Flow rate:	20 mL/min
Oven temperature:	250 ^{o}C
Product analysed	C_1-C_{10}

Offline Analysis

GC-FID

Detector:	FID, T = 350 ^{o}C
Column type:	Capillary column 30 m x 5 _FT, O.D.= 0.53 mm
Stationary phase:	ZB-1
Sample valve temperature:	250 ^{o}C
Carrier gas:	Air
Flow rate:	30 ml/min
Product analysed:	C_{5+}

Oven temperature programme

Oil analysis:

Heat to 60 ^{o}C at 10 ^{o}C /min,
heat to 300 ^{o}C at 12.5 ^{o}C/min,
hold at 300 ^{o}C for 30 min

Wax analysis:

Heat to 220 ^{o}C at 74 ^{o}C /min,
heat to 300 ^{o}C at 10 ^{o}C /min,
hold at 300 ^{o}C for 240 min

APPENDIX B

H_2-uptake analysis conditions

Analysis	Ramp Temp/^{o}C	Temp/^{o}C	Time(min)
Degas He	5	150	60
Evacuate	10	100	10
Flow H_2	2	330	1080
Flow H_2	2	330	60
Evacuate	2	350	240
Leak test	---	35	10
Evacuate	---	35	10
Analyse H_2[(a)]	1	100	--

[(a)]-Pressure points 100, 150,200,250,300,350,400,425 and 450 mmHg.

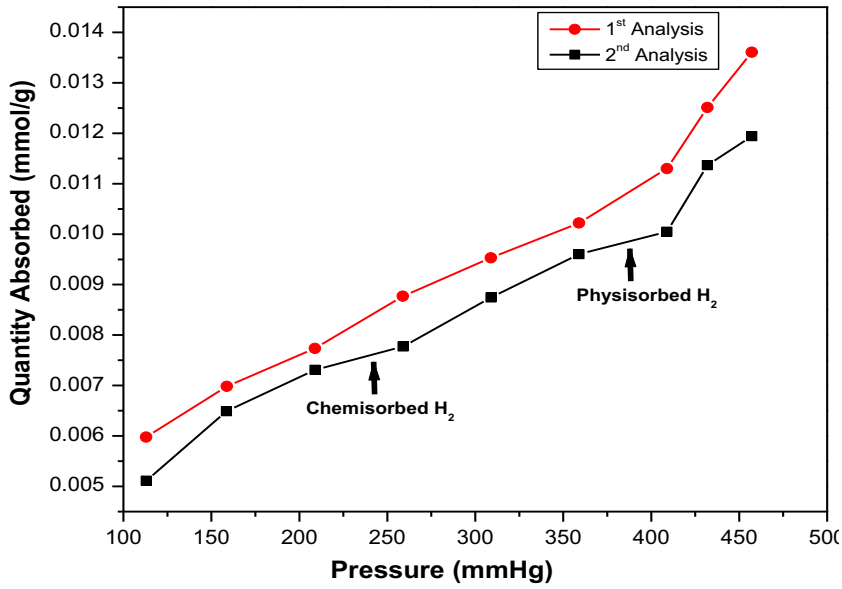


Figure B1: Adsorption isotherm of H_2 uptake during chemisorption analysis.

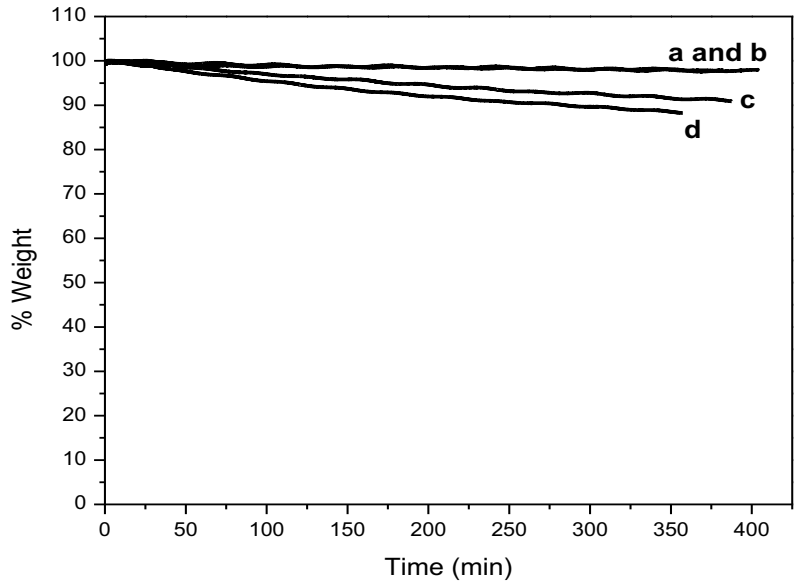


Figure B2: TGA profile of 5 % Co/CS run for 6 h under (a) air at 250 ^{o}C, (b) oxygen at 250 ^{o}C, (c) air at 300 ^{o}C and (d) oxygen at 300 ^{o}C.

Fig. B2c and d show that during the O_2-titration step at 300 ^{o}C ~8 % of the C support material is oxidised to CO_2 or CO whereas at 250 ^{o}C little to no effect on the mass of CSs was observed (Fig. B2a and b). The occurrence of this catalysed oxidation reaction at 300 ^{o}C leads to an increased O_2-uptake resulting in very low cobalt dispersion and larger particle sizes to be calculated.

In-situ XRD studies on the reduction (Fig. B3) and oxidation (Fig. B4) of 5 % Co/CS HNO_3 catalyst was investigated under similar conditions to those employed during chemisorption studies to gain an understanding of the oxidation of Co at 250 ^{o}C in air. Fig. B3 shows that the catalysts were completely reduced to Co^0 at 250 ^{o}C.

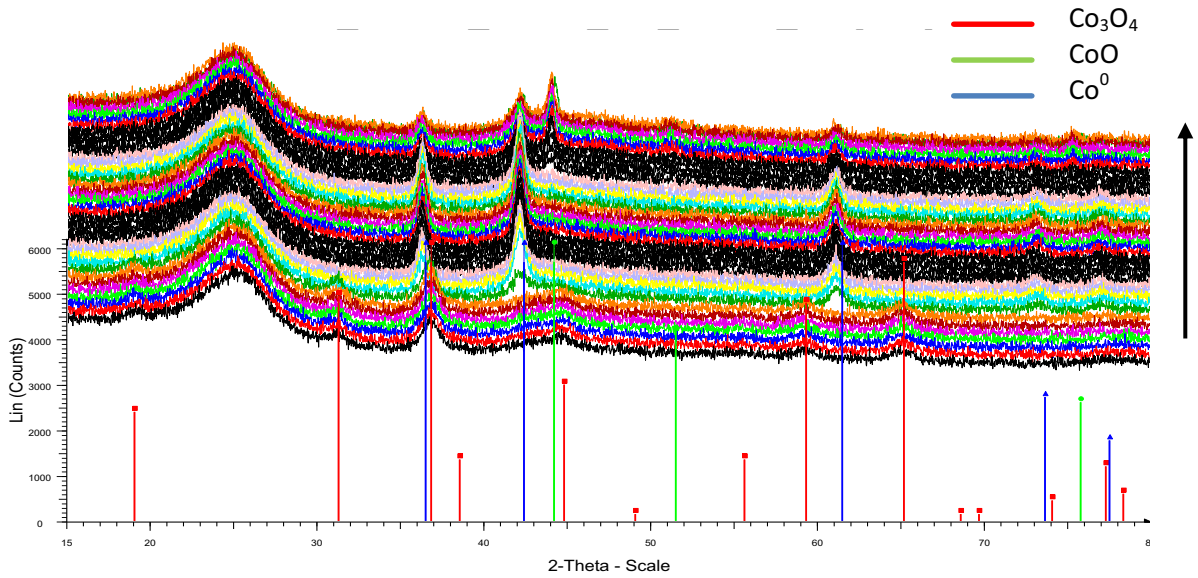


Figure B3: In-situ XRD patterns of reduction of Co_3O_4 phases in 5 % Co/CS HNO_3 catalyst at 350 ^oC for 24 h in 5 % H_2 (balance N_2 gas).

The Co_3O_4 and CoO phases confirmed to be present in the 5 % Co/CS HNO_3 catalyst were reduced to Co^0 at 350 ^oC in 5 % H_2 for 24 h (Fig. B3).

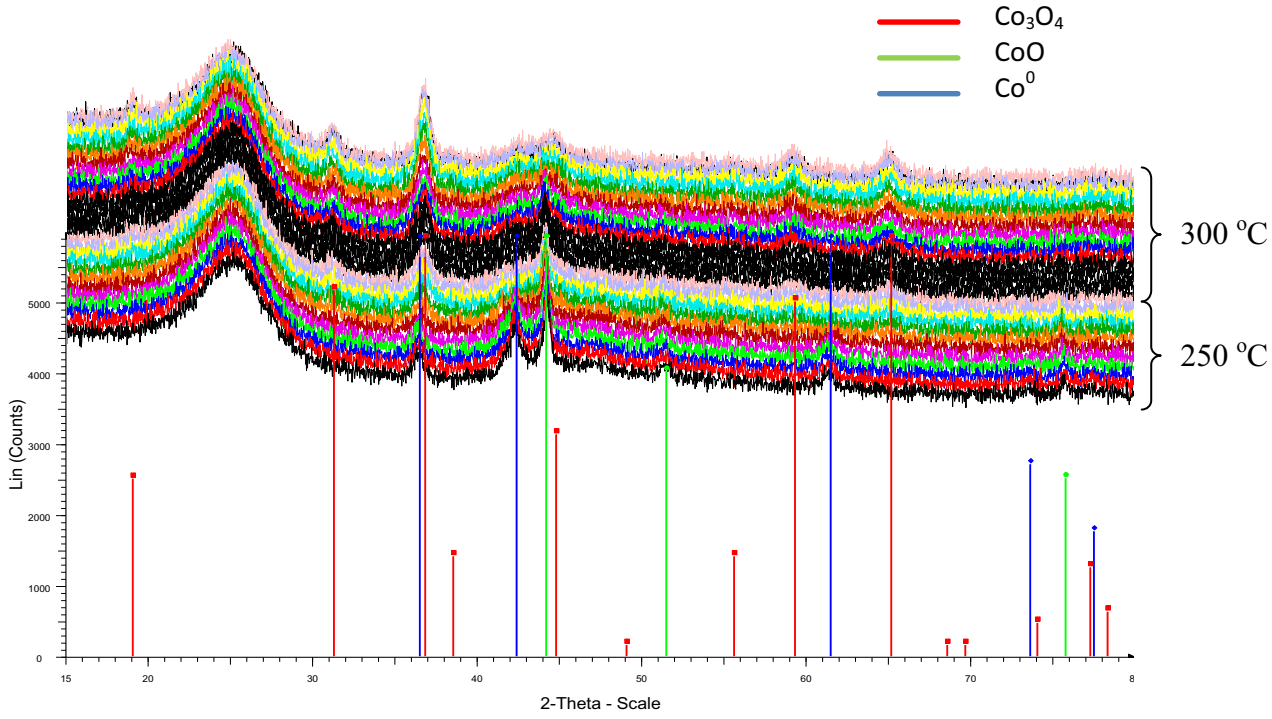


Figure B4: In-situ XRD patterns of oxidation of Co^0 phases in 5 % Co/CS HNO_3 catalyst in air.

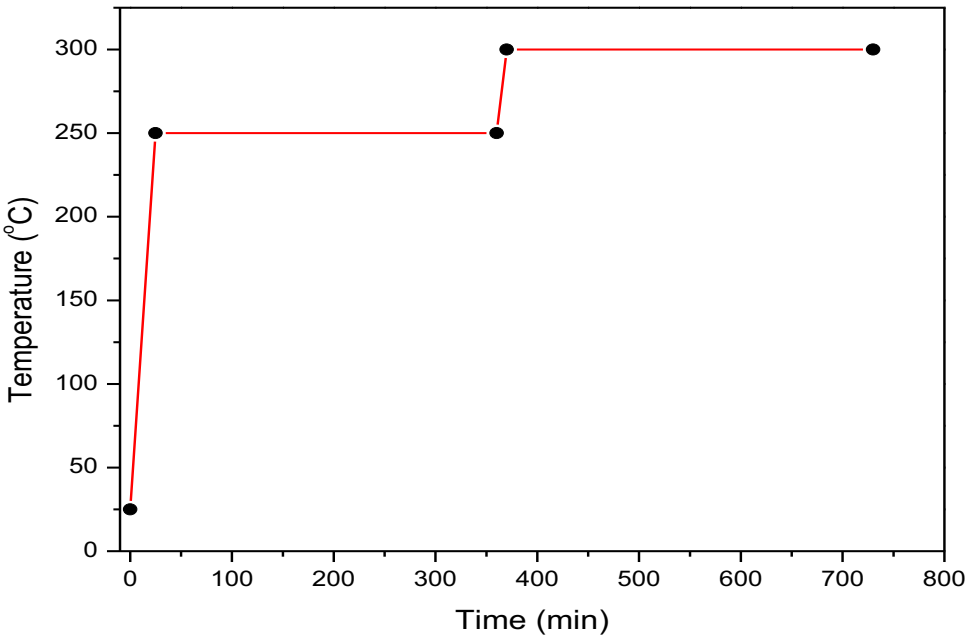


Figure B5: Temperature programme for the oxidation of Co^0 phases in 5 % Co/CS HNO_3 catalyst in air.

The Co^0 phases were oxidised air following a temperature programme presented in Fig. B5. From Fig. 4 revealed that Co^0 was only oxidised to CoO phases at 250 ^oC but to Co_3O_4 phases when the temperature was raised to 300 ^oC. The ratio of Co phases present will be quantified and used in chemisorption calculations in an attempt to obtain more accurate H_2-chemisorption results for Co/C materials.

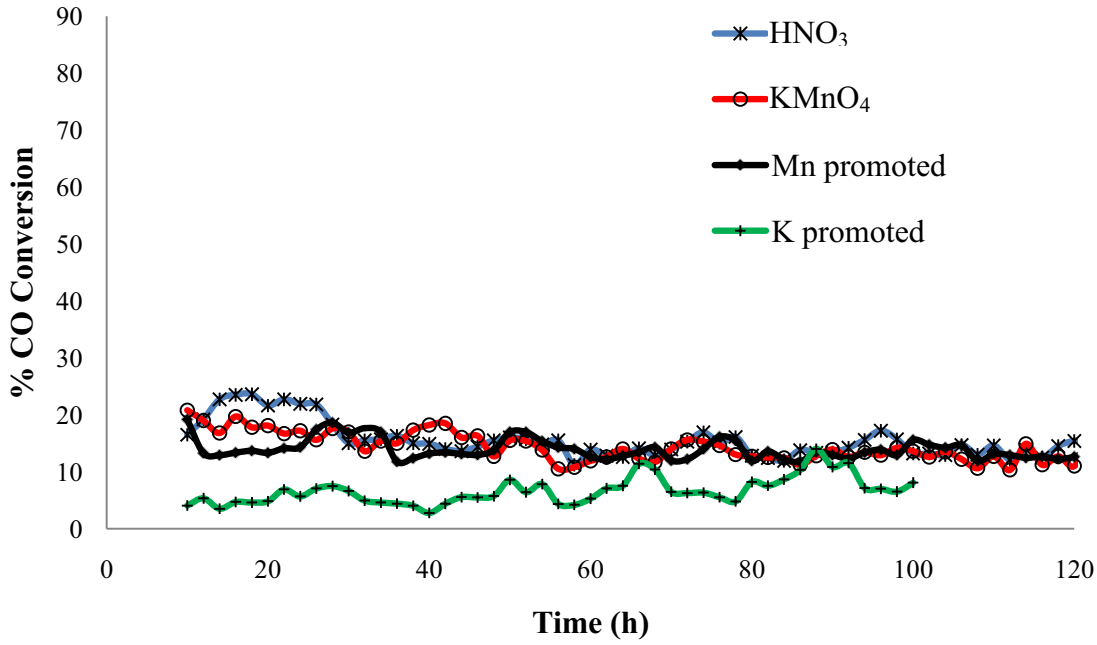


Figure B6: % CO conversion of 5 % Co/CS catalysts.

APPENDIX C

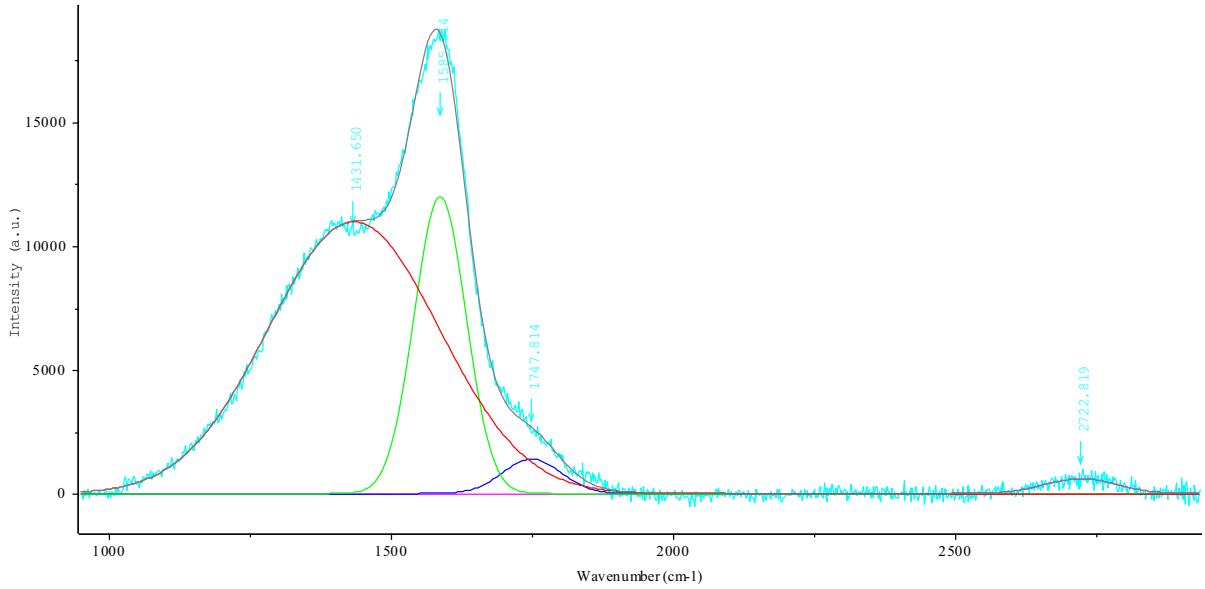


Figure C1: Raman spectra of CS_{hydr} annealed at 250 ^{o}C under N_2 for 2.5 h.

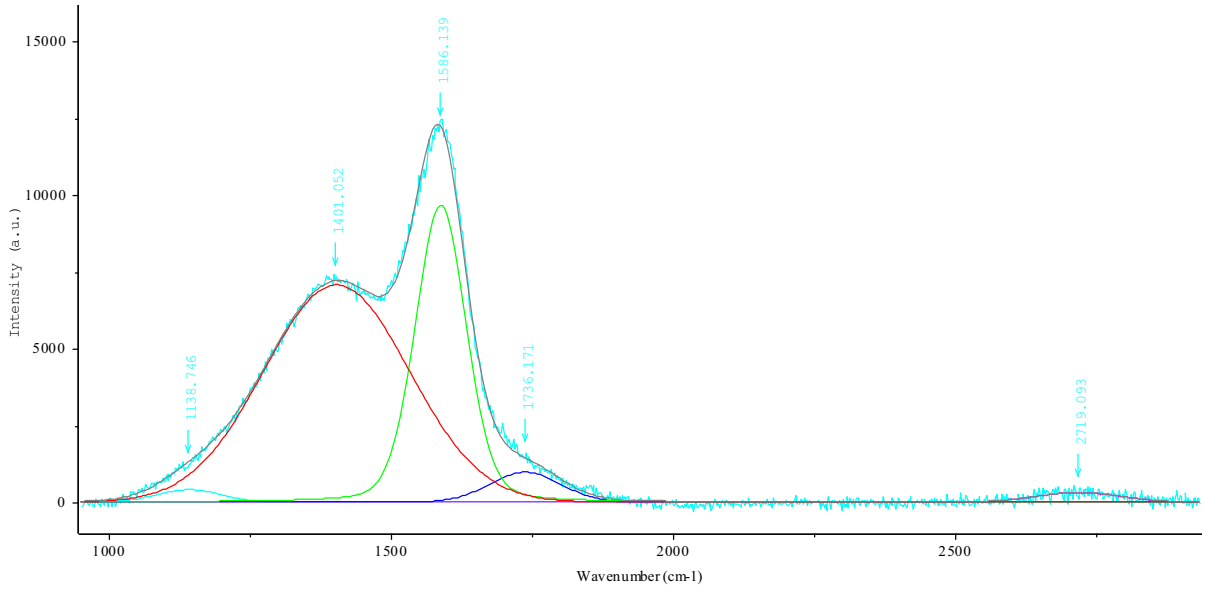


Figure C2: Raman spectra of CS_{hydr} annealed at 350 ^{o}C under N_2 for 2.5 h.

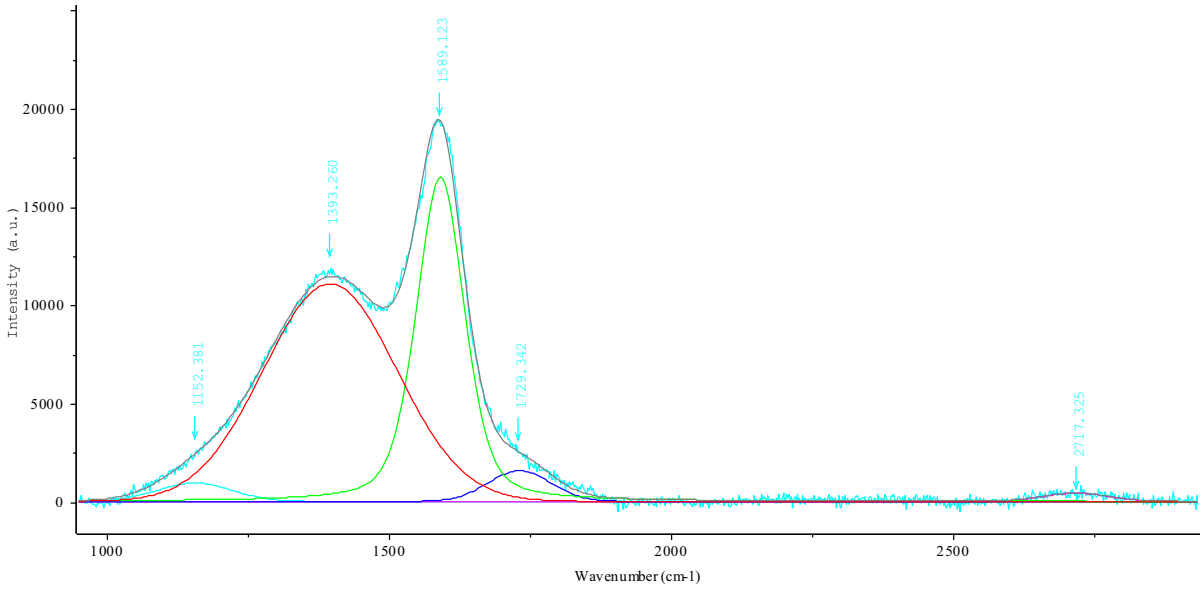


Figure C3: Raman spectra of CS_{hydr} annealed at 400 ^{o}C under N_2 for 2.5 h.

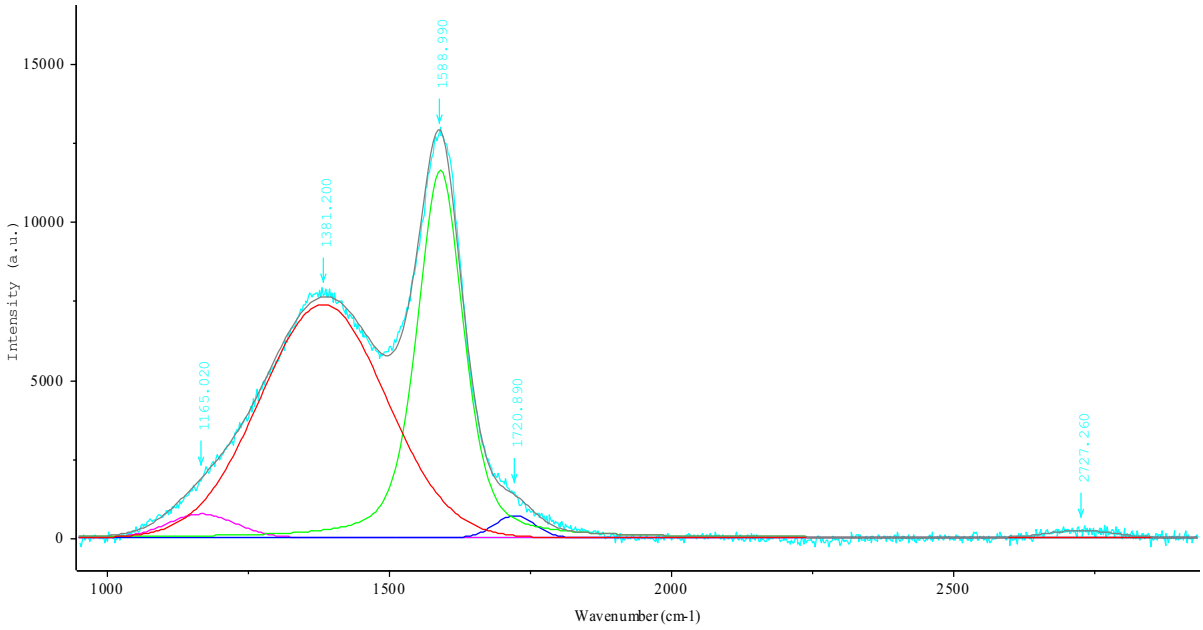


Figure C4: Raman spectra of CS_{hydr} annealed at 450 ^{o}C under N_2 for 2.5 h.

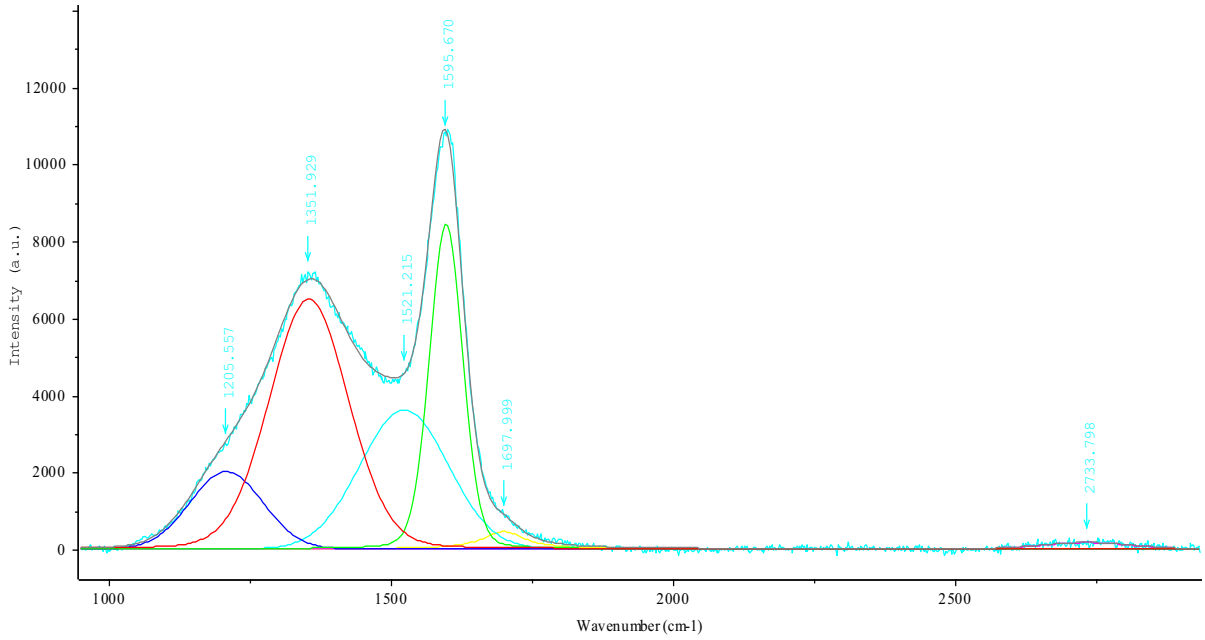


Figure C5: Raman spectra of CS_{hydr} annealed at 600 ^{o}C under N_2 for 2.5 h.

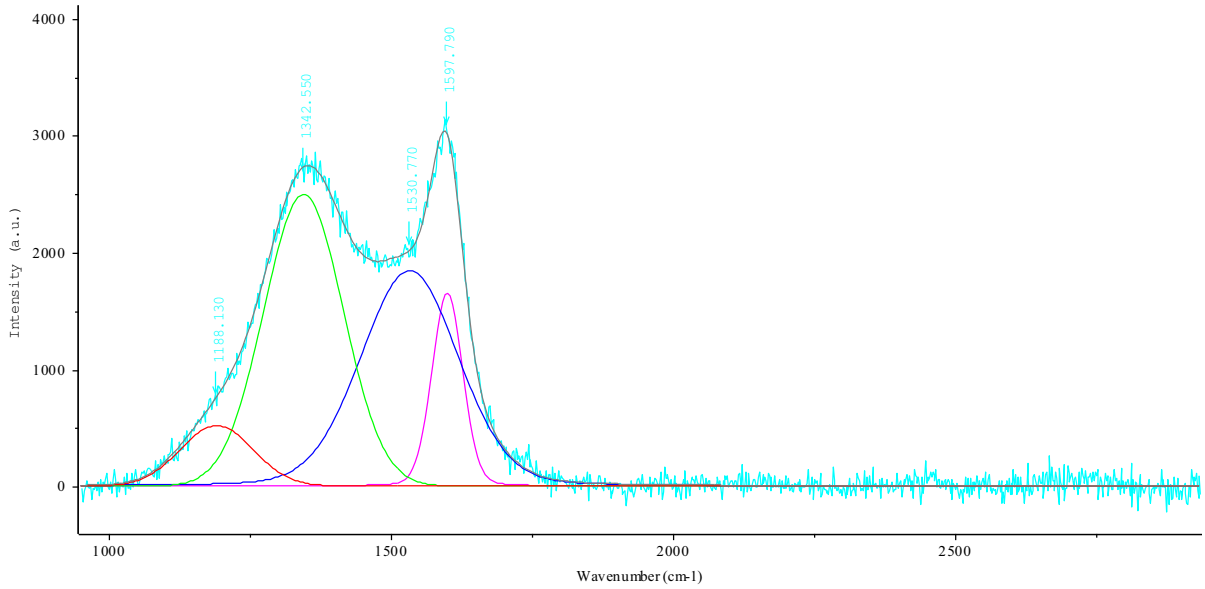


Figure C6: Raman spectra of CS_{hydr} annealed at 800 ^{o}C under N_2 for 2.5 h.

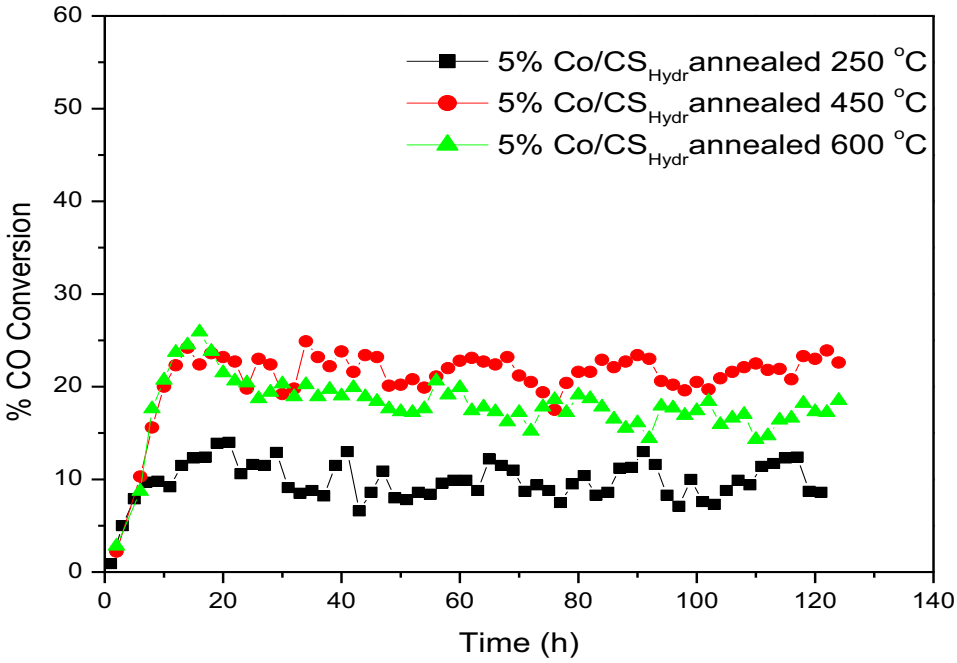


Figure C7: % CO conversion of 5% Co/CS_{hydr} catalysts.

APPENDIX D

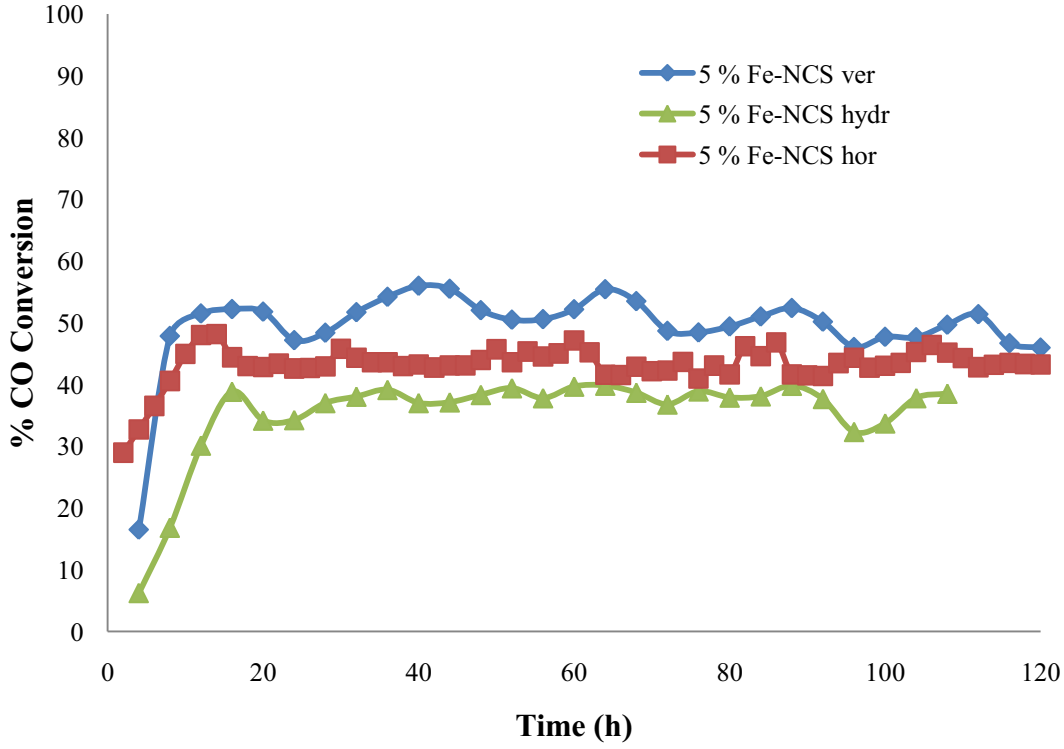


Figure D1: % CO conversion for 5 % Fe/NCS catalysts